CRANFIELD UNIVERSITY

ADNAN SYED

FIRESIDE CORROSION STUDY OF SUPERHEATER MATERIALS IN ADVANCED POWER PLANTS

SCHOOL OF APPLIED SCIENCE

PhD
Academic Year: 2008 - 2011

Supervisor: DR NIGEL SIMMS
PROF JOHN OAKEY
October 2011

CRANFIELD UNIVERSITY

SCHOOL OF APPLIED SCIENCE

PhD

Academic Year 2008 – 2011

ADNAN SYED

FIRESIDE CORROSION STUDY OF SUPERHEATER MATERIALS IN ADVANCED POWER PLANTS

Supervisor: DR NIGEL SIMMS
PROF JOHN OAKEY

October 2011

This thesis is submitted in partial fulfilment of the requirements for the degree of PhD

ABSTRACT

Conventional power plants are major emitters of CO_2 gases, which are believed to be contributing to global warming. An efficient, co-firing biomass-coal power plant with oxy-firing combustion system (running at high steam temperature and pressure), can play a vital role in CO_2 emission reduction. However, these techniques will further worsen the issue of fireside corrosion of heat exchangers. An increase in fireside corrosion rates can cause short component lives and unexpected failures if not dealt with appropriately.

The aim of this PhD study was to use laboratory-based testing to assess the performance of alloy materials under superheater conditions in simulated co-fired (biomass and coal) air and oxy-fired combustion. In this PhD project five different alloys were used. Synthetic deposits were also prepared to simulate superheater deposit compositions. Tests were carried out at temperatures appropriate for metal temperatures in superheaters/reheaters of future power plants. The performance of samples was determined using: mass change data, advanced microscopy techniques, x-ray diffraction and dimensional metrology. Additional tests were carried out to investigate deposit stability and the effect of high concentrations of salts.

The results achieved have confirmed the hypothesis that increased fireside corrosion rates are due to the combined effect of extreme environment: high temperatures, SO_2 and HCl gases, aggressive deposits. Corrosion damage follows trends that resembles ‘bell-shaped’ curve in both air and oxy-fired conditions. Alloy corrosion damage in novel oxy-firing compared to air-firing conditions was significantly higher at 700°C. The peak of the curve shifts from 650 to 700°C in oxy-fired conditions. The alloys with higher chromium content clearly showed better corrosion resistance. The work on deposit chemistry and exposure to high salt concentrations has improved the understanding of corrosion reaction mechanisms. Corrosion damage data have been used to produce basic fireside corrosion mathematical model; which can be used as a stepping stone towards further development of fireside corrosion models.

ACKNOWLEDGEMENTS

All praises to Allah who enabled me to do this study.

I would like to thanks my supervisor Dr Nigel Simms, who was very kind, extremely helpful and provided full guidance during my PhD studies.

I would like to thanks all the members of staff particularly Mr Peter West, Mr Tim Pryor, Ms Christine Chalk, Mr Richard Andrews, Dr T Hussain, Professor J Nicholls, and students particularly Ala Khodier and Mr Masoud Kavosh at Cranfield University for being supportive throughout the accomplishment of this task

I would like to acknowledge SUPERGEN part of EPSRC for the funding of this project

I would like to thanks my parents (Syed Riaz ul Hasan and Rana Sayed) for their prayers and encouragement during my studies

I am also grateful to my wife (Aliya) and children (Moosa, Safa and Mustafa) for their continuous support and patience, which enabled me to concentrate on my studies

I would also like to thanks my brothers (Zia bhai, Shuja bhai, Farhan, Irfan and Adeel) for their inspiration during last three years

And finally thanks to all my relatives and friends for their well wishes.

DEDICATION

With all respect and deep gratitude I dedicated this thesis to my loving grandparents, Syed Mushtaq Hussain (dada), Syed Hafeez uddin (nana), Jehanara begum (dadi) and Salma Masuma Agha (nani). Where I am today is indeed is the result of their prayers. May Allah grant them Al-Jannah.

TABLE OF CONTENTS

LIST OF FIGURES

LIST OF TABLES

LIST OF EQUATIONS

LIST OF ABBREVIATION

IEA	International Energy Agency
PC	Pulverised Coal
CCGT	Combined Cycle Gas Turbine
IGCC	Integrated Gasification Combine Cycle
FBC	Fluidised Bed Combustion
CCS	Carbon Capture Storage
PLE	Plant Life Time Extension
USC	Ultra Supercritical
GHG	Greenhouse Gas
DECC	Department Of Energy And Climate Change
UKERC	United Kingdom Energy Research Centre
SEM	Scanning Electron Microscopy
EDX	Energy Dispersive X-Ray
XRD	X-Ray Diffraction
AS	Atomic Spectroscopy
IC	Ion Chromatography
FCC	Face Cubic Centred
BCC	Body Centred Cubic
CEGB	Central Electricity Generating Board

CCP	Cereal–Co Product
PF	Pulverized Fuel
FGD	Flue Gas Desulphirisation
IPA	Isopropyl Alcohol
CBN	Cubin Boron Nitride
BSE	Back Scattered Electron
SE	Secondary Electron
AAS	Atomic Absorption Spectroscopy
AES	Atomic Emission Spectroscopy

1 INTRODUCTION

1.1 Electrical Energy and Power Generation Industry

Power generation industries are very important for both developed and developing countries since electrical energy has become a fundamental requirement for human beings. The generation of increasing amounts of electricity while simultaneously reducing environmental emissions has become a goal for the power generation industry worldwide. According to international energy agency (IEA) the demand in primary energy will increase by up to 49% by 2035 [1]. The power generation industry around the world is under tremendous pressure to generate a sufficient amount of power which is sustainable, affordable and reliable; and meet the industrial, transport, and domestic requirements. Some of the different sources used to generate electrical energy are: nuclear, solar, wind, hydro, bio-fuel, waste, fuel cell. However, fossil fuels (coal, oil and natural gas) are the main sources used within the power generation industry, and conventional steam turbine power plants are still widely used across the globe as the main source of power generation. Figure 1-1 illustrates the world electric generation from different fuel sources.

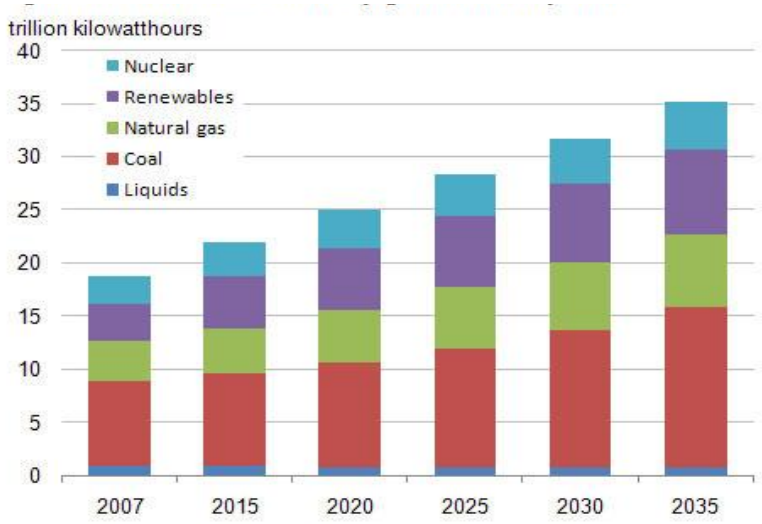

Figure 1-1: World net electricity generation by fuel [1]

1.2 Conventional Steam turbines Power Plants

A conventional steam turbine pulverised coal (PC) power plant is based on the principle where by hot gases produced by burning fuels vaporise pressurised water, which flows through heat exchanger tubes into high pressure superheated steam which drives a turbine and so generates of electricity [2]. As the steam passes through the turbine the temperature and pressure decreases; after further condensation into water this is pumped back into the boiler. This cycle is called the Rankine cycle. These words can be understood by the schematic diagram in Figure 1-2. Steam turbine power plants are widely used as the major source of electricity generation using coal as a primary fuel. According to IEA [1], power plants burning coal produce over 40% of the world's electricity requirement. However China, the highest energy consuming country, generates ~ 70% of its electricity using burning coal.

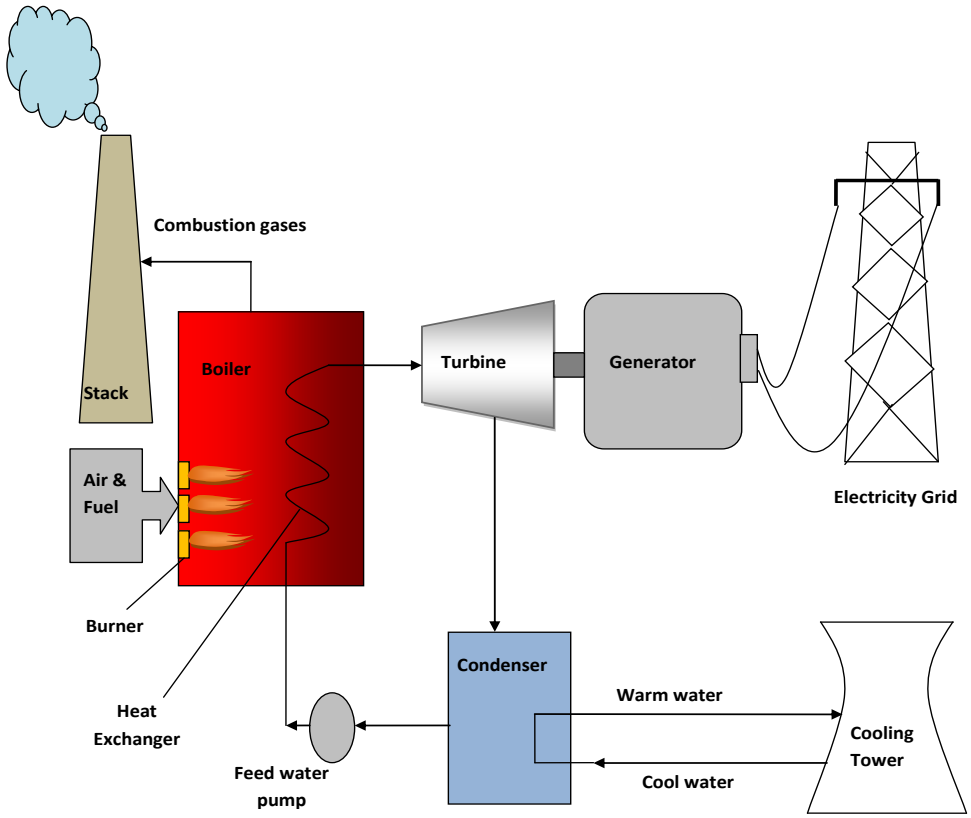

Figure 1-2: Schematic of conventional pulverised coal fired steam turbine power generation plant

Other power generation sources have advantages over PC power plant, for example gas turbines using natural gas as a fuel are more efficient, cheaper and require less space. However, the abundant of coal and its current pricing leads to prediction that large PC power plants will continue to dominate the power generation industry for years to come [1; 3-5]. A great deal of focus is now on developing modifications to the available technologies, for example, combined cycle gas turbine (CCGT); integrated gasification combine cycle (IGCC); fluidised bed combustion (FBC); co-firing blends of biomass-coal; and carbon capture storage (CCS). Particular attention is being given to steam related issues (increased steam temperatures and pressures) so that efficiencies can be increased and carbon dioxide emissions can be reduced. To increase efficiencies in pulverised fuel power plants (a Rankine cycle) it is necessary to use steam systems with higher temperatures and pressures. Targets have increased from traditional 540 – 560 °C steam systems through current 600-610 °C systems to ~650 °C (EU COST programmes), ~700 °C (EU AD 700 programme) and 760 °C (US, Japanese and EU research programmes) [6-9]. The effect of such changes in steam temperatures is to increase the range of metal temperatures that are needed in the heat exchangers in these plants; with superheater/reheater target surface temperatures needing to be increased from the traditional ~590-610 °C to ~650, ~700, ~750 and ~810 °C, respectively for the five cases above [10].

1.3 Plant life time extension (PLE) and the boilers

Plant lifetime extension (PLE) in the power generation industry is extending the life of the power plants by providing protection from effects such as corrosion and steam oxidation. The successful application of PLE will save time, cost and resources for the power generation industries which could be spent on building new power plants. The boilers, the most prominent component in the steam turbine power plants, are extremely large and consist of banks of long metal tubes which carry highly pressurised water and steam [11]. Figure 1-3 is a schematic representation of a boiler, showing the combustion gas flow path and the steam flow by means of tubes/pipes. These heat exchangers are:

superheater, reheater, water wall and economizer depending on their location within the steam system. The superheated steam flows from the superheaters to the high pressurise steam turbine where it drives the turbine-generator [2]. The metal tubes in the heat-exchangers are manufactured from different types of steels. The combustion gas temperature in the boiler varies between 400 and 1200°C.

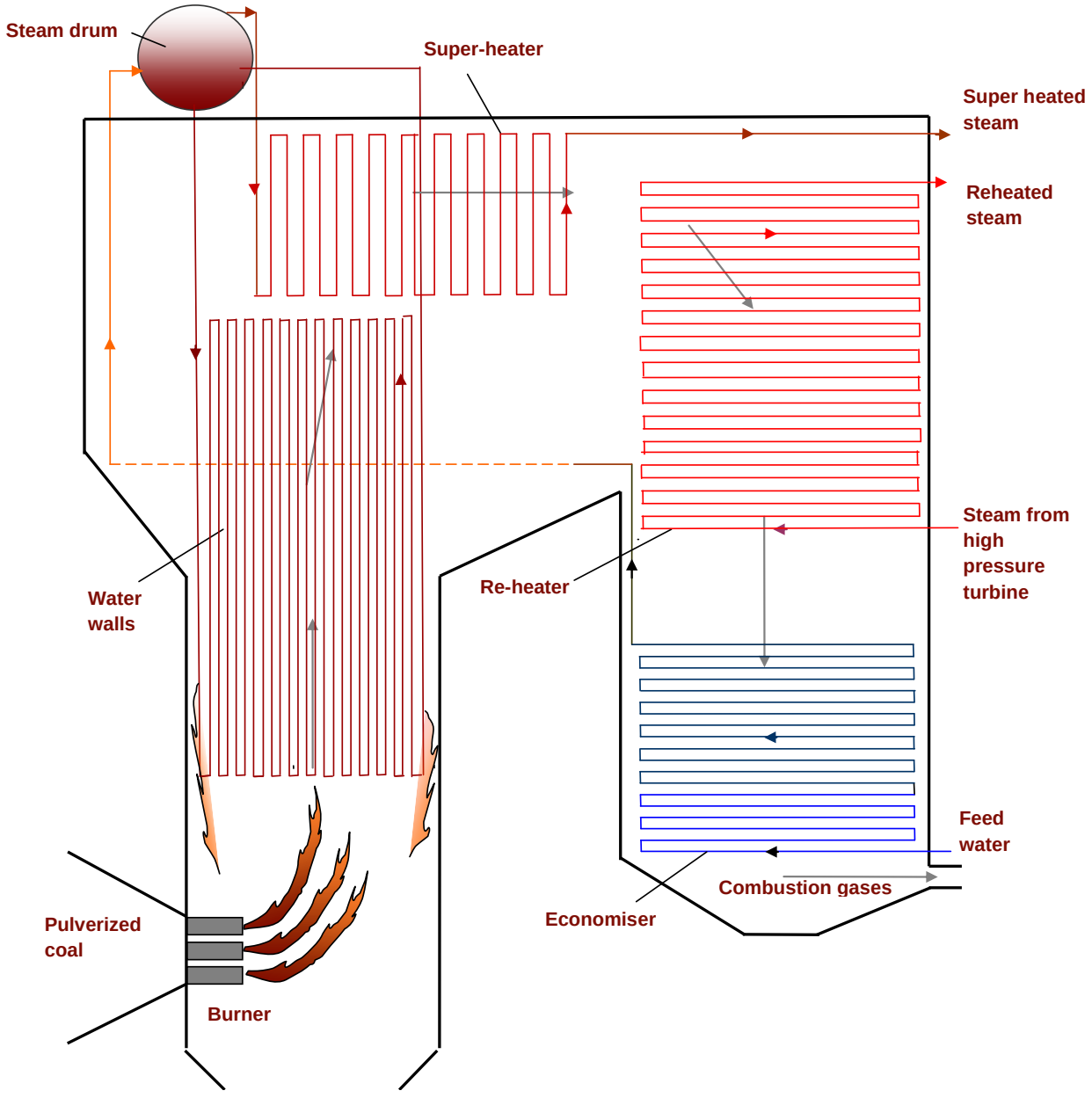

Figure 1-3: Schematic of coal-fired boiler

It is a well-established fact that coal as a fuel has more effects on the heat-exchangers than to oil and natural gas, as can be seen from amounts of deposited ash. However the use of biomass as a fuel could have even more adverse effects than coal (depending on the type) due to presence of high levels of chlorine (Cl) and alkali metals sodium (Na) and potassium (K). For almost half a century due to limiting conditions (steam pressure ~165 bar and temperature ~540°C) within the boiler, the efficiency remained below ~ 38% [12; 13]. Attempts to raise the boiler efficiency by increasing steam pressure and temperature failed, mainly due to the failure of heat exchangers alloys (metal loss) under more severe conditions (steam with higher pressures and temperatures). These boilers are referred to as sub-critical boilers. Newly installed power plants are now running at ~ 600°C steam temperatures with efficiencies above 40%. Work is underway for ultra supercritical (USC) boilers, with target efficiencies of up to 50%. Figure 1-4 is a schematic diagram shows development in main steam temperature, pressure and plant efficiency [12; 13].

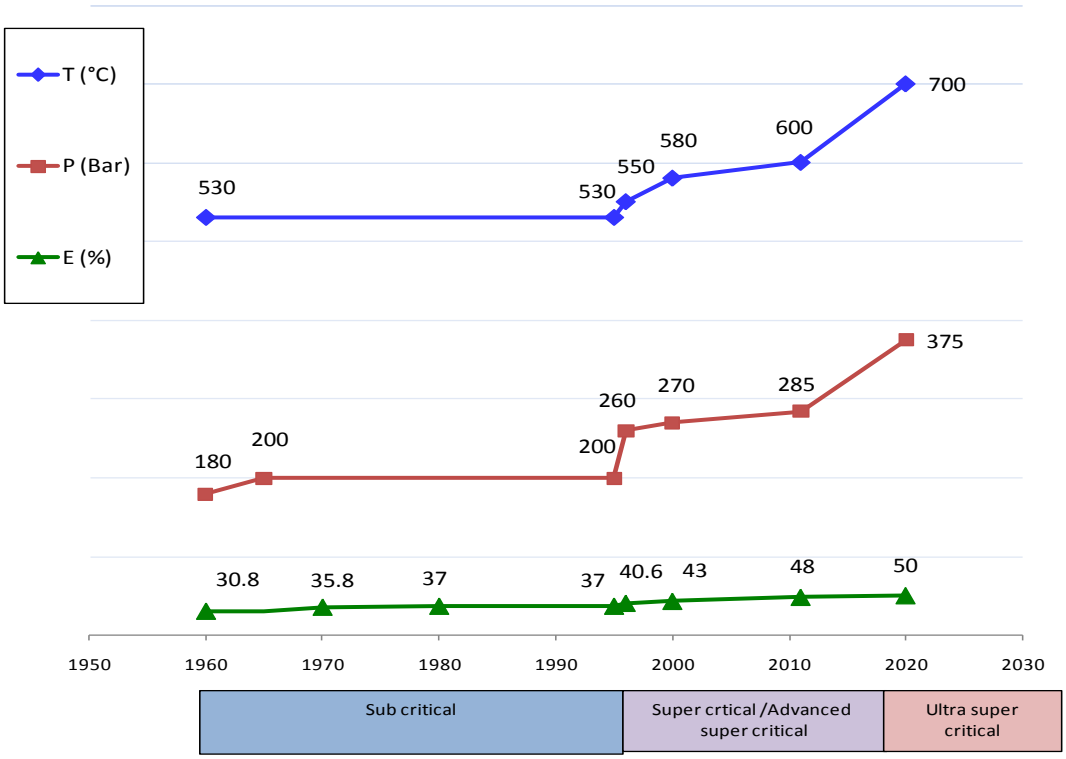

Figure 1-4: Schematic of efficiency development in pulverised coal power plant [12; 13]

The boiler heat exchanger metal tubes not only lose thickness due to oxidation and corrosion but become more insulated due to the formation of layers of oxides and deposit, which leads to reduce heat flux [14]. There are also other degradation modes such as creep and fatigue in the boiler which reduce component lifetimes; the mechanical forms of degradation are not discussed further in this PhD thesis.

1.4 CO_2 Emissions and Role of Co-firing Biomass and Coal and Oxy-fired Systems

One of the major issues currently facing the world is global warming which is believed to be due to the increase in greenhouse gas (GHG) emissions, of which power generation using coal as fuel is a major source [4; 15-17]. The Kyoto protocol agreed in 1997 has had a major influence on UK energy policy and the reduction of GHG; particularly CO_2 which according to UK Department of Energy and Climate Change (DECC) accounts for 85% of UK GHG emissions. The UKERC 'Energy 2050 project' predicts that (a) renewable fuels, such as biomass when used as a fuel (alone or co-fired with coal), and (b) carbon capture storage (CCS) technologies (e.g., oxy-fuel combustion) will both play significant roles in enabling the UK to meet its target of reducing CO_2 emissions to 80% of their 1990 levels by 2050 [17; 18]. Biomass is classed as a carbon neutral fuel and so can be co-fired in a fuel blend with pulverised coal in power plants to facilitate cuts in net CO_2 emissions. Biomass is a major contributor to renewable energy, currently providing approx 70% of renewable energy resources world-wide [17; 19]. Co-firing coal-biomass fuel mixtures in air-firing or oxy-firing conditions has an advantage over biomass only power plants as they can be operated at higher temperatures and also supports the meeting of CO_2 reduction targets.

Oxy-firing is one of the three ways of carrying out CCS: others are post-combustion capture (where CO_2 is removed from the flue gas) and pre-its combustion capture (where carbon is removed from a fuel gas before combustion). Oxy-firing of fuel (fuel combustion in oxygen + recycled flue

gases) is a technology that provides a means of enabling CO_2 capture, and so provides an alternative route for CO_2 emission reductions. Oxy-fired combustion systems are based on an idea of burning the fuel in a mixture of excess oxygen and recycled the flue gases to produce a combustion gas stream that is rich in CO_2 (~60 volume %) and steam (~30 %) and, depending on the exact cycle configuration, can have much higher levels of SO_X and HCl than air-fired systems. However, both co-firing and oxy-firing options to reduce CO_2 emissions result in significant changes to the operating conditions (e.g. metal temperatures, gas temperatures, gaseous environments and deposits) that are anticipated for superheaters in these power systems. Such changes in operating conditions are expected to result in higher rates of fireside corrosion and so reduce the potential lives of these critical components [17; 20-22]. Fireside corrosion of heat exchanger materials and the possible reaction mechanisms involved related issues are discussed in detail in chapter 2.

1.5 PhD Aims and Objectives

Fireside corrosion issues have always been a concern for the power generation industry, but for the last few decades when only fossils fuels, particularly coal, were used as fuels it has been manageable. At present, due to the introduction of new technologies to improve the efficiency and facilitate CO_2 reductions in power plants, fireside corrosion of heat exchangers has become more complicated and a much bigger risk to plant operators and manufacturers. These new areas are also the main research focus of this PhD thesis and required an intensive study of alloy performance in the anticipated novel operating conditions. These can be summarised as:

- Co-firing biomass and coal (causing changes in flue gas chemistry mainly due to high levels of K and Cl in biomass)
- Oxy-firing conditions (due to absence of N_2, high levels of CO_2, moisture and increased levels of corrosive gases such as HCl and SO_2)

- High steam temperatures (as a result of the development of supercritical and ultra supercritical boilers) leading to higher metal surface temperatures

1.5.1 Aim

The overall project aim was to develop a better qualitative and quantitative understanding of fireside corrosion reactions on superheaters/reheaters in advanced power plant environments (co-firing, oxy-firing and with higher metal temperatures)

1.5.2 Objectives

These aims have been broken down into specific objectives for this PhD.

- To carry out a series of fireside corrosion tests targeted at specific superheaters/reheaters environments
- To characterise the corrosion products generated
- To quantify the effects of specific variables on the alloys corrosion performance: with respect to
    - higher temperature
    - gases (firing conditions i.e. air-firing and oxy-firing)
    - deposits
    - alloys composition
- To develop mathematical models of fireside corrosion damage from the data generated

Different analytical tools have been used to gather the information towards these objectives, such as mass change data, scanning electron microscopy (SEM), energy dispersive x-ray (EDX) analysis, x-ray diffraction (XRD) analysis and dimensional metrology. Atomic spectroscopy (AS) and ion chromatography (IC) techniques were also used in the analysis of deposit stability test. A successful achievement of these targets will contribute to a better

understanding of fireside corrosion and development of mathematical models to predict the lifetime of superheater/reheater tubing.

1.5.3 Importance of project

Fireside corrosion causes the power generation industry to incur heavy costs every year from unplanned shutdown of boilers due to tube failures and maintenance issues [23]. A change in fuel, a move toward biomass co-firing and oxy-firing conditions, all make the corrosive environments around the superheater/reheater tubes more aggressive, and have highlighted the need to find a solution. Increasing energy demand needs higher efficiency power plants, which can be achieved if higher steam temperatures are produced. However, this means a more aggressive environment within the boilers, in particulars the superheaters and reheaters, and yet more challenges for corrosion scientists [24]. In response to all these issues, urgent attention is required from the related industries and scientists to overcome the current challenges.

1.5.4 Thesis Overview

This PhD thesis is divided into seven chapters. The background knowledge of the power generation industry, particularly PC power plants and project's aims and objective are focussed in Chapter 1. A detailed literature review is presented in Chapter 2, followed by comprehensive experimental procedures with particular focus on post dimensional metrology technique (used for metal loss data) explained in Chapter 3. Results are presented in Chapter 4 under headings representing different techniques used in this PhD project. The results are discussed in Chapter 5 and finally conclusion and suggestion for future work are included in Chapter 6 and 7 respectively.

This PhD project was funded by EPSRC through its SUPERGEN (sustainable power generation) programme. The SUPERGEN PLE (plant lifetime extension) consortium is a partnership between four universities and eleven industrial partners.

2 LITERATURE REVIEW

2.1 Introduction

This literature review chapter includes a brief discussion on the basics of metal oxidation, associated thermodynamics and kinetics. An extensive corrosion review, particularly 'fireside side corrosion' and related reaction mechanisms, are the central point of this chapter. Current research in the area of co-firing biomass and coal and oxy-firing systems is also reviewed in this chapter.

2.2 Oxidation of Metals

2.2.1 Introduction

Oxidation is a reaction between oxygen and another material. Oxidation can also be defined as a loss of electrons. Gleeson [25] describes oxidation as a gas–solid reaction by which a metal increases its valency; the gaseous oxidising agent could be oxygen, sulphur, nitrogen or chlorine. Oxidation reactions result in the formation of oxide layers that protect the material from further oxidation. Oxygen atoms have a lone pairs of electrons and are highly electronegative; in reactions with non-metals they form a molecular oxide (e.g. water molecule), whereas metal oxides are ionic. In general, the metal oxidation reaction can be represented as:

$$2M(s) + O_2(g) \rightarrow 2MO(s) \qquad (2\text{-}1)$$

The term oxidation is widely used in the metal alloys industry. Like any other material, metals also oxidise; in fact the metallic properties, due to their lattice structure and highly conductive nature, support the oxidation reaction. On reaction the metal atoms lose their electrons, i.e. oxidise, and become cations. Oxygen on the other hand reduces, i.e. gains electron and completes the reaction called a red-ox reaction. These reactions are also called anodic and cathodic reactions.

$$A \rightarrow A^{++} + 2e^{-} \quad \text{(oxidation, anodic)} \tag{2-2}$$

$$B + 2e^{-} \rightarrow B^{2-} \quad \text{(reduction, cathodic)} \tag{2-3}$$

A very well-known example of such metal oxidation is rust, an iron oxidation reaction where the Fe atom oxidises and oxygen reduces and Fe^{+2} and Fe^{+3} oxides are formed:

$$2Fe + O_2 \rightarrow 2Fe^{++} + 2O^{2-} \tag{2-4}$$

$$4Fe^{++} + O_2 \rightarrow 4Fe^{+++} + 2O^{2-} \tag{2-5}$$

In such reactions both the reactants, (the metal and the oxygen) are separated by the oxide layer and in order to continue the reaction one of the reactants has to pass through the oxide layer [26]

Oxidation of a metal at high temperature is a process involving the reaction between a metal and atmospheric oxygen. In fact, oxidation is the most important reaction in the study of high temperature corrosion [27]. Like any other chemical reaction, increases in temperature increase the rate of the metal oxidation reaction. Metal oxidation does not necessarily require ambient oxygen to oxidise the metal; the presence of gases such as carbon dioxide, steam or sulphur dioxide can also result in the formation of oxide layers.

Lai [27] described oxidising and reducing environments as being oxidising when the oxygen activity is high (e.g. due to combustion of excess air) and reducing when the oxygen activity is low.

Different types of metals oxidise in different ways due to their properties. Khanna [28] grouped these metals according to their oxidation resistance. Noble metals, such as gold and platinum, are highly stable and show high resistance to oxidation. Alkali and alkaline earth metals which are highly reactive and oxidise quickly. And finally there are transition metals like iron, nickel and chromium, which show moderate oxidation resistance; alloys of these metals are the choice for heat resistance materials and are used by boiler manufacturers.

2.2.2 Oxidation of Iron

Iron with carbon and other alloying elements (i.e. steels) form the first choice class of alloys used as heat-exchangers in boilers, because of their heat resistance quality and mechanical properties. This makes the studies of iron oxidation and its alloys important for boiler engineers. Addition of different alloying elements can make the steel more useful for a heat resistance application; e.g. by adding chromium the oxidation resistance can be improved while the presence of molybdenum can increase the creep strength. Not only do different elements give different properties to the alloy but the amount in the alloy changes its behaviour too; for example, low chromium ferritic steels show high oxidation rates compared to higher chromium-nickel containing austenitic steels, which form chromium spinel oxides and show higher resistances to oxidation [29].

Khanna [28] and Birks [26] explained the oxidation of pure iron as the best example of multilayer oxide formation. Iron and carbon steels show very similar oxidation behaviour in forming three different oxides if the temperature is high enough: wustite (FeO), magnetite (Fe_3O_4) and haematite (Fe_2O_3). The thickness of each oxide depends on the temperature, oxygen partial pressure and diffusion rates through them. The phases are shown in the iron oxygen phase diagram in Figure 2-1.

The diagram Figure 2-1 clearly shows that below 570°C only haematite and magnetite oxides formed whereas wustite forms above 570°C. Similarly to produce Fe_2O_3 oxide, high oxygen pressure is required. The region below the FeO and Fe_3O_4 line, where no oxidation occurs, is the region of immunity, i.e., the oxygen partial pressure is too low for oxidation reaction to occur. At temperatures above 570°C and oxygen partial pressure above 30 wt%, all the three iron oxides are formed in a sequence as Fe (metal) - FeO-Fe_3O_4-Fe_2O_3-oxygen (gas). At 1000°C wustite, the p-type semiconductors exist over a wide range of stoichiometry, $Fe_{0.95}$ to $Fe_{0.88}$ [26]. And due to the high metal vacancies, the mobility of electrons and cations is very high. Magnetite (Fe_3O_4),

has inverse spinel structure. Haematite (Fe_2O_3) exists in two forms; α haematite which is rhombohedral and β haematite which is cubic in structures. More details of these metal oxides can be found in the text books by Khanna and Birks [26; 28].

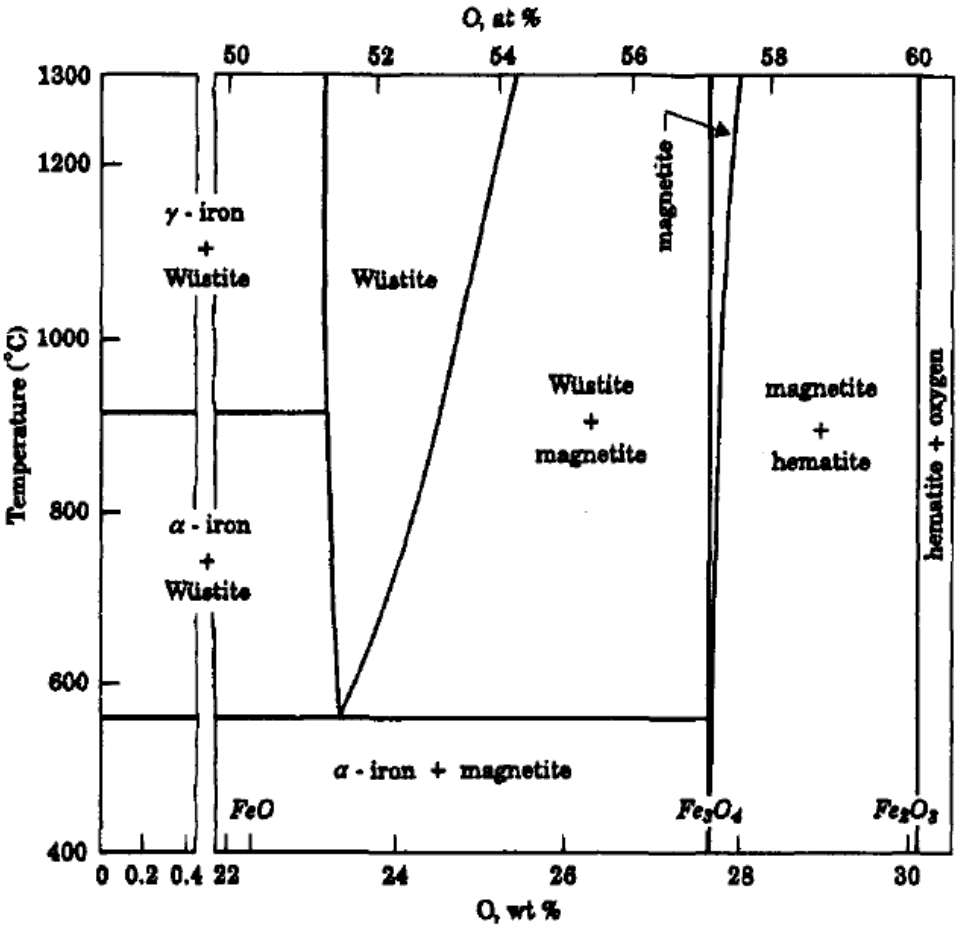

Figure 2-1: Iron- oxygen phase diagram [30]

In Figure 2-2 Khanna and Birks have explained the oxidation reaction mechanism of iron above 570°C. The reactions at the interface are also shown in the diagram to understand the sequence of oxides formation as a result of metal to gas (oxygen) reaction. The reactions can be explained in words as follows:

- Firstly iron oxidised at metal wustite interface

$$Fe = Fe^{2+} + 2e^{-} \quad \textbf{(2-6)}$$

- The electron and metal cations move through the wustite towards the magnetite and at the wustite/magnetite interface the reaction is

$$Fe^{2+} + 2e^{-} + Fe_3O_4 = 4FeO \quad \textbf{(2-7)}$$

- At magnetite haematite interface, magnetite is formed as shown in equation (2-8) where n is 2 for Fe^{2+} and 3 for Fe^{3+}.

$$Fe^{n+} + ne + 4Fe_2O_3 = 3Fe_3O_4 \quad \textbf{(2-8)}$$

- And finally ions and electrons move through the haematite via the ion vacancies and are oxidised to form new haematite as shown in equation (2-9); oxygen also ionises as shown in equation (2-10).

$$2Fe^{3+} + 6e^{-} + \frac{3}{2} O_2 = Fe_2O_3 \quad \textbf{(2-9)}$$

$$\frac{1}{2} O_2 + 2e^{-} = O^{2-} \quad \textbf{(2-10)}$$

At 1000°C the relative thickness ratio for wustite, magnetite and haematite is found to be 95:4:1.

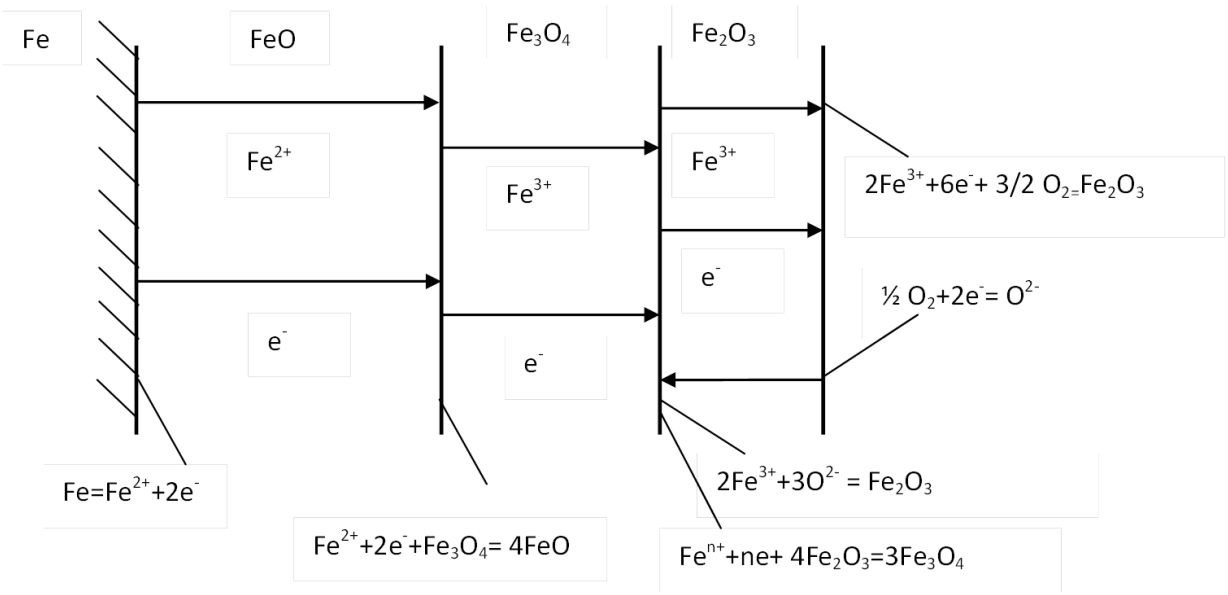

Figure 2-2: Iron oxidation mechanism showing formation of wustite, magnetite and haematite above 570°C [26; 28]

2.2.3 Oxidation and Sulphidation of Alloys in Mixed Gas

When the metal is not as simple as iron but alloys of different elemental composition, and oxidant is not just oxygen but a mixed gas (which is a typical power plants boilers environment), then understanding the reaction mechanisms becomes more complex [28; 31].

After oxidation, the next most important reaction in studies for high temperature corrosion is sulphidation. Sulphur, which is present in the fuel (coal or oil) as an impurity, forms SO_2, SO_3 after combustion or H_2S in reducing environments [26; 28]. The reaction of these sulphur containing gases with a metal is called sulphidation. Studies have found that the level of these gases are often in the range of 1-1000 ppm, However the literature [32] shows that even at such low levels these gases can cause severe damage to materials used in high temperature applications. Therefore, understating of sulphidation reactions is important from an industrial point of view. Sulphur from fuels not only plays a role in formation of sulphur rich gases, but also plays a role in the formation of

vapours that condensed as deposits and can cause even more severe damage to materials.

Researchers [26-28] believe the high temperature alloys rely on their chromium and nickel contents to form oxides scales which then act as shields to protect the alloy from sulphidation reactions. Sulphur and oxygen levels decide the mode of reaction; higher sulphur levels cause sulphidation to be dominant and higher oxygen levels cause, oxidation to be dominant. Thus, when sulphidation is one of the possible reactions in a given environment, the selection of materials needs to take this into account to ensure corrosion protection at high temperature.

2.2.4 Thermodynamics of Metal Oxidation

'Thermo' means heat (energy) and 'dynamics' means movement so this topic is about transformation of energy from one system to another [33]. This branch of science was born in the 19th century when scientists were trying to develop steam engines [34]. Thermodynamics is widely used in field of metallurgy and high temperature materials application [35]. A knowledge of thermodynamics can be applied to determine the possibility of metal oxidation and corrosion reactions. It is a well-known fact, that thermodynamically metals are very unstable and formed different oxides, sulphides etc. Both thermodynamic and kinetic factors are important in order to predict alloys oxidation and corrosion behaviour [36]. The second law of thermodynamic, which determines the possibility of the reaction of metal with its surroundings, can be written as;

$$\Delta G = \Delta H - T\Delta S \qquad (2\text{-}11)$$

Where ΔG= Gibbs free energy change, ΔH= Enthalpy, ΔS= Entropy change and T= Absolute temperature.

Gibbs free energy is the available energy in a system to do work and gives the net effect on the spontaneity of the enthalpy and entropy changes [37; 38]. The Gibbs free energy of metal oxidation in equation (2-1) can be written as:

$$\Delta G° = -RT\ln \frac{a^2{}_{MO}}{a^2{}_{M}.p_{O_2}} \quad (2\text{-}12)$$

Where G = Gibbs free energy, R = Gas constant, T = Temperature, $a^2{}_{MO}$ = Activity metal oxide, p_{O_2} = Oxygen partial pressure and $a^2{}_{M}$ = activity of metal

If the activities of metal and oxide are unity the equation above can be written as:

$$\Delta G° = RT\ln p_{O_2} \quad (2\text{-}13)$$

And can be re written as:

$$p(O_2) = \exp \frac{\Delta G°}{RT} \quad (2\text{-}14)$$

Thermodynamically for metal oxidation, the ambient oxygen reacts with the metal tubes and forms metal oxides only if the oxygen potential is greater than oxygen partial pressure in equilibrium with the oxide [27; 28].

2.2.4.1 Ellingham diagram

An Ellingham diagram can be used to explain metal oxidation thermodynamic trends [39]. It is a plot of Gibbs free energy as a function of temperature that was first created by the physical chemist H. J. T. Ellingham [40]. The diagram shows the temperature and oxygen pressure required for oxide formation; the most common reaction in high temperature corrosive environments. An example of an Ellingham diagram [38] is shown in Figure 2-3. Khanna [28] illustrates ne use of an Ellingham diagram by explaining the dotted line on the plot gives you the partial pressure of oxygen that is in equilibrium with metal oxide at a given temperature. That means in case of Fe_2O_3 for example, data is plotted for the formation of six moles of Fe_2O_3

$$4Fe_3O_4+O_2 = 6Fe_2O_3 \quad (2\text{-}15)$$

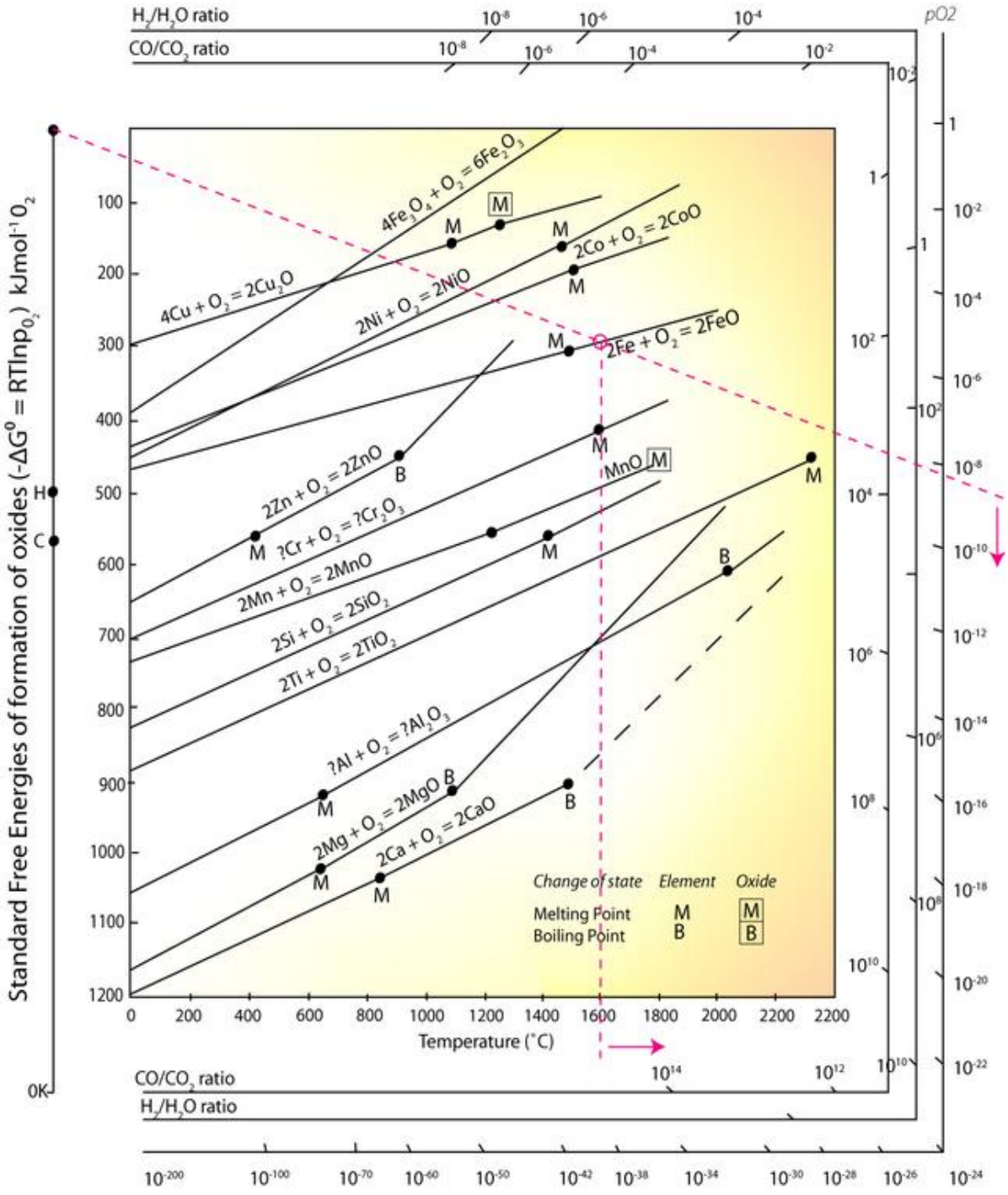

Figure 2-3: Ellingham Diagram [38]

The positions of lines at the top of the plot are of noble metals (un-reactive) and their oxides whereas the lines on the bottom of the diagram (higher negative values of ΔG) are of reactive metals and their oxides. Ellingham diagrams are useful for predicting the conditions for metal ore reduction. All the metals are

reacting with one mole of oxygen gas and forming a condensed oxide. Entropy is decreasing in the reactions as it forming a stable condensed oxide.

Similar diagram are also available for sulphides or chlorides. From the boiler superheaters/reheaters point of view the oxides and sulphides of iron, chromium, and nickel are important. Ellingham diagrams are useful for thermodynamic, guidance, giving information on which way a reaction will go, but do not indicate how fast will it go [35]. Software tools, such as Thermo-calc [41], MTDATA [42] and others, are available to run thermodynamic calculations for metal gas reactions. However, studying thermodynamics using these software is not the focus of this PhD thesis; a wide range of literature is available for possible binary or ternary phase diagrams in the studies of high temperature oxidation and corrosion.

2.2.4.2 Thermodynamic diagrams

Basic thermodynamic diagrams are very important in the understanding of high temperature oxidation and corrosion. Phase equilibrium diagrams are illustrations of phase equilibria (stable-phases), present in a system as a function of the controlling variables; typically alloy composition and temperature [35]. These diagrams can help in the interpretation of metal oxidation reactions. Figure 2-4 is a typical example of phase diagram with two variables: oxygen and sulphur partial pressures. It clearly shows that with an increase in only oxygen partial pressure, and at low S partial pressure, an oxides phase is formed. Similarly with high pS_2, and low pO_2, the metal sulphide is stable. However, when high partial pressures of both oxygen and sulphur are applied a metal-sulphur- oxygen compound is formed (metal sulphate).

Figure 2-5 is another example of a phase diagram which shows the affect of increasing nickel additions to iron: this lowers the temperature of the f.c.c. (face centre cubic) to b.c.c (body centre cubic) transformation from 914 for pure iron to 720°C for Fe-8% Ni stainless steel [43].

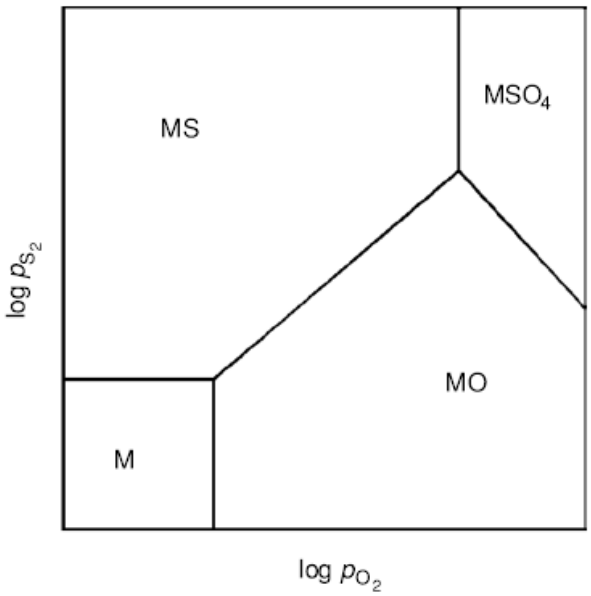

Figure 2-4: A typical metal sulphur-oxygen stability phase diagram [26]

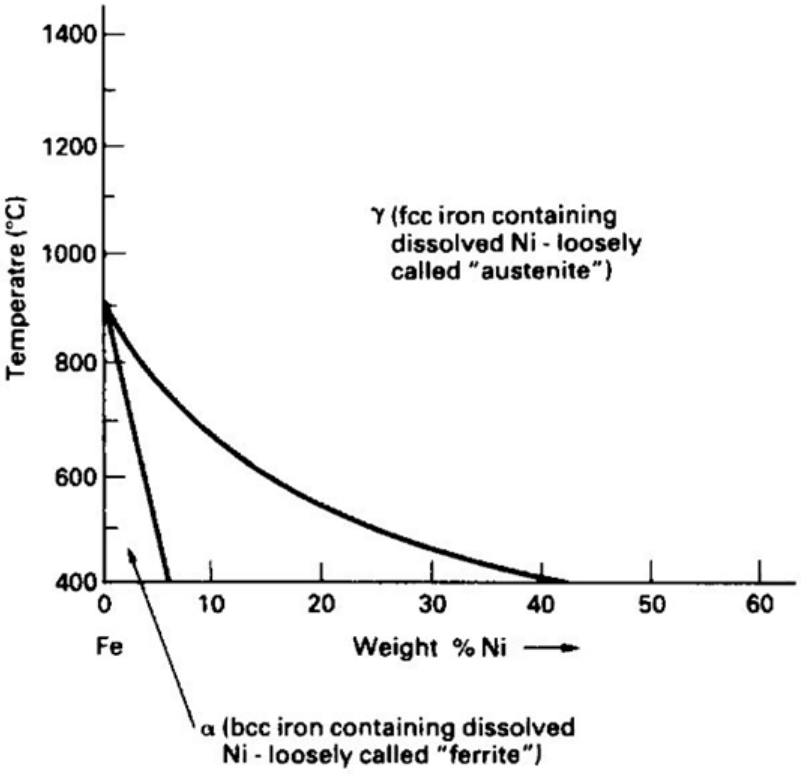

Figure 2-5: A typical Fe-Ni phase diagram [43]

2.2.5 Kinetics of Metal Oxidation

In this PhD thesis one focus was the kinetics of metal corrosion. As discussed earlier, thermodynamics is very useful in the field of high temperature corrosion, but without the kinetics (rate) information for a particular reaction it could be ineffective [35; 44]. For example, if the speed of a reaction is known, for engineers it will be easier to make decisions about a particular machine's maintenance, replacement (boiler; tubes /pipes, turbines; blades) or processes (such as reduction of ores). The kinetics (rate of oxidation) of the reaction depends on different factors such as ambient oxygen, metal surface, temperature, oxygen partial pressure, elapsed reaction time and pre-treatment of metal [45].

Three different kinetic laws are:

2.2.5.1 Linear law

If metal oxidation continues constantly with time and the oxide layer thickness increases steadily it means the metal is following a linear law of kinetics, or in simple words that the oxidation rate is constant. This law can be applied to non-protective oxide layers (e.g. porous oxides). This type of oxidation is often undesirable and is sometime called catastrophic oxidation.

Mathematically can be written as:

$$\frac{dx}{dt} = k_l \tag{2-16}$$

After integration

$$x = k_l.t + c \tag{2-17}$$

Where k_l is the linear rate is constant and c is integration constant.

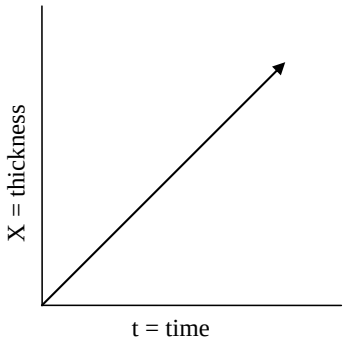

Figure 2-6: Schematic illustration of linear oxidation

2.2.5.2 Parabolic law

If the rate of metal oxidation decreases with an increase in oxide thickness, that often means that the system following a parabolic kinetics.

And mathematically can be expressed as:

$$\frac{dx}{dt} = k_{\frac{p}{x}} \tag{2-18}$$

After integration

$$x^2 = kpt + c \tag{2-19}$$

Where kp = parabolic rate constant and c = integration constant.

Many metals at elevated temperatures can show parabolic oxidation. Unlike linear oxidation for which the reaction rate is independent of time, the rate of parabolic oxidation decreases with time due to the increase in oxide thickness, and thus is dependent on the metal and gas consumed in the reaction.

Parabolic oxidation at high temperature implies that thermal diffusion (due to a concentration gradient) is the rate determining step [45].

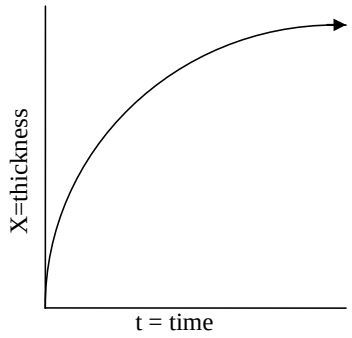

Figure 2-7: Schematic illustration of parabolic oxidation

2.2.5.2.1 Wagner theory of diffusion

The mechanism of parabolic kinetics was explained by Wagner [31], it is the most established, well understood and highly applied theory to the oxidation of many alloys today [31]. It is documented in Talbot and Talbot [46] that according to Wagner theory of oxidation "the oxide grows by complementary reactions of oxygen at the oxide/atmosphere interface and with the metal at the metal /oxide interface and its rate of growth is controlled by the rate at which reacting species diffuse through the oxide via lattice defects".

Wagner believed in a neutral oxide development during the oxide growth. This requires that the positively charged cations moving through the oxide equals to the negatively charged anions and electrons (both electrons and anions move in the same direction or opposite to the cations) through the film in unit time [31].

The theory suggested that the driving force of the reaction is the free energy change associated with the formation of oxide MO from metal and oxygen, and as a result concentration gradients of the components are established through the oxide [45].

2.2.5.3 Logarithmic law

This law applies to oxidation layer formation at relatively low temperatures; with low temperature being 300- 400°C, or below, for most of the metals. The oxidation damage rises very quickly at the beginning but then slows down. This can be represent as

$$x = klogt + c \quad (2\text{-}20)$$

Where k= rate constant, c= integration constant

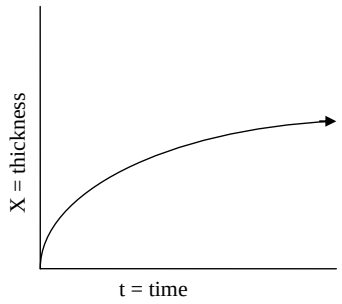

Figure 2-8: Schematic illustration of logarithmic oxidation

A combination of laws can govern the oxidation reactions. Classic examples are scale cracking or the detachment of thick oxides which allow direct oxidation and a change from parabolic to linear kinetics [26]. The kinetics becomes more complicated when the substrate is not pure metal but an alloy, which can oxidise to form various oxides. The details of both the kinetics and thermodynamics of metal oxidation reactions give better insights into oxide layer formation [28].

2.2.6 Oxides structures

Knowledge of the oxide microstructures formed and crystal lattice dimensions are key steps in assessing oxidation mechanisms. Most metal oxidation reactions are based on the diffusion of ions via an oxide crystal lattice; hence the knowledge of types of lattice defects is important [26; 28; 31]. These lattice structure defects are based on ion vacancies (formed as a result of missing metal or oxygen ions), interstitial (formed as a result of metal or oxygen ions displacement from their lattice position). At high temperature many metal oxidation reactions followed Wagner's theory of oxidation and the oxides formed exhibit both electronic and ionic conductivity. They can be n-type or p-type semiconductors. The basic concept of Wagner model of semi-conductors is that they are not stoichiometric in composition rather become stable with excess anions or cations.

2.2.6.1 n-type semiconductors (oxides)

In these semi-conducting oxides the current is carried by electrons. Khanna [28] and Birks [26] describe n-type oxides (M_{1+x} O or MO_{1-x}) as having the addition of foreign cations with a higher valance than the parent cations that decreases the concentration of oxygen vacancies in MO_{1-x} or interstitial metal ions in MO_{1-x} and causing lower oxidation rates. Similarly the addition of foreign cations, with a lower valance than the parent cations will lead to higher oxidation rates. Figure 2-9 illustrates an example of n type semiconductors oxides.

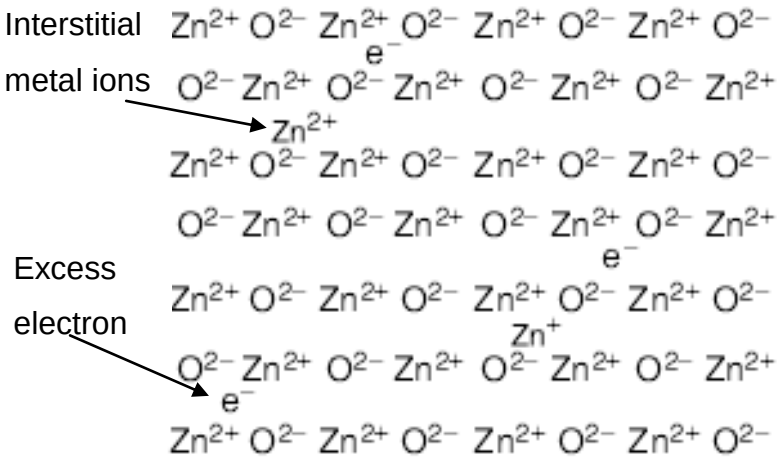

Figure 2-9: An n type metal–excess semi conductor (interstitial cations and excess electrons in ZnO [26]

2.2.6.2 p-type semiconductors (oxides)

In these semi-conductors, the electric charge is carried by electron holes (positive carriers). For p-types oxides semiconductors (M_{1-x} O or MO_{1+x}), an addition of cations of a higher valance than the parent cations will increase the concentration of oxygen vacancies in MO_{1-x} or interstitial metal ions in MO_{1+x} and cause as higher oxidation rates. Similarly the addition of foreign cations, of lower valance than the parent cations will lead to lower oxidation rates. An example of a p-type oxide is shown in Figure 2-10.

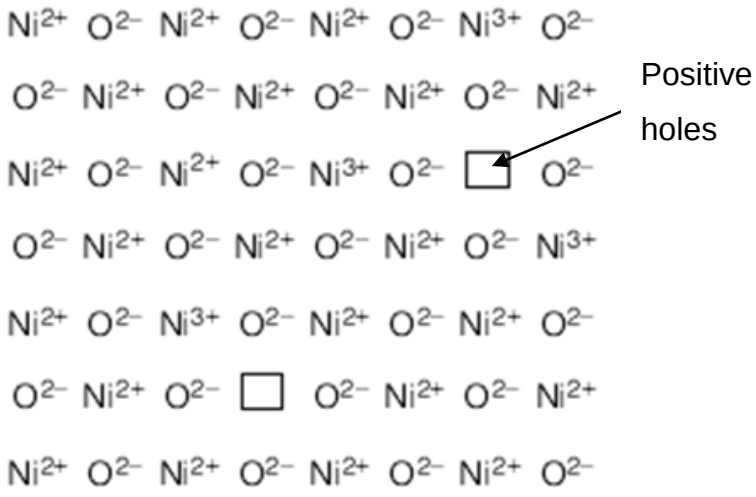

Figure 2-10: A p type metal–deficit semi conductor (NiO with cations vacancies and positive holes) [26]

2.2.7 Mechanism of Oxidation

Kubaschewski [31] has emphasised that in order to understand the metal oxidation mechanism, the characteristic information of the oxide layers for every metal–gas reaction is essential. Figure 2-11 is a schematic representation of diffusion mechanism of a metal oxidation system. In order to cause diffusion to take place an activity gradient is required. The transport of metal ions through an oxide lattice is opposite to oxide cations vacancies and anions. The model further shows a gradual decrease in oxygen partial pressure as it moves towards metal, and a metal activity decrease, as it moves towards oxide gas interface. Kubaschewski [31] further explains the arrangements of oxide layer based on the metal oxidation state; if metal has several oxidation states, various layers of oxides (compounds) will be formed. He further explains that if a compound is richer in the gas component, it will formed at gas/oxide interface and if a compound is richer in the metal component then it will formed at metal/oxide interface. Figure 2-11 is a schematic representation of oxide formation on metal surface following Wagner's theory of diffusion [26].

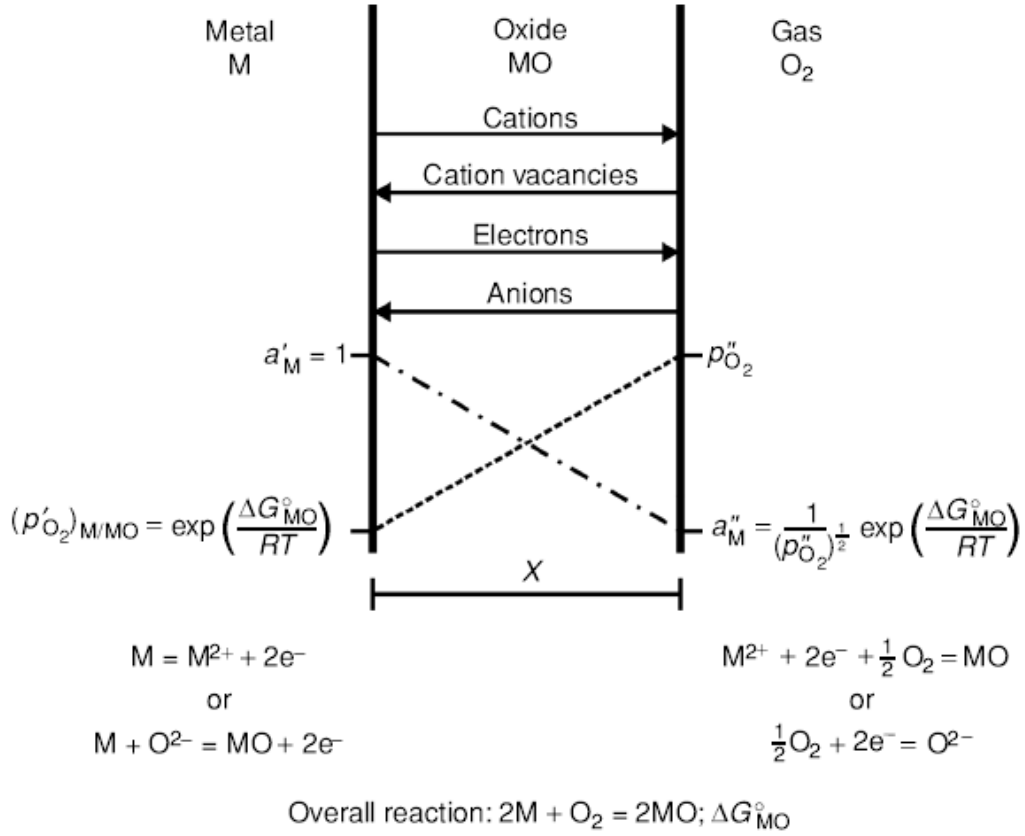

Figure 2-11: A typical metal scale formation according to Wagner diffusion model [26]

Further details; on metal oxidation, (thermodynamics, kinetics, mechanisms or oxide defects structure) can be found in the available text books [26; 28; 31; 45].

2.3 Corrosion

2.3.1 Introduction

Most of the literature [47; 48] defines corrosion as a loss or disintegration of a material caused by its surrounding, by means of physiochemical reaction. This material could be ceramic, plastic or metal. Corrosion weakens the material and if it continues then it destroys the material completely.

Cahn [49] points out those obvious (atmospheric) corrosion areas are very well understood, but corrosion at high temperature (such as fireside, steam and gas turbine) is still a technical and an economical challenge which requires intensive research. He further explained that the corrosion rates accelerate at the high temperatures desired in the industrial world and this makes the subject even more difficult.

An extensive two-year study by Koch [23] on metallic corrosion entitled "Corrosion costs and prevention strategies in the United States" was carried out in United States in 2002 and shows that the country is losing an astonishing 3.1% of their Gross Domestic Product (GDP) that is **$276 billion dollars per year** due to corrosion related issues. The Electrical Power Research Institute EPRI (C.A.) published a report as part of the same study and estimate the corrosion cost for the electric power industry contributes 17.3 billion dollars per year. Obviously, this huge loss can be reduced if preventative measures are taken by using protective coatings, corrosion resistance alloys, polymer and other measures depending on the nature of the industry.

2.3.2 Types of Corrosion

From this PhD research perspective, corrosion can be divided into two main types; atmospheric corrosion and high temperature corrosion. These types are also known as aqueous and dry corrosion respectively. As discussed earlier, aqueous or atmosphere corrosion is a well understood area where mechanism is mainly based on water as an electrolyte. The available literature [47; 48]

describes many unique forms of corrosion, their mechanisms and prevention in detail. The brief descriptions in this section give some of these corrosion forms. Even though some of these following examples of corrosion are known as types of aqueous corrosion, similar type of morphologies (such as pitting, and intergranular cracking) observed as a result of high temperature (fireside) corrosion. Figure 2-12 shows an attempt to classify fireside corrosion and possible mechanisms in relation to aqueous corrosion.

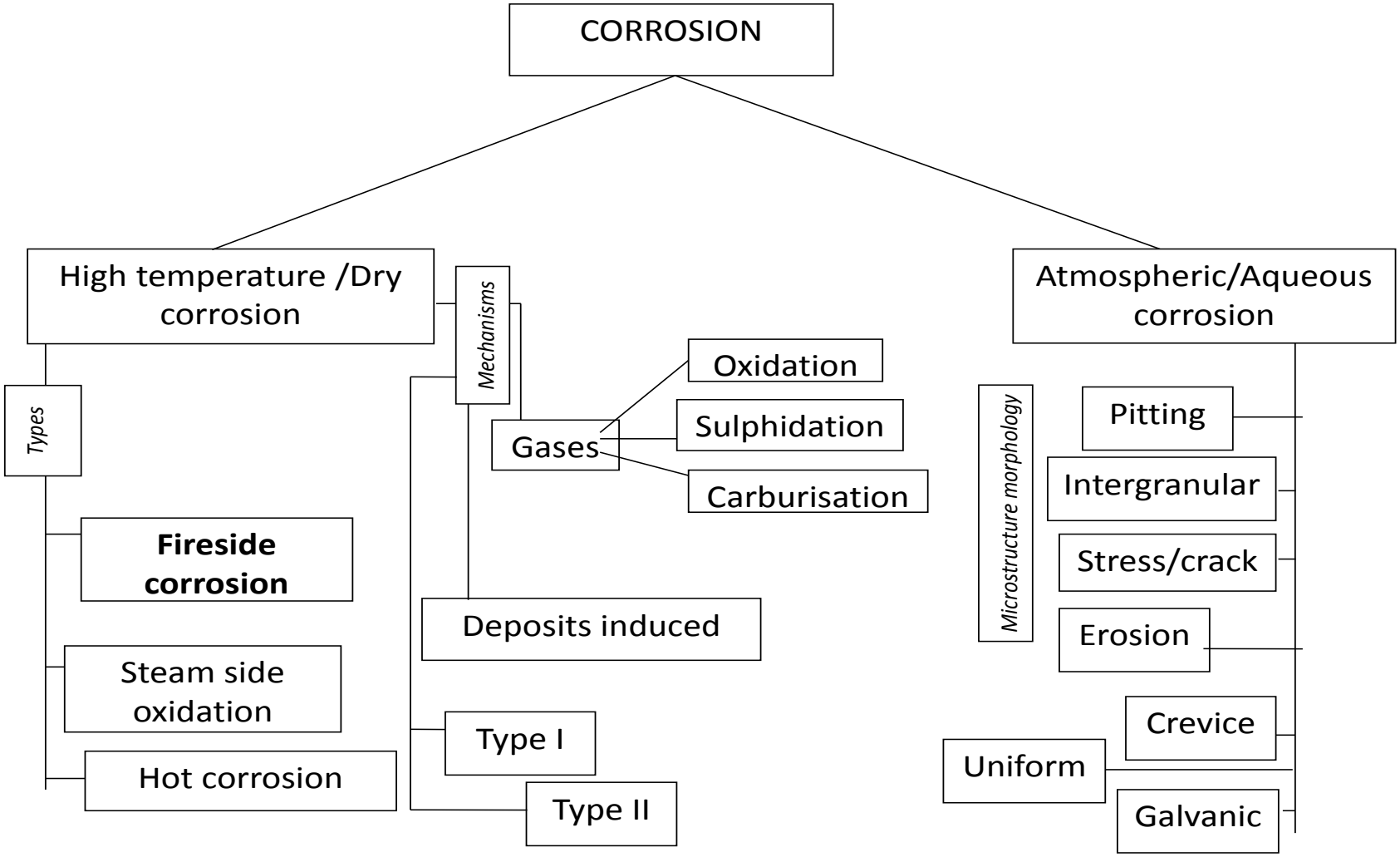

Figure 2-12: Flow diagram for fireside corrosion mechanisms

The following types of aqueous corrosion are available in detail in the literature [47-49] however described briefly in this section

2.3.2.1 Uniform Corrosion

It is the most common type of corrosion in which corrosion spreads uniformly over a wide surface area and the corrosion rate is predictable. Uniform corrosion can be protected by coating, inhibitors or cathodic protection. Since the corrosion rate for uniform corrosion can be predicted, this type is not much of a concern.

2.3.2.2 Galvanic Corrosion

This type of corrosion is usually a result of the poor design of a system; basically when dissimilar materials come in contact with each other in a corrosive environment the potential difference produces an electron flow between them which leads to corrosion. The driving source in galvanic corrosion is the potential developed between the two different metals.

2.3.2.3 Pitting

This type of corrosion is extremely localised and usually results in small holes in the metal and gives a rough surface look. It may be considered as an intermediate stage between general overall corrosion and complete corrosion resistance; it often occurs in aluminium and its alloys, but can also be found in other metals. It is the most destructive type of corrosion and difficult to predict by laboratory testing.

2.3.2.4 Stress Corrosion

A type of corrosion that occurs due to the presence of tensile stresses and a corrosive environment and results in cracks spreading from a metal surface. Many researchers have classified all cracking failure occurring in corrosive medium as stress corrosion cracking. During stress corrosion, the alloy or metal is usually not attacked over most of its surface, while fine cracks progress through it.

2.3.2.5 Intergranular corrosion

Intergranular corrosion is localised attack adjacent to grain boundaries, with relatively little corrosion of the grains. As a result grains can fall out and the alloy is weakened.

2.3.2.6 Crevice corrosion

This type of corrosion is intensively localised, occurs within the crevices and other shielded areas on metal surfaces.

2.3.2.7 Erosion-Corrosion

When the flow of the surrounding medium (either liquid, solid or gas) around a material changes the corrosion rate, such corrosion is called erosion/corrosion. It is characterised by grooves, waves and valleys, and usually exhibits a directional pattern.

The above types of corrosion are example that are of industrial interest but are beyond the subject of this thesis hence are not discussed further.

2.3.3 High Temperature Corrosion

Corrosion of materials at elevated temperature is known as high temperature corrosion [27; 28]. As a general rule, the rate of chemical reaction increases with temperature, so corrosion rates can become significant at higher temperatures. Industries such as power generation, aero-space and petrochemical are examples of those experiencing high temperature corrosion.

Fireside corrosion, steam oxidation and hot corrosion are different types of high temperature corrosion. Fireside and steam side corrosion affect the heat exchangers in boilers and are named according to their location on the boiler tubes, whereas hot corrosion occurs in gas turbines. Some researcher [28; 50; 51] believes that the type II hot corrosion mechanism could be applied to both hot and fireside corrosion, and therefore it will be briefly discussed in this section.

2.3.4 Hot Corrosion Type I and II

Hot corrosion is one of the mechanism types of high temperature corrosion [52]. Boilers [53], turbines [54] and waste incinerators [55] all suffer from different forms of hot corrosion. According to Birks et al [26] hot corrosion is “an attack on the alloys in a combustion environment by speeding up an oxidation process due to salt deposits usually a sulphate on a metal or metal oxide”. The severity of the attack depends on exact exposure conditions, such as temperature, gas composition, alloy composition and the amount of salt deposits [27; 28]. It is a hard subject to understand because of the number of variables.

Sully [56] describes the complex salts in the deposits and their role in hot corrosion as being dependant on their melting points (basically their capacity to wet the metal surface). Once hot corrosion has been initiated its results can be catastrophic, including fluxing oxide; selective removal of elements from an alloy; and formation of low melting point eutectics.

Hot corrosion is divided into two types; Khanna [28] explained them as follows:

2.3.4.1 Hot corrosion type I

This type of corrosion occurs at high temperature range, the corrosion rate is high right from the start when the salt deposit is present in a melt form. The kinetics shows approximately linear rate kinetics.

2.3.4.2 Hot corrosion type II

This type of hot corrosion takes place in low temperature range i.e. lower than the melting point of the initial deposits. Initially there is slow corrosion but soon the salt reacts with oxidation products and forms a complex salts whose melting point is lower than the original salt deposits, and then the corrosion rate suddenly increases.

Coleman [50] describes that in coal and biomass fired combustion power plants, fireside corrosion involves a form of hot corrosion type II. Both NaCl and KCl can be deposited onto superheater and reheater components during

combustion and these react with the SO_2/SO_3 in the environment to form Na_2SO_4 or K_2SO_4. It is well know that alkali sulphates are not molten at this temperature range. Na_2SO_4 melts at 884°C and K_2SO_4 melts at 1069°C [57]. Superheater and reheater temperatures range from 500°-650°C so hot corrosion does not begin until the salts react with SO_3 to form pyrosulphates or alkali iron tri-sulphates. In the case of K_2SO_4 the formation of pyro-sulphates is given by

$$K_2SO_4 + SO_3 = K_2S_2O_7 \quad (2\text{-}21)$$

Once the pyrosulphates of potassium and sodium are formed, their melting points are 398 and 454°C respectively, a harsh hot corrosion is a result. Hot corrosion is very well recognized area in the field of high temperature corrosion and details can be found in books by Birks [26], Khanna [28] and publications by Nicholls [58] and Simms et al [58; 59].

2.4 Fireside Corrosion

2.4.1 Introduction

Corrosion on a material surface that is exposed to a boiler combustion environment (hot environment) is fireside corrosion. A detail description of fireside corrosion can explained in the following words:

The flue gases produced as a result of burning fuel (either fossil fuels, biomass or municipal waste) enables metal reactions with combustion gases (O_2, SO_2, HCl), the incombustible material such as alkali salts (K_2SO_4, Na_2SO_4 or KCl) and fly ash deposits on the metal surface of the heat exchangers; and the resulting tube metal wastage is known as fireside corrosion [9; 32; 60-62].

Fireside corrosion of boiler heat exchanger materials, particularly superheaters and reheaters, is an issue that has been known to the power generation industry since the 1950s [61; 63]. Fireside corrosion is believed to be one of the major causes of tube failures in the boilers in conventional steam turbine power plants [9; 17; 32; 60; 63; 64]. However, recent development involving co-firing

biomass-coal mixtures, oxy-firing and the use of higher metal temperatures for superheaters/reheaters are leading to changes in the compositions of the flue gases and deposits. These changes in operating conditions may enhance the rates of fireside corrosion and so reduce the potential lives of the heat exchangers, unless appropriate precautions are taken [65]. Figure 2-13 is the schematic illustration of fireside corrosion of superheater/reheater tubes.

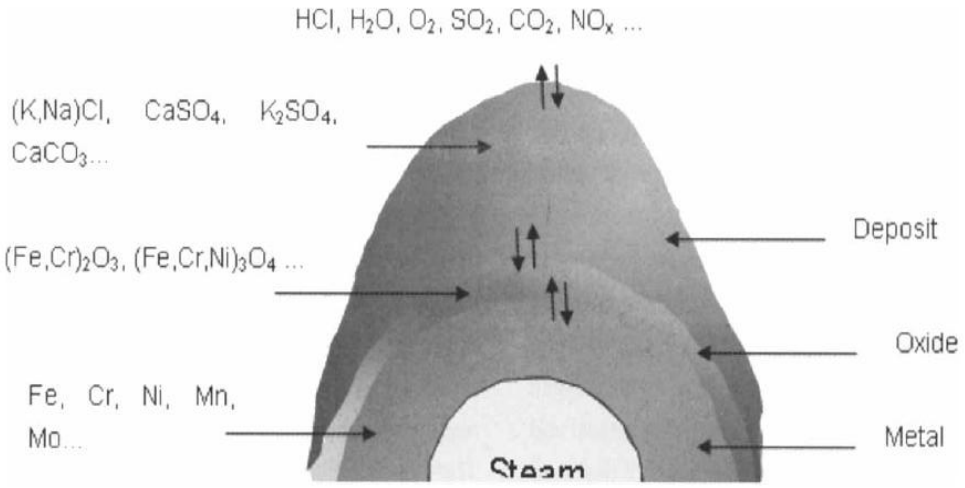

Figure 2-13: Schematic illustration of the fireside environment of superheater tube in the boiler [66]

Fireside corrosion of superheater/reheater tubes in a pulverised coal power plant is very much dependant on the coal chemistry, combustion conditions and operating temperatures. The amounts of chlorine, sulphur and ash, as well as the composition of the ash, in the coal are key factors. It is believed that sulphur in a coal is critical to superheater/reheater corrosion, with the SO_x gases produced as a result of combustion forming various types of sulphated species within deposits. It is the sulphur compounds formed with iron, oxygen and alkali metals (potassium and sodium) that are held mainly responsible for fireside corrosion [9; 32; 60; 63; 67; 68]. According to Natesan and Park [60] extensive work on the structural material and the corrosion occurrence has been carried out by Reid [63] and Wright et al [69] and the regime in given temperatures can be summarized in the Figure 2-14.

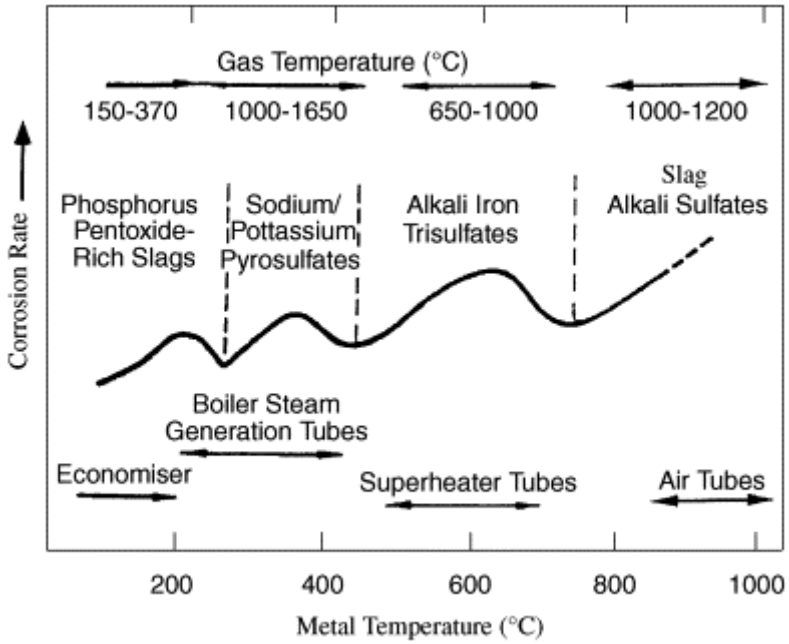

Figure 2-14: Regimes of fireside corrosion in coal-fired boilers [60]

Figure 2-14 illustrates how the rate of corrosion varies with the gas temperature and how different types of corrosion are caused on different parts of the boiler when coal is used as a fuel. The results may be different if biomass is used as the fuel alone or co-fired with coal. James and Pinder [70] and Shim et.al [71] believe that fireside corrosion is a major cause of tube failure in the boiler and it is one of the factors that has held the industry at 540°C steam temperatures for last four decades [28]; hence it requires significant attention.

As the focus of this research project is fireside corrosion resulting from co-firing of coal and biomass, basically the fuel combustion products (gases and deposits) and their interactions with alloys (superheater and reheater) will be further discussed within this chapter.

2.4.2 Superheater/Reheater Materials

It is necessary to be very clear about the design lay out and the materials used in a boiler in order to understand their corrosion behaviour. The boiler consists of a complex network of pipes and tubes: the heat exchangers carry water that boils into a highly pressurised steam due to heat transfer from the hot flue gases around them. The hottest tubes in the steam boiler are superheaters and

reheaters. The other, lower temperatures, heat exchangers in the boiler are the economizer and the water walls. Figure 1-3 is a representation of the coal-fired steam boiler. Although all the heat exchangers within the boiler suffer from corrosion issue, this thesis will only be focused on the fireside corrosion of superheaters and reheaters. The power generation industry relies on various grades of steels for different heat-exchangers in the boiler depending on their location, operational temperature, conditions and other mechanical functions. Literature [2] shows that in the process of material selection for the boiler components, corrosion resistance has not been the primary criterion; instead, the mechanical properties (creep, fatigue or toughness) are the main requirements. Alloying elements such as Cr, Ni and Al are crucial for the heat exchanger materials, their levels within the alloys affect the mechanical and chemical (corrosion resistant) properties [72]. The minimum lifetime expected from a large power plant is at least twenty years and at least ten years for heat-exchangers materials.

The alloy fireside corrosion data available in the literature [73] reports mostly tests carried out in a coal/air combustion environment, with less data published in conditions simulates co-firing, and very little data on oxy-firing environment.

A detailed discussion of material selection is beyond the scope of this thesis, but in short the types of steels are in use in the industry are low chromium ferritic (2-12%Cr) steels and high chromium austenitic (>18%Cr) steels. More recently Ni-based alloys are being considered as candidate materials for the main superheaters/reheaters [74] as the industry is moving towards higher performance targets (steam temperature ~700°C and pressure ~ 375 bars).

2.4.2.1 Ferritc steel

In brief, ferritic steels are body centred cubic (bcc), packed structures. Their properties (such as low cost, low coefficient of thermal expansion, higher thermal conductivity and high resistance for stress corrosion cracking) have made ferritic alloys preferable over austenitic steels [75]. However, low chromium ferritic alloys, such as T22 do not have sufficient corrosion or creep

resistance for future power plants. The role of Cr in resisting corrosion in alloys used for superheaters/reheaters is well recognised [76; 77]. An example of the oxidation behaviour of different steel types has been given by Stringer [2]: ferritic alloys with very little chromium such as T22 at temperatures below 570°C form oxide layers of an inner thick magnetite Fe_3O_4 and outer thin haematite oxides Fe_2O_3. The addition of more chromium, such as T91 (9%Cr and 1%Mo) produces another ferritc alloy which can be used up to 649°C as the maximum temperature and shows combination of oxides as Fe_2O_3 and Cr_2O_3.

2.4.2.2 Austenitic steel

Austenitic steels are face cubic centred (fcc), packed structures. The austenitic alloy 347 (18%Cr, 11%Ni-Nb) can be used at temperatures as high as 760°C and would form a single-phase Cr_2O_3 oxide. Wright et al [29] also reports the different oxidation behaviour of ferritic and austenitic alloys, and further explains that low chromium ferritic steels tend to form iron oxide scales based on magnetite sometimes with a thin outer layer of haematite which are less protective than the Cr-containing spinel oxides formed by the austenitic steels.

Oakey et al [3] also explains in his report that experience within the Central Electricity Generating Board (CEGB) in the 1970s, for power plant with final steam temperatures of 565ºC and burning coal of 0.15%, chlorine levels showed that these low alloy steels (T22) do not resist fireside corrosion. Consequently, the 500MW units required selective re-tubing with the austenitic steels.

A work by Masuyama [78; 79] in testing heat resistance alloys gives detail information on ferritc and austenitic alloys performance, and the qualitative and quantitative roles of different elements (such as Mo, W, Nb and V, etc) in the oxidation corrosion resistant and particularly creep strength.

2.4.2.3 Nickel based alloys

Nickel-based alloy is one of the three superalloys types; the other two (Fe based and Co based) superalloys are beyond the scope of this thesis and not

discussed. Ni-based alloy are widely used in gas turbine in the power generation industry and aeroplane engines. They are well known for their high temperature strength and surface stabilities [76; 80]. Insufficient fireside corrosion resistance for these alloys is suspected [74], and so these alloys are being investigated in fireside corrosion research so that they can be used in the boiler manufacturing if necessary in the future.

2.4.3 Corrosive Deposits

Underperformance of boilers due to wastage of metal heat-exchangers became a significant problem in 1950s [57]. In the conventional PC power plant the heat exchangers tubes are exposed to combustion products and incombustible minerals in the flue gas, which deposit and enable volatile components to condense on tube surfaces resulting in severe metal loss (much higher than expected in simple oxidation). The deposits' corrosiveness is dependent on the flue gas and deposit chemical composition. Figure 2-15 illustrates the schematic of scales and deposits on superheater tube.

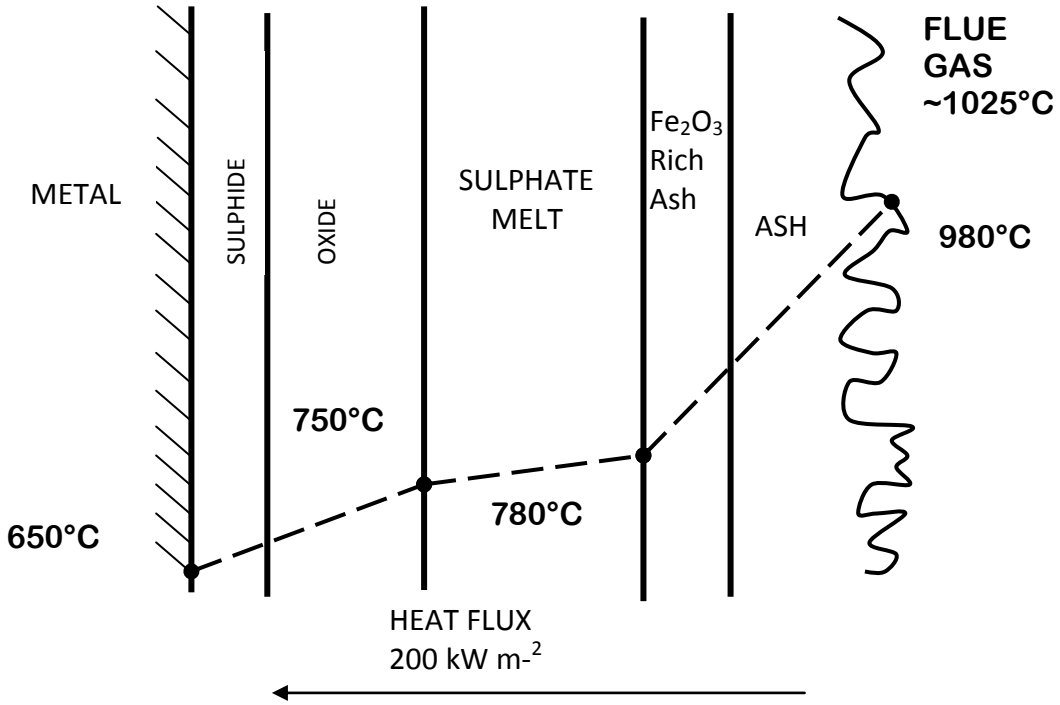

Figure 2-15: Schematic representation of ash deposit and temperature gradient at the super heater tubes in coal-fired power plant [81; 82]

The Figure 2-15 shows that sulphate deposits are molten where the corrosion rate is higher and follow a sulphidation mechanism [81; 82].

2.4.3.1 Alkali Iron Tri-sulphates

A wide range of literature shows the presence of molten alkali iron tri-sulphates [$Na_3Fe(SO_4)_3$ and $K_3Fe(SO_4)_3$] play a key role in fireside corrosion [53; 57; 75]. According to Bryers [67] as early as 1945 Reid et al [83] identified the presence of alkali-iron tri-suphates and pyrosulphates on superheaters and furnace walls respectively, as responsible for tube wastage.

The mechanism believed for the formation of alkali iron trisulphate is not just one chemical reaction that leads metal loss. Instead, various different chemical reactions and mechanisms occur on the metal surface. Extensive work on fireside corrosion was performed by Natesan [60] and Srivastava [84].

Their work explains the mechanism: alkali sulphates (derived from alkalis and sulphur from the fuel) deposit on the scales on the heat exchanger materials. With an increase in temperature due to the thermal gradient that builds up, alkali sulphate becomes sticky at the outside surface, and more fly ash is captured. With further increase in temperature these sulphate compounds are decompose. The SO_3 required for the formation of alkali-iron-trisulphates, is generated by reaction of SO_2 with O_2 over Fe_2O_3. The resulting SO_3 migrates toward the cooler surface of the metal. With further build-up of the deposits the temperature of this sulphate layer falls and SO_3 at the tube reacts with iron oxides in the ash to form alkali-iron-tri-sulphate.

An increase in SO_3 also increases the acidity of the molten salt and results in increased solubility of the oxide layer on the metal [61]. A series of reactions can be written as below.

Iron oxide reacts with SO_3 then forms a mixed alkali iron tri-sulphate:

$$Fe_2O_3 + 3SO_3 = Fe_2(SO_4)_3 \quad (2\text{-}22)$$

$$3Na_2SO_4 + Fe_2(SO_4)_3 + 3SO_3 = 2Na_3Fe(SO_4)_3 \quad (2\text{-}23)$$

Molten alkali iron tri-sulphates are stable in the range of 600-700°C where high corrosion reaction rates occur, with a maximum at 670°C [28]. At higher temperatures, the tri-sulphate dissociates and causes a decrease in the corrosion rate as shown in the inset to Figure 2-16 (the bell shape curve).

These compound are stabilised by SO_3 [has to be at least 25 pa (25×10^{-5} bar or 250 vppm)] and melt at a lower temperature than alkali sulphates (e.g., $K_3Fe(SO_4)_3$ at ~618 °C) [32; 63]. The corrosion rates increase with temperature in the presence of these deposits, but then decrease when these complex compounds become unstable (due to a reduction of SO_3 levels with increasing temperature). This corrosion rate has been reported in several publications to be at its highest between 650-670°C [28; 60; 63].

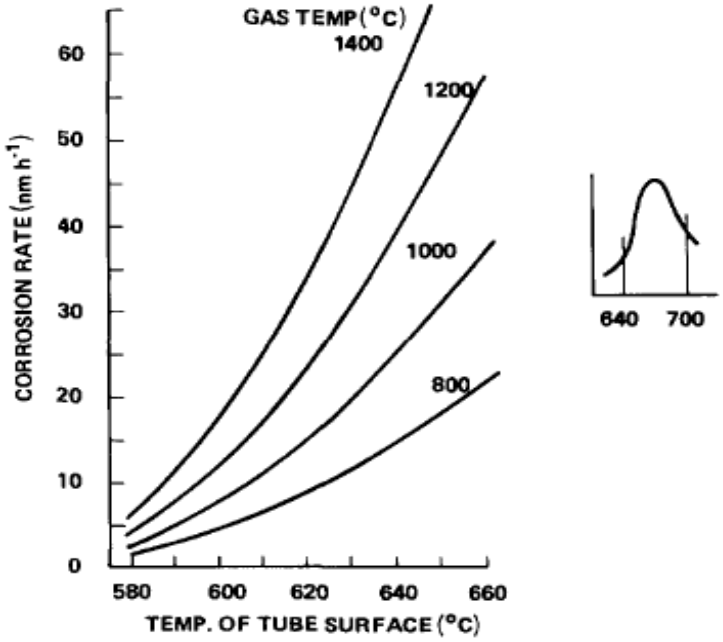

Figure 2-16: Empirical corrosion rates of austenitic tubes in coal-fired boilers. The inset shows the bell-shaped form of the corrosion rate temperature relation derived from probe trials [64]**.**

2.4.3.2 Pyrosulphates

Alkali-pyrosulphates ($Na_2S_2O_7$ and $K_2S_2O_7$) are other sulphate products involved in metal loss by dissolving metal oxides. Srivastava [84] explained molten pyrosulphates exist at lower temperatures and perform corrosion reaction in the range between 400- 482°C. Both the pyrosulphates ($Na_2S_2O_7$ and $K_2S_2O_7$) are likely to exist as deposits on heat-exchangers in the presence of sufficient SO_3. Figure 2-17 shows the melting point of alkali pyrosulphates and their dependence on SO_3 concentration.

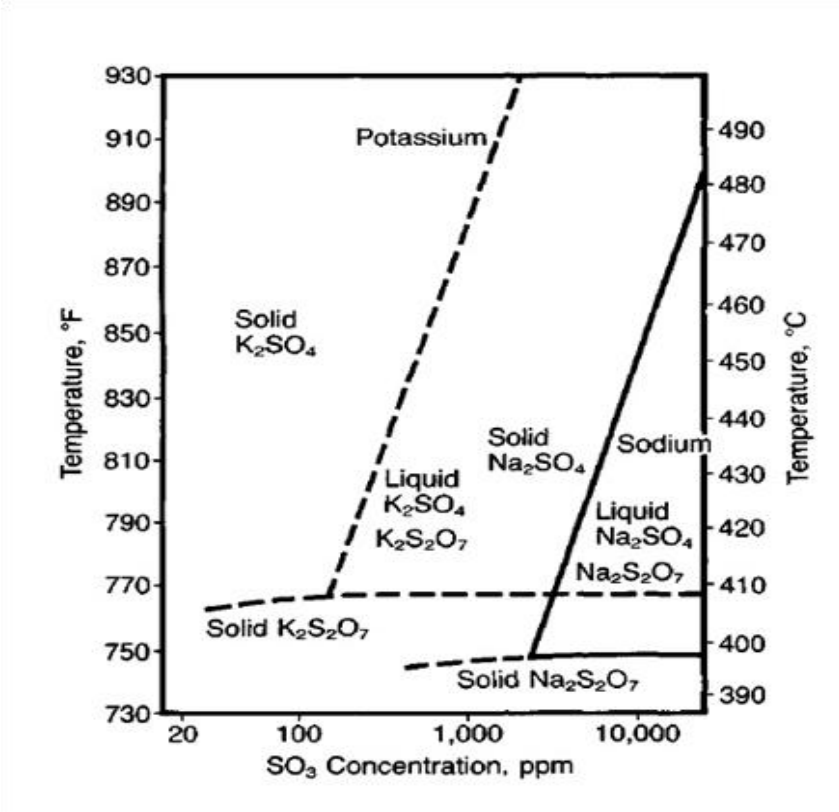

Figure 2-17: Melting points in system Na_2SO_4-SO_3 and K_2SO_4 [63]

The corrosion mechanism consists of the deposition of alkali sulphates on exposed metal surfaces followed by conversion of these to $Na_2S_2O_7$ and $K_2S_2O_7$ by reaction with SO_3 and then reaction with oxide films on metal surfaces, according to the reactions:

$$Na_2SO_4 + SO_3 = Na_2S_2O_7 \quad (2\text{-}24)$$

$$3Na_2S_2O_7 + Fe_2O_3 = 3Na_2SO_4 + Fe_2(SO_4)_3 \quad (2\text{-}25)$$

Or

$$4Na_2S_2O_7 + Fe_3O_4 = 4Na_2SO_4 + Fe_2(SO_4)_3 + FeSO_4 \quad (2\text{-}26)$$

Finally, further oxidation of the metal occurs in order to replace its surface oxide film, followed by the consequent metal loss. Khanna [28] suggested an alternative reaction mechanism as below.

$$K_2S_2O_7 + 3Fe = K_2SO_4 + Fe_2O_3 + FeS \quad (2\text{-}27)$$

2.4.3.3 Alkali Chlorides

UK coals have high chlorine contents and this has been blamed as a cause of high fireside corrosion rates found in the power generation industry in this country [64; 70]. The average Cl level in the British coal varies between 0.2-0.6% compared to 0.1% Cl in an American coal. The corrosion varies almost linearly with Cl content [57]. The literature shows no definite mechanism of Cl reaction mechanism with alloys. It is believed that the combustion of coal releases 90% of chlorine as HCl which then reacts with minerals to release alkali metal from stable silicates to form low melting corrosive sulphates [64; 67] . This phenomena of releasing sodium and potassium has made the chlorine affect on fireside corrosion more difficult to determine. Figure 2-18 illustrates the deposition rate of alkali sulphates varies with Cl concentration.

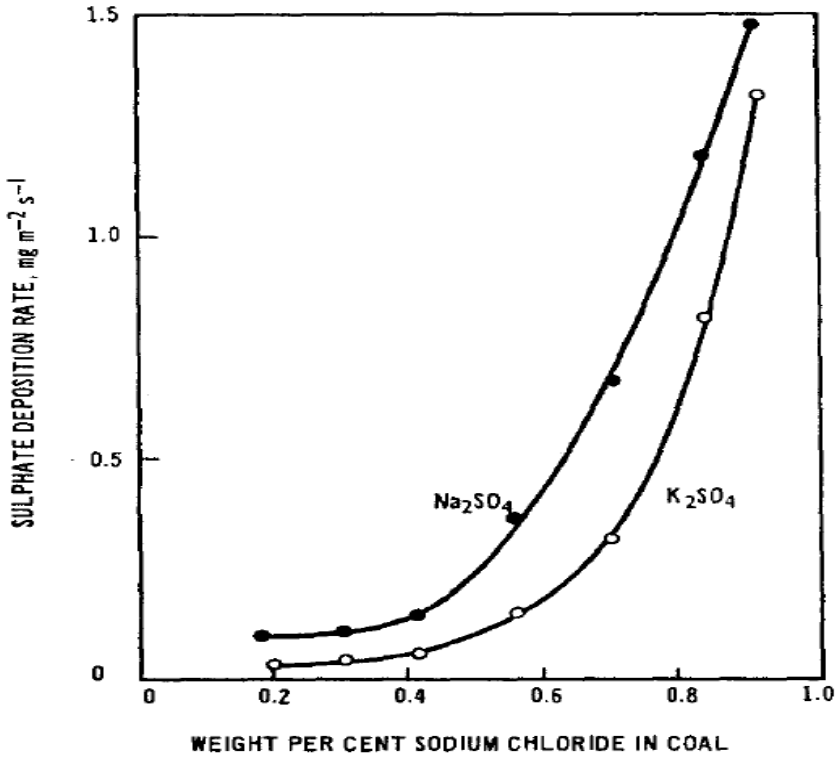

Figure 2-18: Alkali sulphates deposition relation with Cl content in PC boiler [81]

A wide range of literature [81; 85-87] shows, that Cl in coal formed metal chlorides through a series of mechanisms, which significantly increased corrosion rates. Uusitalo [86] suggests that metal chlorides formed on the heat exchanger surface are more corrosive than a direct Cl_2 gas attack.

One mechanism proposed for metal chloride induced corrosion is called an 'active oxidation'. This suggests that metal chlorides form under a deposit due to low oxygen partial pressure (thermodynamically favoured) and that the Cl compounds presence as a melt enables the protective oxide layer to be fluxed; and so metal is lost. These volatile metal chlorides diffused outward and once in the oxidising environment decompose to release Cl_2, which penetrates again to close the Cl_2 cycle. Figure 2-19 shows the thermodynamics of phase stabilities of metal chlorides at different partial pressures of Cl_2 and oxygen.

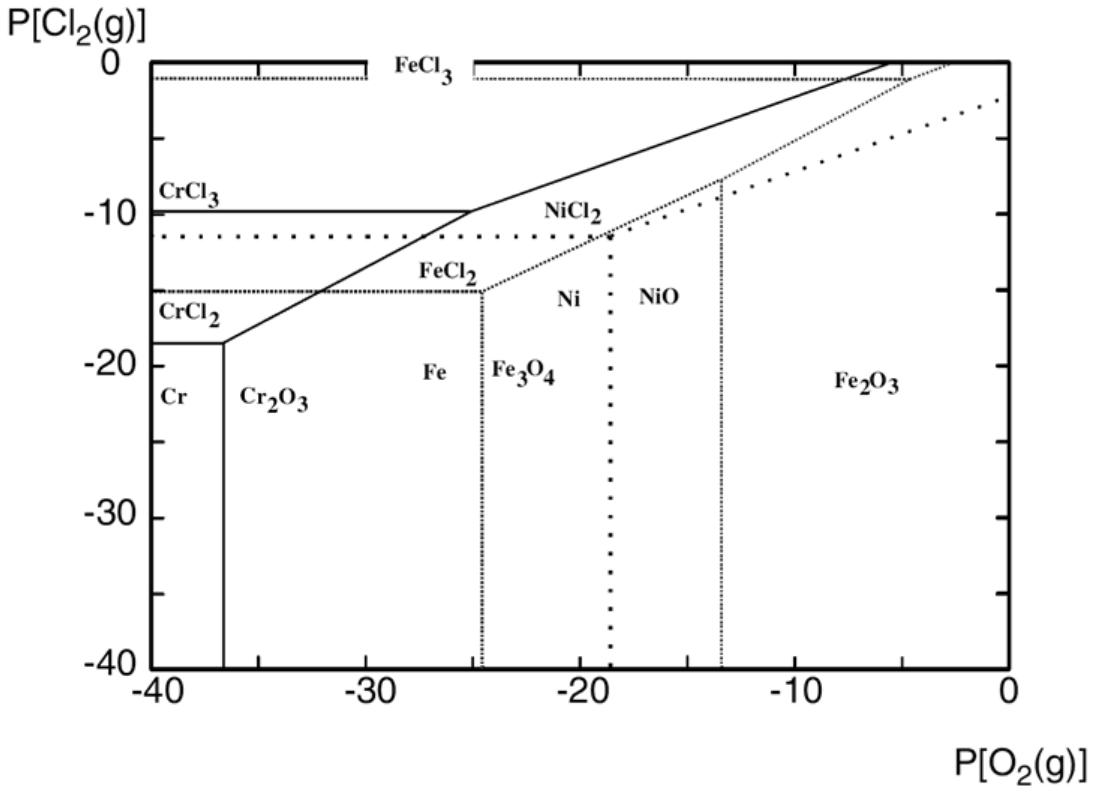

Figure 2-19: Phase stability (super imposed) diagram of (Fe, Cr, Ni)-O-Cl system at 550 °C [86]

According to Ahila et al [87] the overall reaction (two steps) for metal chloride formation can be written as:

$$2NaCl+SO_2+\frac{1}{2}O_2+H_2O = Na_2SO_4+2HCl \quad \textbf{(2-28)}$$

$$MO + 2HCl = MCl_2 = H_2O \quad \textbf{(2-29)}$$

The HCl is believed to be oxidised to form Cl_2 and Grabke et al [88] suggest the following intermediate steps:

$$2HCl + \frac{1}{2}O_2 = Cl_2 + H_2O \quad \textbf{(2-30)}$$

$$2NaCl + Fe_2O_3 + \frac{1}{2}O_2 = Na_2Fe_2O_4 + Cl_2 \quad \textbf{(2-31)}$$

$$Fe + Cl_2 = FeCl_2 \quad \textbf{(2-32)}$$

Whereas most of the literature supports the fact that Cl has an effect on the corrosion rates, there is also some literature which also suggests that Cl level in coal does not have a major effect on corrosion rates [89; 90]. Establishing a role of chlorine in fireside corrosion is still a challenge [64]. The Cl content of deposits formed in biomass and co-fired power plant is an on-going concern, which will be discussed under the headings 2.5.2.1 and 2.5.2.

2.4.4 Combustion Gases

Fuel (coal, biomass and waste) combustion in power plant boilers results in flue gases with the main gases produced including: CO_2, O_2, NO_x, SO_x, HCl and H_2O. Literature [4; 72; 91; 92] has emphasised the importance of flue gas chemistry and its role in fireside corrosion, therefore its understanding is very important for this PhD thesis. The flue gas chemical composition is mainly dependent on the two factors (a) composition of the fuel, and (b) the fuel-oxidant ratio.

Coal from different parts of the world has both different chemical and physical properties. For example, UK coal is higher in S than coal from South America.

If the fuel combustion process is not carried out properly (e.g. not enough oxygen supplied for total fuel combustion) it will result in a reducing environment, which according to literature has a much more corrosive effect than an oxidising environment.

As discussed earlier, in the study of fireside corrosion oxidation is the key reaction in the gas-metal reaction. However this does not simply mean that oxidation is a metal/oxygen reaction, rather a possible oxidation of metal in a mixed gas environment (SO_x, CO_2 NO_x). Oxidation of metal has been discussed earlier and will not be discussed any further; however, the effect of corrosive gases such as SO_2 and HCl, in the combustion gas environment will be briefly discussed.

2.4.4.1 SOx gases

Reid [63] reports that as long ago as 1945 Corey et al [93] collected data which confirmed the effect of SO_2 on low carbon metal. Figure 2-20 illustrates the SO_2 corrosion effect increases with the increase in temperature. The data show that at low temperature SO_2 gas has no more significant behaviour than O_2. However, at approx 800°C the SO_2 corrosive nature triggered and at 870° C the corrosion damage caused by SO_2 was more than 3 times that from O_2 alone. More recently Srivastava [84] reported that other work carried out at ~725°C show an increase in 10 percent of SO_2 gas will double the corrosion damage.

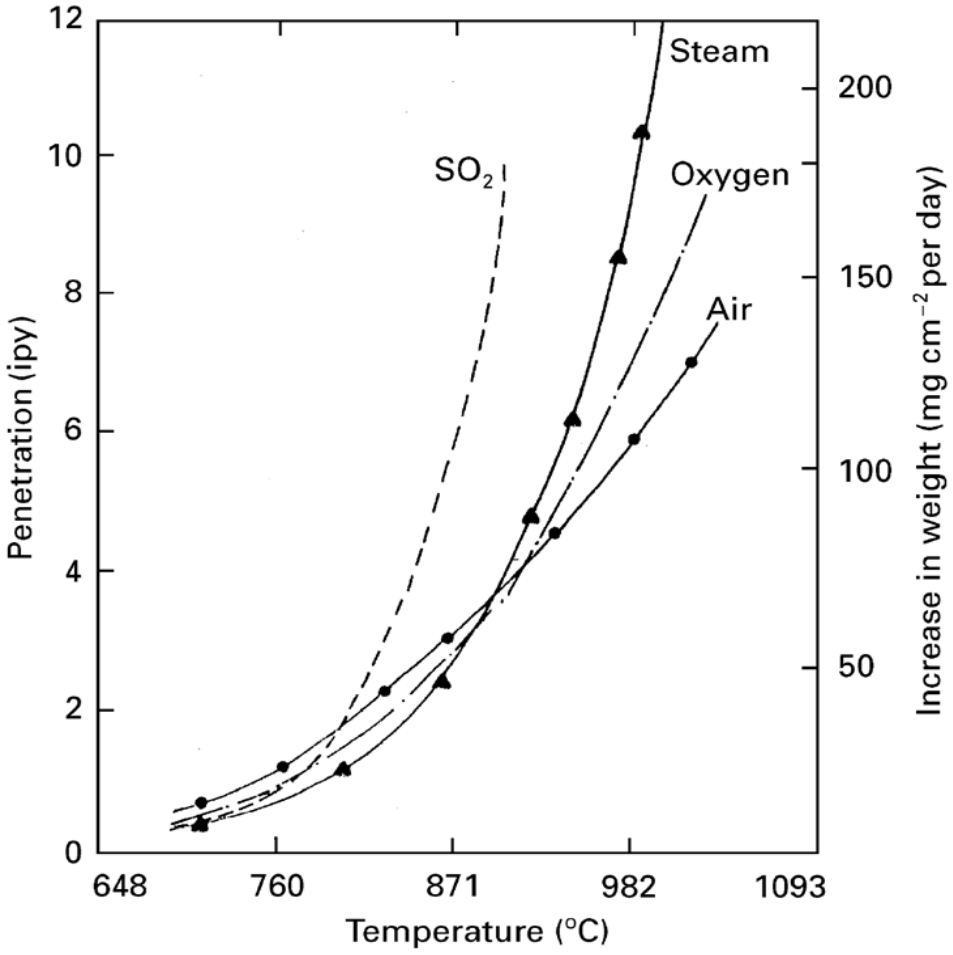

Figure 2-20: Corrosion effect of various atmospheres on low carbon steel [84; 93]

2.4.4.2 HCl/Cl_2gases

Fuels containing Cl (e.g. biomass and coal) give rise to flue gases containing Cl_2 and HCl as a result of combustion processes. However, HCl formation is favoured thermodynamically [67]. Nielsen [67] and co-workers explain that Cl_2 ability of penetration through scales (pores and cracks) and caused severe attack on metal surface. He further explains the reaction of metal surface with Cl_2 or HCl formed volatile chlorides which further react with oxygen to release Cl_2 and formed metal oxides (loose/porous) and enables further Cl_2 attack. Nielsen [67] explains the reaction as follows:

$$M(s) + Cl_2(g) = MCl_2(s) \quad \textbf{(2-33)}$$

$$M(s) + 2HCl(g) = MCl_2(s) + H_2(g) \quad \textbf{(2-34)}$$

$$MCl_2(s) = MCl_2(g) \quad \textbf{(2-35)}$$

$$3MCl_2(g) + 2O_2(g) = M_3O_4(s) + 3Cl_2(g) \quad \textbf{(2-36)}$$

Where M = Fe, Cr or Ni

The effects of HCl or Cl_2 on the corrosion rate (via deposition or direct reactions with the metal surface) are well documented in the literature [85; 86; 88]. An example, is shown in Figure 2-21 which suggested the level of corrosion increases with higher levels of Cl.

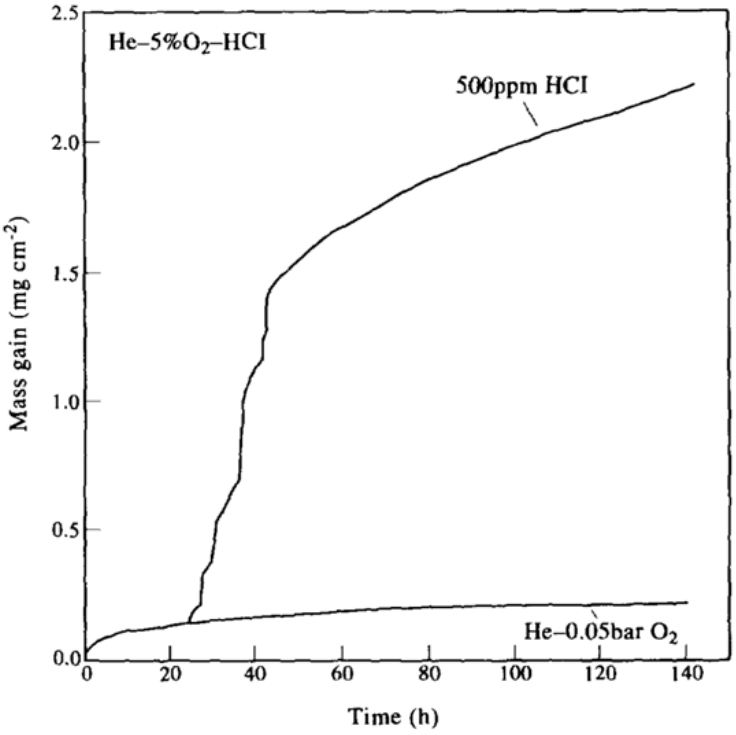

Figure 2-21: Mass gain data of 2 $\frac{1}{4}$ Cr steel after 24 hours exposure to He-O_2 and He-O_2-HCl gases at 500°C [88]

2.5 CO_2 Emission Reduction Routes

2.5.1 Introduction

Fossil fuels are still the main source of fuel used in power plants all over the world. Since the issue of global warming and pollution are on governments' main agenda, industries are pressurised to cut down on greenhouse gas emissions especially carbon dioxide. In the sprit to meet this challenge, there are different routes being suggested so that CO_2 emissions can be reduced. The two routes which are also the focus of this PhD thesis are:

(a) Co-firing biomass-coal power plants, the co-firing of biomass in existing traditionally coal-fired power generation systems has proved to be a successful route to introducing biomass fuels into power generation

(b) Oxy–firing coal/biomass, as an example of a carbon capture technology. There are many technical challenges related to this method, including the

performance of the heat exchanger tube materials under much more aggressive operating conditions

2.5.2 Co-firing power plants

Co-firing is the combustion of two fuels, or some define it as a simultaneous combustion of different fuels in the same boiler [94]. In this thesis the combustion gases simulate the gases produced by one coal (Thoresby) and one biomass; (cereal–co product, CCP). Co-firing specific coals and low levels of biomass additions appears to be the best way to generate the same power as coal firing, but with lower net CO_2 emissions. Co-firing biomass and coal is an emerging technology which has expanded rapidly in the last 10 years, with hundreds of power plants now in operation all over the world [95]. Co-firing coal and biomass in advanced pulverised fuel power plants offers the most efficient use of biomass to generate electricity, as such plants operate at much higher efficiencies than power plants firing biomass alone [96].

2.5.2.1 Biomass

Biomass is classified as a sustainable and CO_2 neutral fuel (as the CO_2 uptake during its growth equals the CO_2 emissions produced during its combustion). Biomass (wood; logs) alone have been used as fuels for centuries mainly for a heating purposes. The building blocks of biomass are carbon, hydrogen and oxygen derived from a process called photosynthesis in plants. At present, biomass is being used in many power plants either as co-fired with coal or on its own in a biomass only power plant. The concept of using biomass as an alternative fuel emerged as a solution to the CO_2 emission issue and is currently used in many UK power plants. However, burning biomass on its own can lead to serious problems like slagging and fouling of superheaters, as a result of the release of KCl into the flue gas, which can condense onto the superheaters/reheaters and form complex compounds. These compounds are highly corrosive with low melting points, and can lead to serious fireside corrosion at any metal temperature above 520°C, which limits the power plant efficiency. Therefore the idea of co-firing has been adopted more [97-99].

Biomass is a major contributor to renewable energy, contributing some 70 % world-wide [19]. While its sustainability, zero net carbon dioxide emissions and widespread supply are advantages, its moisture content, low densities and cost are large drawbacks.

According to Baxter et al [100] biomass can be divided into three main categories:

(1) Herbaceous materials (straw and grass) which lead to rapid and excessive fouling of boiler heat exchanger, straws are cheaper and contain less sulphur than coals, but rich in components such as K and Cl and difficult to transport in large quantities needed for big power stations [70; 101-103].

(2) Shell and other by-product of ligneous nature and

(3) Wood derived products. The biomass fuel of choice with low levels of potassium, chlorine and sulphur, but limited due to cost and availability.

2.5.2.2 Biomass chemistry

Different types of biomass have different effect on fireside corrosion, since straw and cereal co-products (CCP) are the biomass of particular interest, in this project, this research survey will be more focussed on these types. Biomass contains carbohydrates along with different inorganic elements: potassium and chlorine which deposit on the heat exchangers through condensation in different forms and leads to the fireside corrosion; sulphur is also present but less than in coals [101]. In general, biomass contain lower levels of sulphur than coals, so co-firing of coal with biomass will result in reductions in SO_x levels in the flue gases [9; 17; 65; 68; 70]. In contrast, the fuel chlorine levels for biomass are usually found to be in a similar range to many coals (~0.03 – 0.65 wt %), although some can be higher (up to ~2.5 wt %). According to Kilgallon et al [104] high levels of ash (> 20%), moisture (20-50%) and K are also the main challenges for biomass to be used as a fuel. The comparative much lower heating values and bulk densities of biomass than coal are also significant draw backs of biomass which affect the combustion process [95]. However, these

topics are not the focus of this PhD thesis. The high potassium and chlorine levels in straws compared to other biomass levels are shown in the Figure 2-22 and Figure 2-23.

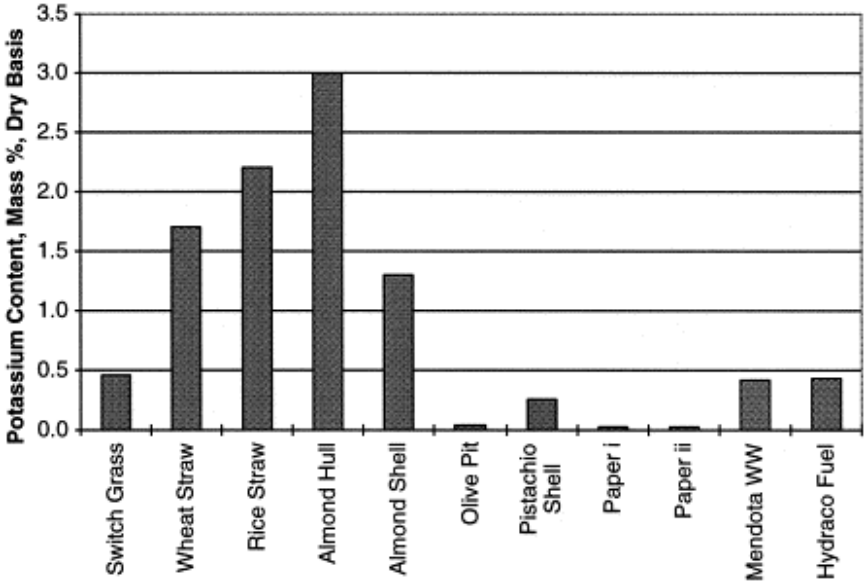

Figure 2-22: Potassium concentration as a function of fuel type [100]**.**

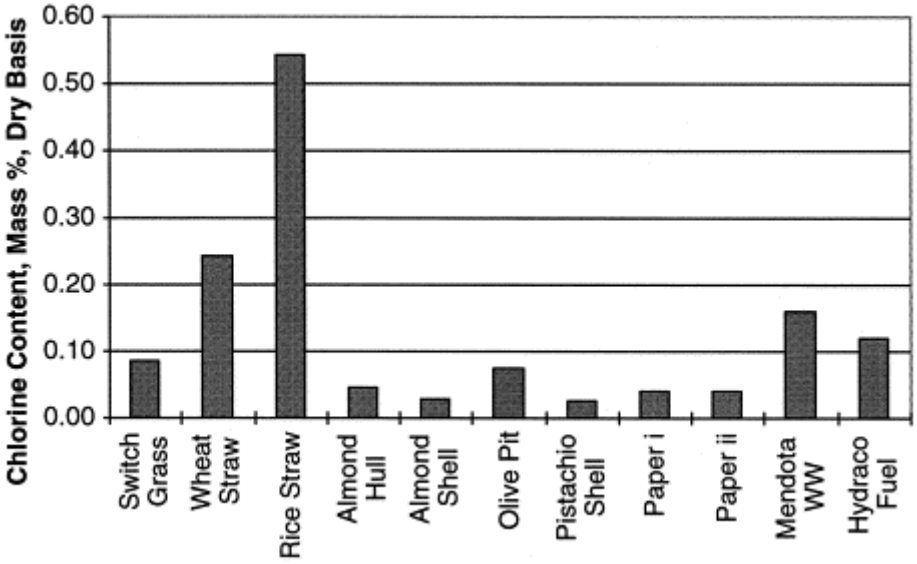

Figure 2-23: Chlorine concentration as a function of fuel type [100]**.**

Potassium (an alkali metal) can be about ~0.1- ~3% in dry biomass and is mainly responsible for fireside deposits whereas chlorine works as a facilitator [19; 100]. An extensive work by a Swedish group on K role in high temperature corrosion of steel was carried out by Pettersson et al [105; 106] shows that austenitic alloys failed to form a chromia protective layer due to a formation of

potassium chromate (K_2CrO_4) the slow outward diffusion of Cr did not match the Cr loss in formation of chromate. They further revealed that once the protective layer is destroyed, the Cl penetration into the scale (anion diffusion) caused further damage resulted in a duplex scale (outer haematite and inner Fe-Cr-Ni spinel). More recently Pettersson et al group [107] demonstrated that K cations rather than Cl ions play the main role in protective chromia layer damage which leads to corrosion. This claim was confirmed by using potassium salts (K_2CO_3) which showed higher corrosion damage than KCl.

2.5.2.3 Biomass power plant

The focus of this PhD thesis is co-firing biomass and coal rather than biomass alone as a fuel. However, if Cl rich deposits are formed then Cl attack on superheaters/reheaters will be of similar nature as has been suggested in literature for biomass power plants [67].

At present power plants biomass use alone as fuels can encounter great challenges (such as fouling, deposition, corrosion and agglomeration) which restricted the steam temperatures and hence produce less efficient power plants. However such problems can be significantly minimised by biomass-coal combustion [19; 65; 96; 97]. As an illustration of the differences between the fuels, biomass fuels, especially ones resulting from rapid growth, tend to have higher levels of readily volatised potassium and chlorine than coals; this can result in the formation of more aggressive deposits on superheater/reheater tube surfaces. Some examples of reaction mechanism involved, where biomass alone used as a fuel and chlorine attack is dominant over sulphate are given in section 2.4.4.2

Studies by Nielsen et al [101] showed that one approach to minimise the biomass corrosion effect, which in fact is a result of KCl condensation on heat exchangers, is **co-firing** with coal; successful results show very low or no chlorine due to the presence of SO_x and the formation of sulphate rich deposits.

2.5.2.4 Co-firing biomass-coal fireside corrosion

Co-firing coal/biomass fuel mixes is a debateable topic: on one hand it supports reaching some of the targets of UK energy strategy (economical and environmental issues) [18] whereas on the other hand it raises various concerns for the power generation industry, with an increase in the fireside corrosion rates of heat exchangers (mainly superheaters and reheaters) being one of them. As discussed earlier, generally biomass has lower sulphur levels than coal, therefore co-firing of coal with biomass will result in reduced sulphur oxides (SO_x) levels in the combustion gases.

Compared to firing coal alone, co-firing coal and biomass can cause significant changes in the chemistry of the flue gas stream and the deposits that form on the surfaces of heat exchangers, which can in turn lead to increased corrosion damage to the heat exchangers. As increased corrosion damage rates will lead to shorter component lives and more boiler shut-downs for either routine maintenance or due to unexpected tube failures, this effect of biomass co-firing has become a challenge for power plant designers and operators in terms of selecting (or developing) materials for the use in heat exchangers in these power plants.

It is believed that fireside corrosion of superheater/reheater tubes is the result of a complex series of processes that can involve: (a) the formation of molten deposits (including various sulphate and/or chloride species) on their surfaces and the reactions between the tube materials, these deposits and the surrounding flue gases at high temperature; and/or (b) the reaction of chloride species with the tube materials to produce volatile metal chlorides [65; 75; 102]. Some detailed reaction pathways have been suggested, and a detailed explanation was documented in the literature [65; 82].

A recent work by Lith et al [108] confirmed that in co-fired power plant KCl deposits strongly enhance the corrosion rate along with internal attack. They further suggest that HCl presence in the flue gas increase the corrosion rate; however this is not required for KCl induced corrosion. A commonly believed

chemical reaction in co-firing of biomass coal is reported in equation (2-37). Montgomery et al. [109] and Johansson et al. [66] explained how the sulphation reaction of KCl occurs and the formation of HCl and Cl_2 gases; where HCl is released into flue gas and Cl_2 remained around the deposits for the corrosion attack. The equations can be written as:

$$2KCl(s) + SO_2(g) + \frac{1}{2}O_2(g) + H_2O(g) = K_2SO_4(s) + 2HCl(g) \quad (2\text{-}37)$$

$$2KCl(s) + SO_2(g) + O_2(g) = K_2SO_4(s) + Cl_2(g) \quad (2\text{-}38)$$

Potassium salts (KCl and K_2SO_4) are bonding agents on the metal surface which help trap fly ash particles. Reaction mechanisms in such complex environments are part of on-going research and are currently being developed, but all depend critically on the composition of the fuel(s) entering the power plant, the heat exchanger operating conditions (especially the metal surface temperature) and the heat exchanger material(s).

The rate of fireside corrosion is also depend on the fuel mixtures used: experienced gained in existing co-fired plants (with lower temperature/pressures steam systems, 560°C/160bar) suggest that the use of 5% (by energy) of biomass does not cause significant problems and that the use of up to ~20% of some biomass/coal combustion may be possible [65; 96; 104].

In Figure 2-24 a piece of work by Simms et al [102] to observe the co-firing effect on heat exchangers showed the potential gas compositions from using one coal with 10% wheat straw or willow wood gave gas compositions that are well within the ranges predicted for firing different coal compositions alone.

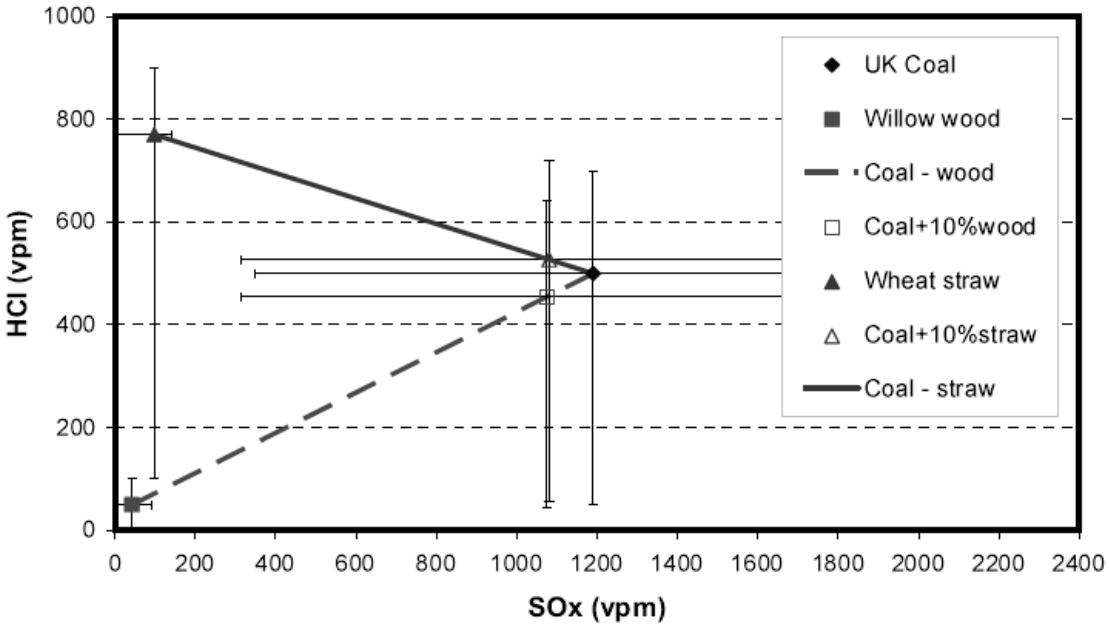

Figure 2-24: Gas compositions predicted for two biomass and coal-biomass mixtures [102]

In a paper by Montgomery [65] it is shown that several attempts have been made to increase the biomass ratio in co-firing; until now up to 20% biomass (straw) can be used to substitute coal and give reasonable results. Possible use of biomass up to 20% was also reported by Aho et al. [103] and Zheng et al. [110]

2.5.2.5 Advantages over coal and Biomass only Power Plants

One of the main advantages of co-firing biomass and coal is its easy implementation on pulverised coal power plants without any major modifications. Simms et al. [96] present an example of the benefit of a co-firing over a biomass only power plant: using a 5% uptake of biomass in a 500 MWe coal power plant generates 25MWe biomass derived power compared to ~21MWe power from the same quantity of biomass fired in a biomass only power plant. The allowable ratio of coal and biomass in co-firing is still under investigation, however reports show that up to 20% of selected biomass can be co-fired with particular coals without having any severe corrosion and depositions issues [65; 103].

A quote from Steve Segrest, Director Common Purpose Institute, U.S. Department of Energy [111] emphasises the importance of Co-firing;

"Current regulatory and market realities do not make it cost-effective for utilities to build stand-alone biomass-based power plants. Co-firing with biomass fuels utilizes existing power plant infrastructure to minimize capital costs while maximizing environmental and economic benefits"

Some of the benefits of co-firing to the industry are

- rapid introduction of renewable and CO_2 neutral fuels into the power generation market
- Overall reduction in SO_x
- Minimise Cl attack on superheater due to sulphation reaction
- Completion of CO_2 cycle due to biomass
- Low deposition and corrosion (major issue for biomass only power plant)
- Eliminate building requirement of new power plants for biomass fuel only
- Opportunities for farmers to grow energy crops
- Meaningful way of consuming agricultural waste.

2.5.3 Oxy- firing technology

2.5.3.1 Introduction

Oxy-firing, or using oxy-fuel technology, is another route to reduce emissions of greenhouse gases from future power plants. The six greenhouse gases identified under the Kyoto agreement are carbon dioxide (CO_2), methane, nitrous oxide, hydrofluorocarbons, perfluorocarbons and sulphur hexafluoride. From a power generation industry point of view the target gases are CO_2 and NO_x.

Oxy-firing is one of three ways of carrying out carbon capture and storage (CCS), it is an emerging option believed to be the lowest risk involved in CCS technology [112]. The other two types are pre-combustion capture (where carbon is removed from the fuel before combustion) and post-combustion capture (where carbon-dioxide is removed from the flue gas after the

combustion); however, these are not the research areas of this PhD, and will not be discussed further in this report.

The oxy-fuel firing concept is to carry out the fuel combustion in an O_2-recycled flue gas (mostly CO_2 and steam) environment instead of air and so to produce a flue gas stream with minimal N_2 content, but still containing excess O_2. In typical coal oxy-fuel combustion, based on hot wet flue gas re-cycling prior to any desulphurisation step and a 95% pure O_2 supply, the bulk flue gases are expected to contain 60% CO_2–30% H_2O–4% O_2–5% N_2 [9; 16; 17], whereas in traditional air-firing conditions the combustion gases contain 74% N_2–12% CO_2–9% H_2O–4% O_2 [9; 17] (both gases also contain other minor species). In the oxy-fuel fired systems, the flue gases are recycled through the fuel burners to maintain the mass flow that passes through the heat exchangers: the process is explained in detail elsewhere [9; 16; 21; 113].

The products of combustion in an oxy-fuel environment are a matter of concern for the boiler components (e.g. superheaters and reheaters), as the increased levels of CO_2 and H_2O can be coupled with increased levels of corrosive gases such as HCl and SO_2 (up to 5 times the levels found in conventional boilers using the same fuel, depending on the flue gas re-cycling configuration [9; 16]). Compared to conventional combustion systems, oxy-fuel firing is expected to result in different gas chemistries, deposit compositions and potentially corrosion reaction mechanisms on the heat exchangers (superheaters/reheaters and water walls). Other issues associated with oxy-firing technology are its costly air separation unit, higher flame temperatures, and overall efficiency loss [20]. Figure 2-25 presents the basic schematic of oxy-fuel firing technology [114].

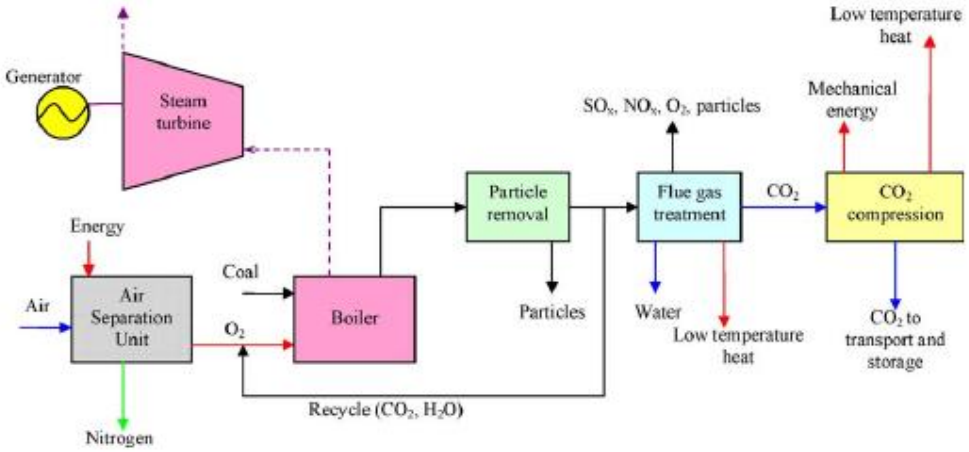

Figure 2-25: Schematic of oxy firing of fuel (system with hot gas recycle before desulphurisation) [114]

There are many power companies working toward variation on oxy-firing CCS technology. However, the technology is still only partially developed and in trials in pilot plant facilities across Europe. This PhD is only concerned with the influence of oxy-firing on the heat exchanger materials within a boiler; an area which requires intensive effort in order to have assurance so that the technology can be applied to the existing and new power plants.

2.5.3.2 Difference between air-firing and oxy-firing conditions

Oxy-firing, a technology for power plants initiated in 1980s [113], is based on combustion with oxygen instead of air, so the flue gases mainly consist of CO_2 and H_2O [115]. Literature shows oxy-firing of fuel can bring the following changes in the system:

- Approx 60% (by volume) CO_2 in the flue gas stream, i.e. ~4-5 times more than air fired conditions
- Approx 31% H_2O in the flue gas i.e. ~4 times more than air fired conditions
- After drying the flue gas, CO_2 is approx 95% pure and provides an ideal situation for geo-sequestration of CO_2 [116]
- Due to the recycling of the flue gas, the corrosive gases, such as SO_2 and HCl levels, are also higher (by ~ 4-5 times)

- Factors such as separation of O_2 from air and compression of CO_2 to give a liquid output for transportation significantly lower the power generation efficiency

One benefit of oxy-firing technology is that it can be retrofitted in existing power plants; however with such obvious changes in the flue gas chemistry, it requires an extensive study of the effects of these gases on materials performance. Table 2-1 summaries the gas composition in the furnace for dried lignite combustion for air firing and oxy-firing in pulverized fuel (PF) boilers.

Table 2-1: Gas composition in the furnace for dried lignite combustion in air-firing and oxy-firing conditions [16]

Gas composition in Furnace		
Lignite vol%	Oxy-fuel fired PF (%)	Air-fired PF (%)
N_2	4.8	71.3
O_2	1.9	2.5
CO_2	58.9	15.3
H_2O	31.8	10.0
Ar	2.1	0.8
SO_2	0.49	0.13

2.5.3.3 Fireside corrosion and other issues with Oxy-firing technology

All the major issues related to oxy-fuel combustion, such as the oxygen purity requirement, proportion of the gases recycled, SO_x and NO_x removal from recycle stream and related work are well documented in the literature [113]. General issues such as the cost of ASU units, flame temperature, boiler designs and operation, recycling of flue gases, removal of SO_2 from the flue gas, dehydration and removal of NO_x are not the research interest of this PhD. The main issue of oxy-firing highlighted in this PhD is the performance of materials in superheaters/reheaters under such aggressive environments. A recent work by Bordenet and Kluger [22] emphasized the need for laboratory-based oxy-fuel corrosion testing.

2.5.3.3.1 CO_2 and moisture effect

An approximately four times increase in the levels of moisture and CO_2 levels in the flue gas stream is one of the most remarkable features of oxy-fuel firing. A wide range of literature shows the change in metal oxidation properties with high levels of H_2O and CO_2. However, most of it does not include excess O_2 needed to simulate oxy-firing conditions correctly. A recent work by Pirón Abellán et al. [117] shows that steel oxidation in high CO_2/H_2O gases resulted in the formation of Fe rich oxides and the suppression on chromia layer formation due to internal oxidation as a result of high levels of CO_2 gas which supported the formation of carbides. Such chromia behaviour was also reported by D J Young et al [118] of further decreased chromium activity and diffusion toward the surface. Similarly the high moisture content helped rapid hydrogen diffusion and that increased the oxygen solubility in the alloy, resulting in internal chromium oxidation.

In another research group [119] work was carried out to test carburisation of ferritc and austenitic steels in $CO_2/H_2O/O_2$ environment show formation of duplex layer of $FeO/Fe_3O_4/Fe_3C$ between oxide and base metal. Their studies further reveal that different carbide morphologies observed suggested carburisation is dependent on temperature, pressure, alloys and as composition. Another group [120] carried out corrosion test and suggest that carburisation occurred in above any temperature 500°C where CO_2 is dominant. They further suggested that carburisation in $CO_2/H_2O/O_2$ and CO_2/H_2O are comparable for alloys contain < ~11%Cr where similar in alloys contain Cr >~11%.

More recently work by Young and co-workers [121] also highlighted the importance of carburisation risk of steel in high CO2 environment. Their work show under layer formation of carbides $(FeCr)_7C_3$ due to low activity of oxygen (metal oxide equilibrium). It was also suggested that carburisation was faster in dry gas than wet gas (water vapour lowers the carbon activity). The paper also presented reactions to show how carburisation can occur within scale /oxide interface.

$$CO_2(g) = CO(g) + \frac{1}{2} O_2(g) \quad \textbf{(2-39)}$$

$$2\,CO(g) = CO_2(g) + C(s) \quad \textbf{(2-40)}$$

The group's thermodynamic model carbide prediction agreed with the experimental data (Cr rich carbides) obtained. In order to fill the gap in knowledge with respect to materials, researchers [9; 20; 22] have emphasized need for lab based experiments before commercializing the technology.

2.5.3.3.2 SO_x effect

The high concentration of SO_x gases, due to the recycling process of the flue gases, and its corrosive effect on the heat exchangers material are of a great concern. The high levels of SO_3 produced due to high availability of SO_2 could form a deposit rich in "alkali iron tri-sulphates" which are believed to be the main contributors to fireside corrosion [20]. Thermodynamic modelling work [22] and recent pilot plant experiments [112] report the high levels of both SO_2 and SO_3 in the flue gases of oxy-firing systems. Stanger et al [112] reported the work of Ochs et al [122] showed a rise in SO_2 concentration from 200 to 900 ppm whereas Kakaras et al [115] suggested an approximate increase from 200 ppm to 800 ppm when firing conditions changed from air to oxy-firing and lignite was used as a fuel.

There are many options under development to reduce the SO_x levels in the flue gases so the corrosion aspect can be eliminated. However these options such as flue gas desulphurisation (FGD) is not the main interest of this PhD thesis. Therefore, oxy-firing tests carried out simulate flue gases generated using a recycle after particle removal and before FGD are discussed. Laboratory based experiments carried out by Covino et al [123] show that oxy-fired gases (high SO_x) gases have high corrosion effects when bare samples are exposed. However, when samples are covered with deposit there was no difference in corrosion was observed in both conditions (air and oxy-fired). More recently a pilot plant test was carried out at E-ON UK [124] also suggests that both co-firing and oxy-firing have higher corrosion rates on superheaters than corrosive rates observed in coal-only air combustion system.

Extensive work carried out by Orchard et al [125] showed the sulphidation mechanism of austenitic alloys resulted in nickel-rich sulphides. A high H_2S gas partial pressure was used (S activity was higher) to show the austenitic alloys sulphidation mechanism and concluded that Ni reacted more rapidly than Cr and formed duplex layer of Fe-Ni-S (outer) and Fe-Cr-S (inner layer). H_2S gas was used in this rather than SO_2; however this case is mentioned here to show the Ni behaviour towards high concentrations of S and so emphasise the risk of corrosion damage of superheaters/reheaters in oxy-firing flue gases. Researchers [20; 22] have also emphasised the need to fill the gap in the knowledge from the material viewpoint and the need for laboratory based experiments before commercialising the technology. Almost all the literature highlighted under the headings 2.5.3.3.1 and 2.5.3.3.2 were carried out in gas phase environments. However, the real superheaters/reheaters suffering from fireside corrosion are exposed to both deposits and combustion gases. The understanding of the reaction mechanism in oxy-firing systems is still a challenge for researchers.

3 EXPERIMENTAL METHODS

3.1 Introduction

This chapter is mainly divided into three sub sections, (a) pre-exposure work, (b) fireside corrosion testing and (c) post exposure work. 'Pre-exposure works' describes the work carried out prior to the sample exposure in the furnace, and includes materials and deposit preparation. The 'fireside corrosion testing' section, contains procedures for furnace setup, exposure conditions and sample monitoring via mass change data. The 'post-exposure work' describes the sample preparation, and investigations carried out after the fireside corrosion testing of samples.

During the first two and a half years of this PhD course, nine fireside corrosion tests were carried out. Each test run of 1000 hours was divided into five cycles of 200 hours (approximately two months) with continuous monitoring followed by extensive sample preparation procedures and analysis (using different tools). Six out of nine tests were performed in oxy-firing conditions and the remaining three tests in air-firing conditions. All the tests were carried out in the temperature range of 600 to 750°C. Five different alloys (two ferritic, two austenitic and one nickel based) were used in this PhD project.

Ten different composition deposits were prepared; however, only the first 4 deposits (D1, D2, D3, and D4) were used in the eight out of the nine tests. Thus these four deposits (D1-D4) are the ones deposits used in this PhD project. Test number 9 (the last test) was an experimental trial for deposit stability and material exposure to the high levels of some salts (deposits D5-D10). The overall conditions set for all the nine tests carried out during this PhD project (test matrix) are listed in Table 3-4. The tests were carried out in the same sequence as listed in the Table 3-4.

3.2 Pre-Exposure work

This section is about providing the materials (measured and clean specimens), the preparation of synthetic deposits and other laboratory preparations required (temperature profiles and gas supply etc) for fireside corrosion testing.

3.2.1 Materials

The selection of the materials (metal alloys) was the very first step required in the experimental work. In this PhD project five alloys were selected that are used in heat exchangers in the power generation industry. The materials were: two low chromium ferritc alloys (T22, T92); two austenitic alloys (347HFG, HR3C); and, a nickel based alloy 625.The alloy compositions are given in the Table 3-1. The original materials were received as long tubes which were machined and cut into rings and finally into curved specimens. The typical dimensions of specimens (of tube segment shape) were ~ 15 mm chord length x ~15 mm height and ~ 4 mm wall thickness. All the surfaces of specimens were given a UK 600 grit finish. An example of tube, ring and curved specimen is shown in Figure 3-1.

Figure 3-1: An alloy tube, ring and curved samples

3.2.1.1 Cleaning

The material cleaning procedure involved placing samples in an ultrasonic bath in volasil for 20 minutes followed by another ultrasonic bath in Isopropyl alcohol (IPA) for another twenty minutes. Crucibles for each specimen were also cleaned in the same manner. After the cleaning procedure, the samples were dried and pre-exposure dimensional metrology was carried out using a digital micrometer.

3.2.1.2 Pre-Exposure dimensional metrology

The pre-exposure dimensional metrology was essential for mass change and metal loss data calculations. A digital micrometer with a resolution of ±0.001mm was used for the measurements. Chord length and height were measured in three different positions, and the thickness along the sample length in eight different positions. Using the average of these measurements the surface area of each sample was calculated (for use in mass change calculations). The sample thickness data were used for metal loss calculations.

The pre-exposure measurements of the samples were very important because they were to be compared to measurements made after exposure to calculate changes in sample dimensions. These data were to be subsequently used for statistically analysis of metal wastage and for modelling materials performance.

Once the samples were clean and measured, they were kept in individually labelled airtight plastic bags to minimize the air exposure. The furnace could only take up to 24 samples at a time. An example of a clean sample placed in a clean crucible before prior to fireside corrosion test is shown in Figure 3-2. A shallow hole was drilled in the samples (as illustrated in Figure 3-2) which are used as a reference point for future metrology investigations.

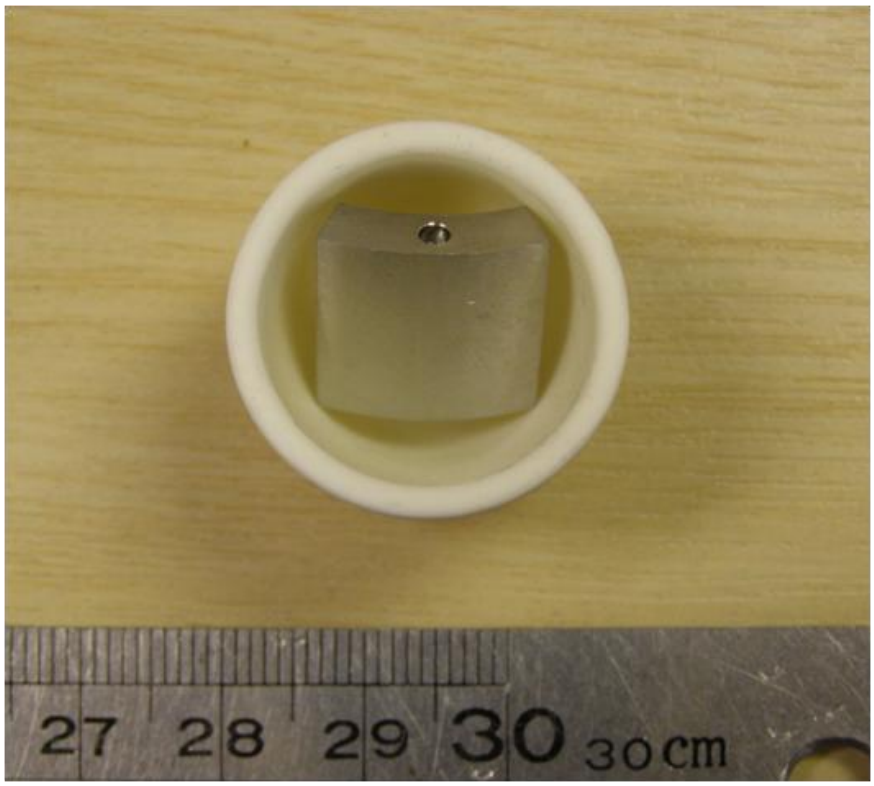

Figure 3-2: A clean T22 sample in a clean crucible

Table 3-1: Nominal compositions of materials used in fireside corrosion testing

Material	Nominal composition (weight %)									
	C	Si	Mn	P	S	Cr	Mo	Ni	Fe	Others
T22	0.15	≤0.50	0.3-0.6	≤0.03	≤0.03	1.9-2.6	0.87-1.13	-	Bal	-
T92	0.13	≤0.50	≤0.60	≤0.02	≤0.01	9.5	0.6	-	Bal	0.09 Nb; 0.07 N; 0.25 V; 2 W
347HFG	0.08	≤0.50	≤2	≤0.05	≤0.03	17-19	-	9-13	Bal	Nb, Ta
HR3C	0.1	0.75	≤2	≤0.04	≤0.04	25	-	20	Bal	0.4 Nb; 0.2 N
Alloy 625	0.1	≤0.50	≤0.50	≤0.02	≤0.02	20-23	8-10	Bal	5	1 Co; 0.4 Al

3.2.2 Deposits

In this PhD project ten different deposits were prepared with the compositions listed in Table 3-2. Deposits D1 to D4 were main deposits used for the fireside corrosion testing. These deposits simulate the deposits that form on the heat exchangers in real power plant.

- D0: no deposit (i.e. bare alloy surface exposed to the gas atmosphere)
- D1: a standard deposit composition that is widely used in screening tests; it represents a composition of alkali–iron trisulphate that has been identified from many investigations as the principal cause of fireside corrosion in superheaters/reheaters in coal-fired power stations [9; 17; 32; 126]

- D2: the alkali–iron tri-sulphate compositions from D1 diluted with 80% kaolinite ($Al_2O_3 \cdot 2SiO_2 \cdot 2H_2O$) to represent the clay minerals usually found in coals. This mixed deposit represents that formed by mixed deposition routes (particle and vapour deposition) on superheater/reheater surfaces [16; 17; 32; 96; 126; 127]
- D3: is similar to D2 but with the addition of 1% KCl to assess the impact of co-firing a biomass containing significant quantities of K and Cl with a UK S containing coal
- D4: is similar to D3, but with more KCl (5%) to investigate the sensitivity of corrosion damage to this change in composition as a result of biomass co-firing combined with different deposit formation mechanisms–deposit compositions are anticipated to vary around and along superheater/reheater tubes, as well as with biomass/coal mixing options
- Deposits D5-D10 (simplified compositions) were only used in one test (test 9)

The deposits were mixtures of different compounds that had been dissolved/dispersed in IPA to form a slurry/paste which were easier to paint on the samples. In fireside corrosion testing (test 1-8) four samples of each alloy

that had been painted with the deposits (D1-D4) were exposed in each test. In addition one sample of each alloy (except alloy 625 due to limited furnace capacity) was used without a deposit as a blank or a reference sample to assess gaseous oxidation performance. The deposit compositions were based on the chemical compositions of the fuels (biomass and coal). The molar ratios of the compounds were varied to simulate the different fuels types and their deposition effects.

In test 9 three alloys T92, 347HFG and alloy 625 were used. Each alloy was painted with deposits (D5-D10). An example of a sample with its painted deposit is shown in Figure 3-3.

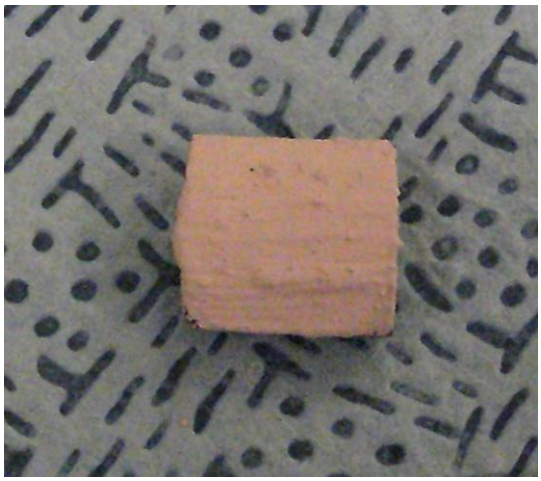

Figure 3-3: Sample covered with deposit prior to heat exposure.

The mole percentage ratios of the compounds in each deposit are listed in the Table 3-2.

Table 3-2: Deposit composition used in fireside corrosion tests

Nominal Deposit Compositions (moles %)						
Deposit No	Kaolnite*	Na_2SO_4	K_2SO_4	KCl	Fe_2O_3	SiO_2
D0	-	-	-	-	-	-
D1	-	37.5	37.5	-	25	-
D2	80	7.5	7.5	-	5	-
D3	80	7	7	1	5	-
D4	80	5	5	5	5	-
D5	-	-	100	-	-	-
D6	-	-	-	100	-	-
D7	-	-	50	-	50	-
D8	-	-	50	-	-	50
D9	-	-	-	50	50	-
D10	-	-	-	50	-	50

***$Al_2O_3.2SiO_2.2H_2O$**

3.2.3 Gases

The exposure conditions for the fireside corrosion tests were set following a detailed investigation of the gas and deposit environments that could be produced using coals and biomass available for use in UK power stations. Figure 3-4 illustrates examples of the chlorine and sulphur contents of different potential coal and biomass fuels.

The chemical composition of many potential fuels is available in research literature [127]. Such values have been used together with a mass balance spreadsheet to calculate gas composition (in % volume). The gases used simulate the flue gases of co-fired power plants at a ratio of 80:20 wt% coal: biomass which is higher than currently used, but a target for future operations. The gas compositions are listed in Table 3-3.The composition of gas1 simulates air-firing

conditions, with approximately 0.1% SO_2 and 0.04% HCl and represents the combustion products from 20% CCP and 80% of a UK coal fired with air [102]. Similarly, gas 2 is also a result of 1:4 CCP and coal combustion, however it contains high levels of CO_2, moisture and corrosive gases as expected in an oxy-fuel firing process with flue gas re-cycle after particle removal but before flue gas desulphirisation [22]. These gas compositions have been simplified to their key active components for the purposes of corrosion testing in simulated superheater/reheater environments (e.g. Ar and traces of CO have been omitted) and SO_X is supplied as SO_2.

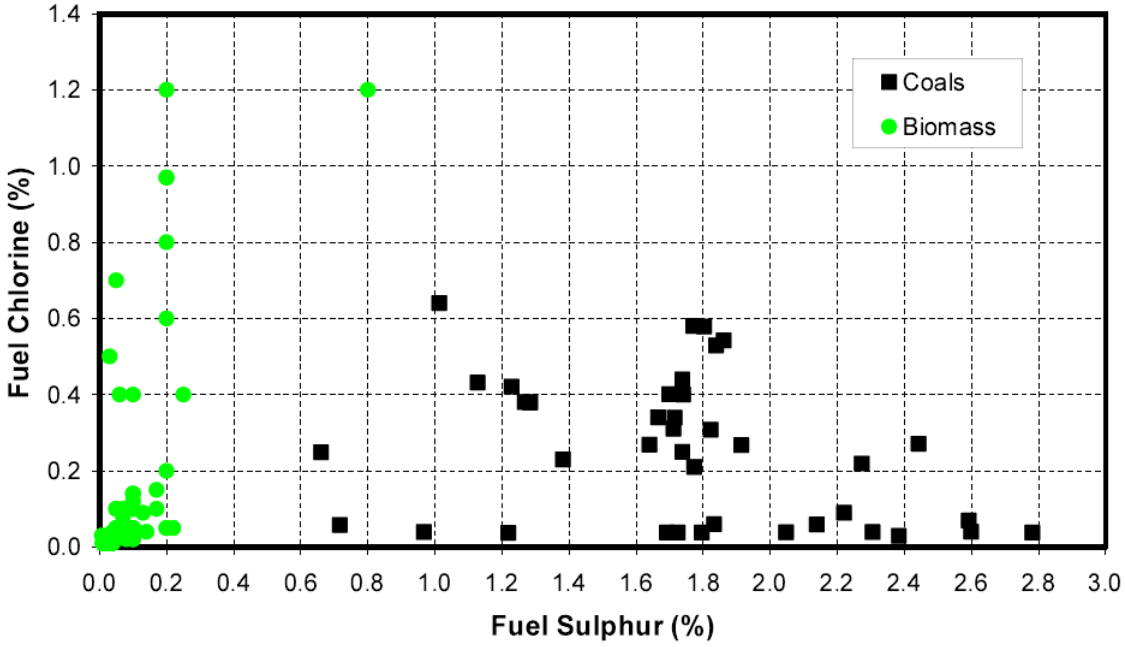

Figure 3-4: Variation of fuel chlorine and sulphur contents for a range of biomass and coals [127]

Table 3-3: Gas compositions used in fireside corrosion testing

Nominal Gas Composition						
Gas	N_2	O_2	CO_2	H_2O	SO_2	HCl
	%	%	%	%	vppm	vppm
1 (Air-fired)	Bal	4	14	8	1300	400
2 (Oxy-fired)	Bal	4	59	31	6260	1700

3.2.4 Temperature

As the power generation industry is considering supercritical and ultrasupercritical (USC) steam conditions and moving toward higher temperatures to be more efficient, the metal temperature of superheater and reheater are expected to go higher [60]. In this PhD project the fireside corrosion test simulating air-firing conditions were carried out at three different temperatures 600, 650 and 700°C, whereas for oxy-firing conditions, tests were carried out at four different temperatures 600, 650, 700 and 750°C. Prior to every test, a temperature profile was carried out to ensure that temperature ± 5°C was attained in the furnace as programmed.

3.2.5 Deposit stability and high levels salt exposure test

As discussed earlier, test 9 is trial for two different research interests: (a) deposit stability and (b) materials exposure to simplified deposit compositions. As discussed in the literature review chapter, the slagging and fouling within power plants boilers results in thick deposits accumulating on heat exchanger surfaces.

Some researchers [22] have emphasised the importance of lab based studies to determine the thermal stability of these deposits in novel conditions. Test number 9 was an attempt towards gaining a better understanding of the stability behaviour of deposits, when exposed to conditions simulating oxy-fired conditions (for 200 hours at 650°C). An inert sapphire disc material was used as the substrate for deposit stability testing. The dimensions of these discs were 10

mm ± 0.1 diameter and 3 mm ± 0.1 thicknesses. The discs were painted with the deposits (slurries) using a paint brush; as for the corrosion samples.

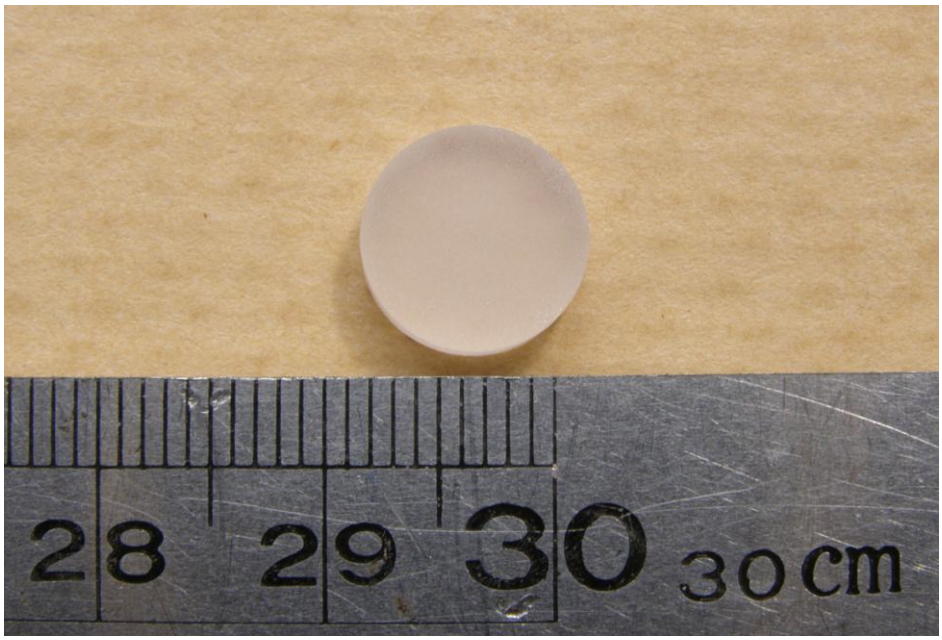

Figure 3-5: A clean sapphire disc used for deposit stability test

In the same test (test 9), three different alloys (T92, 347HFG and alloy 625) were painted with simplified deposit compositions (D5-D10). All the other experimental procedures were carried out in the same manner as for the earlier tests.

Table 3-4: Test condition for fireside corrosion testing

Test No	Gas/Firing Condition	Temperature (°C)	Time (hours)	Materials	Deposits
1	Air	600	1000	T92, 347HFG, HR3C, 625	D0, D1, D2, D3, D4
2	Air	650	1000	T92, 347HFG, HR3C, 625	D0, D1, D2, D3, D4
3	Oxy	600	1000	T92, 347HFG, HR3C, 625	D0, D1, D2, D3, D4
4	Oxy	650	1000	T92, 347HFG, HR3C, 625	D0, D1, D2, D3, D4
5	Oxy	700	1000	T22,T92, 347HFG, HR3C, 625	D0, D1, D2, D3, D4
6	Oxy	700	1000	T22,T92, 347HFG, HR3C, 625	D0, D1, D2, D3, D4
7	Air	700	1000	T22,T92, 347HFG, HR3C, 625	D0, D1, D2, D3, D4
8	Oxy	750	1000	T22,T92, 347HFG, HR3C, 625	D0, D1, D2, D3, D4
9	Oxy	650	1000	T92, 347HFG, 625 sapphire disc	D1,D4,D5, D6, D7, D8, D9, D10

3.3 Fireside Corrosion Testing

3.3.1 The Furnace

The fireside corrosion tests were carried out in an alumina-lined vertical controlled-atmosphere furnace. The furnace is designed to accommodate 24 samples at a time, in individual alumina crucibles sitting in a frame (known as the furniture). Multiple gases to simulate the flue gases in power plants were supplied into this furnace. The flow rates of the gases were controlled by using mass flow controllers. The required temperature and time were also set using the main control unit. The corrosive hot gases coming out from the furnace were neutralised by passing through the scrubber (NaOH solution) before being vented. The breakdown of the gas compositions are given in Table 3-3.

Figure 3-6: A bank of four fireside corrosion vertical furnaces facility at Cranfield University.

The furnace setup was also a little different for both tests. To generate the simulated air-fired combustion gas, air was passed through the de-ionised water bubbler placed in a water bath at a set temperature (41°C i.e.58.3 torr) so that the required amount of moisture was added to this gas stream, before it was mixed with those containing SO_2 and HCl as shown in schematic representation in Figure 3-7. However due to high volume of moisture was required to simulate oxy-firing conditions, a direct deionised water supply (using a peristaltic pump) was used, as shown in Figure 3-8. In the oxy-firing tests due to the high moisture content, some other modifications were also carried out to avoid condensation in the upper region of furnace which can leads to cracks in the alumina reaction tube and also outlet blockage. Hot water at 80°C was circulated within the flange to ensure that all the moisture left as steam and did not cause any breakages or blockages. The exhaust gases from the furnace passed through an initially empty bottle to trap the condensate produced (a very acidic solution with pH 0). To maximise the condensation from the exhaust gases, an extra cooling loop was introduced within the condensate bottle which carried antifreeze liquid at 2°C.

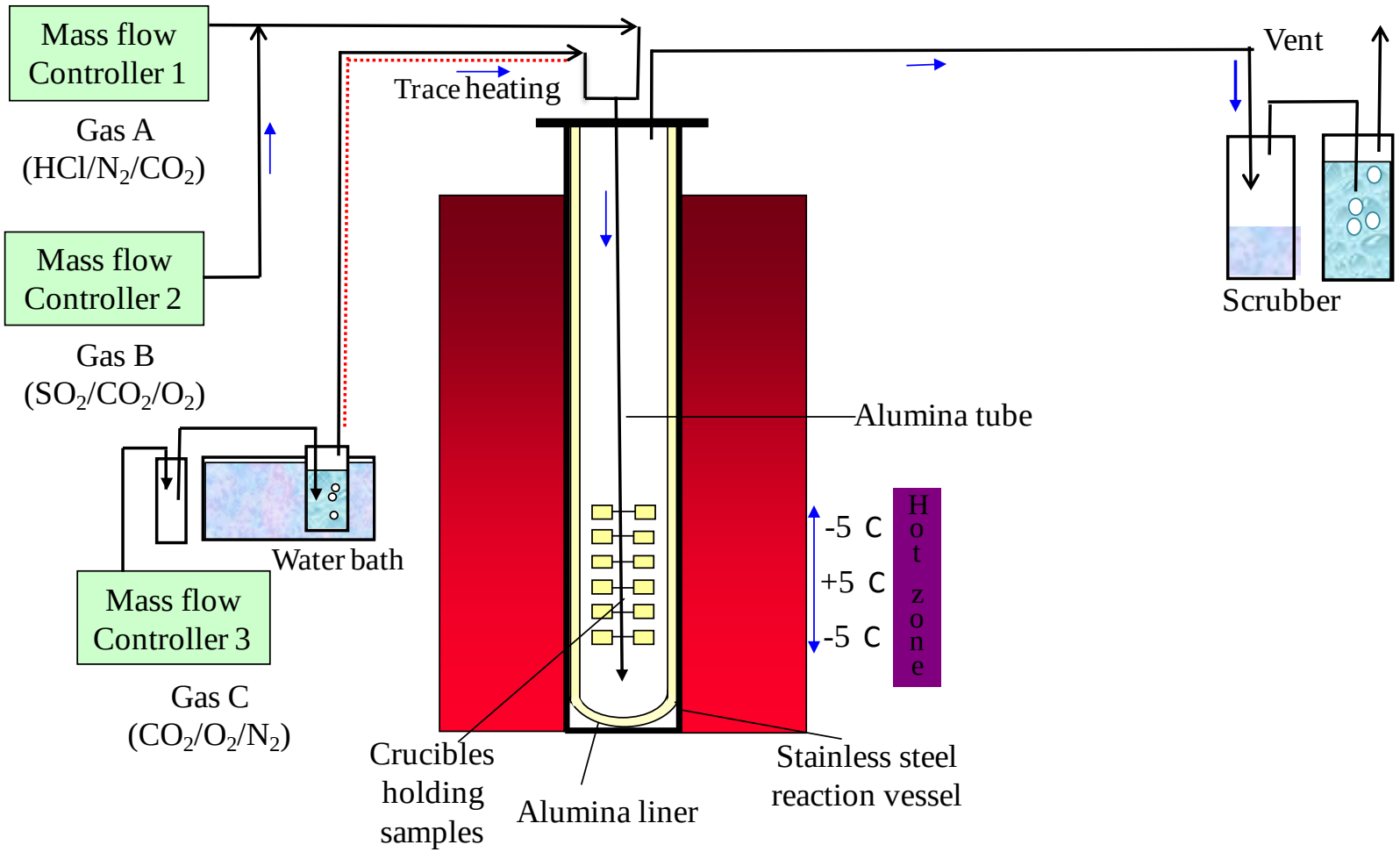

Figure 3-7: Schematic diagram of a vertical controlled atmosphere furnace setup for fireside corrosion exposures in simulated air-firing combustion gas

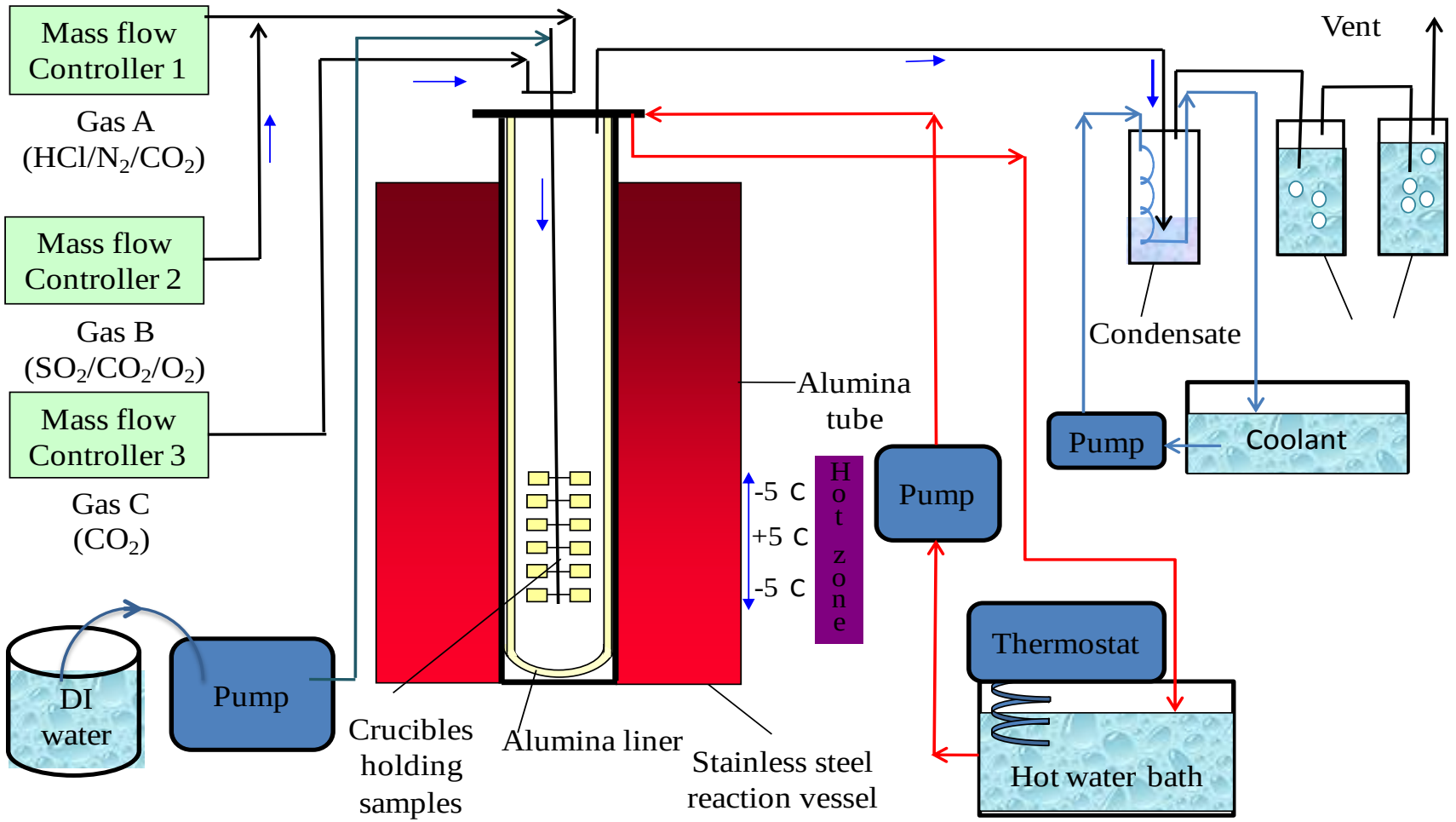

Figure 3-8: Schematic diagram of a vertical controlled atmosphere furnace setup for fireside corrosion exposures in simulated oxy-firing combustion gas

3.3.2 Gravimetric measurements

In this PhD project each test was run for 1000 hours, a minimum time scale required to find out the metal loss due to fireside corrosion. A well established 'deposit recoat' technique was used as the method for fireside corrosion testing. [17; 92]. Mass change data is the traditional technique to observe materials (oxidation and corrosion kinetics) performance at high temperature [17; 92]. However, it is not the ideal method to interpret corrosion damage for various reasons, for example: due to spalling of scales or corrosion/deposit products during the test mainly as a result of thermal cycles (intermediate intervals of samples cooling and heating) [17; 28; 92]; the formation of internal oxides/sulphides.

Before starting up the test all the 24 cleaned samples and the crucibles for each sample were weighed alone. Then the samples along with their crucibles were weighed. Then, the samples were painted with deposit slurries, by using a paint brush to give a coverage of ~ 20 mg/cm^2, of dried deposit, weighed again and loaded into furnace. Each 1000 hours test was divided into five cycles of 200 hours each. After each cycle, the samples are unloaded from the furnace, weighed along with crucible, and weighed alone.

After the weight measurements, the samples were repainted again with the same deposits, and weighed again along with the crucibles, and loaded into the furnace for another cycle. The same procedure was carried out after every cycle. Finally, after the fifth cycle the samples and samples along with their crucible were weighed. This procedure is illustrated in Figure 3-9, in which summarises the route for fireside corrosion testing in this PhD thesis. This discontinuous testing enables sample monitoring and the repainting of deposits on samples every 200 hours. Similar gravimetric measurements were also carried out for bare samples, so that it provided a gravimetric check on their performance (and enabled the calculation of traditional specific net mass change data). The same methodology was applied in all the tests.

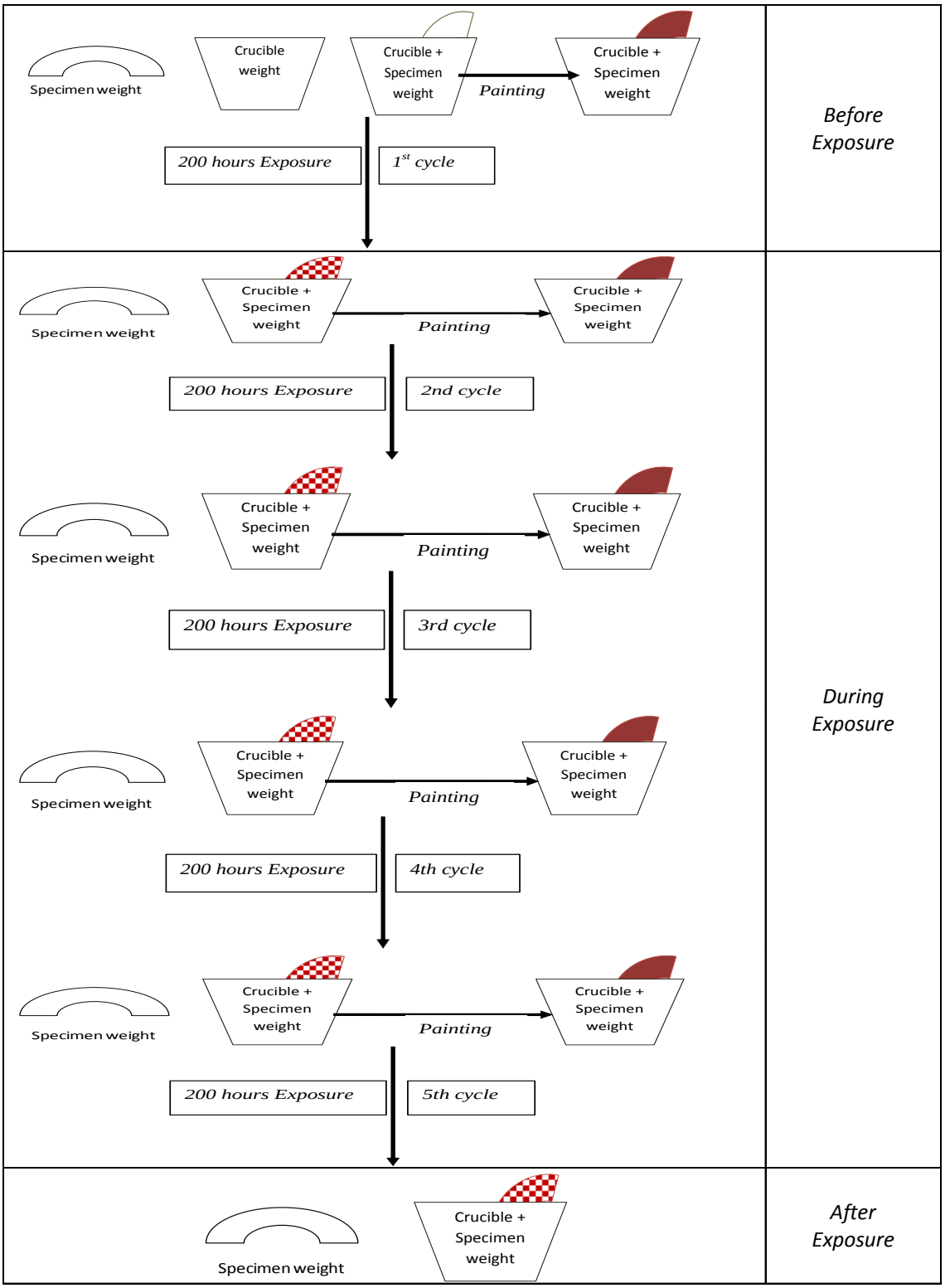

Figure 3-9: Schematic representation of weight measurements for fireside corrosion testing

3.4 Post Exposure work

Once the samples had completed their 1000 hours exposures, the final readings of mass changes were recorded and the samples were kept into airtight plastic bags. So later, they could be prepared for further analysis

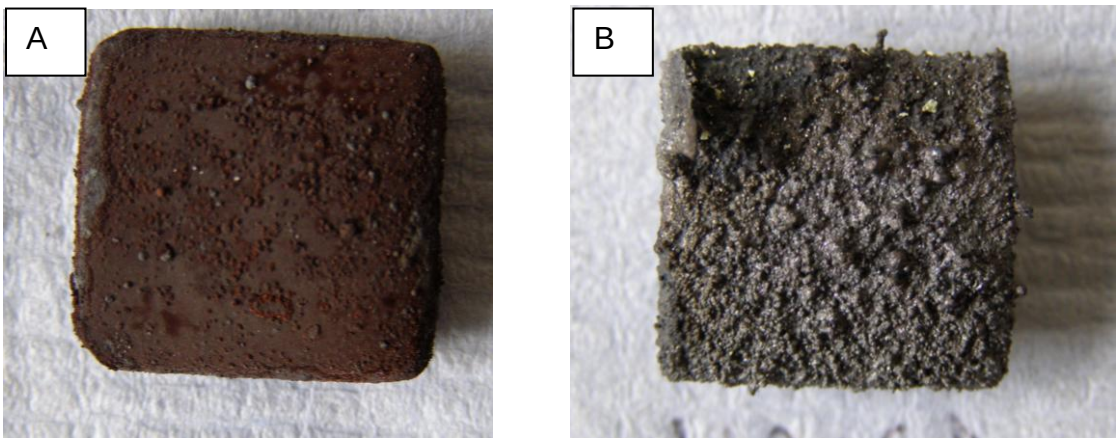

Figure 3-10: Post corroded T22 samples bare (A) and covered with deposit D1 (B) at exposed to simulated oxy-firing conditions at 750°C for 1000 hours

3.4.1 Mass change data

Mass change data is the traditional technique to observe materials (oxidation and corrosion kinetics) performance at high temperature [17; 92] and widely used in as standard academic method for such research. Mass change data were calculated for each sample during the tests and were then used to plot graphs of mass change versus time. This is a gravimetric method often used to analyse the progression of metal reactions. The curves obtained clearly show the different behaviour of alloys at high temperature.

Although the mass change data gives useful information, however it is not the ideal method to interpret corrosion damage because of various reasons in particular due to spalling of scales or corrosion/deposit products during the test mainly as a result of thermal cycles (intermediate intervals of samples cooling and heating) [17; 28; 92] A detailed microscopic analysis can only provide the information required to produce metal loss data and the statistical models needed to predict the lifetime of components.

3.4.2 Sample Preparation

In metallographic studies, it is a common practice to produces polished cross-sections to examine the typical microstructures of alloys. After the 1000 hours exposure were completed, cross-sections of the samples were prepared using a cold mounting process (ballatoni filled low shrinkage epoxy resin) followed by cutting, grinding and polishing using non-aqueous lubricants.

3.4.3 Mounting

The sample mounts were prepared in a bespoke moulds as shown in Figure 3-11. The mould was first greased using high vacuum grease (Dow Corning, USA) as a lubricant so the prepared mount can easily be removed from the mould. The two pins were then inserted and samples were placed into the mould in such a way that the sample reference hole faced sideways. The sample stood in the mould supported by two pins and the spring-loaded blade pushed the sample toward the pins. A schematic of mounting process is shown in Figure 3-12. Then a mixture of epoxy and hardener (Epofix resins, Buehler, USA) together with 50% volume ballatoni (glass spheres) was prepared and poured into the mould. The ratio proportion used for resin and hardener was followed according to manufactures instructions. The resin was further vacuumed under pressure at ~ 800 mbar in a desiccator connected to high vacuum pump for approximately two minutes to evacuate any air bubbles trapped within the resin. The embedded samples were left overnight to dry. When the resin had dried, the mount was taken out carefully from the mould for further preparation.

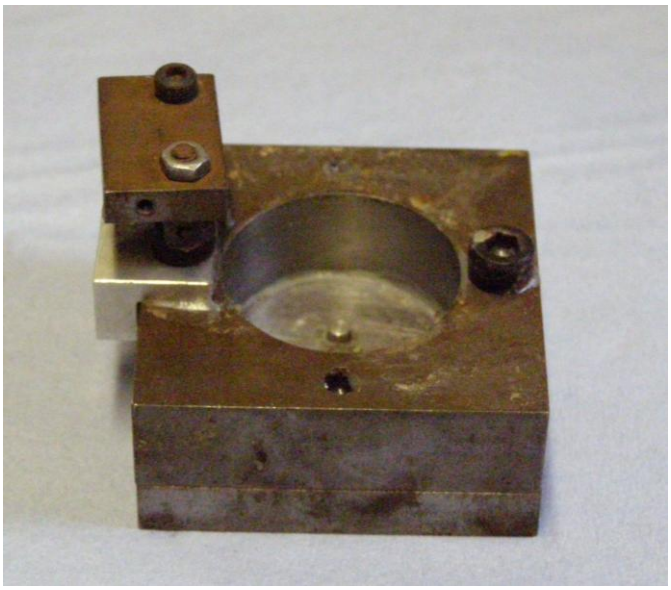

Figure 3-11: Mould used for mounting corrosion samples embedded in resin

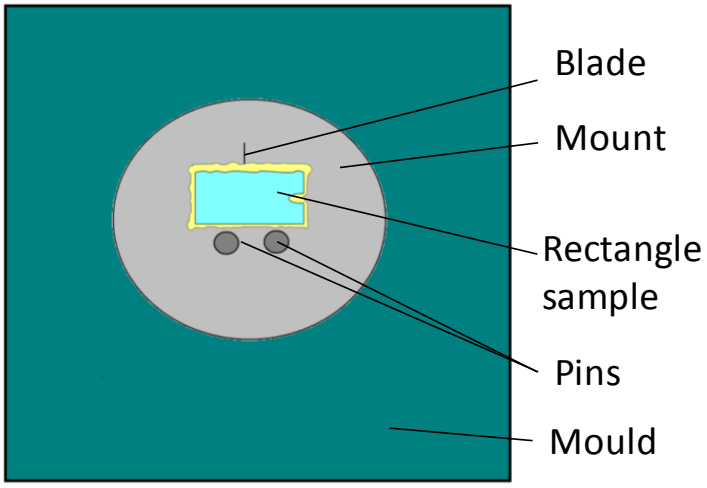

Figure 3-12: Schematic representation of mounting in a mould

3.4.4 Cutting, Grinding and Polishing

Buehler's Isomet 5000 (Buehler USA), a linear precision saw, was used to cut the resin and sample cut into half just above the reference point (a drilled hole, as previously explained); so a rectangular cross section is obtained which helps in the dimensional metrology. Cubin boron nitride (CBN) blade was used for cutting the mounts. The blade rotation was set as 2500 rpm with a feeding rate

of 2.5 mm/min. After cutting the samples, the grinding and polishing steps were performed with an oil-based lubricant using Buehler Metaserv Motopol 12 machines. A series of silicon carbide abrasive paper discs, of different grades were used for grinding. Each grade was used two times for grinding. After grinding from each grade, samples were thoroughly rinsed with the IPA solution. The ground samples were polished using an oil based diamond suspension until a clean polished surface was obtained. The load applied on each sample was set as 5 psi. The very first rotation in the grinding process was set as counter rotation of sample holder to grinding plate, followed by the same rotation direction as the grinding plate for the remaining grinding and polishing. The details of grinding and polishing processes are listed in Table 3-5.

Table 3-5: Grinding and polishing table

Grade Grit/	Time (min)	Rotation (rpm)
120	2	125
240	2	125
1200	2	125
2500	2	125
6 diamond suspension (μm)	3	140
3 diamond suspension (μm)	3	140

3.4.5 Dimensional Metrology

The most informative technique in this PhD project was the use of a digital image analyser, as a dimensional meteorological tool. The software Axiovision acquires images and then allows x-y position data to be acquired and recorded. The excel spread sheets were used to generate metal loss data involves calculations for measuring the surface position of the metal after exposure compared with the thickness measurements recorded before exposure (by digital micrometer). These data are the requirement for development of mathematical corrosion damage models. Figure 3-13 illustrates the digital image analyser facility at Cranfield University.

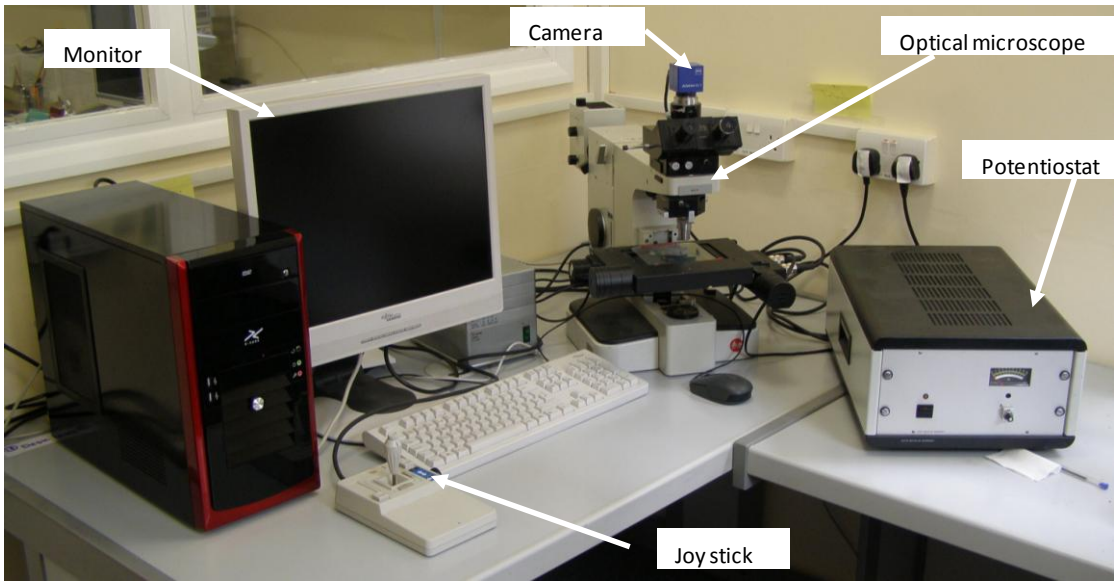

Figure 3-13: A digital image analyser facility at Cranfield University

The digital image analyser is connected to an optical microscope via a lens with a magnification of times 20 and a high resolution digital camera. The system also includes a computer-controlled motorised x-y stage with positioning accuracy of ± 1 μm. Stage movement control is a key part of the system, using either a joy stick or programme. A communication box and a monitor also form part of the system. The software Axiovision v4.6 (with bespoke sub-routines) was used to control the data acquisition by the image analyser. Figure 3-14

presents the mounted polished cross-section placed on the x-y stage for the post- exposure dimension metrology (measurement of key features).

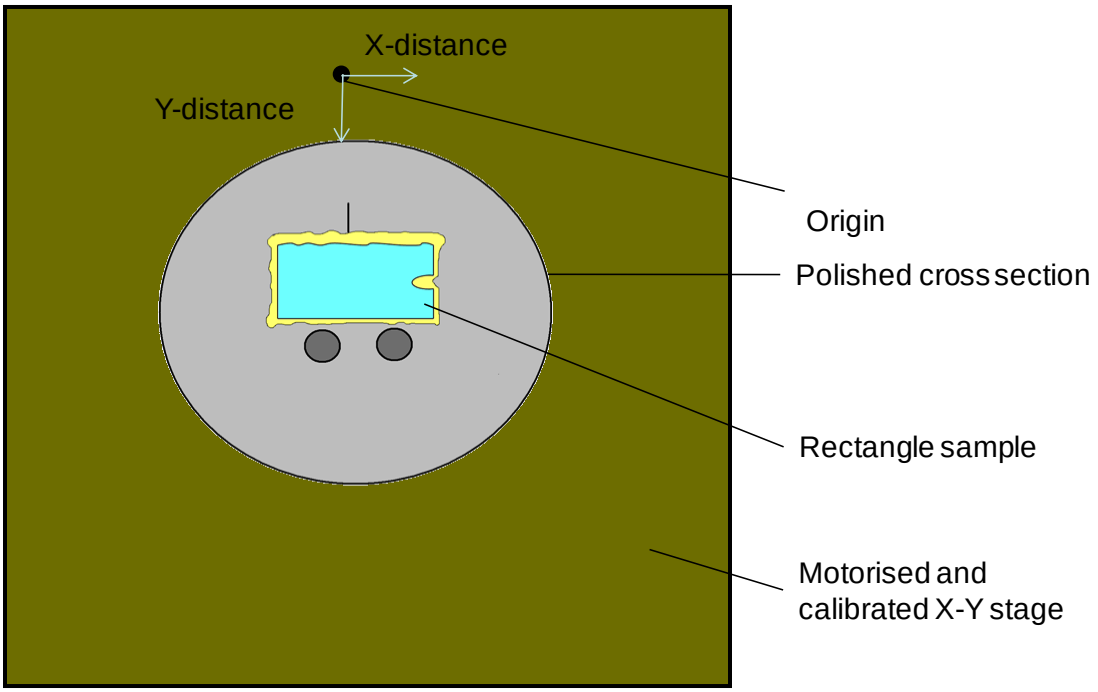

Figure 3-14: Schematic representation of rectangular cross-section on image analyser

3.4.5.1 Functioning of image analyser; various stages

There are number of steps that need to be carried out in order to acquire the x-y co-ordinates needed as inputs in the spreadsheets developed to calculate the metal loss probabilities. The polished cross-section was first put on a glass slide on top of plasticine and levelled with the help of manual presser. Once the sample mount was levelled it was then placed on the stage. Before starting the analysis the long side of the sample was aligned manually parallel to the x-motion of the stage to get straight horizontal lines on the monitor by moving the stage in each direction. After the sample alignment the extreme points were set as top, bottom, right and left. The image analyser then calculated the x-y co-ordinates of ~50 desired measurement positions around the edge of the sample. The system then moved to each of these points in sequence and took a group of nine pictures around each point. Once all the groups of pictures had

been acquired, the nine individual pictures in each group were stitched together to give a total of 50 composite images. These composite images were then manually examined to pin-point the features of interest and record their positions (relative to a common reference point) using the software system. Figure 3-15 illustrates three measurement/points (effectively three images) around the corroded sample. The software then calculated the x-y co-ordinates values. For example at point B the x value would be b2 and y co-ordinate value would be a2.

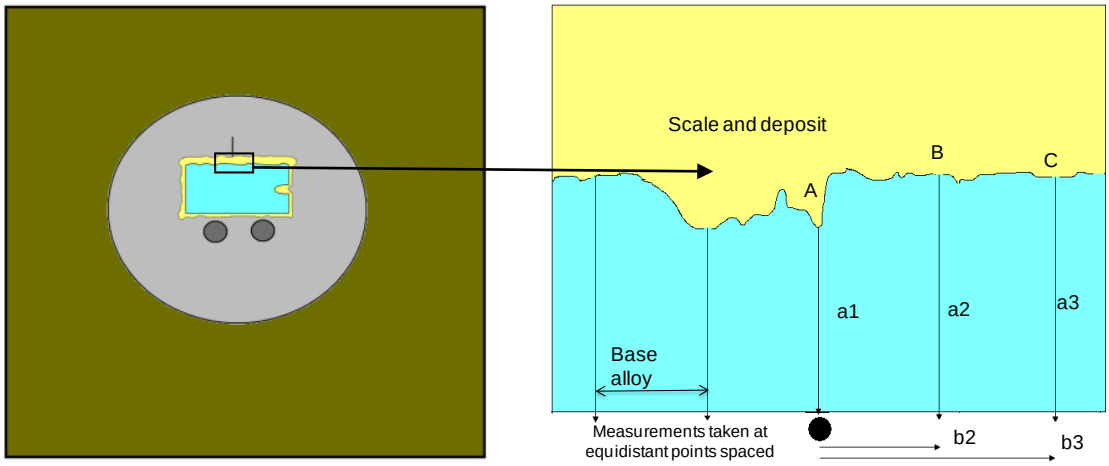

Figure 3-15: schematic representation of fireside corrosion measurement of rectangular cross-section

3.4.5.2 Data analysis spread sheets

These measured x-y co-ordinates were transferred into a spreadsheet and combined with the pre-exposure dimensional measurements so that the metal loss (and internal damage) of the sample during the exposure period could be determined. Figure 3-16 illustrates one set of post-exposure co-ordinate data. The first step in the data analysis involved the orientation of the post-exposure data to align with the pre-exposure measurements using rotation and translational routines. Then the software calculated the metal loss in terms of change in metal and percentage cumulative probability as shown in Figure 3-17 (or change in sound metal loss if internal damage is present). These

distributions of metal losses (and sound metal losses if internal damage is present) are one of the main outputs of this work. In combination with a large number of data sets from other studies, these data are used for the development of mathematical models of fireside corrosion damage that are targeted at giving quantitative assessments of the effects of changes in operating / exposure conditions.

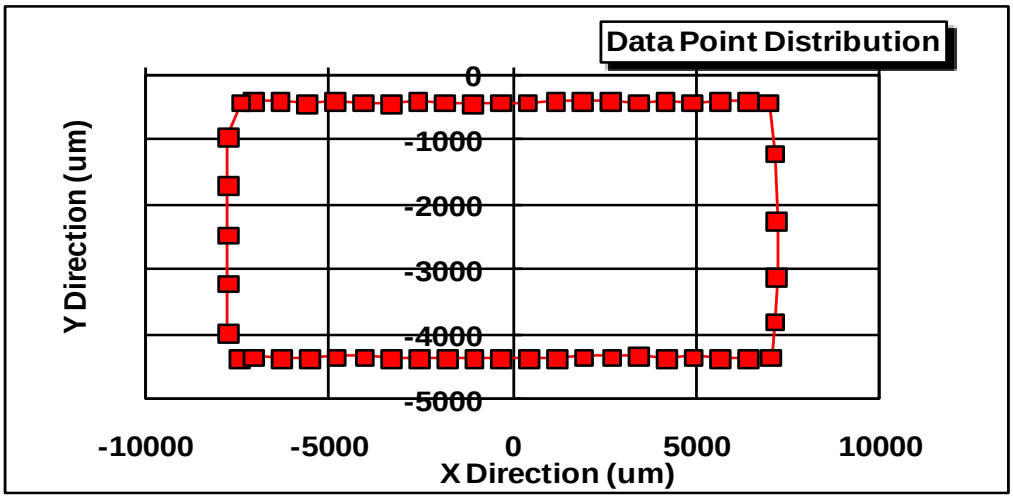

Figure 3-16: A graph of x-y co-ordinates values after plotted into spread sheet

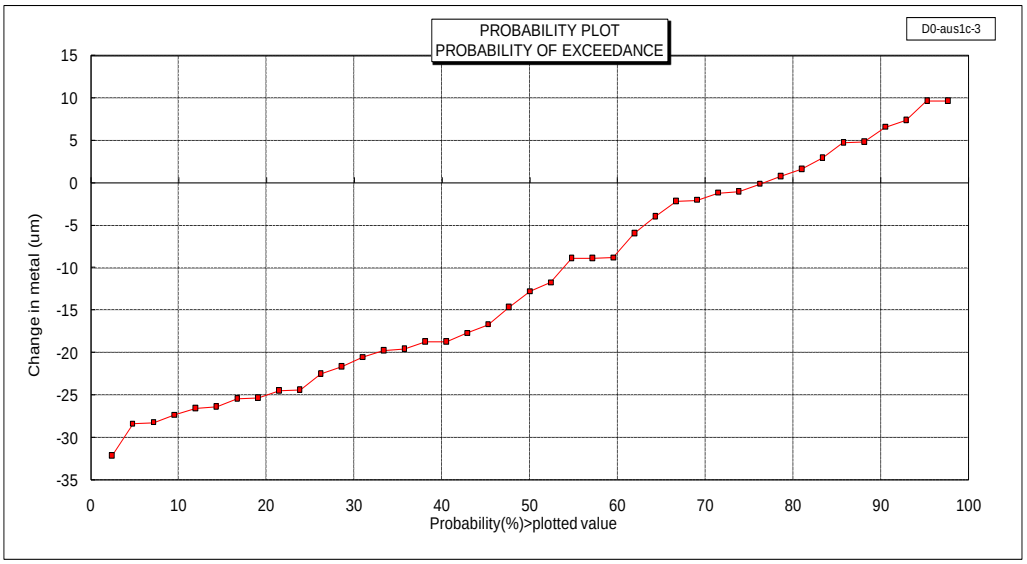

Figure 3-17: An example metal loss cumulative probability curve

3.4.6 Exposed deposit preparation

The deposit stability test was carried out for 200 hours at 650 °C in conditions simulating oxy-fired combustion gas. After the 200 hours cycle of exposure the discs with deposits were prepared for elemental analysis. The target analytes were K, Na, Fe, Al, SO_4^{2-} and Cl^-. Some of the sample deposits were prepared for analysis for alkali metals, Fe and Al, and some sample were prepared for Cl^- and SO_4^{2-} analysis. This is due to different analytical techniques set up for the chemical analysis at Cranfield University. For alkali metals (Na, K), Fe and Al an aqua-regia microwave digestion method was used to ensure all the compounds in the deposits salts constituent are dissolved. However samples for SO_4^{2-} and Cl^- analysis were prepared simply by dissolving in deionised water. The routes followed for solution preparations are listed in Table 3-6.

3.4.6.1 Sample preparation for SO_4 and Cl

The discs with deposits were weighed and placed in a beaker. Approximately 20 ml of de-ionised water was added and the beaker was placed in an ultrasonic bath for 5 minutes. After the ultrasonic the disc was removed from the beaker and the sample solution was poured into a 100 ml volumetric flask and filled up to this mark with deionised water. Another 10 time dilution was carried out and then sample solutions were given to the technician for analysis.

Figure 3-18: Disc with deposit D4 after 200 hours exposure in simulated oxy-fired combustion gas at 650°C

Table 3-6: Deposit preparation

Atoms/ions	Solvent medium	Preparation method	Analytical technique
Na, K	Acidic	Microwave digestion	Atomic emission
Al, Fe	Acidic	Microwave digestion	Atomic absorption
Cl^-, SO_4^{2-}	Aqueous	Ultrasonic	Ion chromatography

3.4.6.2 Microwave digestion method

Alkali metals (Na, K), Fe and Al samples were prepared using microwave digestion method. This method involves metal extraction with a hydrochloric/nitric acid mixture using a micro wave digestion system (Multiwave 3000 Perkin Elmer). The sample discs were weighed and placed in microwave digestion liners (test tubes designed for microwave digestion). An aqua regia solution i.e. 6ml of HCl acid (1.18 SG) and 2 ml of HNO_3 acid (1.42 SG) were added into the liner and left (sample soaked) over night. The next day liners with sample discs were placed into the pressure vessel and screw cap was closed. Then all the vessels were placed into the rotor and covered with the lid and finally placed into the microwave. The microwave digestion was carried out at 175°C, under 17.5 bar pressure for approximately 40 minutes. After the microwave digestion the machine was allowed to cool down and the vessels were removed. Each liner was taken out with care (vented away) in the fume cupboard. The liner content was filtered into a 100 ml volumetric flask using Whatman 542 filter paper. The liners were further rinsed with deionised water and added into the appropriate flasks and finally made up to 100 ml mark with deionised water. A further 10 times dilution was carried out and the samples were analysed.

Figure 3-19: Microwave digester facility at Cranfield university

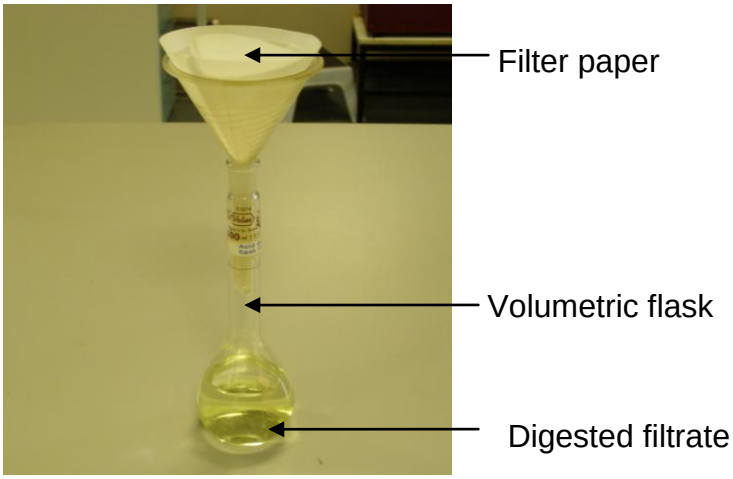

Figure 3-20: Sample filtrate after microwave digestion

3.5 Analytical Tools

The analytical tools used in this PhD project involved scanning electron microscope (SEM), energy dispersive x-ray (EDX), optical microscopy, x-ray diffraction (XRD), for fireside corrosion testing, and ion chromatography (IC), atomic spectroscopy (AS) were used for deposit stability test. A detail

explanation of these techniques is not desired in this PhD thesis however a brief introduction of these techniques is included in this chapter.

3.5.1 Scanning Electron Microscopy

Scanning electron microscope (SEM) is a powerful analytical technique widely used for the morphological study of materials. In brief, SEM is a microscopic surface analysis technique based on the principle that a high voltage electron beam is scanned over the sample and electronic interactions in the near surface region are monitored. Various signals emerged as a result of electron substrate interaction. However the signals studied in this PhD thesis are secondary electrons, backscattered electrons and X-rays.

If the high voltage electrons strike the sample and interact with the nucleus and electrons of the atom, the electrons produced are called secondary electrons (SEs). On the other hand if these electrons are reflected back with a minimum collision with the surface (electrons in orbit and nucleus) then these are called back scattered electrons (BSEs). Most of the analysis was carried out using BSE, due to phase contrast (more electrons reflected by heavier elements). X-ray energy analysis relies on each element producing characteristic x-ray. SEM coupled with energy dispersive X-ray analysis (EDX) is an effective way to study the different chemical compositions in this PhD project.

An environmental scanning electron microscope (ESEM) FEI XL30 microscope (FEI Europe, Eindhoven, Netherlands) operating at 20 kV in high vacuum mode was used to produce SE images to assess the morphology of sample surfaces. The EDX elemental analysis was also performed at 20 kV and the data was analysed using INCA software from Oxford Instruments. SEM/EDX examinations of the non conductive polished cross-sections were carried out in the ESEM using the low vacuum mode (with water vapour addition). A backscattered detector was used due to its ability to distinguish phases in this project (e.g. the metals and their oxides in the samples). EDX analysis provided important information such as from elemental mapping, which gives both qualitative and quantitative estimations of the metal oxides and other

corrosion/deposit products in samples. Figure 3-21 gives a schematic diagram of SEM operation.

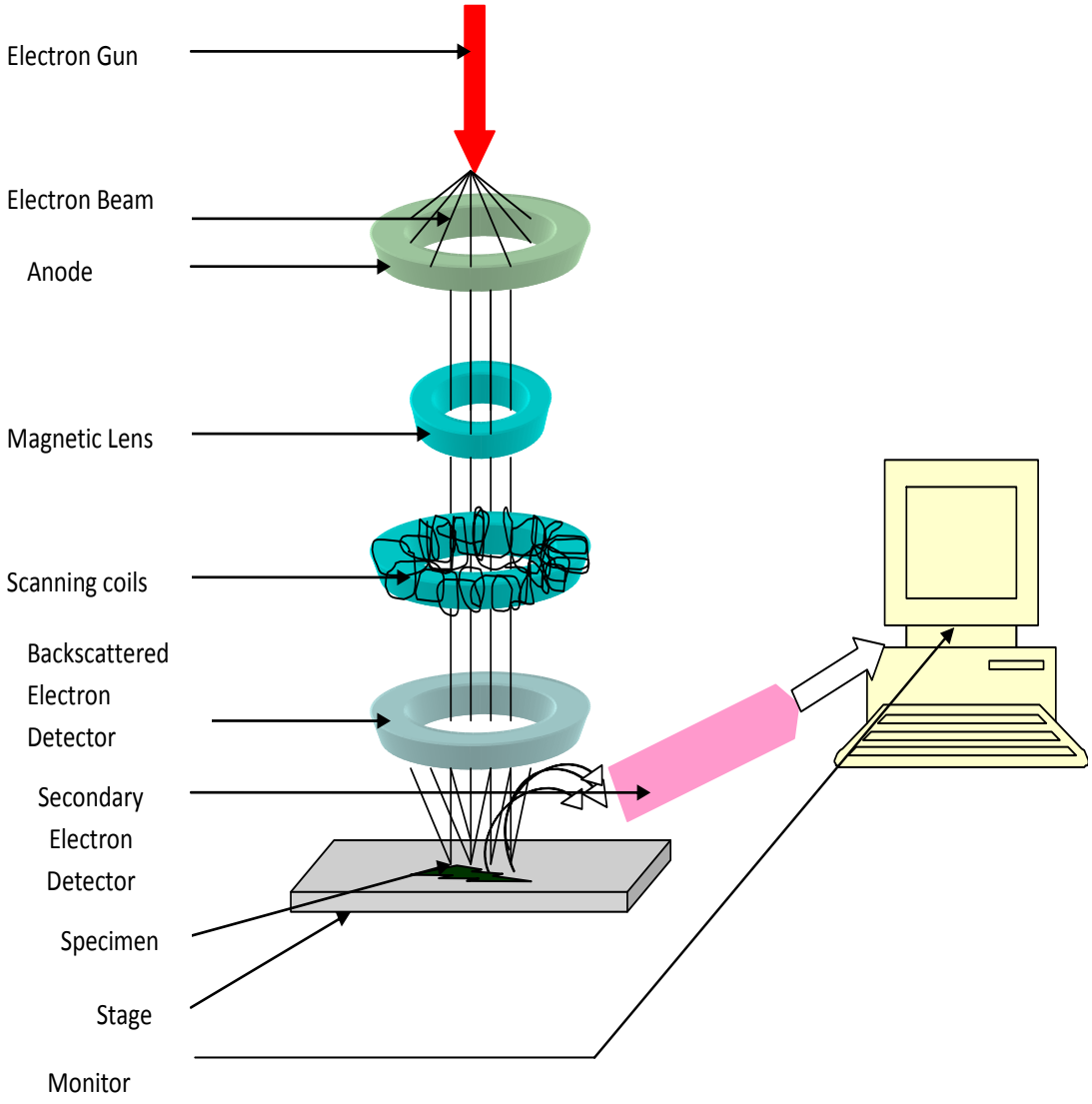

Figure 3-21: Simplified schematic of SEM analysis

3.5.2 X-ray Diffraction

The alloys tested in the fireside corrosion experiments (bare and covered with deposits) analysed using X-ray diffraction.. A Siemens X-ray diffractometer D5005 was used for X-ray diffraction with XRD commander version 2.4.1 software controlling the system.

The X-ray diffraction method of analysis is mostly applied to the materials that are crystalline in structure. Khanna [28] describes how XRD technique involved the sample material (contain one or more diffracting regions) diffracting the targeted X-ray beam. The angle (θ) of the diffracted beam is dependant on the distance (d) between the atomic planes and the X-ray wavelength (λ), and the intensity of diffracted beam is dependant on arrangements of atoms in the planes. Figure 3-22 gives a schematic representation of X-ray diffraction and Bragg's law.

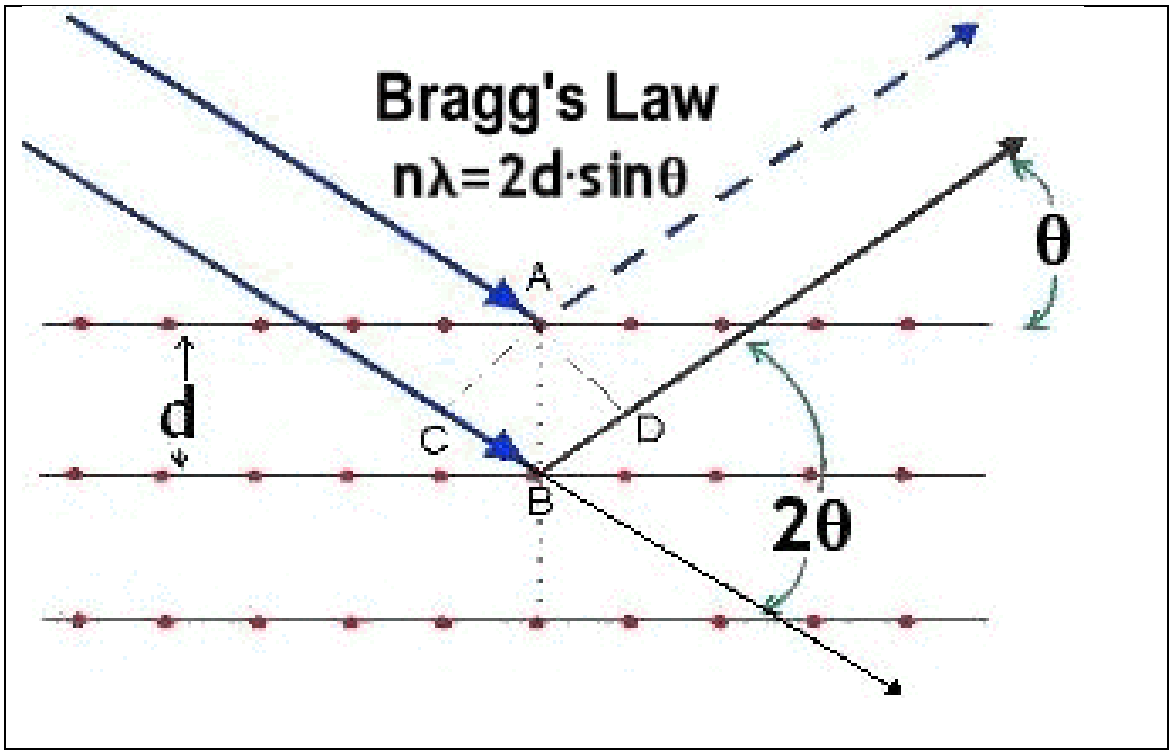

Figure 3-22: Schematic of x-ray diffraction by crystal [128]

3.5.3 Atomic Spectroscopy

As discussed earlier, test number 9 was an attempt to determine the stability of deposits exposed to complex environment. Due to the limited capacity for samples in the furnace, and the wish to carry out simplified deposit composition exposures in the same test (test 9), only few samples could be used for the deposit stability work. These samples were further divided into two sets, so that Cl^- and SO_4^{2-} (water soluble) could also be analysed (by Ion chromatography), whilst metal ions were analysed were analysed by atomic spectroscopy.

The sample solutions for metals ions were prepared (as explained in section 3.4.6.2) and quantitative analysis was carried out using atomic absorption spectrometer (AA Analyst 800, Perkin Elmer). The alkali metals Na and K were analysed using atomic emission spectroscopy AES, a technique in which the radiation emitted (characteristics for each element) by the atomic species are measured and Al and Fe were analysed using atomic absorption spectroscopy AAS, a technique where the external source emits radiation (carried energy required for that target element electronic transitions) and that absorbed by the atomic species are measured. The techniques details can be found in instrumental analysis books by Braun [129] and Willard et al [130].

3.5.4 Ion Chromatography

The ion chromatography (IC) technique was used to analyse Cl^- and SO_4^{2-} ion concentrations (in a Dionex DX 500 UK). This technique is based on the ion exchange principle due to their charges [129].IC technique can be used for cations or anions analysis , however in this PhD study the techniques could only be used for anions.

Braun [129] explains the IC technique, contains ion exchange resins packed in columns, used as a stationary phase. It usually includes synthetic, cross-link polymers which are attached with ionisable functional groups. Sample ions which introduced to an IC column are attracted to the oppositely charged, (stationary) ionic sites on the resin and if the attraction between the sample and the stationary ions is greater than that counter ions, the sample ions will attached to the ion-exchanger and replace the counter ions, this process is called ion exchange. Further details on the technique can be found in the text book [129].

4 RESULTS

4.1 Introduction

This chapter includes results from every technique used in this PhD project. The fireside corrosion tests have been carried out primarily in two different conditions (air-firing and oxy firing), test number 6 is a repeatability of test 5 and test number 9 was dedicated to study deposit stability and high (%) level of salt exposure test.

The results are presented from each set of condition. Four different techniques (mass change, SEM/EDX, XRD and dimensional analysis) have been used to monitor and analyse the fireside corrosion damage on the exposed samples. IC and AA analysis results are presented for deposit stability test carried out in test number 9.

The mass change data recorded for each test is a useful way of it while it is running, and provides some indication of corrosion kinetics. SEM/EDX analysis gives morphology and elemental mapping of the corroded samples. The corrosion/deposits products are also characterised by XRD. The data needed for the development of fireside corrosion models of heat exchangers (one of the objectives of this research project) is generated by dimensional metrology using an optical microscope/image analyser.

4.2 Mass change data

4.2.1 Introduction

Mass change data for all samples tested at different temperatures in both firing conditions (air and oxy-firing), covered with different deposits are given in this section.

4.2.2 Air-firing tests

4.2.2.1 T22

The results in Figure 4-1 illustrate the mass gain values for alloy T22 bare and covered with four deposits exposed to 1300 vppm SO_2/400 vppm HCl at 700°C for 1000 hours. These data show the alloy T22 covered with deposit D1 gained the highest mass (approx 142 mg/cm^2) followed by samples covered with other deposits and bare sample.

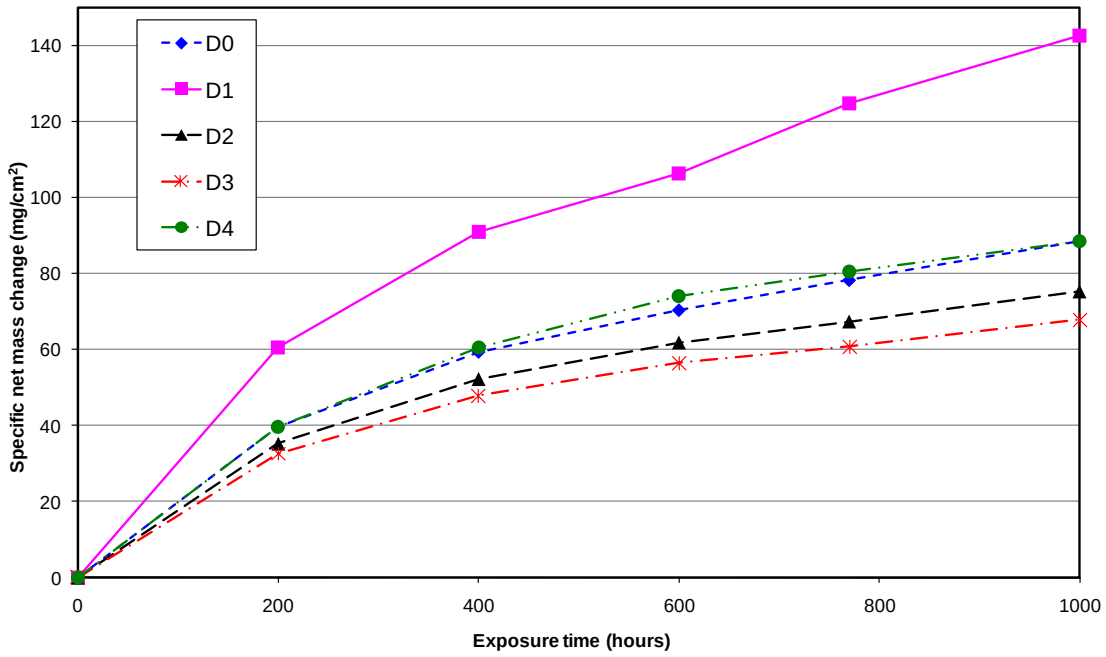

Figure 4-1: Specific net mass change data for alloy T22 bare and covered with four synthetic deposits exposed to simulated air-fired combustion gases (with 1300 vppm SO_2/400 vppm HCl) for1000 h at 700°C

The bare sample and the sample covered with deposit D4 showed very similar trends. The sample covered with deposit D3 gained the minimum mass (approx i.e. 68 mg/cm^2).

4.2.2.2 T92

Figure 4-2 to Figure 4-4 illustrate the mass change data obtained for alloy T92 covered with different deposits exposed to 1300 vppm SO_2/400 vppm HCl at 600, 650, and 700°C for 1000 hours. Figure 4-2 illustrates that alloy T92 covered with deposit D1 shows the highest mass gain followed by the bare alloy

and then T92 samples covered with the other deposits. An upward and downward trend was observed for sample covered with deposit D1. The drop in mass change observed was probably due to spalling, either during the exposure or while handling the sample during weight measurements. Samples covered with deposit D2, D3 and D4 showed lower overall mass gains.

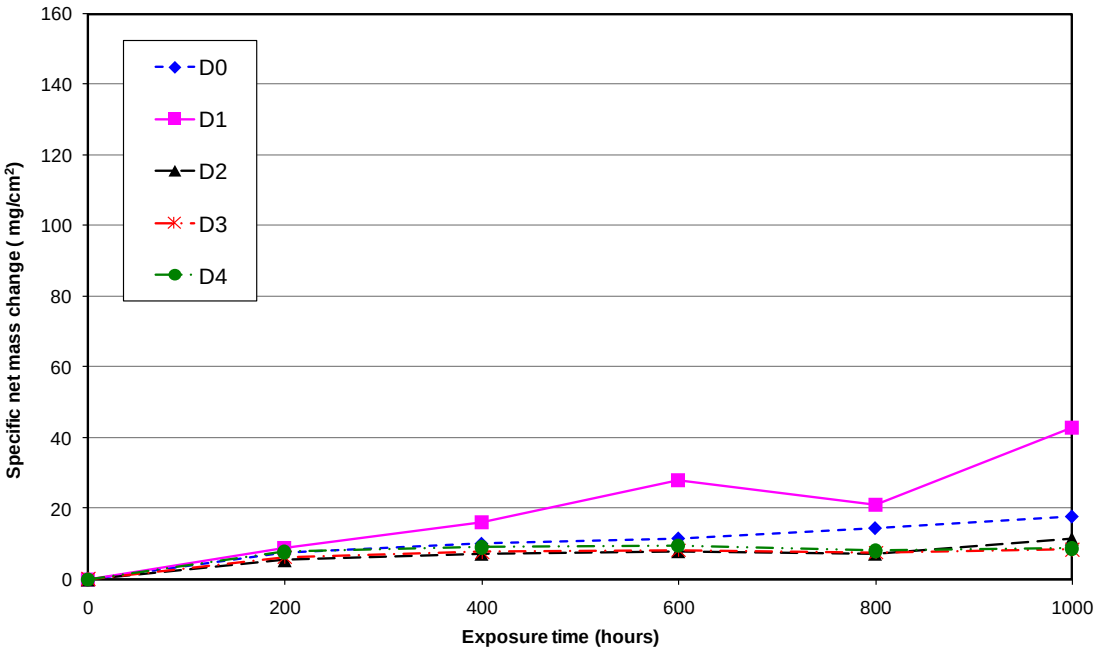

Figure 4-2: Specific net mass change data for alloy T92 bare and covered with four synthetic deposits exposed to simulated air-fired combustion gases (with 1300 vppm SO_2/400 vppm HCl) for 1000 h at 600°C

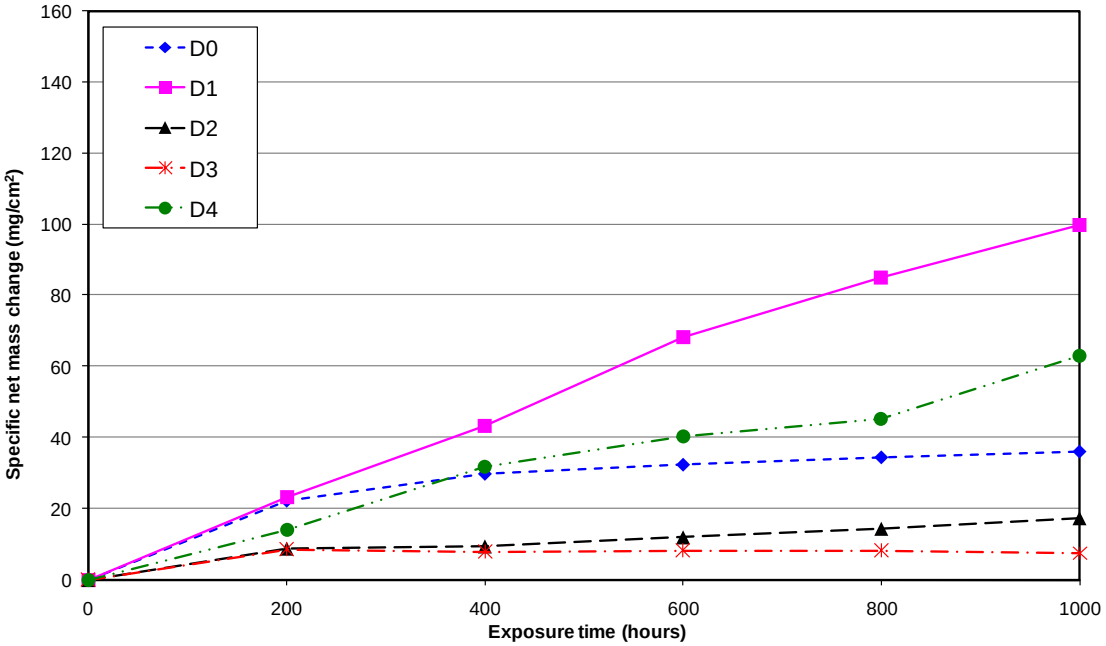

Figure 4-3: Specific net mass change data for alloy T92 bare and covered with four synthetic deposits exposed to simulated air-fired combustion gases (with 1300 vppm SO_2/400 vppm HCl) for 1000 h at 650°C

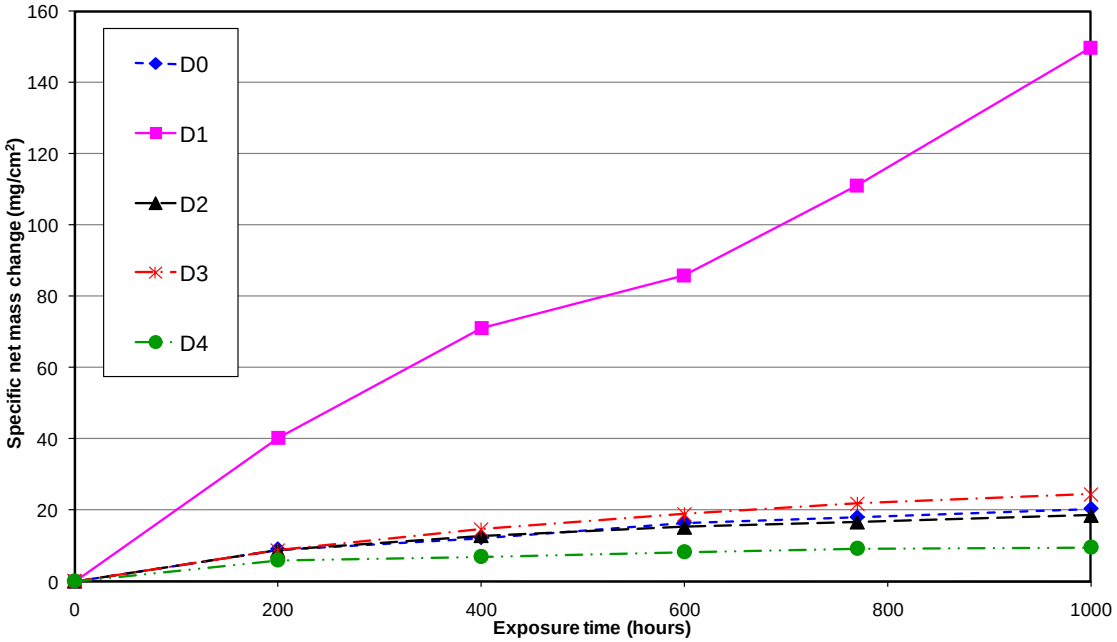

Figure 4-4: Specific net mass change data for alloy T92 bare and covered with four synthetic deposits exposed to simulated air-fired combustion gases (with 1300 vppm SO_2/400 vppm HCl) for 1000 h at 700°C

In Figure 4-3, with the increase of 50°C to 650°C, the mass gain values for T92 covered with deposit D1 was more than doubled from ~40 mg/cm^2 to ~100 mg/cm^2. Samples of the bare alloy and covered with other deposit composition show mass gains of ~10 to ~60 mg/cm^2.

Figure 4-4 illustrates a rapid increase in a mass for alloy T92 covered with aggressive deposit D1 at a higher temperature; the increase was almost three times that of the mass gain at 600°C. However mass gain values for alloy T92 bare or covered with deposit D4 were lower than observed at 650°C.

4.2.2.3 347HFG

Figure 4-5 to Figure 4-7 gives mass change data for alloy 347HFG, bare and covered with different deposits at 600, 650 and 700°C respectively.

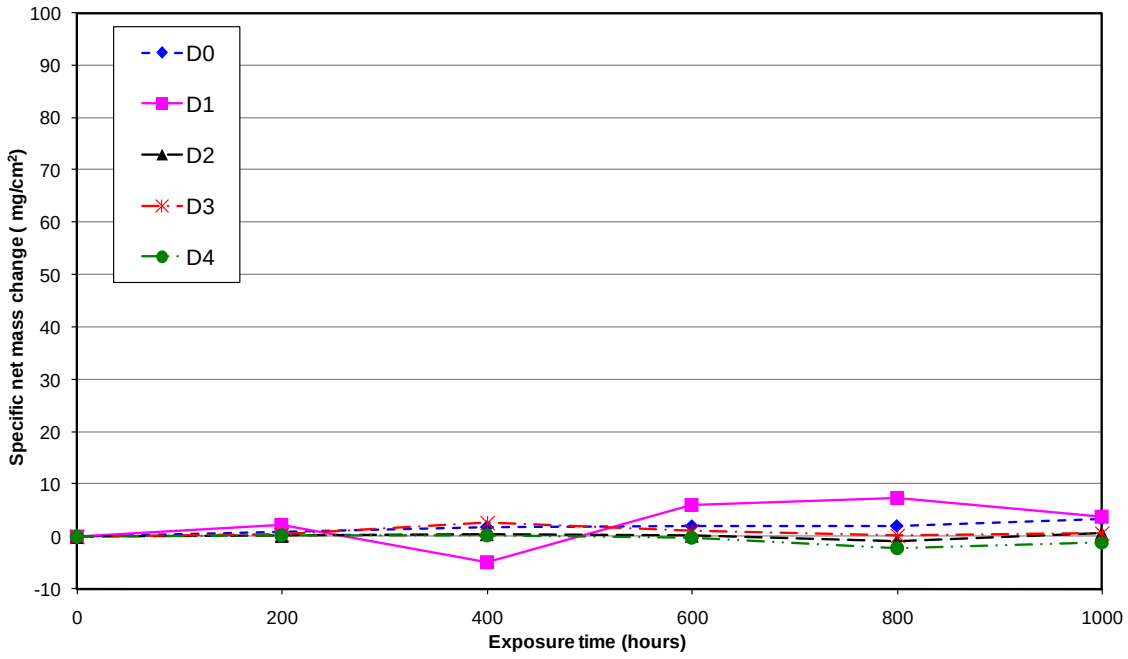

Figure 4-5: Specific net mass change data for alloy 347HFG bare and covered with four synthetic deposits exposed to simulated air-fired combustion gases (with 1300 vppm SO_2/400 vppm HCl) for 1000 h at 600°C

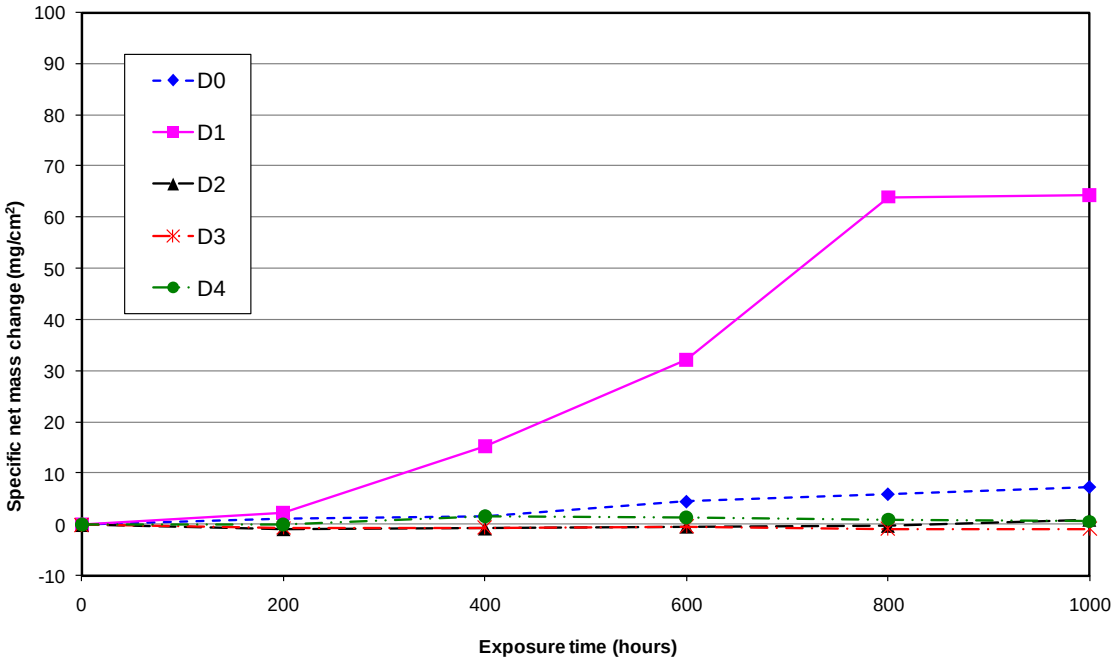

Figure 4-6: Specific net mass change data for alloys 347HFG bare and covered with four synthetic deposits exposed to simulated air-fired combustion gases (with 1300 vppm SO_2/400 vppm HCl) for 1000 h at 650°C

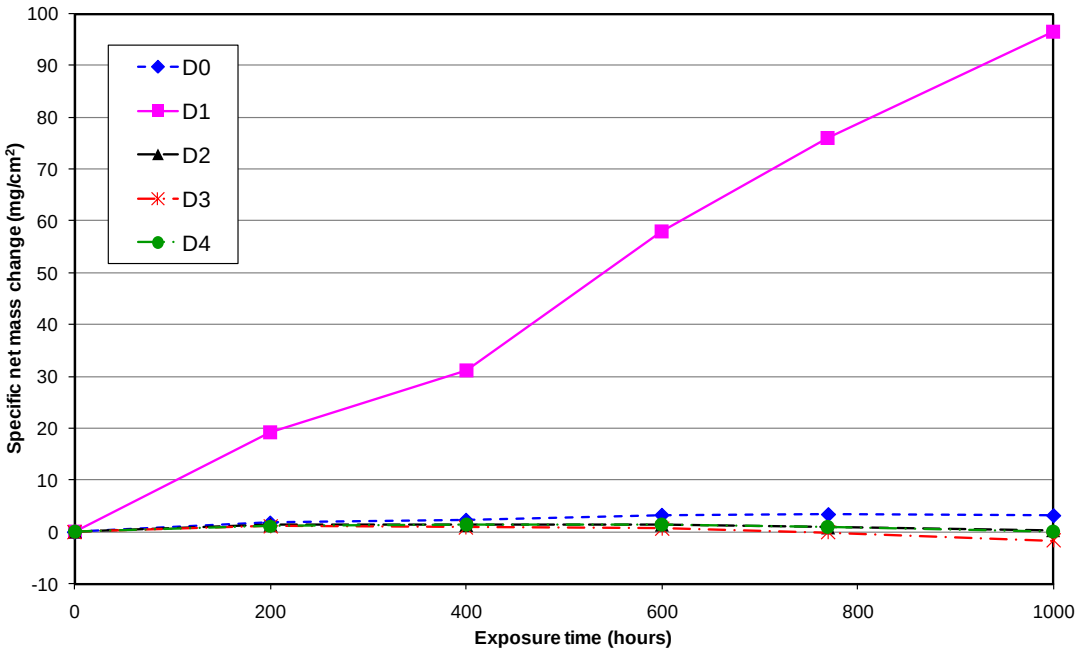

Figure 4-7: Specific net mass change data for alloys 347HFG bare and covered with four synthetic deposits exposed to simulated air-fired combustion gases (with 1300 vppm SO_2/400 vppm HCl) for 1000 h at 700°C

In Figure 4-5, at 600°C, low mass gain values were observed. Even with the aggressive deposit D1 less than 10 mg/cm^2 mass was gained, through a mixture of both upward and downward kinetic trends indicated possible

spallation. In Figure 4-6 the alloy 347HFG covered with deposit D1 showed a rapid mass gain whereas at 700°C as shown in Figure 4-7 mass gain value for sample covered with deposit D1 further increased. The mass values of alloy 347HFG covered with deposit D1 increases from approx 65 mg/cm^2 at 650°C to approx 100 mg/cm^2 at 700°C. At all three temperatures (600, 650 and 700°C) deposit D1 caused the highest mass values, followed by bare alloy 347HG and then the samples with other deposits (D2, D3 and D4). Deposit D4 (Table 3-2) has high level of KCl (5%) compared to deposit D3 (1%) and deposit D2 (0%). However, the mass change data from alloys covered with these deposits do not show any significant differences.

4.2.2.4 HR3C

Figure 4-8 to Figure 4-10 show the mass change data from alloy HR3C in the same gas environment at three different temperatures (600, 650 and 700°C). Figure 4-8 shows that at 600°C only small overall mass gain values were observed. Deposit D1 has little effect on the alloy, with a mass gain of less than 10 mg/cm^2. However a rapid mass gain was observed by the sample with deposit D1 at 650°C, with a value of almost 10 times (~100 mg/cm^2) more than at 600°C.

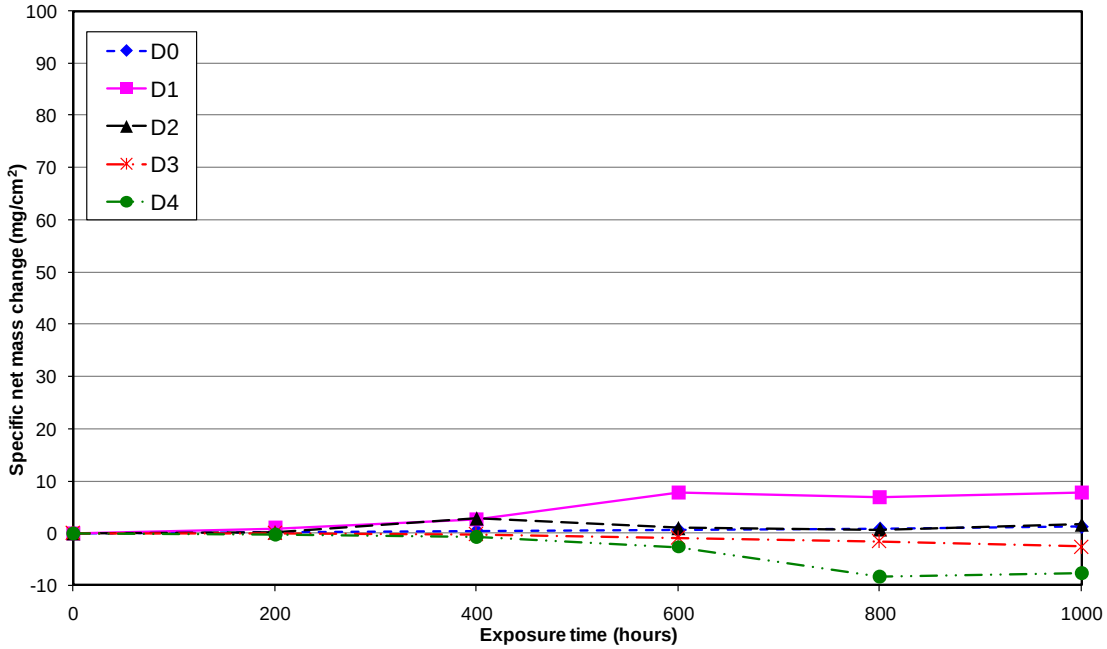

Figure 4-8: Specific net mass change data for alloy HR3C bare and covered with four synthetic deposits exposed to simulated air-fired combustion gases (with 1300 vppm SO_2/400 vppm HCl) for 1000 h at 600°C

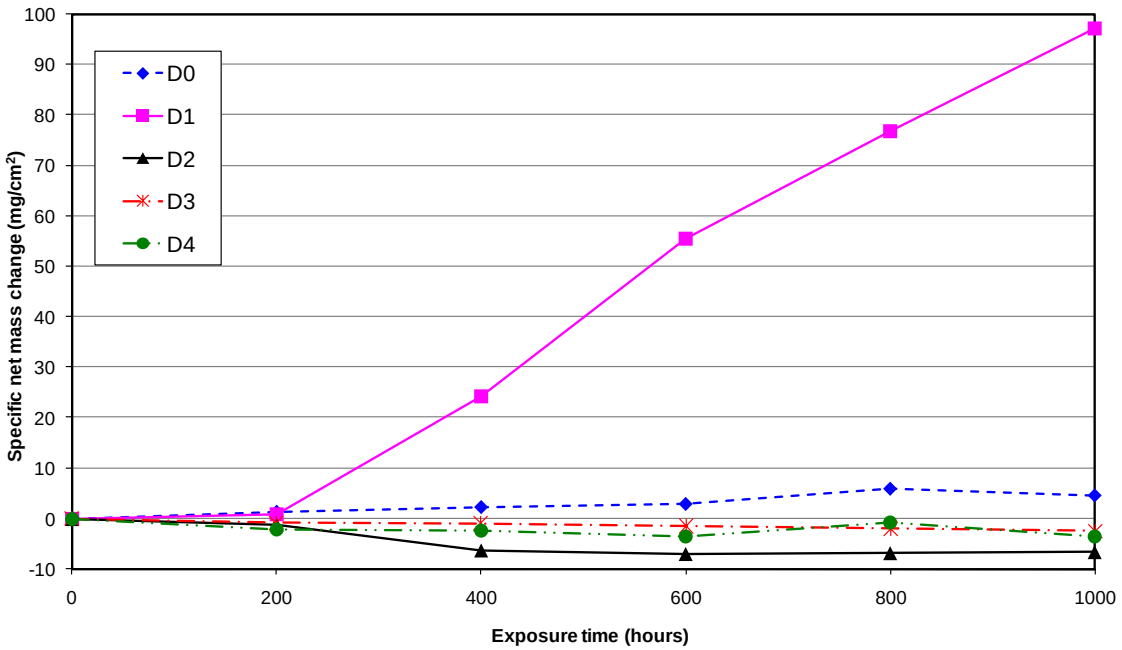

Figure 4-9: Specific net mass change data for alloy HR3C bare and covered with four synthetic deposits exposed to simulated air-fired combustion gases (with 1300 vppm SO_2/400 vppm HCl) for 1000 h at 650°C

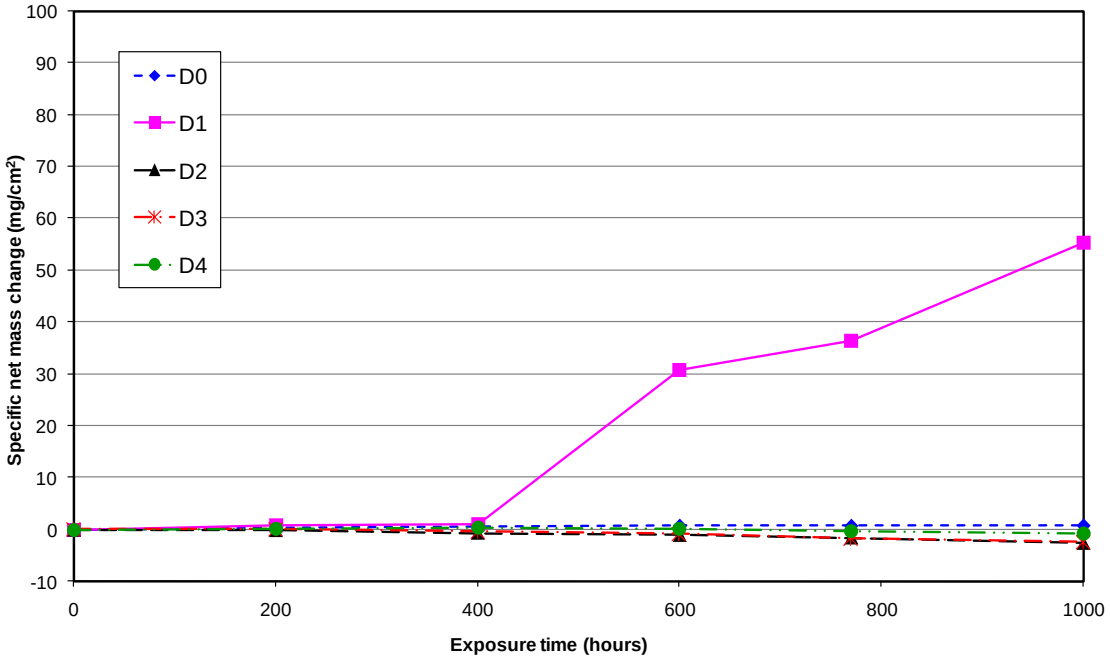

Figure 4-10: Specific net mass change data for alloy HR3C bare and covered with four synthetic deposits exposed to simulated air-fired combustion gases (with 1300 vppm SO_2/400 vppm HCl) for 1000 h at 700°C

At 700°C, as shown in Figure 4-10 the mass gain value for alloy HR3C covered with deposit D1 decreases to approx 55 mg/cm^2, almost half of observed at 650°C (100 mg/cm^2).

4.2.2.5 Alloy 625

Figure 4-11 to Figure 4-13 illustrate the mass change data for alloy 625 covered with deposits in the same gas environment and at (600, 650 and 700°C). As expected alloy 625 covered with deposit D1 exhibited significant mass gain values at all three temperatures. A noticeable feature for alloy 625 with deposit D1 was the rapid increase at 650°C almost three times the mass gain at 600°C; a similar behaviour to HR3C at 650°C. However both alloys (HR3C and 625) showed less mass gain at 700°C than 650°C. The high mass gain values for both alloys (HR3C and 625) covered with deposit D1 at 650°C were also similar (~95 mg/cm^2). At 700°C total mass change value of alloy 625 covered with deposit D1 decreased to ~45 mg/cm^2. Alloy 625 covered with other deposits (D2, D3 and D4) showed some example of sample mass loss at all three temperatures (600, 650 and 700°C).

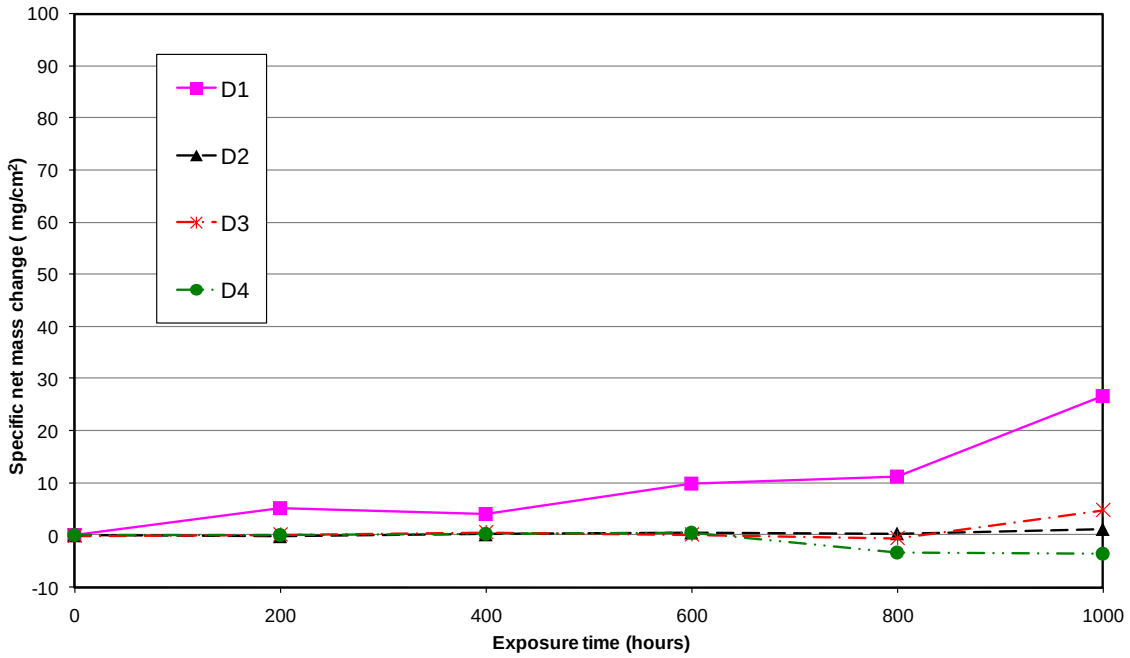

Figure 4-11: Specific net mass change data for alloy 625 covered with four synthetic deposits exposed to simulated air-fired combustion gases (with 1300 vppm SO_2/400 vppm HCl) for 1000 h at 600°C

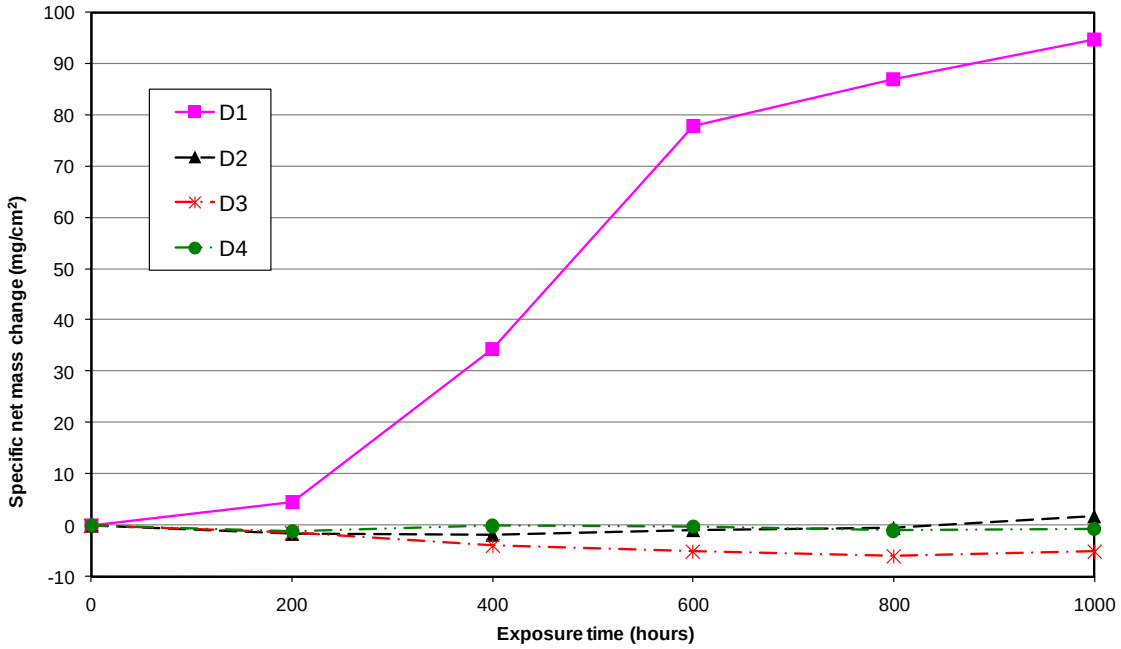

Figure 4-12: Specific net mass change data for alloy 625 covered with four synthetic deposits exposed to simulated air-fired combustion gases (with 1300 vppm SO_2/400 vppm HCl) for 1000 h at 650°C

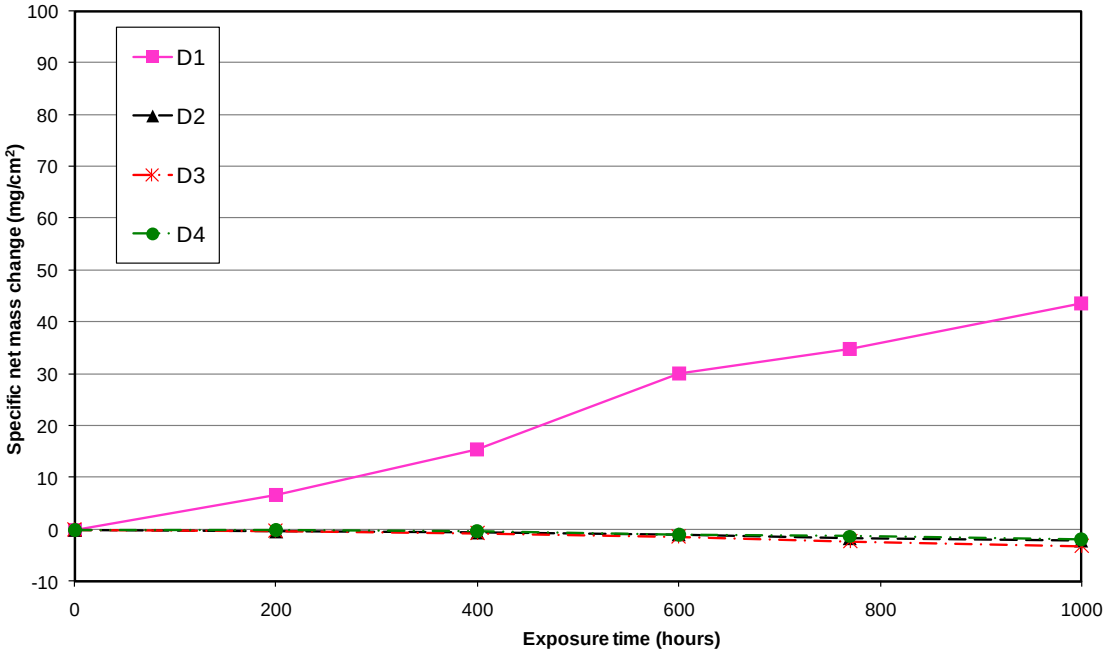

Figure 4-13: Specific net mass change data for alloy 625 covered with four synthetic deposits exposed to simulated air-fired combustion gases (with 1300 vppm SO_2/400 vppm HCl) for 1000 h at 700°C

4.2.3 Oxy-firing tests

4.2.3.1 T22

Figure 4-14 and Figure 4-15 illustrate mass change data for ferritic alloy T22 exposed to oxy-firing conditions (6260 vppm SO_2/1700 vppm HCl) for 1000 hours at 700 and 750°C respectively. The mass gain values of each T22 sample in Figure 4-14 (oxy-firing conditions) at the same temperature are much higher than the mass gain values of their compared T22 samples in Figure 4-1 (air-fired simulation). A noticeable feature in Figure 4-14 is the similar mass gain values for samples covered with deposits D3 and D1 this is unusual as most of the previous data showed the aggressive nature of deposit D1 with samples coated with it having high mass gain values. The anticipated trend was observed in Figure 4-15 (at 700°C), with high mass gain values for sample covered with deposit D1 (high levels of alkali sulphates), followed by D0 (bare sample) and then samples painted with more realistic deposits in the order D4 (5 mole% KCl) > D3 (1 mole% KCl)> D2 (0 mole% KCl).

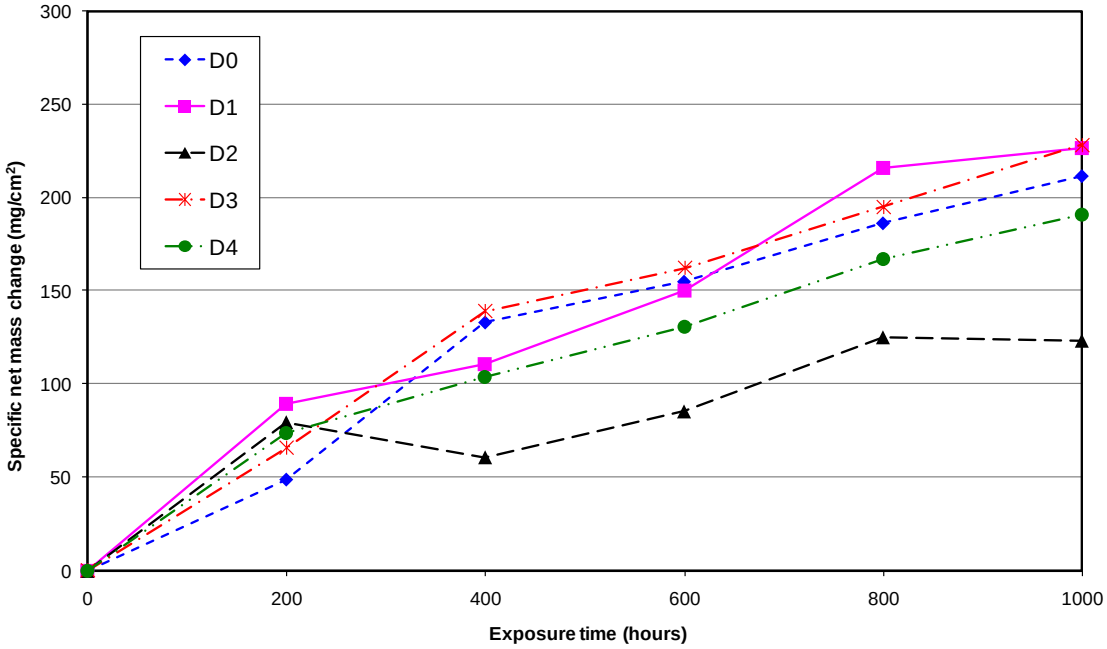

Figure 4-14: Specific net mass change data for alloy T22 bare and covered with four synthetic deposits exposed to simulated oxy-fired combustion gases (with 6260 vppm SO_2/1700 vppm HCl) for 1000 h at 700°C

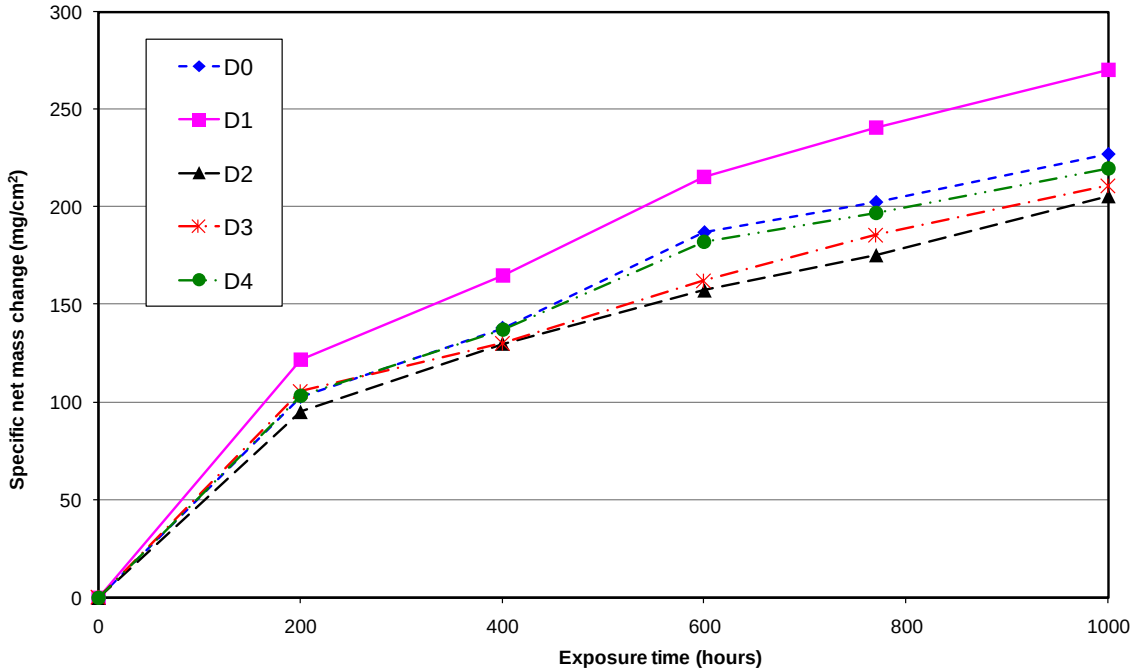

Figure 4-15: Specific net mass change data for alloy T22 bare and covered with four synthetic deposits exposed to simulated oxy-fired combustion gases (with 6260 vppm SO_2/1700 vppm HCl) for 1000 h at 750°C

4.2.3.2 T92

In Figure 4-16 to Figure 4-19 the effect of temperature is demonstrated. For T92 samples exposed to oxy-fired gas environment (6260 vppm SO_2/1700 vppm HCl) at 600, 650, 700 and 750°C respectively. Samples covered with deposit D1 showed an increase in mass change with the increase in temperature (particularly at 650°C a rapid increase was observed); overall mass gain values for sample T92 covered with deposit D1 were found to be 54, 94, 192 and 193 mg/cm^2 at 600, 650, 700 and 750°C respectively. At all the tested temperatures the high mass gain values were observed for samples painted with deposit D1, followed by bare samples in each case. The overall mass gain values for bare T92 sample at different temperature also followed the same trend i.e. increased in mass gain values up to 700°C. However, at 750°C the mass change values decreased relative to those at 700°C.

At 700°C not only the sample with deposit D1 showed high mass gain but also samples covered with other deposits (D2, D3 and D4). These mass change values for D2, D3 and D4 were in a range of ~60-70 mg/cm^2, whereas samples covered with same deposits at other temperatures (600, 650 and 750°C) showed overall mass gain values of < 40 mg/cm^2. Overall higher mass gain values were found for alloy T92, bare or covered with deposits, in simulated oxy-firing conditions compared to air firing conditions; showing the effect of changing the combustion gas composition.

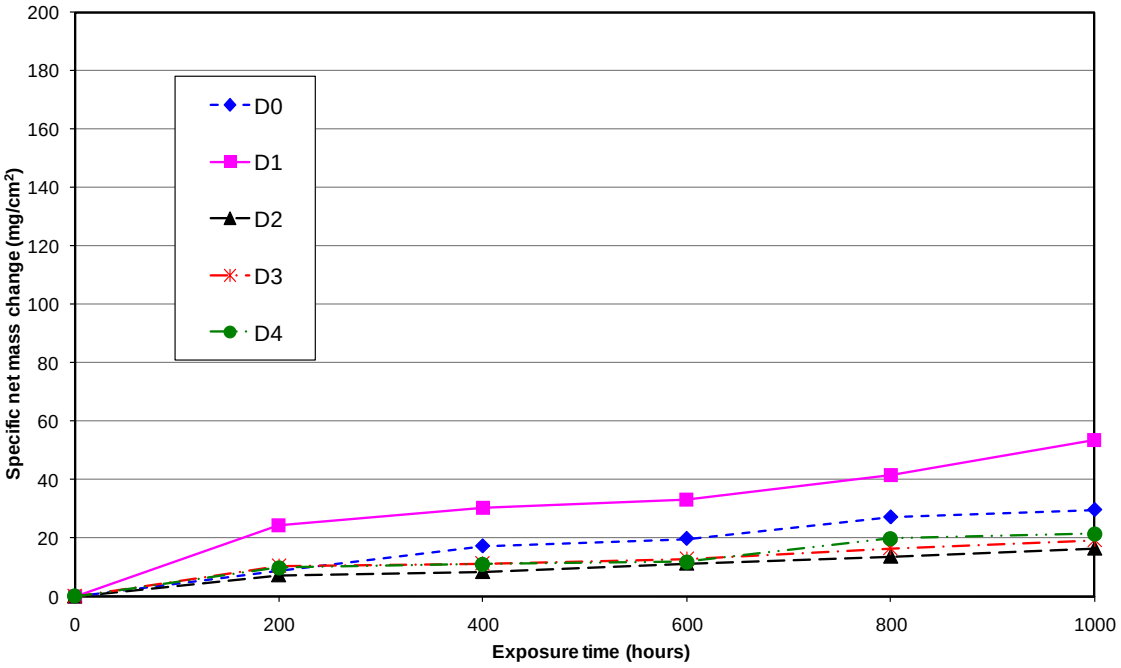

Figure 4-16: Specific net mass change data for alloy T92 bare and covered with four synthetic deposits exposed to simulated oxy-fired combustion gases (with 6260 vppm SO_2/1700 vppm HCl) for 1000 h at 600°C

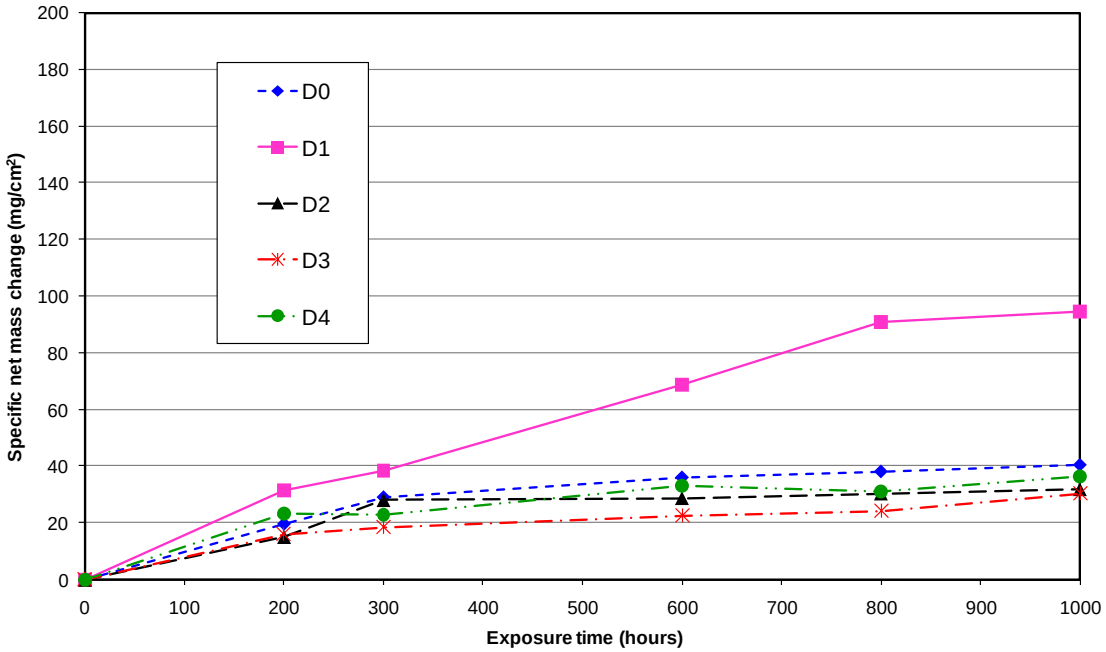

Figure 4-17: Specific net mass change data for alloy T92 bare and covered with four synthetic deposits exposed to simulated oxy-fired combustion gases (with 6260 vppm SO_2/1700 vppm HCl) for 1000 h at 650°C

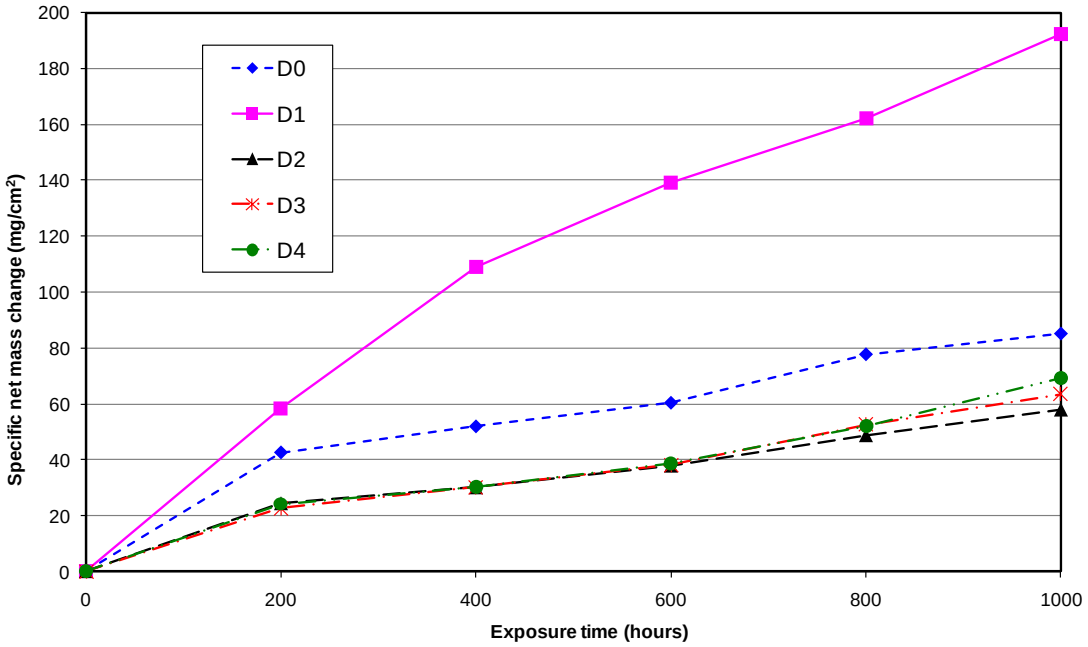

Figure 4-18: Specific net mass change data for alloy T92 bare and covered with four synthetic deposits exposed to simulated oxy-fired combustion gases (with 6260 vppm SO_2/1700 vppm HCl) for 1000 h at 700°C

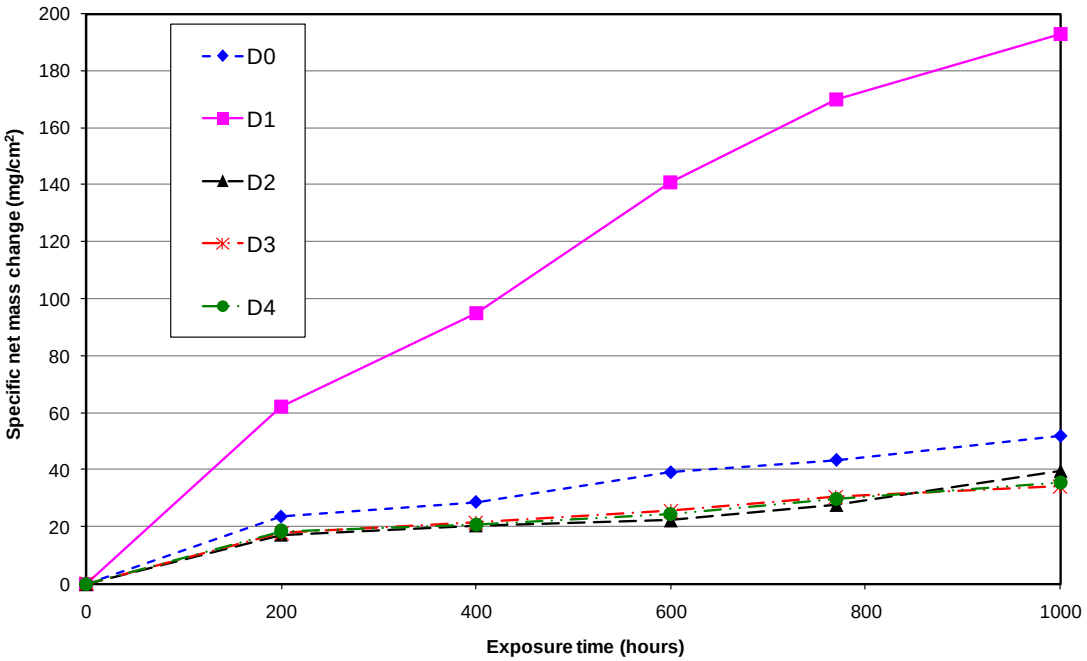

Figure 4-19: Specific net mass change data for alloy T92 bare and covered with four synthetic deposits exposed to simulated oxy-fired combustion gases (with 6260 vppm SO_2/1700 vppm HCl) for 1000 h at 750°C

4.2.3.3 347HFG

The results in Figure 4-20 to Figure 4-23 show the mass change data for alloy 347HFG in the same gas environment (oxy-firing) and at four different temperatures (600, 650, 700 and 750°C). As expected samples 347HFG covered with (aggressive) deposit D1 gained the highest mass at each temperature.

Test number 5 carried out at 700°C was found to be the most critical temperature (in oxy-firing conditions) for alloy 347HFG, it produced the highest mass gain values for samples bare or covered with deposits (compared to 347HFG samples at the other four temperatures). The mass gain value with deposit D1 at 700°C was (~170mg/cm^2) approx 8 times more than the mass gain at 600°C, 3 times more than the at 650°C and 1.5 times more than at 750°C. Samples covered with other deposits (D2, D3 and D4) at 600, 650 and 750°C showed small overall mass gains.

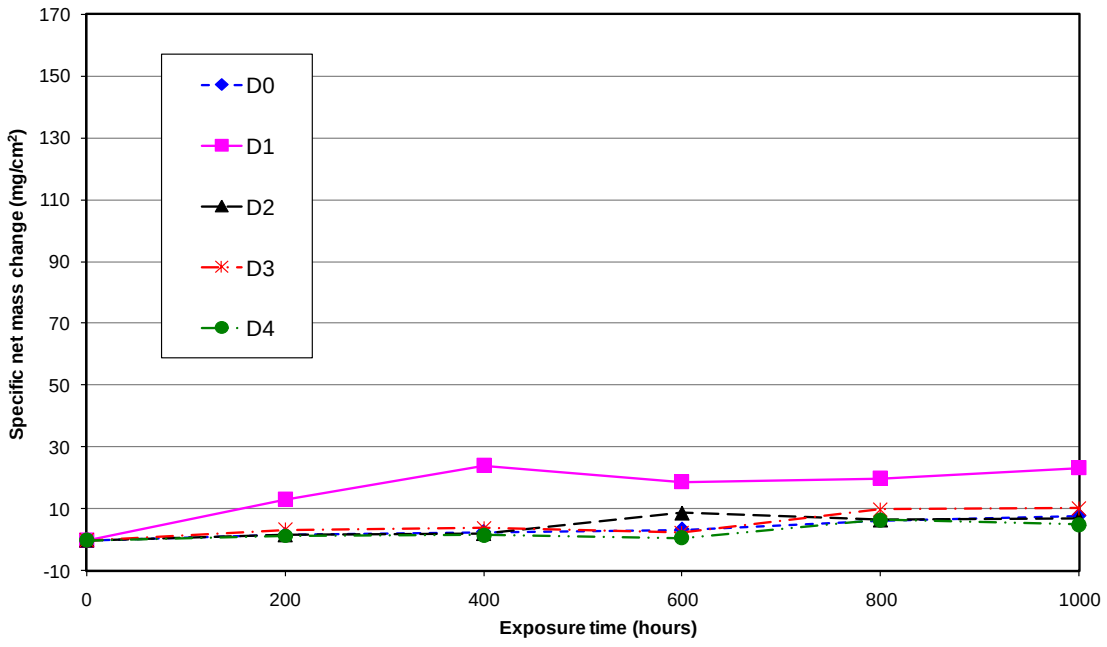

Figure 4-20: Specific net mass change data for alloy 347HFG bare and covered with four synthetic deposits exposed to simulated oxy-fired combustion gases (with 6260 vppm SO_2/1700 vppm HCl) for 1000 h at 600°C

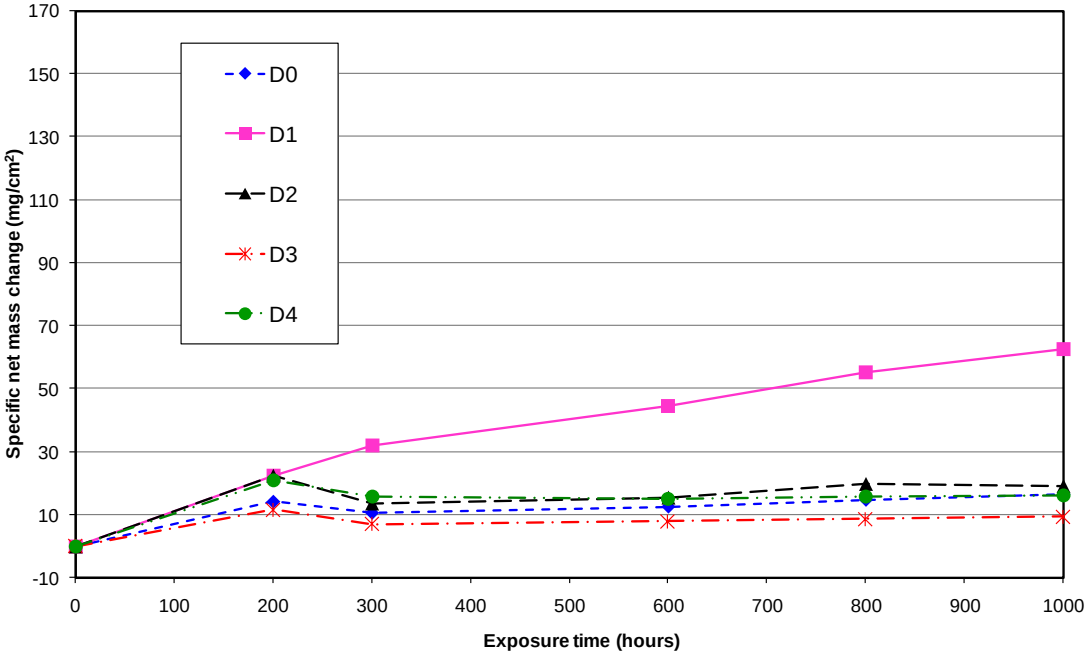

Figure 4-21: Specific net mass change data for alloy 347HFG bare and covered with four synthetic deposits exposed to simulated oxy-fired combustion gases (with 6260 vppm SO_2/1700 vppm HCl) for 1000 h at 650°C

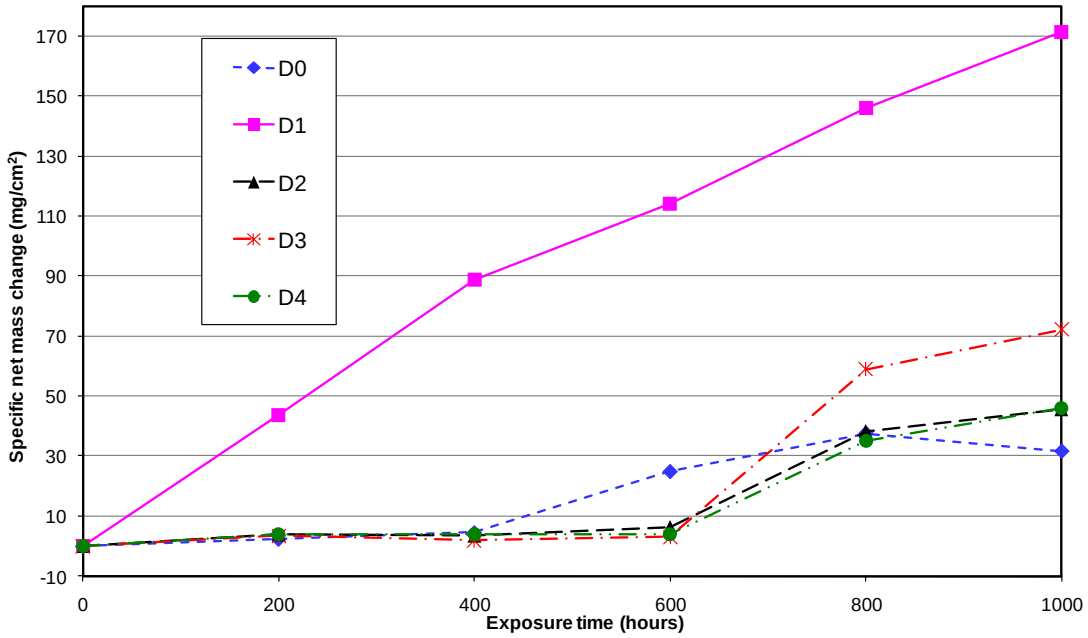

Figure 4-22: Specific net mass change data for alloy 347HFG bare and covered with four synthetic deposits exposed to simulated oxy-fired combustion gases (with 6260 vppm SO_2/1700 vppm HCl) for 1000 h at 700°C

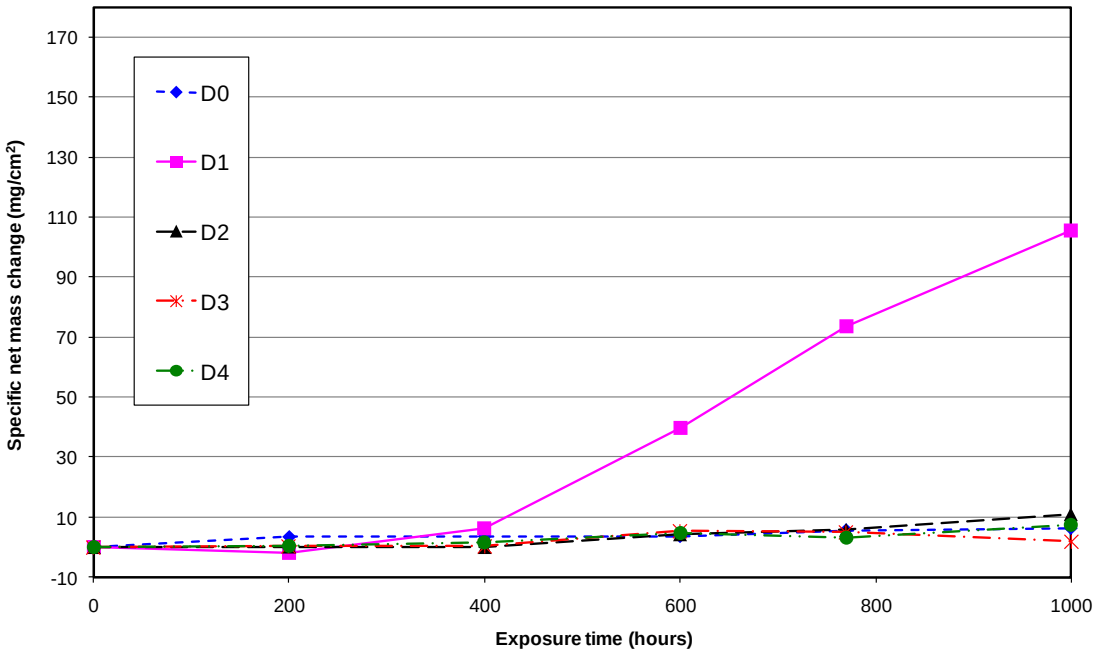

Figure 4-23: Specific net mass change data for alloy 347HFG bare and covered with four synthetic deposits exposed to simulated oxy-fired combustion gases (with 6260 vppm SO_2/1700 vppm HCl) for 1000 h at 750°C

4.2.3.4 HR3C

In Figure 4-24 to Figure 4-27 the effect of temperature is demonstrated for HR3C samples exposed to the simulated oxy-fired gas at 600, 650, 700 and 750°C, Alloy HR3C samples covered with deposits D1 followed the same trend as observed for T92 and 347HFG, with the highest mass value at 700°C.

Figure 4-25 at 650°C shows a noticeable rapid mass gain in the first cycle followed by a downward trend in the next cycle and further very little mass gain in the remaining cycles. At the same temperature samples covered with more realistic deposits (D2, D3 and D4) showed significant mass gain values whereas at other temperatures(i.e. 600, 700 and 750°C) these samples showed much lower mass changes consistent observations on the other alloys. The highest mass gain was observed at 700°C (approximately 70 mg/cm^2 with deposit D1).

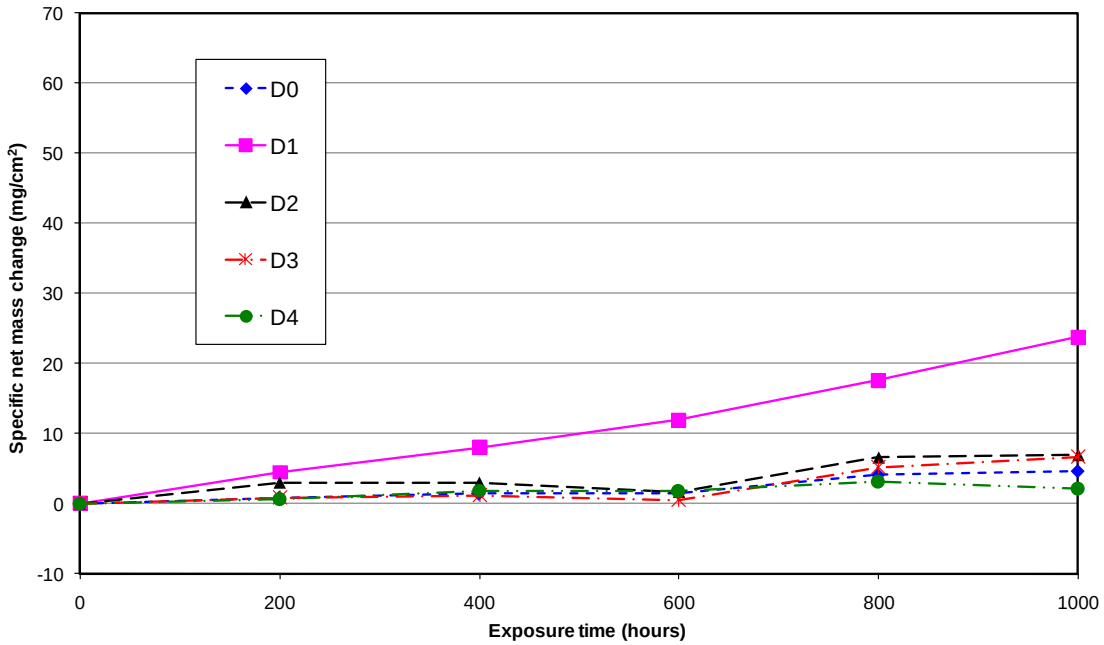

Figure 4-24: Specific net mass change data for alloy HR3C bare and covered with four synthetic deposits exposed to simulated oxy-fired combustion gases (with 6260 vppm SO_2/1700 vppm HCl) for 1000 h at 600°C

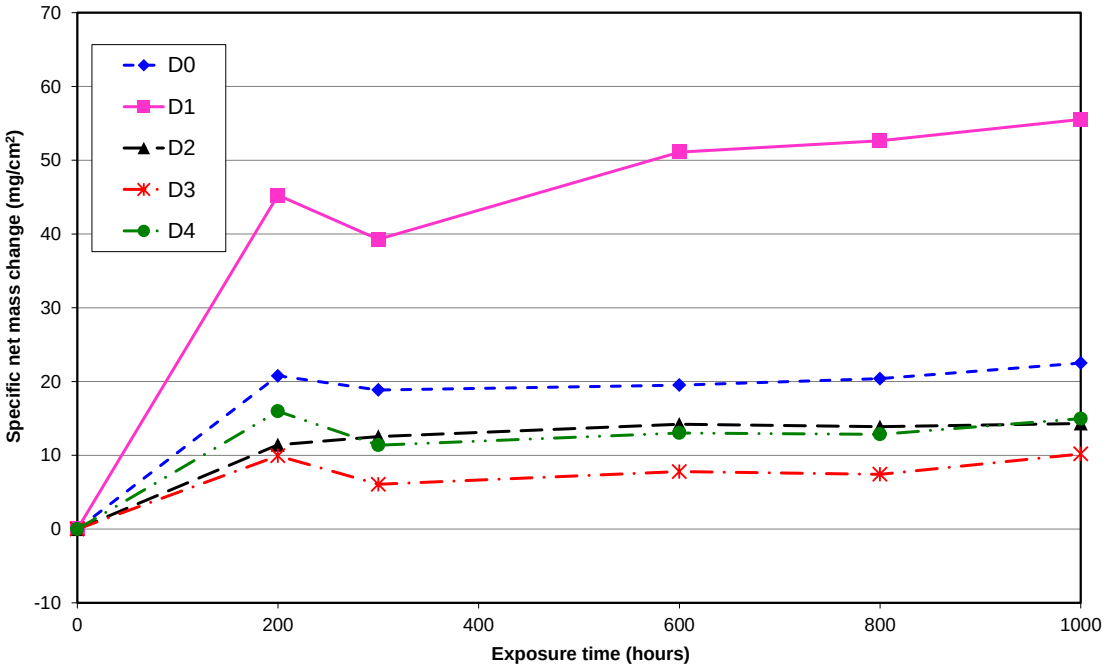

Figure 4-25: Specific net mass change data for alloy HR3C bare and covered with four synthetic deposits exposed to simulated oxy-fired combustion gases (with 6260 vppm SO_2/1700 vppm HCl) for 1000 h at 650°C

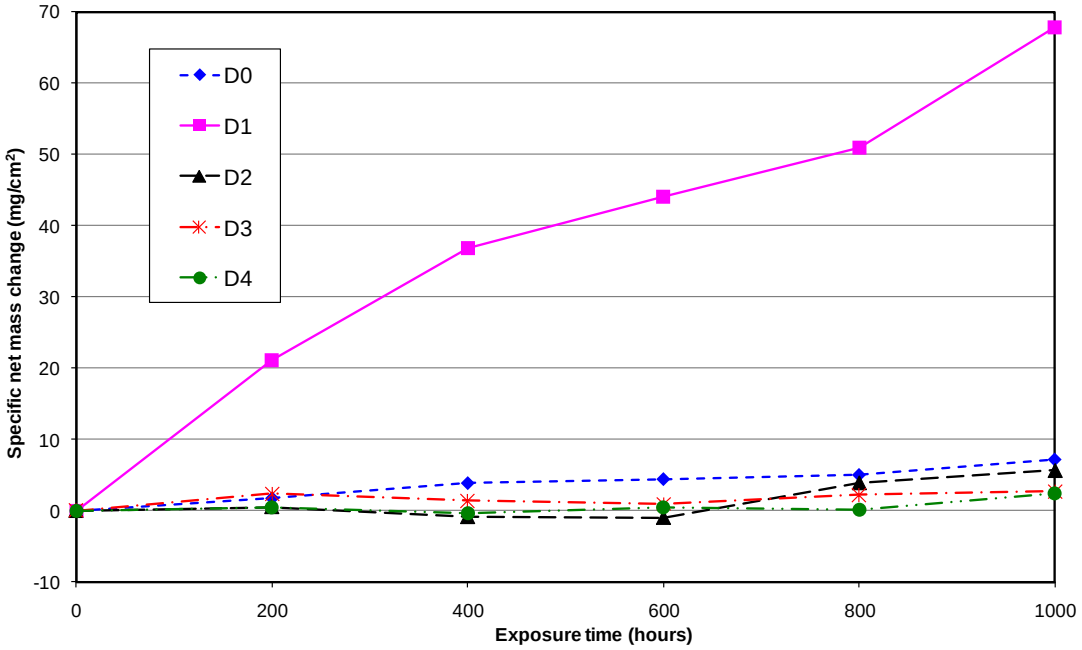

Figure 4-26: Specific net mass change data for alloy HR3C bare and covered with four synthetic deposits exposed to simulated oxy-fired combustion gases (with 6260 vppm SO_2/1700 vppm HCl) for 1000 h at 700°C

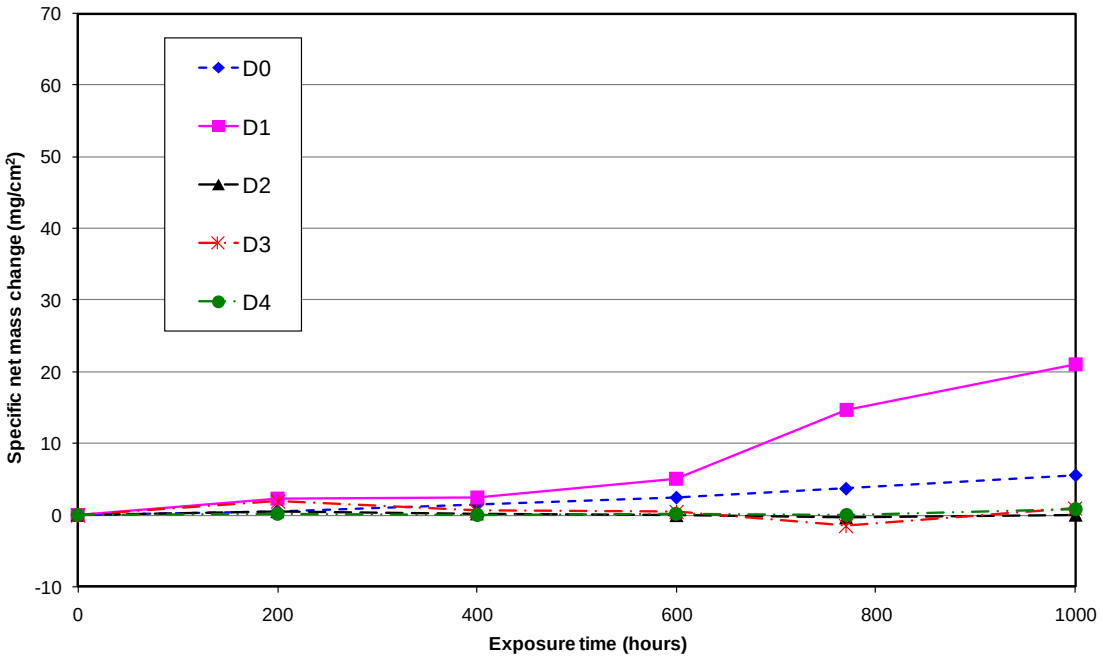

Figure 4-27: Specific net mass change data for alloy HR3C bare and covered with four synthetic deposits exposed to simulated oxy-fired combustion gases (with 6260 vppm SO_2/1700 vppm HCl) for 1000 h at 750°C

4.2.3.5 Alloy 625

Figure 4-28 to Figure 4-31 illustrate specific net mass change data for alloy 625 at different temperatures. These results clearly show that samples covered with deposit D1 exhibit significant mass gain values. Like austenitic alloys (HR3C and 347HFG) the highest mass gain value was also observed at 700°C. The mass gain values for alloy 625 samples with deposit D1 were found to be higher compared to alloy HR3C at all the temperatures and higher than alloy 347HFG at 600, 650 and 700°C.

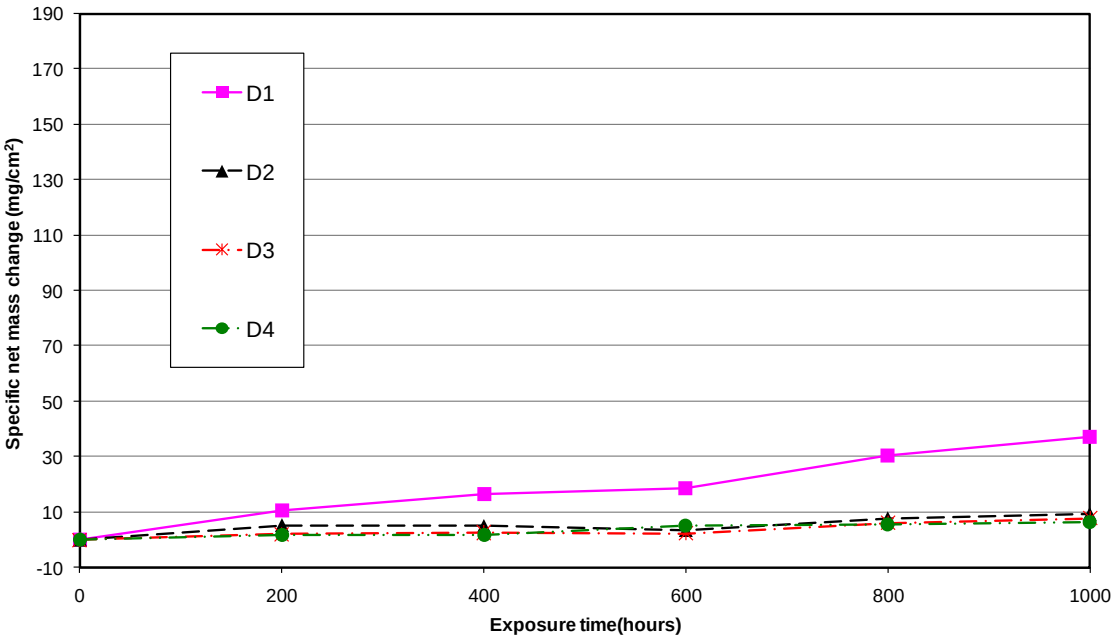

Figure 4-28: Specific net mass change data for alloy 625 covered with four synthetic deposits exposed to simulated oxy-fired combustion gases (with 6260 vppm SO_2/1700 vppm HCl) for 1000 h at 600°C

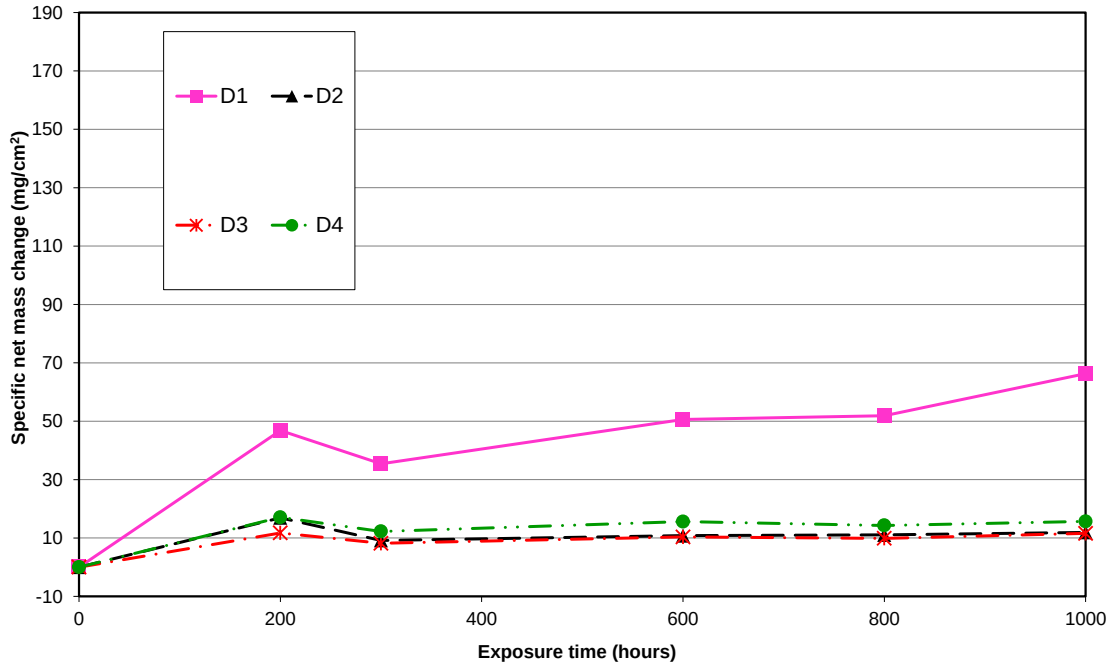

Figure 4-29: Specific net mass change data for alloy 625 covered with four synthetic deposits exposed to simulated oxy-fired combustion gases (with 6260 vppm SO_2/1700 vppm HCl) for 1000 h at 650°C

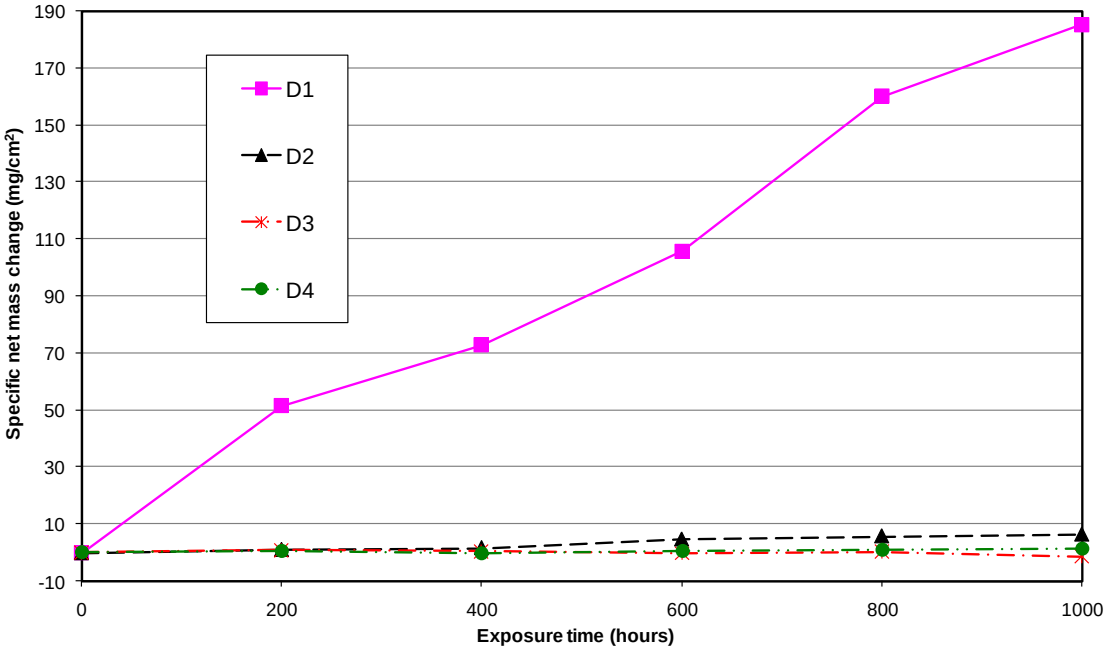

Figure 4-30: Specific net mass change data for alloy 625 covered with four synthetic deposits exposed to simulated oxy-fired combustion gases (with 6260 vppm SO_2/1700 vppm HCl) for 1000 h at 700°C

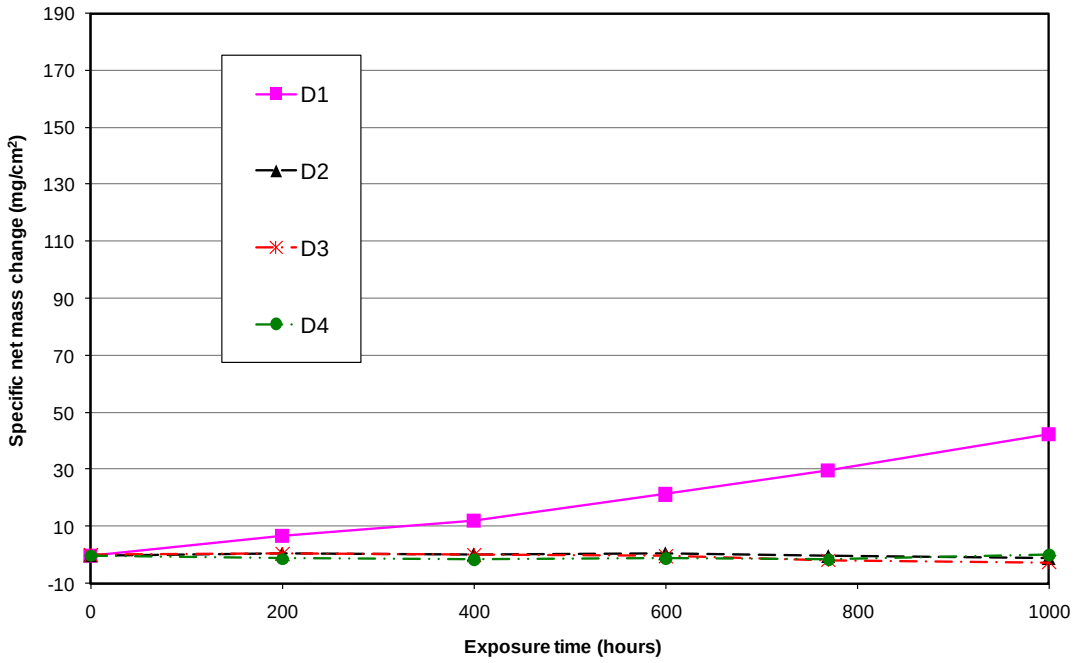

Figure 4-31: Specific net mass change data for alloy 625 covered with four synthetic deposits exposed to simulated oxy-fired combustion gases (with 6260 vppm SO_2/1700 vppm HCl) for 1000 h at 750°C

At 700°C the mass gain value with deposit D1was approx 185 mg/cm^2, i.e. ~ 3 times more than for HR3C and ~ 15 mg/cm^2 more than for 347HFG. Alloy 625 covered with other deposits showed low levels of mass change at all four temperatures.

4.3 SEM/EDX

4.3.1 Introduction

SEM/EDX analysis was performed to study the morphology, scale layer thicknesses and detailed information on the scale/deposit layers formed during the high temperature corrosion experiments. X-ray mapping was carried out using EDX to study the elemental distribution.

4.3.2 Surface Morphology

Secondary electron imaging analysis was carried out on the material surfaces before and after their exposure and found to be useful way of observing the development of the surface scales.

4.3.2.1 Air firing tests

Figure 4-32 shows the surface morphology of the initially bare alloys T92 and HR3C before and after the fireside corrosion test with simulated air-fired combustion gas at 650°C. For T92 (a ferritic steel), threadlike growths were observed together with large nodular growths, whereas for HR3C (an austenitic steel), finer scale oxides were formed, some with more crystalline morphologies.

Figure 4-33 shows the surface morphology of the bare alloys T22 and 347HFG before and after 1000 hours fireside corrosion test at 700°C. The scale formed on alloy T22 compared to austenitic alloy 347HFG is very thick, and resembles spongy, tightly packed flowers. Such thick scale formation on the low chromium alloy T22 is also supported by the mass change data (in section 4.2.2.1.) where the mass gain value of bare T22 is 8 times more that for bare 347HFG.The morphology of scales formed on austenitic alloys are comparatively thinner and flaky, but uniformly covered the sample surfaces.

.

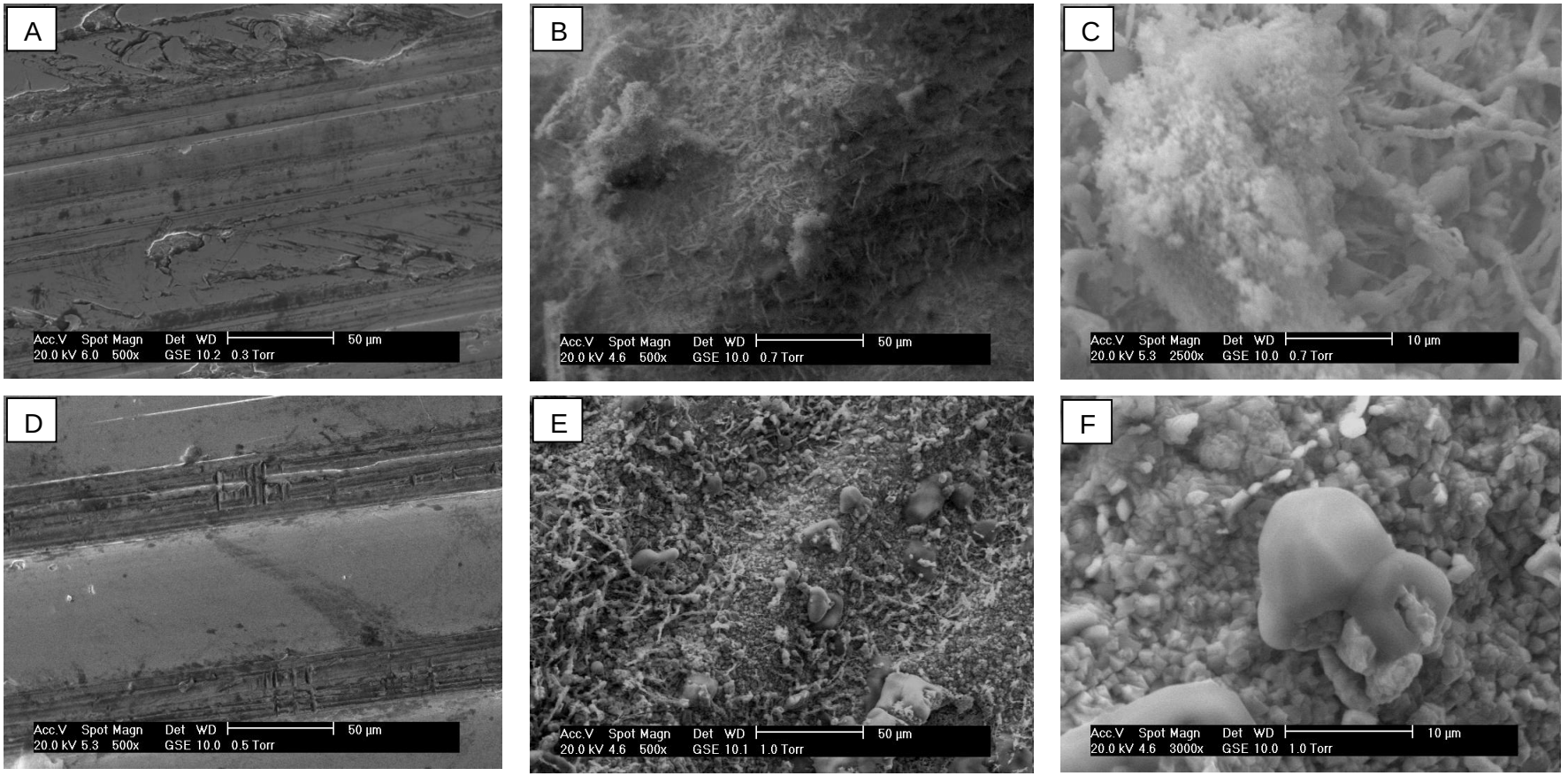

Figure 4-32: SEM images of bare alloy T92 (A) prior, (B,C) after 1000 hours and alloy HR3C (D) prior, (E,F) after 1000 hours exposed to 1300 vppm SO_2/400 vppm HCl at 650°C.

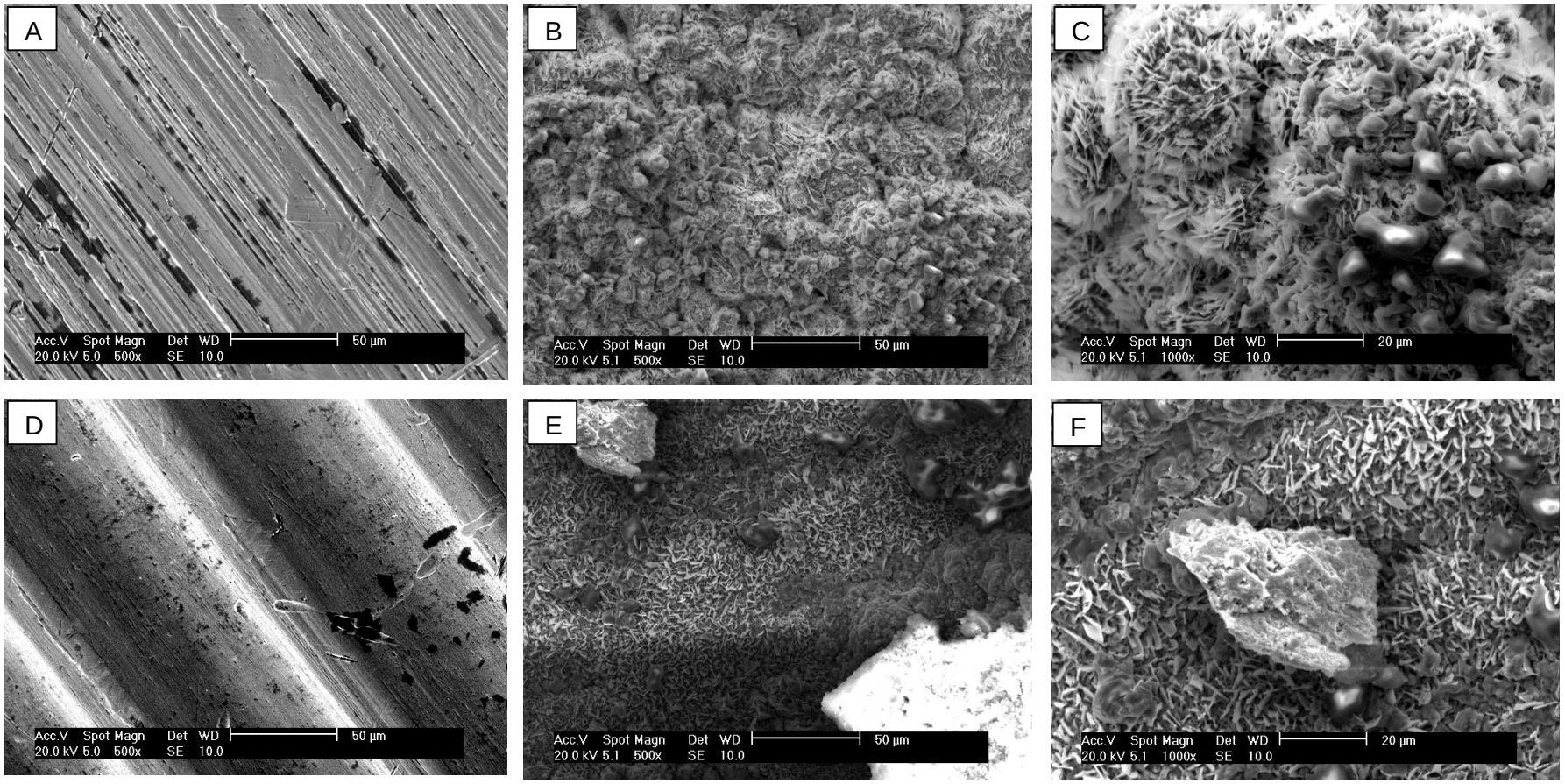

Figure 4-33: SEM images of bare alloy T22 (A) prior, (B,C) after 1000 hours and alloy 347HFG (D) prior, (E,F) after 1000 hours exposed to 1300 vppm SO_2/400 vppm HCl at 700°C.

4.3.2.2 Oxy-firing tests

Figure 4-34 shows the development of surface morphologies on the initially bare surfaces of alloy T92 and 347HFG during exposure in simulated oxy-fired combustion gases at 700°C (bare sample= sample covered with no deposit [D0] that is exposed to gas environment only). The surface analyses were carried out before exposure and after 600 hours and 1000 hours of exposure. The scale growth on the T92 surface after 600 hours is more granular compared to the platelet growth on alloy 347HFG. The scale surface on T92 after 1000 hours has become more uniform and nodular in appearance, whereas the 347HFG sample shows evidence of the spallation of its outer oxide layer.

Figure 4-35 presents the development of the surface morphology on the initially bare surfaces of alloy T22 and alloy HR3C during exposure in simulated oxy-fired combustion gases at 700°C. These surface analyses were carried out before exposure and after 600 and 1000 hours exposure. The morphology on T22 appeared to be a thread-like flaky growth whereas alloy HR3C scales had more crystalline structures. Figure 4-35(C) (after 1000 hours exposure) shows denser scale morphologies compared with Figure 4-35(B) (after 600 hours exposure). This is consistent with the mass change data showing higher mass gain with the time. However the morphology observed for HR3C in Figure 4-35(F) (after 1000 hours exposure) is similar to Figure 4-35(E) (after 600 hours exposure)

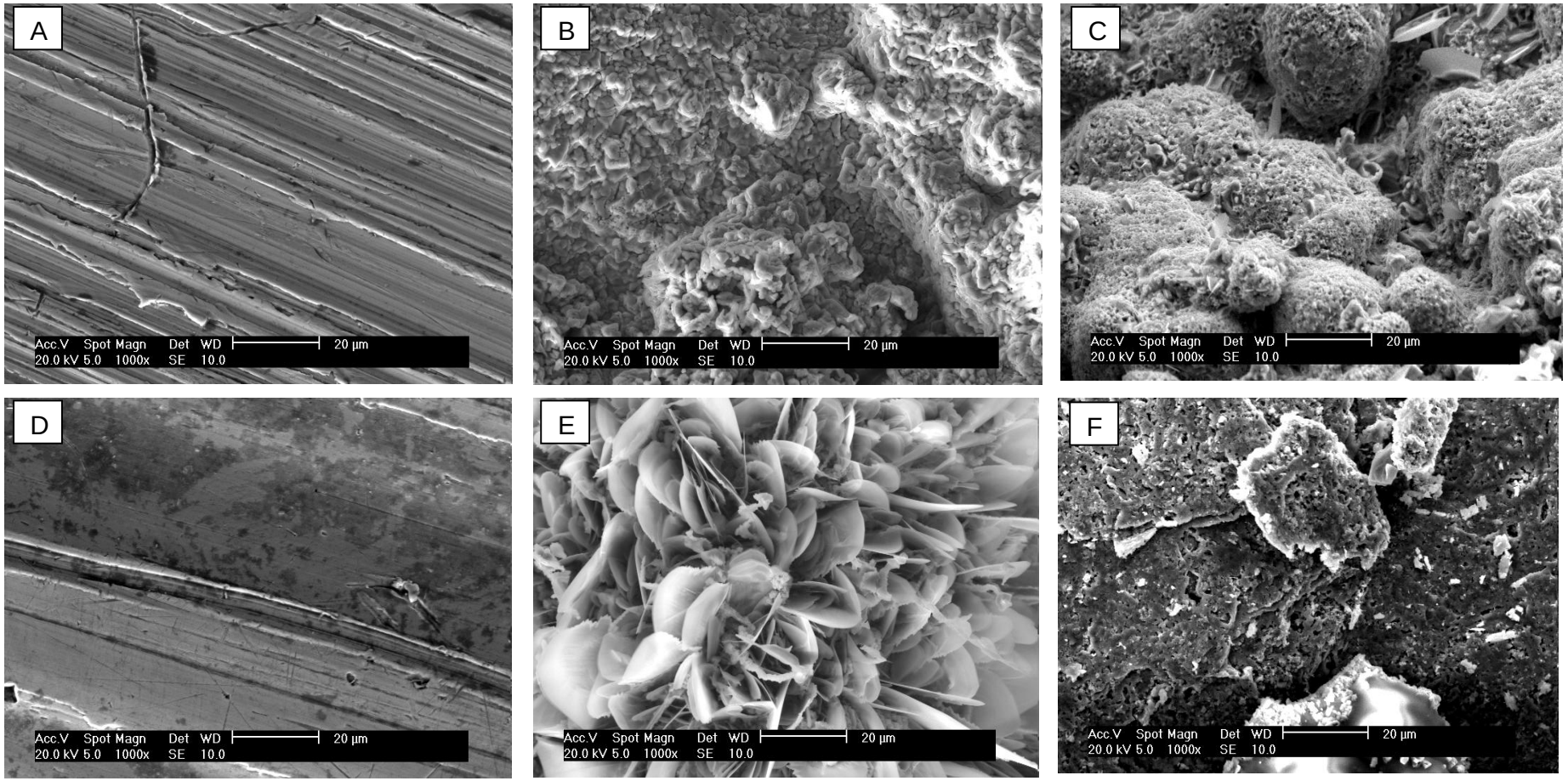

Figure 4-34: SEM images of bare alloy T92 (A) prior, (B) 600 hours and (C) 1000 hours and alloy 347HFG (D) prior, (E) 600 hours and (F) 1000 hours exposed to 6260 vppm SO_2/1700 vppm HCl at 700°C.

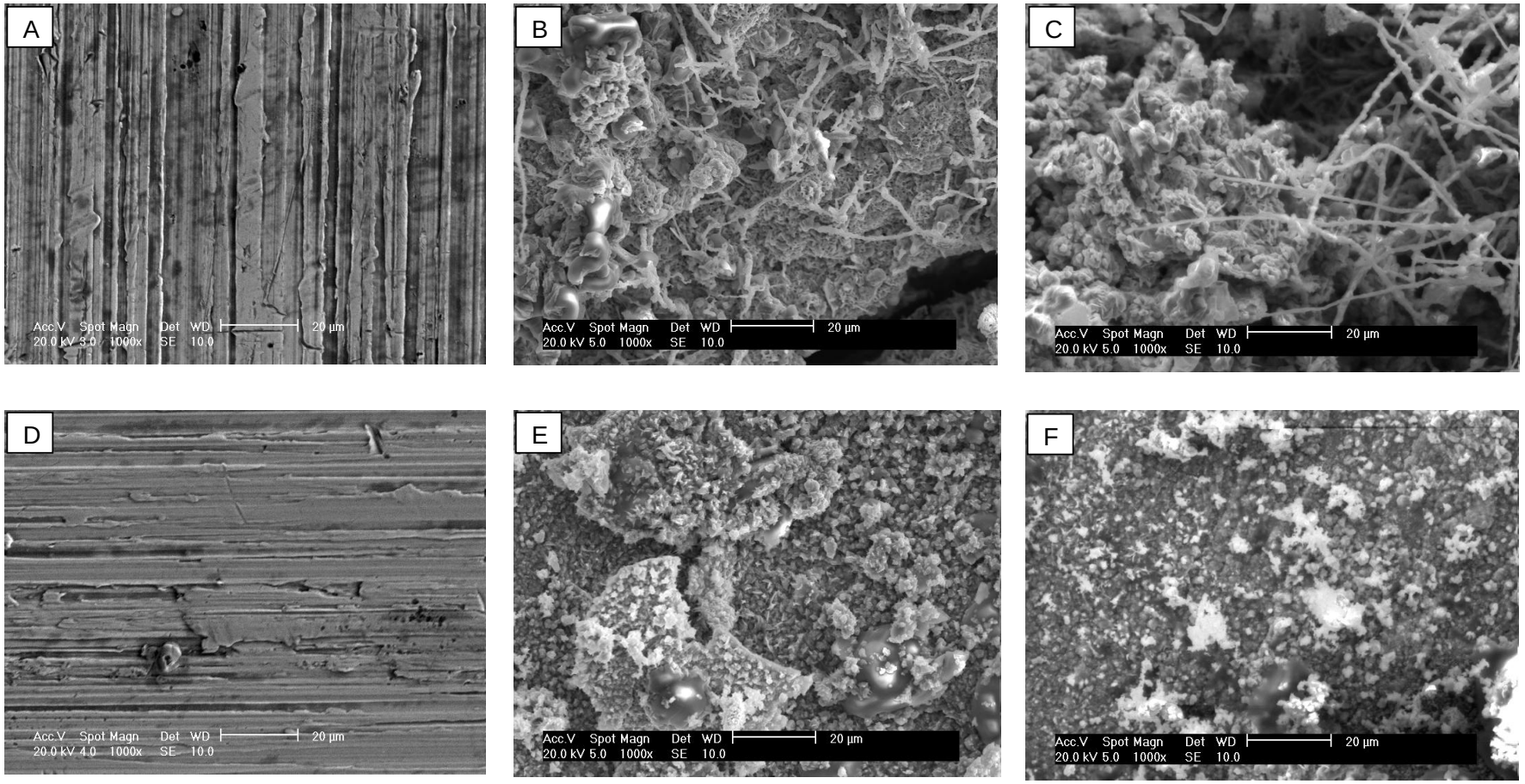

Figure 4-35: SEM images of bare alloy T22 (A) prior, (B) 600 hours and (C) 1000 hours and alloy HR3C (D) prior, (E) 600 hours and (F) 1000 hours exposed to 6260 vppm SO_2/1700 vppm HCl at 700°C.

4.3.3 Scale thickness

The thickness measurement of scale layers is one way to evaluate the degradation rate of the materials. Many researchers [65; 98; 108] have used this way of analysis determine the material corrosion performance.

4.3.3.1 Air firing tests

Figure 4-36 illustrates cross-sections through the scales formed on bare ferritc T92 and austenitic 347HFG and HR3C alloys after exposure for 1000 hours at 600, 650 and 700°C in simulated air-fired combustion gases. A thick multi-layered metal oxide formed on initially bare T92 during these exposures. A thicker scale formed at 650°C than 600°C, with both showing void formation within the scales. However at the highest temperature (700°C) the scale formed is not as thick as that at 650°C. The results show the scale thickness of T92 is ordered (highest to lowest) as: 650 > 700 > 600°C. This is consistent with mass change data. These thicker oxides show a tendency for their outer layers to spall, but for the inner compact spinel layer to remain adherent with no sign of internal oxidation within the alloy beneath it. As expected the scales formed on austenitic alloys are much thinner compared to ferritic alloy T92. The scales formed on both austenitic alloys (347HFG and HR3C) at 650°C are thicker than scales formed at 700°C, particularly HR3C where almost no scale was observed at 700°C. Internal damage is also clearly observed in both (347HFG and HR3C) alloys at the higher temperatures, but particularly at 650°C.

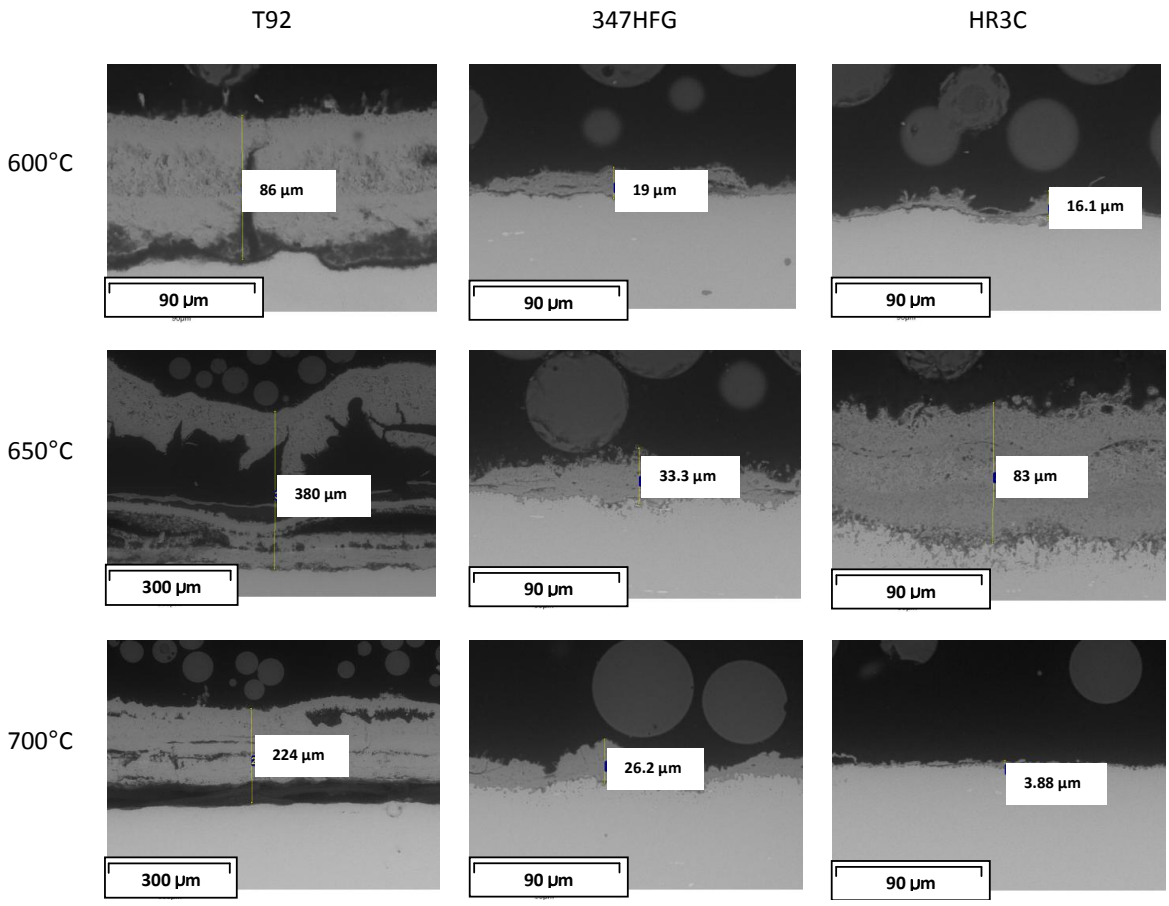

Figure 4-36: BSE images of cross-sectioned scales on bare T92, 347HFG and HR3C exposed to simulated air-fired combustion gases (with 1300 vppm SO_2/400 vppm HCl) at 600, 650 and 700 °C for 1000 hours

Figure 4-37 illustrates cross-sections through the scales formed on ferritc T92, austenitic 347HFG and HR3C and alloy 625 covered with deposit D1 after exposure for 1000 hours at 600, 650 and 700°C. The scales formed on the alloys surface as shown in Figure 4-37 are an oxide/sulphate/sulphide/deposit mix (analysis in section 4.3.4.1). The deposit/scales on alloy T92 are more compact particularly at 700°C where scale is present as a thick band. The deposit/scales formed on alloy 347HFG at all the temperatures are also very thick but contain numerous voids. However, the scale formed at 700°C is much denser close to metal scale interface. Alloy HR3C showed poor behaviour with deposit D1 at 650°C and 700°C, where significant scale thicknesses (multi-layered scales) can be observed; such corrosion damage of this alloy is in line with mass change data. Nickel-based alloy 625 showed scale

(deposit/sulphate/oxide/ sulphide mix) present at 600°C, however there was no sign of scales at 650 or 700°C, possibly due to spallation.

Figure 4-38 illustrate scale morphologies for ferritic alloy T92, austenitic 347HFGF, HR3C and nickel based alloy 625 covered with deposit D4 exposed to air-firing conditions (1300 vppm SO_2/400 vppm HCl) for 1000 hours at 600, 650 and 700°C. In Figure 4-38 cross-sections through samples exposed with deposit D4 clearly show distinctive layers of deposit and sulphates/oxide/sulphide scales. This is in contrast to samples covered with deposit D1 (where deposit D1 aggressively reacted with metal surface and the scales formed are mixture of deposits and sulphates/oxide/sulphides). Alloy T92 showed thick (multi-layered) deposit scales formed at 650°C with thicknesses almost 10 times more than those formed at 600 and 700°C. The deposits/scales formed on austenitic alloys (347HFG, HR3C) at 600, 650 and 700°C are thinner as expected when compared to alloy T92 at the same temperature. Some of these deposits/scales have detached from the metal surface, particularly for alloy 347HFG. Alloy 625 appeared to have minimal reaction with deposit D4; only at 600°C localised corrosion was observed, whereas at 650 and 700°C very little corrosion damage was observed.

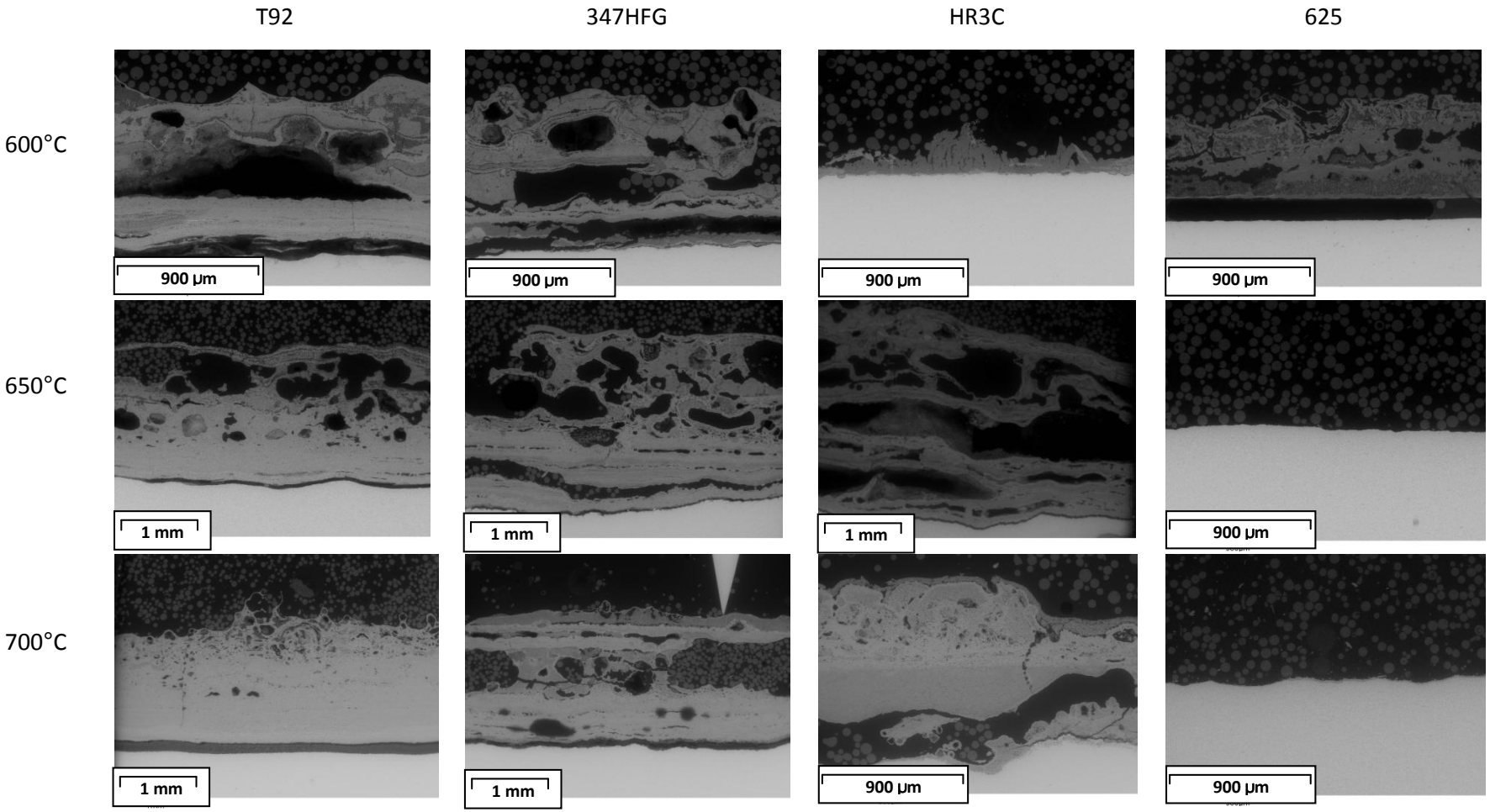

Figure 4-37: BSE images of cross-sectioned scales on T92, 347HFG, HR3C and alloy 625 covered with deposit D1 exposed to simulated air-fired combustion gases (with1300 vppm SO_2/400 vppm HCl) at 600, 650 and 700 °C for 1000 hours

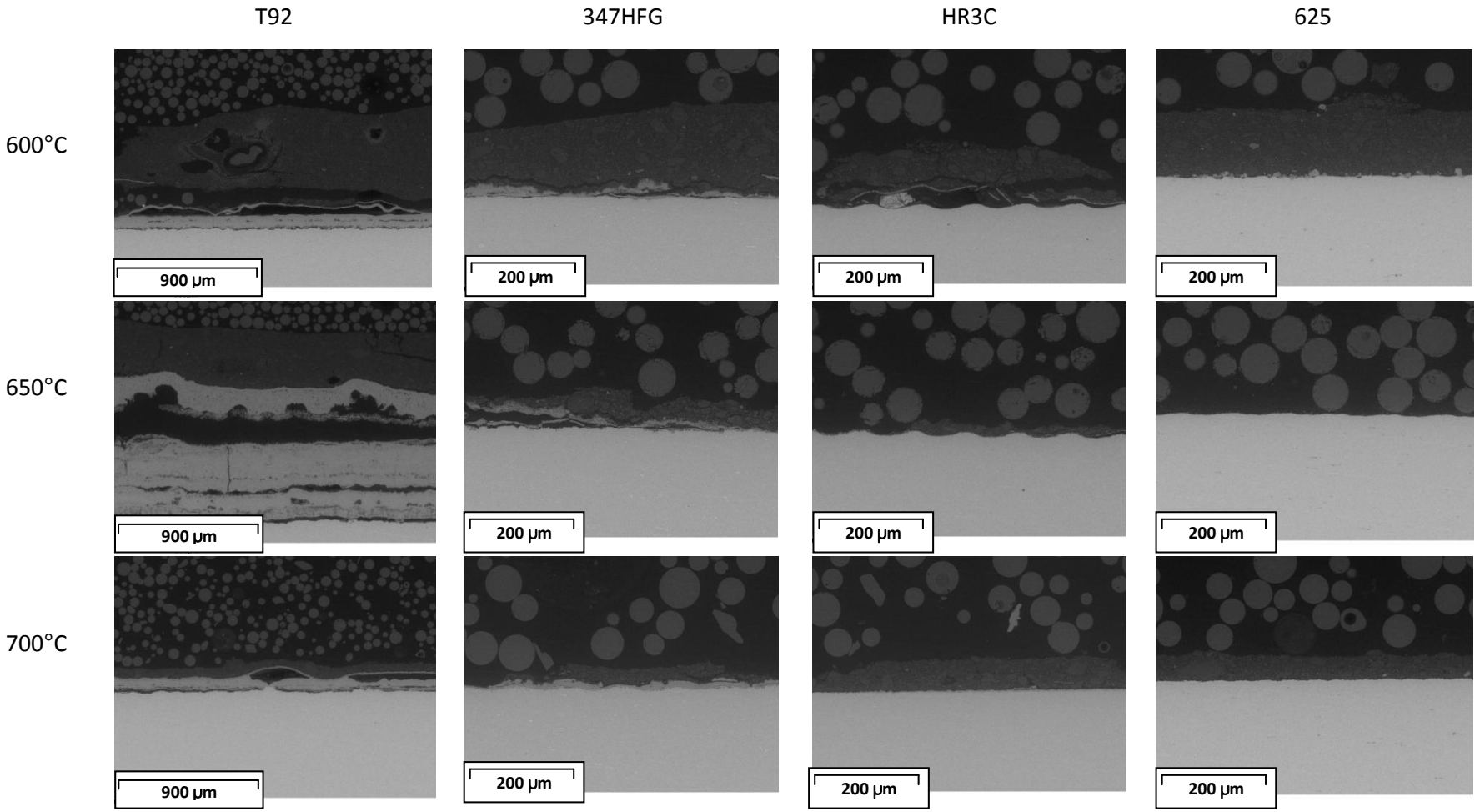

Figure 4-38: BSE images of cross-sectioned scales on T92, 347HFG, HR3C and alloy 625 covered with deposit D4 exposed to simulated air-fired combustion gases (with 1300 vppm SO_2/400 vppm HCl) at 600, 650 and 700 °C for 1000 hours

4.3.3.2 Oxy-firing tests

Figure 4-39 illustrates cross-sections through the scales formed on initially bare ferritic T92 and austenitic 347HFG and HR3C alloys after exposure for 1000 hours at 600, 650, 700 and 750°C. At these exposure temperatures the scales formed on bare T92 are mostly thick compared to those formed on the austenitic alloys. The multi-layered scales formed on bare T92 are an inner Fe-Cr spinel layer under a thicker magnetite layer with a thinner haematite layer at the scale/gas interface. The scales formed on alloy T92 at 700°C are much thicker than scales formed at any other temperature (600, 650 and 750°C);e.g. the scale formed at 600°C is thinner by a factor of ~6 compared to that formed at 700°C. The results show the scale thicknesses of T92 can be ordered (highest to lowest): 700 > 750 > 650 > 600°C.

As expected the scales formed on the austenitic alloys are thinner compared to ferritic T92 due to their significantly higher chromium levels. The thickest scale on 347HFG was formed at 750°C and was more than double the thickness of the scale formed at 600°C. These data show that the scale thickness increases with temperature in the range 600 to 750 °C. An important feature observed for alloy 347HFG at all the temperatures was the internal corrosion damage, particularly at 700°C where inter-granular attack was significant. The scales formed on HR3C at 600, 700 and 750°C are thin, as expected when compared to alloys T92 and 347HFG at the same temperatures. However, the scale formed at 650°C is thicker compared to scales formed on 347HFG, which is also in agreement with the results of the mass change data at this temperature. The scale formed on alloy HR3C at 650°C was thicker than scales formed at 600, 700 and 750°C. For HR3C, the most significant internal damage was found on samples exposed at 650 and 700°C.

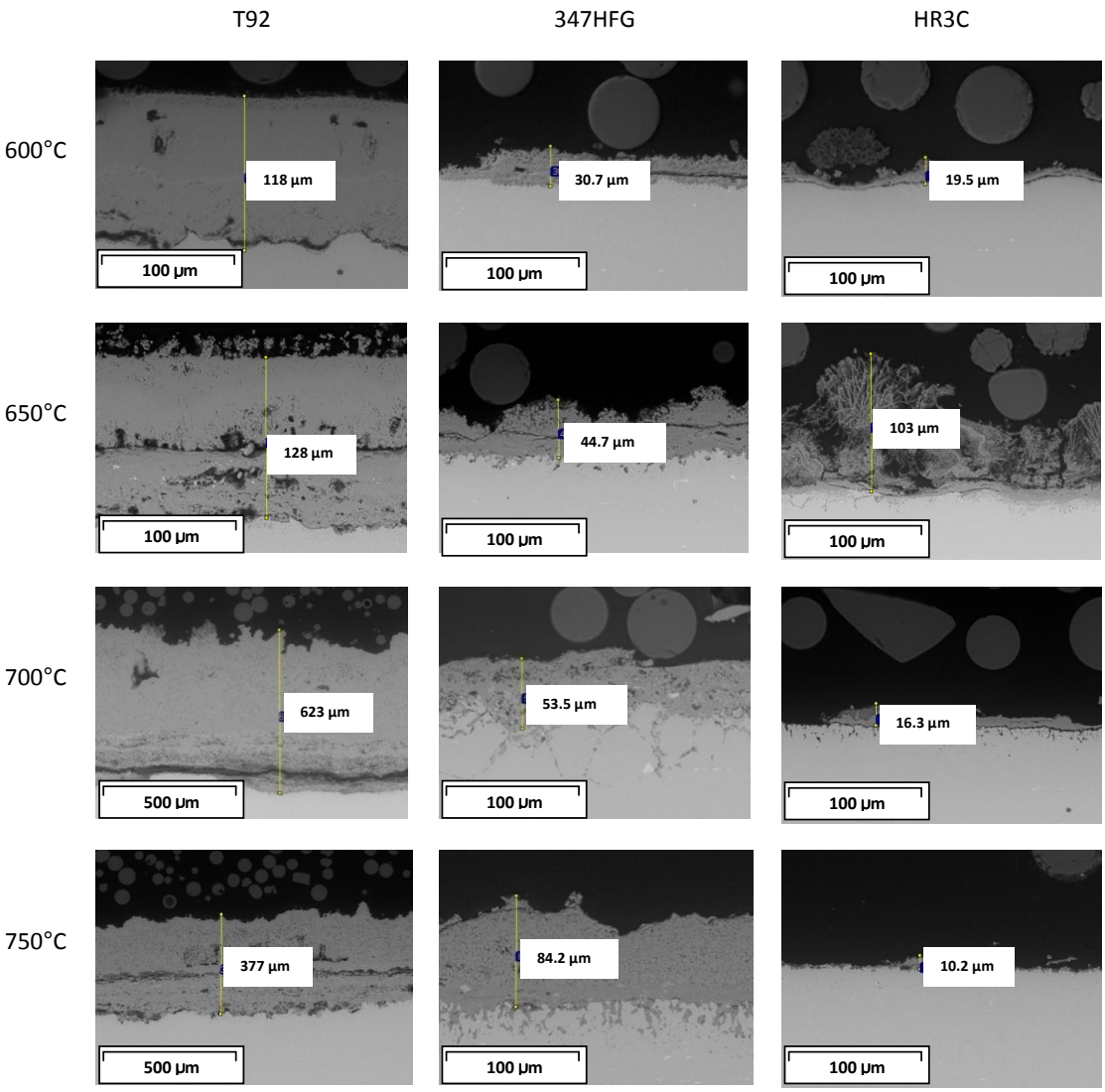

Figure 4-39: BSE images of cross-sectioned scales on bare T92, 347HFG and HR3C exposed to simulated oxy-fired combustion gases (with 6260 vppm SO_2/1700 vppm HCl) at 600, 650 700 and 750 °C for 1000 hours

Figure 4-40 shows cross-section through scales on alloys T92, 347HFG, HR3C and 625 covered with deposit D1 after exposure to simulated oxy-firing combustion gases for 1000 hours at 600, 650, 700 and 750°C. The deposits/scales formed on alloy T92 are thick and dense adjacent to metal surface. The thickest deposit/scale formed on alloy T92 at 700°C in agreement with mass change data and is almost 3 times more than scale formed at 600°C and also scales were mostly missing from alloy 347HFG at 600 and 650°C, probably as a result of spallation.

However, the deposits/scales formed on alloy 347HFG at 700 and 750°C are thick and adherent to metal surface. The deposit/scale formed on alloy 347HFG at 700°C is almost as thick as that formed on alloy T92 at the same temperature. Alloy HR3C also shows corrosion damage (multiple deposit/scale layers) with aggressive deposit D1 at all the temperatures (600, 650, 700 and 750°C). The thickest scale formed at 700°C which is consistent with mass change data. Alloy 625 also showed deposits/scales formation at all the temperatures (but thinner than those formed on austenitic and ferritic alloys at the same temperatures).The deposits/scales formed on all the alloys (T92, 347HFG, HR3C and alloy 625) covered with deposit D1 appears to be thickest at 700°C.

Figure 4-41 shows the cross-section through deposit/scales formed on ferritic T92, austenitic 347HFG and HR3C and nickel-based alloy 625 covered with deposit D4 exposed to same gas environment (oxy-firing) and at four different temperatures (600, 650, 700 and 750°C) for 1000 hours. The deposits/scales formed on alloy T92 are much thicker at 700°C compared to deposits/scales formed at 600, 650 and 750°C; which is in agreement with mass change data. The scales formed on alloy 347HFG at all the temperatures are also significant, but with some scales partially or fully detached from the metal surface. The internal corrosion damage to alloy 347HFG, particularly at 700°C, is also clearly observed. Alloy HR3C showed corrosion damage with deposit D4, particularly at 650 and 700°C where significant scale and internal corrosion can be observed; this is also in line with mass change data. Nickel-based alloy 625 covered with deposit D4 also showed corrosion damage at all the temperatures. At 750°C the deposit/scale formed completely detached from the metal surface in some areas. At other temperatures (600, 650 and 700°C) the scale and deposit are mixed (metal diffuse into deposits).

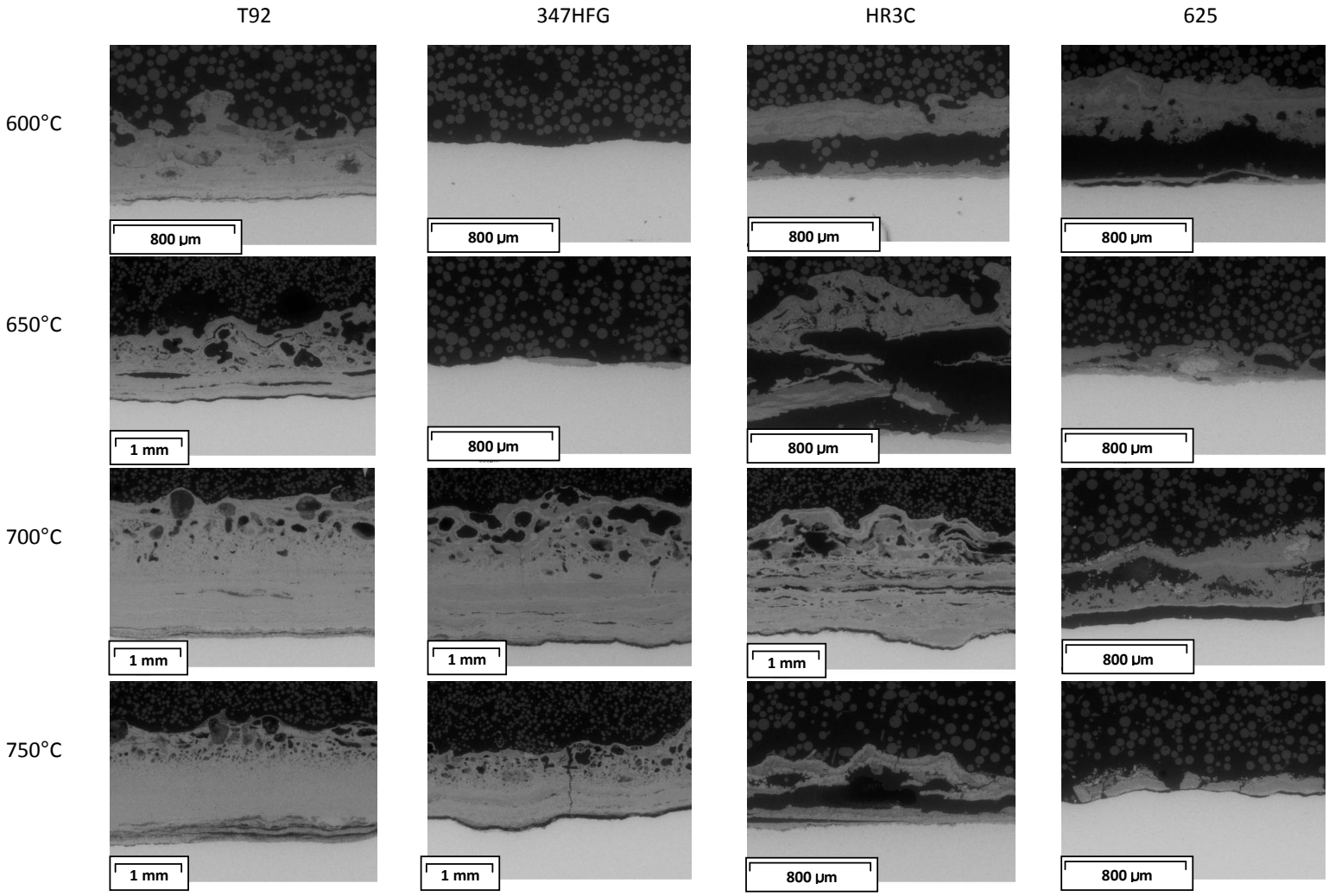

Figure 4-40: BSE images of cross-sectioned scales on T92, 347HFG, HR3C and alloy 625 covered with deposit D1 exposed to simulated oxy-fired combustion gases (with 6260 vppm SO_2/1700 vppm HCl) at 600, 650 and 700 °C for 1000 hours

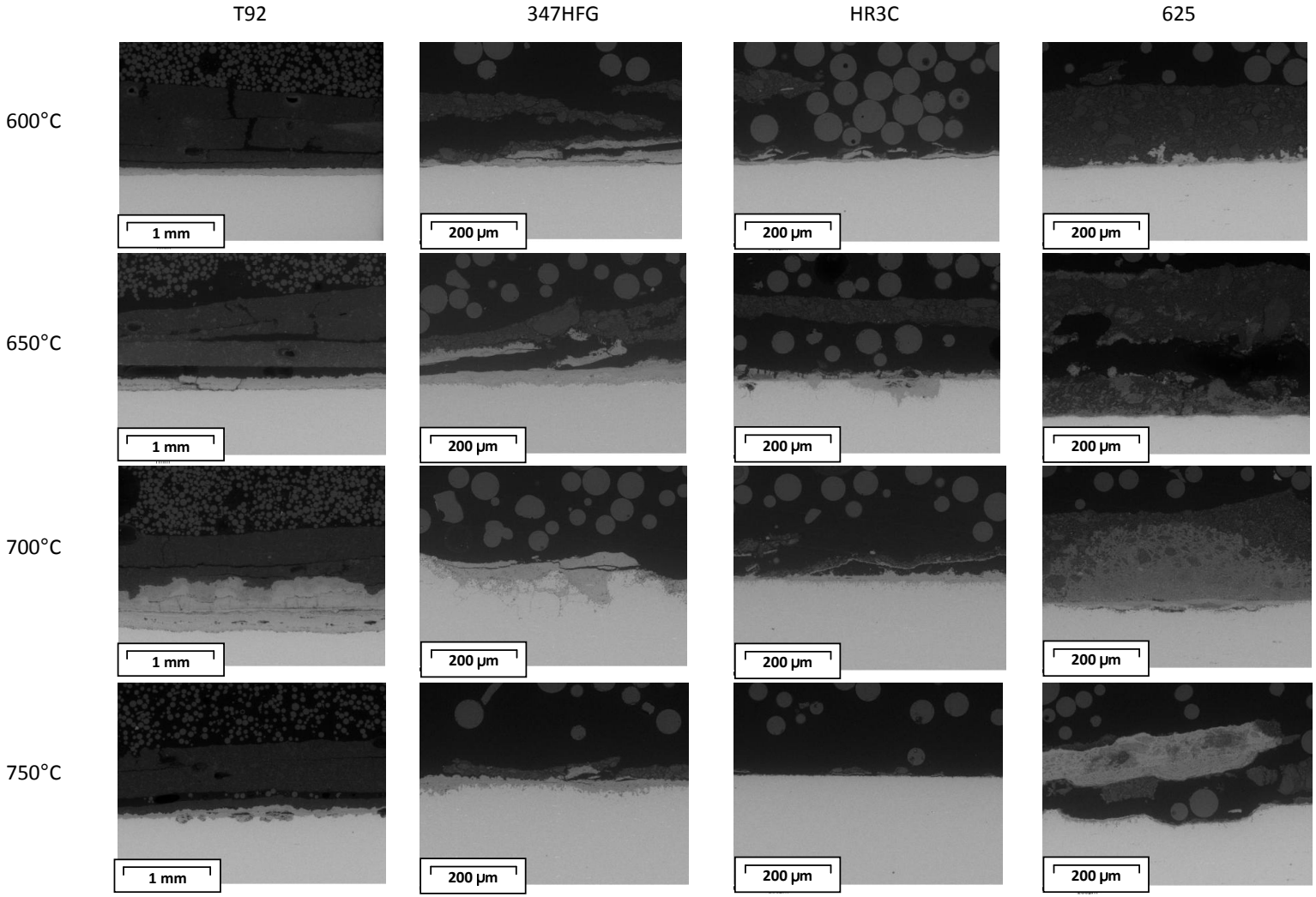

Figure 4-41: BSE images of cross-sectioned scales on T92, 347HFG, HR3C and alloy 625 covered with deposit D4 exposed to simulated oxy-fired combustion gases (with 6260 vppm SO_2/1700 vppm HCl at 600, 650 and 700 °C for 1000 hours

4.3.4 EDX mapping

The chemical compositions of the deposits and corrosion products on the metal surfaces were studied using EDX by elemental mapping. However EDX mapping only gives qualitative data and so quantitative data were generated using EDX line profiles, which will be presented under heading 4.3.5. Examples of the EDX mapping performed on samples (initially bare or covered with deposit in both firing conditions) are presented in this section.

4.3.4.1 Air-firing tests

Figure 4-42 shows EDX mapping of bare T92 exposed to simulated air-fired combustion gas at 650°C for 1000 hours. Oxygen is distributed throughout the scale, but chromium is located only in the inner scale layer. As expected, iron was present throughout the scale as well as in the underling alloy. The iron is richer toward the surface of the scale (in the magnetite and thin haematite layers), whereas it is less concentrated in the spinel layer (Fe, Cr-oxide). The highest levels of S/Mo were detected within the spinel layer close to the scale/alloy interface and at gas scale interface. It should be noted that distinction between sulphur and molybdenum was not possible Traces of sodium were also detected at scale surface.

Figure 4-43 illustrates EDX mapping of a cross-section through a T92 sample covered with deposit D1 exposed to simulated air-fired combustion gases at 650°C for 1000 hours. These maps show the distribution of oxygen throughout the deposit and scale. Chromium is located in the spinel oxide layer close to the alloy. Both sodium and potassium are concentrated towards the surface of the deposit/scale mix and are present at lower levels deeper into these layers. Sulphur shows a concentration distribution that similar to the alkali metals, but in addition, there is a further concentration in patches at the alloy/scale interface.

Figure 4-44 illustrates EDX mapping of a cross-section through an initially bare HR3C sample exposed to simulated air-fired combustion gases at 650°C for

1000 hours. These maps clearly show a pit-type attack and inward growing damage. The maps show a distribution of oxygen throughout the scale, but with it being relatively more concentrated in a chromium-rich inner layer. The sulphur is also detected in the inner scale (where chromium is depleted) and in the internal damage zone. Iron is richer toward the surface of the scale. Nickel was detected in layers of the scale and in the internal damage zone (as well as the underlying alloy).

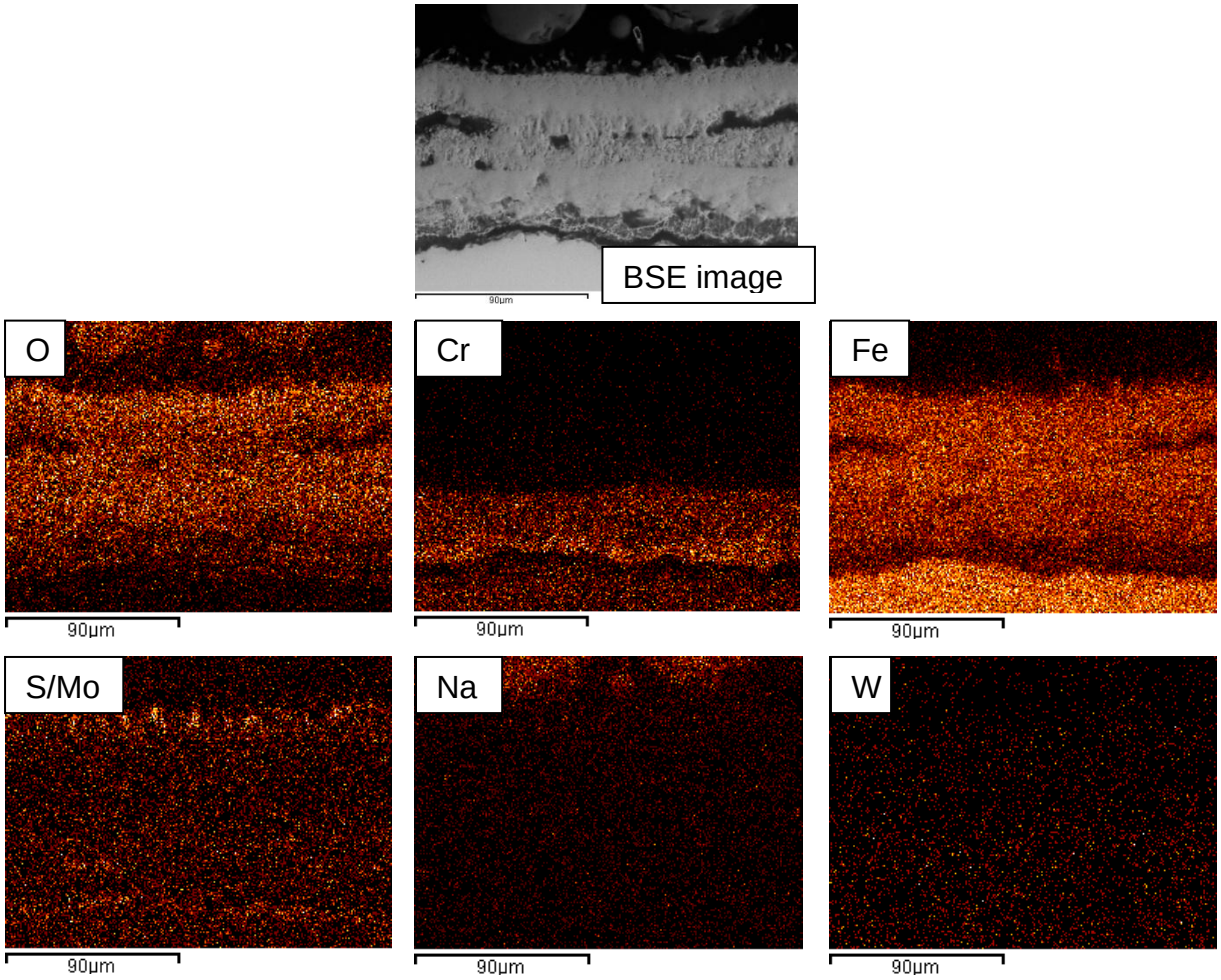

Figure 4-42: BSE image and x-ray maps of cross-section through bare T92 alloy exposed to simulated air-fired combustion gases (with1300vppm SO_2/400vppm HCl) at 650°C for 1000 hours

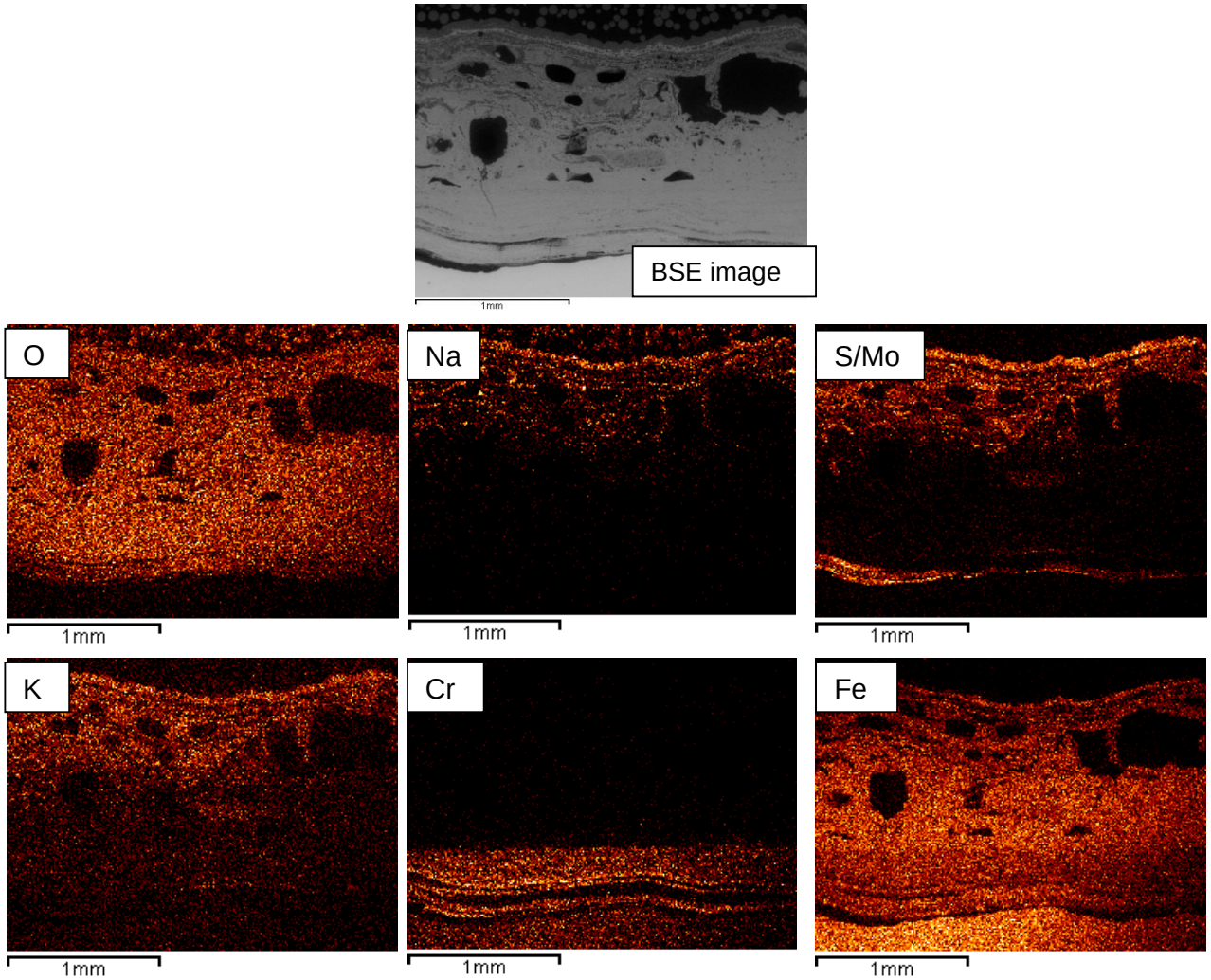

Figure 4-43: BSE image and x-ray maps of cross-section through T92 covered in deposit D1 exposed to simulated air-fired combustion gases (with1300vppm SO_2/400vppm HCl) at 650°C for 1000 hours

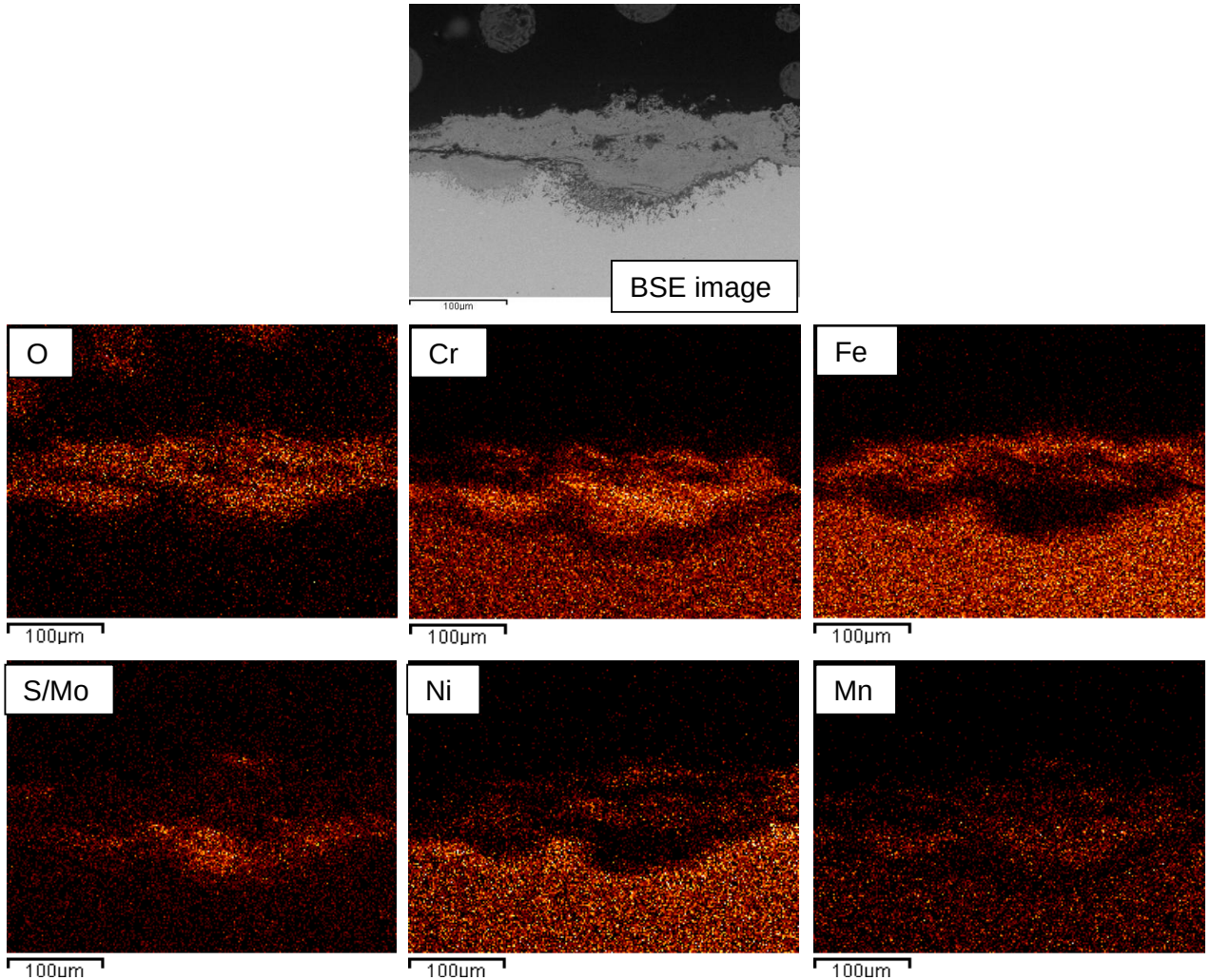

Figure 4-44: BSE image and x-ray maps of cross-section through bare HR3C alloy exposed to simulated air-fired combustion gases (with1300vppm SO_2/400vppm HCl) at 650°C for 1000 hours

4.3.4.2 Oxy-firing tests

Figure 4-45 presents EDX maps of an initially bare alloy 347HFG exposed to simulated oxy-fired combustion gases at 600°C for 1000 hours. The maps show the elemental distribution through the scale and at the alloy interface. The BSE image shows obvious inner (~12μm) and outer (~22 μm) scale layers. A rich layer of sulphur is concentrated at the scale/gas interface as well as deeper in the inner scale layer, and confirms that sulphur plays a role in the attack mechanism. In the outermost layer oxygen, manganese and iron were also detected. Iron is much richer I the outer scale. Chromium is concentrated in the inner, which indicates chromium trying to form protective layer. Nickel is enriched beneath the chromium rich oxide layer (due to outward Cr and Fe diffusion). Traces of potassium were detected at the scale surface.

Figure 4-46 illustrate EDX mapping of a cross-section through an initially bare T92 sample exposed to simulated oxy-fired combustion gases at 700°C for 1000 hours. Figure 4-46 clearly shows that the scales formed on the initially bare alloy T92 have a uniform oxygen distribution throughout the ~500 μm thick scale. Chromium is located in the spinel layer(s) close to the alloy but in a multi-layer arrangement rather than a thick band. Iron was present throughout the scale and in high levels at the scale surface (magnetite and haematite) and depleted in bands within the spinel region (iron, chromium oxides). Sulphur is concentrated in patches in the inner spinel close to the alloy interface. Traces of potassium (at scale surface) and manganese (within inner scale region) were also detected.

Figure 4-47 shows EDX mapping of a cross-section through alloy T92 covered with deposit D1 exposed to simulated oxy-fired combustion gas at 700°C for 1000 hours. The aggressive behaviour of deposit D1 (high levels of alkali sulphates /iron oxide) towards alloy T92 can be clearly observed, with a thick deposit/scale being formed. The mapping shows oxygen is uniformly distributed throughout the deposit/scale. Fe is also present in the scale but richer towards

the gas interface and in the alloy as expected. The Fe level is depleted where the chromium level increases in the layered spinel closer to the alloy. S/Mo is detected beneath the chromium rich layer and at the surface along with alkali metals (potassium and sodium).

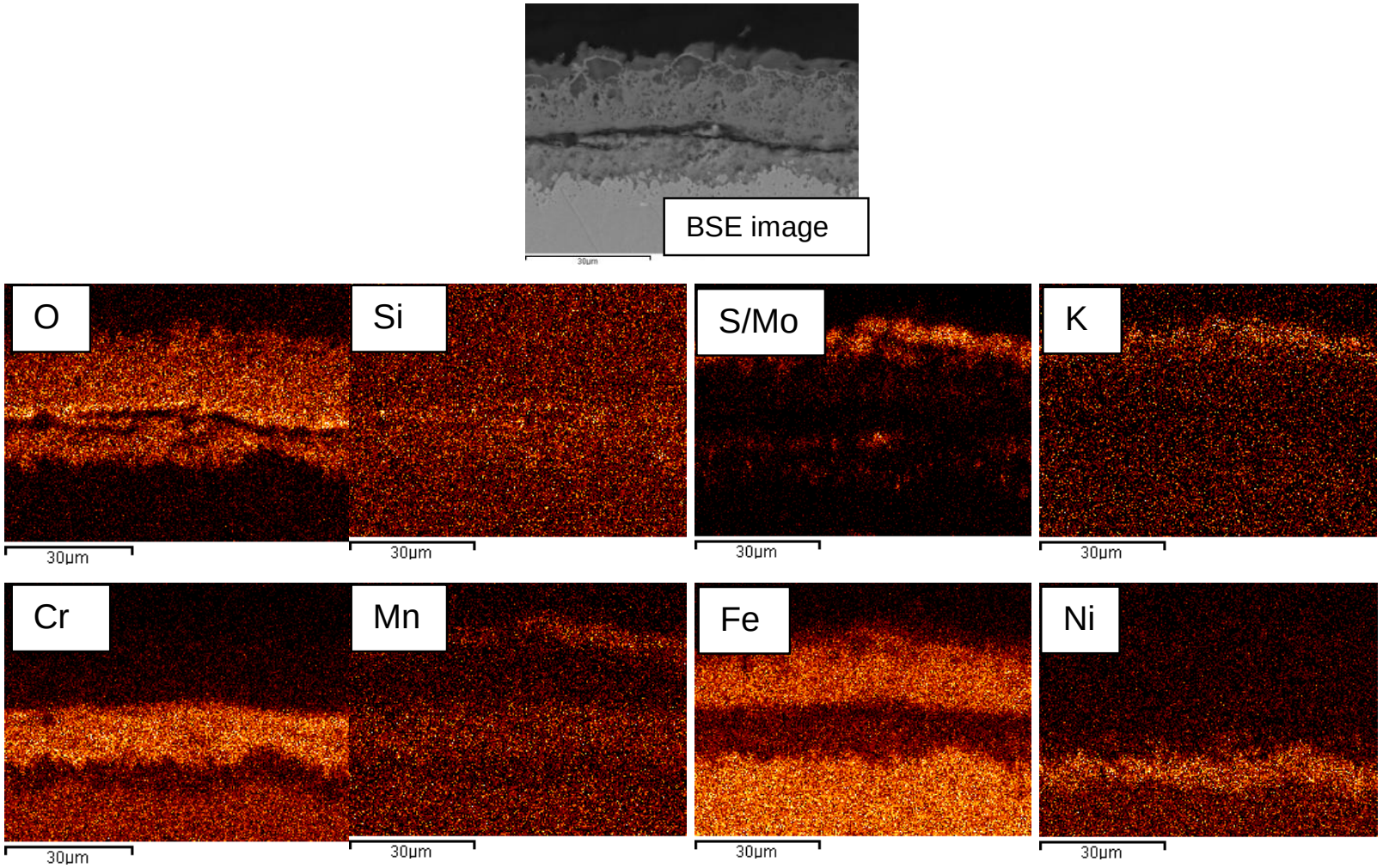

Figure 4-45: BSE image and x-ray maps of bare 347HFG alloy exposed to simulated oxy-fired combustion gases (with 6260 vppm SO_2/1700 vppm HCl) at 600°C for 1000 hours

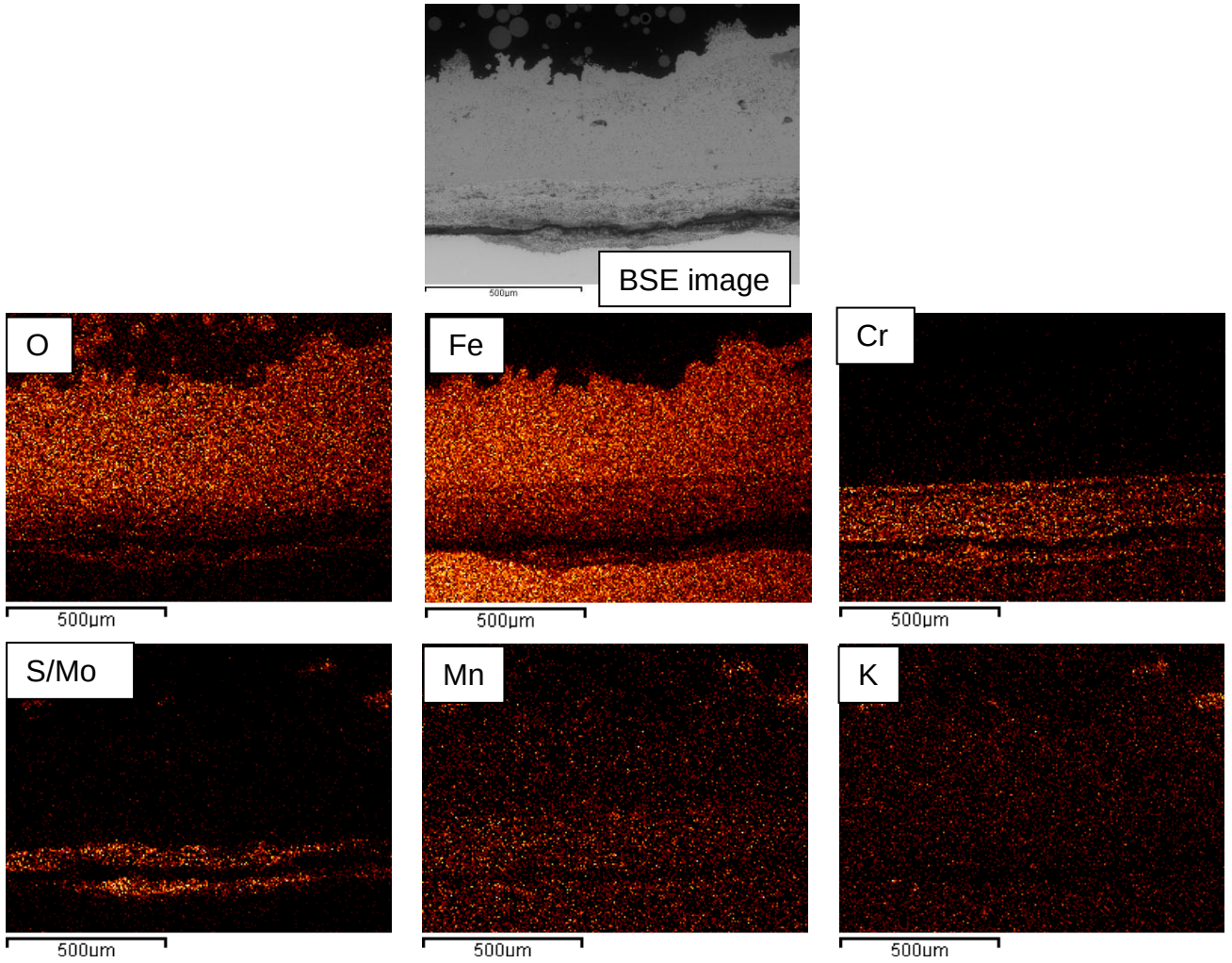

Figure 4-46: BSE image and x-ray maps of bare T92 alloy exposed to simulated oxy-fired combustion gases (with 6260 vppm SO_2/1700 vppm HCl)at 700°C for 1000 hours

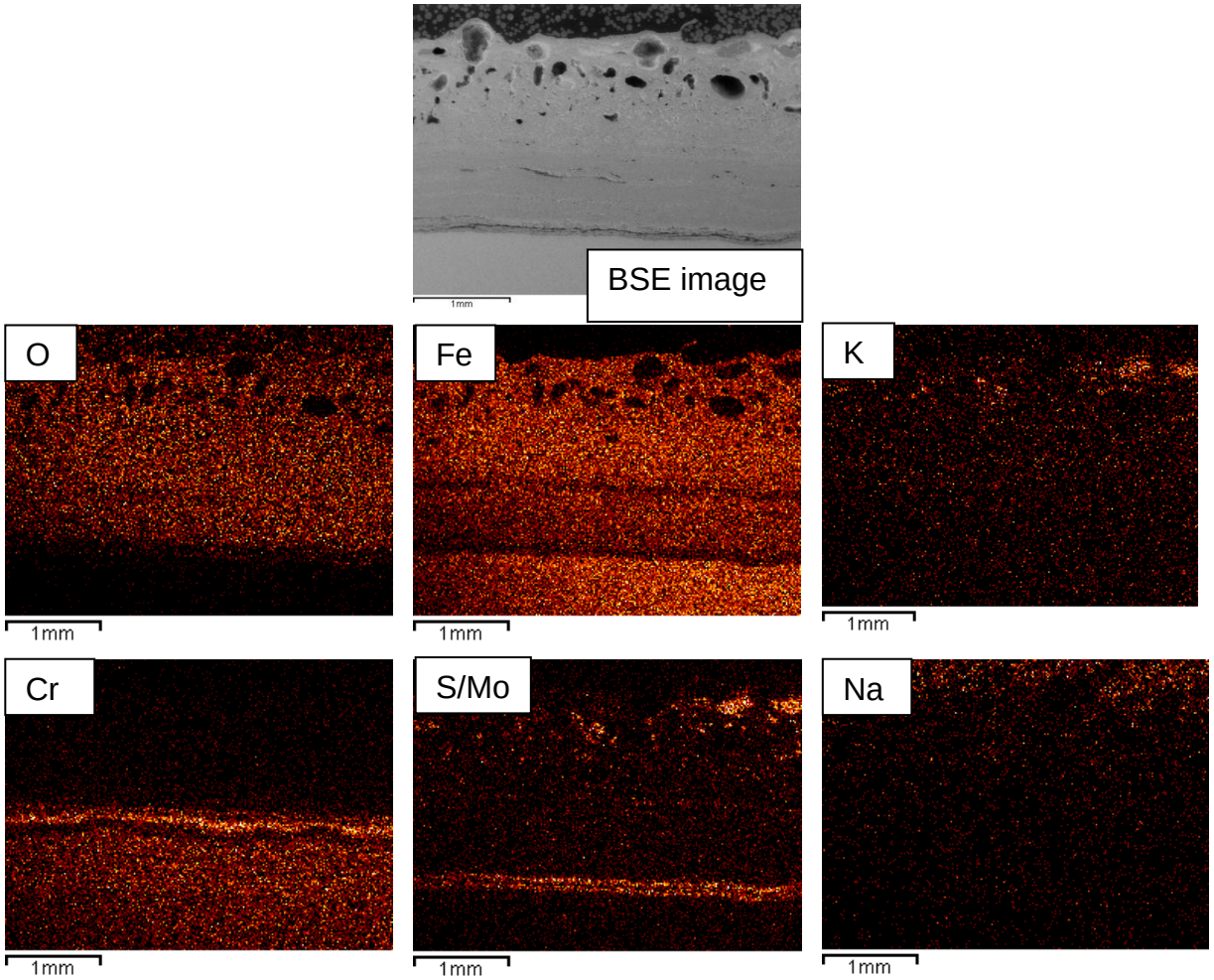

Figure 4-47: BSE image and x-ray maps of alloy T92 covered with deposit D1 exposed to simulated oxy-fired combustion gases (with 6260 vppm SO_2/1700 vppm HCl) at 700°C for 1000 hours

4.3.5 EDX profiles

EDX line profiles were also carried out along with EDX mapping so that quantitative values for elemental distribution through the deposit/scale could be determined.

4.3.5.1 Air-firing tests

Figure 4-48 illustrates a BSE image and EDX profile for a cross-section through an initially bare alloy T92 exposed to simulated air-fired combustion gases (with 1300 vppm SO_2/400 vppm HCl) at 600°C for 1000 hours. The result shows the presence of high chromium level at spectrum 3 combined with a lower iron value. (Data really shows Fe, Cr and O in spinel layer if compared with Fe, O in magnetite/ haematite). Silicon was concentrated at spectrum 4 but then decreased before increasing at spectrum 10 (at scale surface). Sulphur is detected between spectrum 2-5 and at spectrum 9 and 10, with highest value at spectrum 2. Tungsten was also detected between spectrum 1and 6 (alloy and spinel region). Elements such as manganese, molybdenum and vanadium are present in low concentrations (mostly in alloy and spinel). Low levels of chlorine at spectrum 3 (in spinel) and at surface were detected.

Figure 4-49 presents a BSE image and EDX profile through a cross-section of alloy T92 exposed with deposit D1 to simulated air fired combustion gases (with 1300 vppm SO_2/400 vppm HCl) at 650°C for 1000 hours. A gradual depletion of first chromium and then iron levels are observed at points moving away from the base metal. An increasing trend in the concentration of alkali metals and sulphur level is also clear on moving towards the sample surface. Higher concentration of Na than K indicates more Na rich products than K.

Figure 4-50 shows a BSE image and EDX profile through a cross-section of an initially bare alloy HR3C exposed to simulated air fired combustion gases (with 1300 vppm SO_2/400 vppm HCl) at 650°C for 1000 hours. These data show high values of oxygen as expected at spectrums moving away from the alloy (due to the formation of oxides). Trends such as, rapid depletion of iron and nickel from

spectrum 3, whereas after dropping at spectrum 2 the Cr being stable between spectrums 3 to 6 before dropping away are clearly seen. High values of nickel and iron at spectrum 10 indicate nickel and iron oxides. Low concentrations of alkali metals (sodium and potassium) were also detected at spectrums away from base metal (possible contamination during the furnace exposures). High level of sulphur was detected at spectrum 5 indicate internal sulphides.

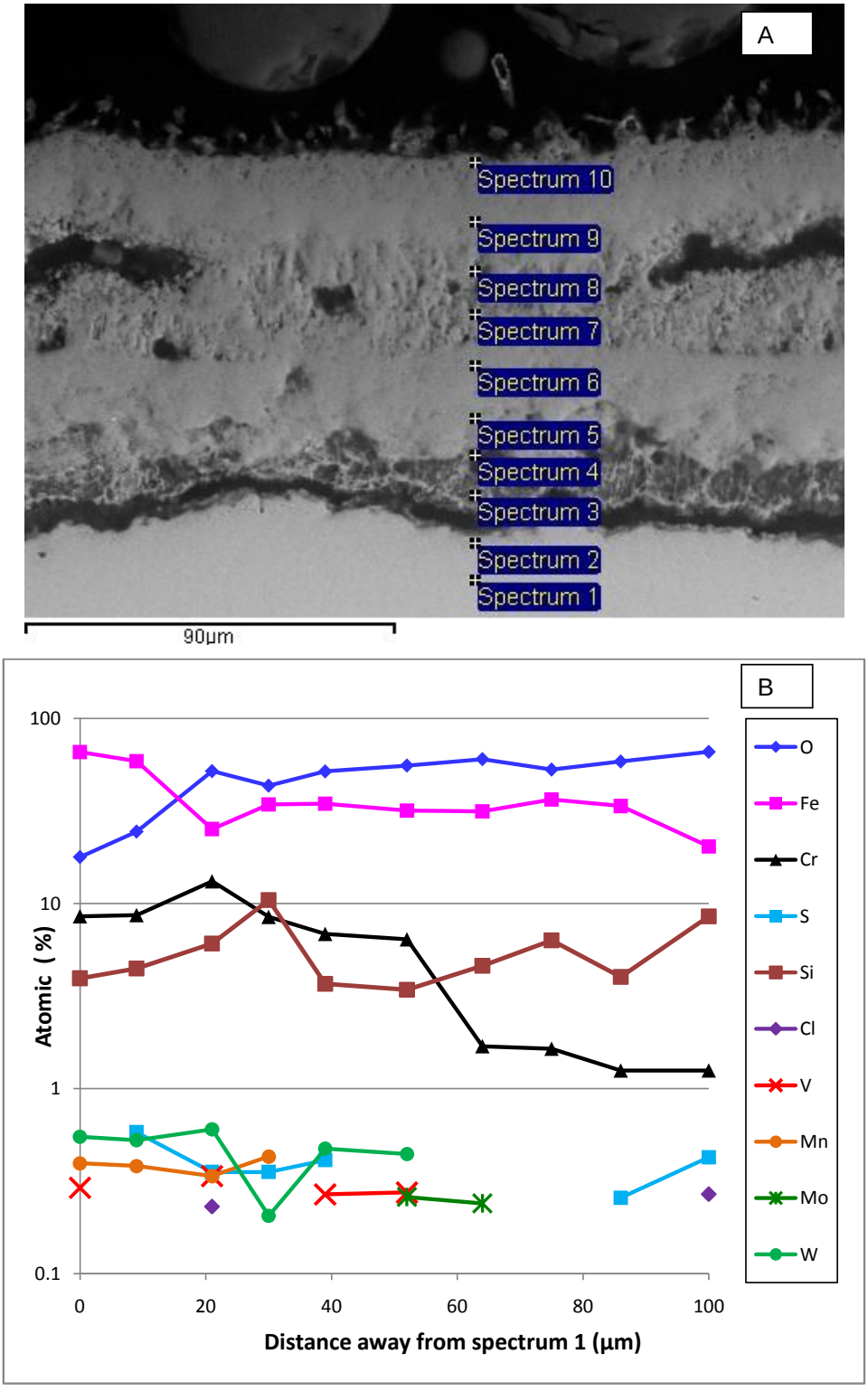

Figure 4-48: (A) BSE image and (B) EDX profile of cross-section through T92 bare alloy exposed to simulated air-fired combustion gases(with 1300vppm SO_2/400vppm HCl) at 600°C for 1000 hours

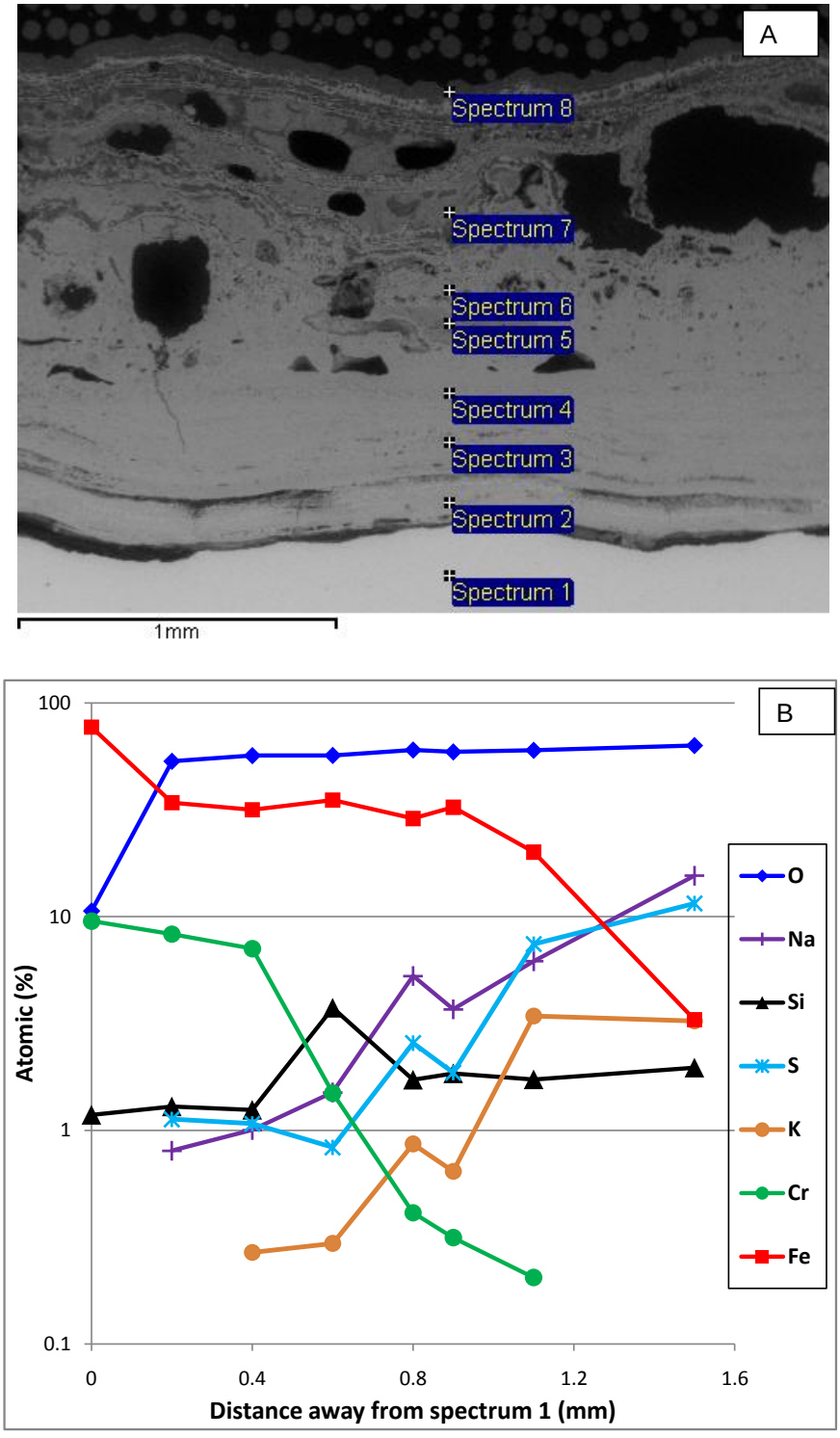

Figure 4-49: (A) BSE image and (B) EDX profile of cross-section through T92 covered in deposit D1 exposed to simulated air-fired combustion gases(with 1300vppm SO_2/400vppm HCl) at 650°C for 1000 hours

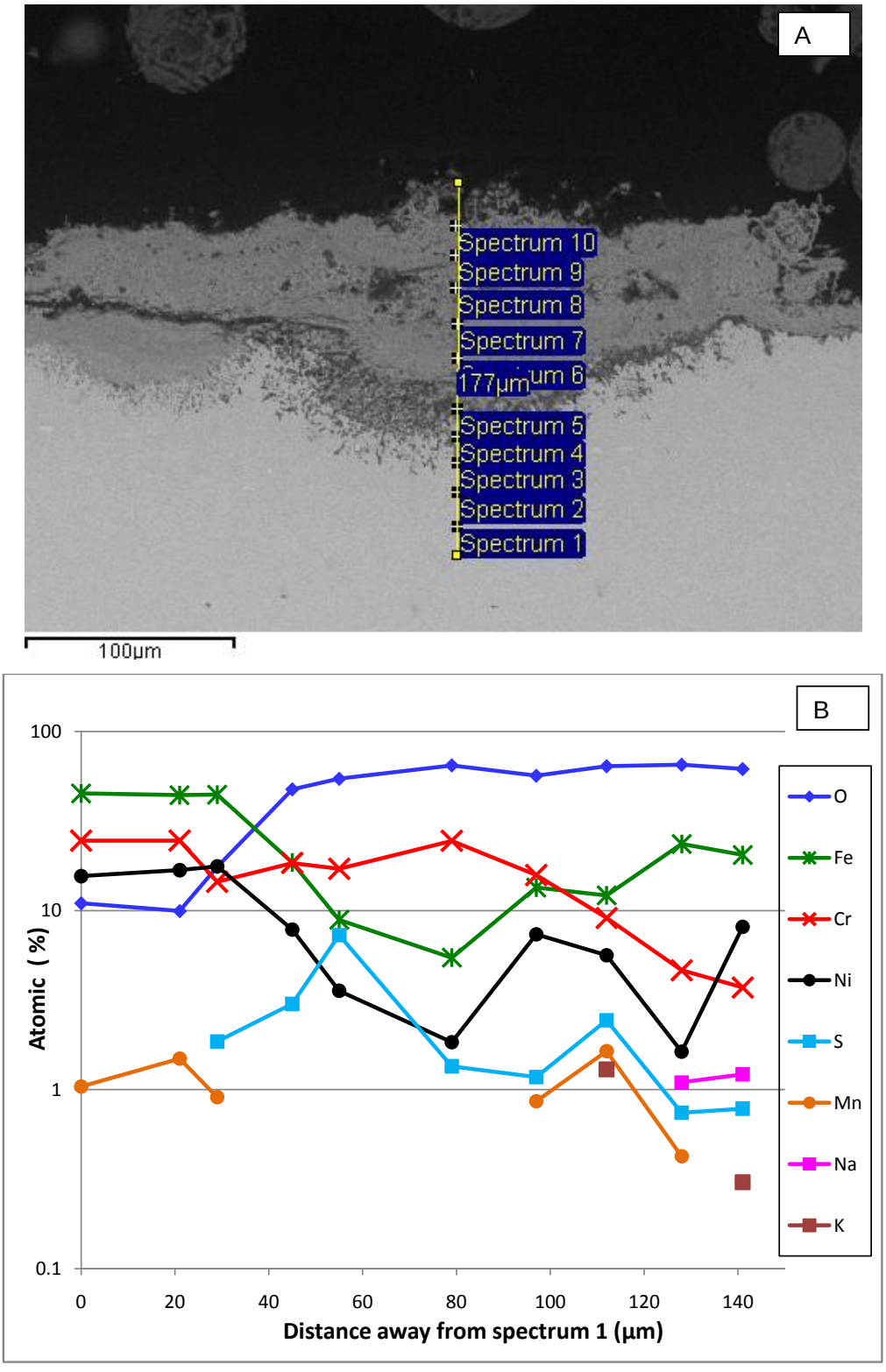

Figure 4-50: (A) BSE image and (B) EDX profile of cross-section through initially bare HR3C alloy exposed to simulated air-fired combustion gases(with 1300vppm SO_2/400vppm HCl) at 650°C for 1000 hours

4.3.5.2 Oxy-firing tests

Figure 4-51 shows a BSE image and EDX profile through a cross-section of an initially bare alloy 347HFG exposed to simulated oxy-fired combustion gases (with 6260 vppm SO_2/1700 vppm HCl) at 650°C for 1000 hours. The result shows the presence of high chromium levels at spectra 4 and 5, whereas iron exhibits its lowest values at the same points. Nickel was concentrated in the alloy at spectrum 3 and then rapidly declined in the scale and become stable at a low level between spectrums 6-8. Sulphur was detected between spectrum 2 and 8, with high levels at spectrum 7 and 8. A high level of S was observed at spectrum 3, indicate sulphur diffusion/penetration through the scale and into the internal damage zone.

Figure 4-52 presents a BSE image and EDX profile for a cross-section through an initially bare alloy T92 exposed to simulated oxy-fired combustion gases (with 6260 vppm SO_2/1700 vppm HCl) at 700°C for 1000 hours. The data shows a rapid increase in oxygen and chromium levels to spectrum 3, where iron depletion indicates formation of Fe-Cr scale. However, from spectrum 3 to 9 iron and oxygen levels stabilised, whereas a rapid decrease in chromium level was observed from spectrum 5 moving away from the base metal. Sulphur exhibit highest value at spectrum 3 and is lowest at the scale surface, indicating a sulphidation mechanism (via diffusion through the scale or initial sulphur attack). Low concentrations of vanadium and manganese were also observed within the base alloy and inner scale.

Figure 4-53 illustrates a BSE image and EDX profile through a cross-section of alloy T92 exposed with deposit D1 to simulated oxy-fired combustion gases (with 6260 vppm SO_2/1700 vppm HCl) at 700°C for 1000 hours. The result shows a depletion trend of chromium between spectrum 1 and 7. The iron value decreased from spectrum 2 to 3 then stabilised. The oxygen level increase up to spectrum 3 then stabilises. Sulphur is concentrated below and at the base of the spinel layer (spectrum 3) as well as the outer part of the deposit/scale (spectrum 10) Tungsten was also detected in spectra 3-5 (in spinel region).

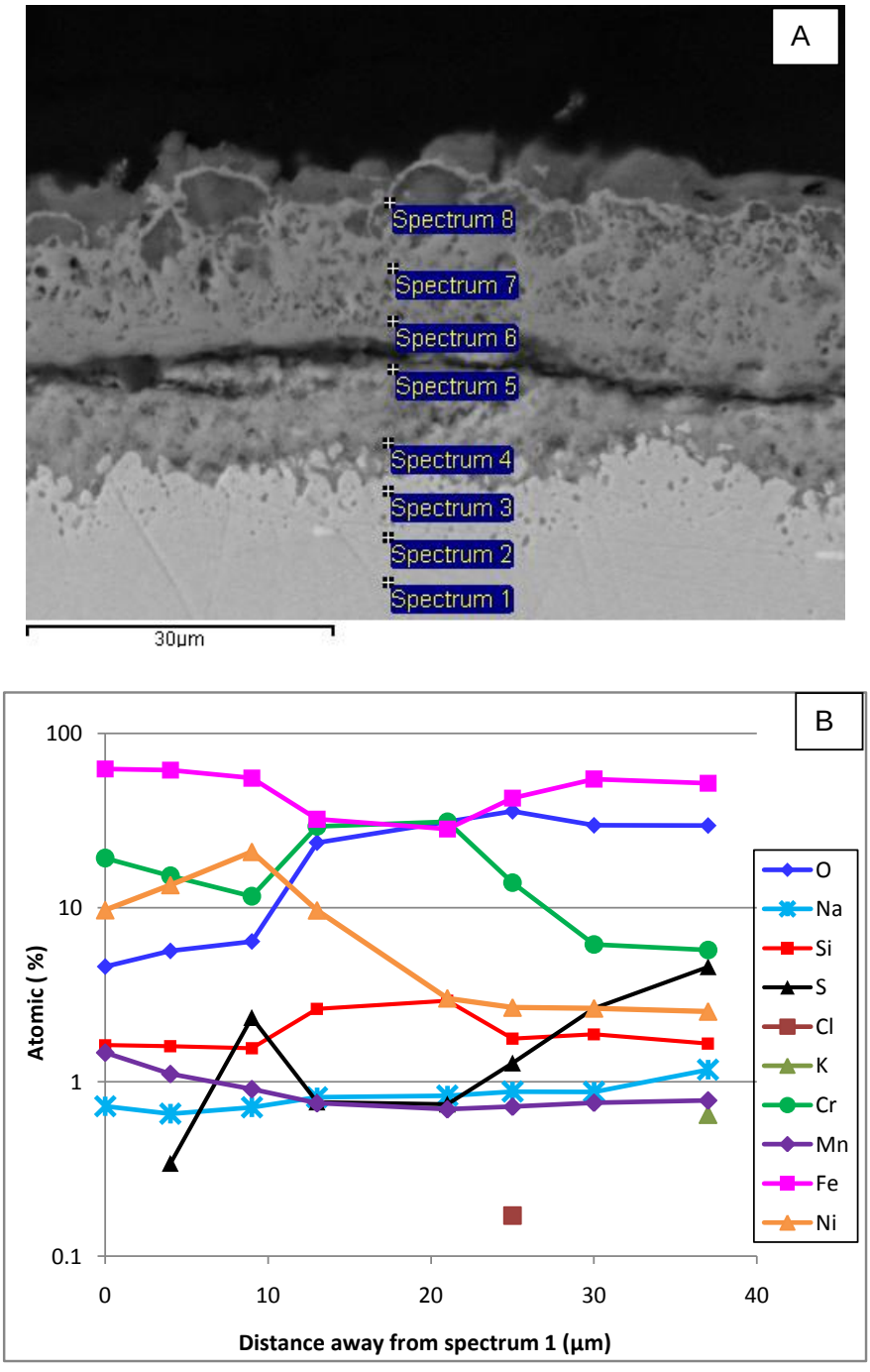

Figure 4-51: (A) BSE image and (B) EDX profile of cross-section through initially bare 347HFG alloy exposed to simulated oxy-fired combustion gases (with 6260 vppm SO_2/1700 vppm HCl) at 650°C for 1000 hours

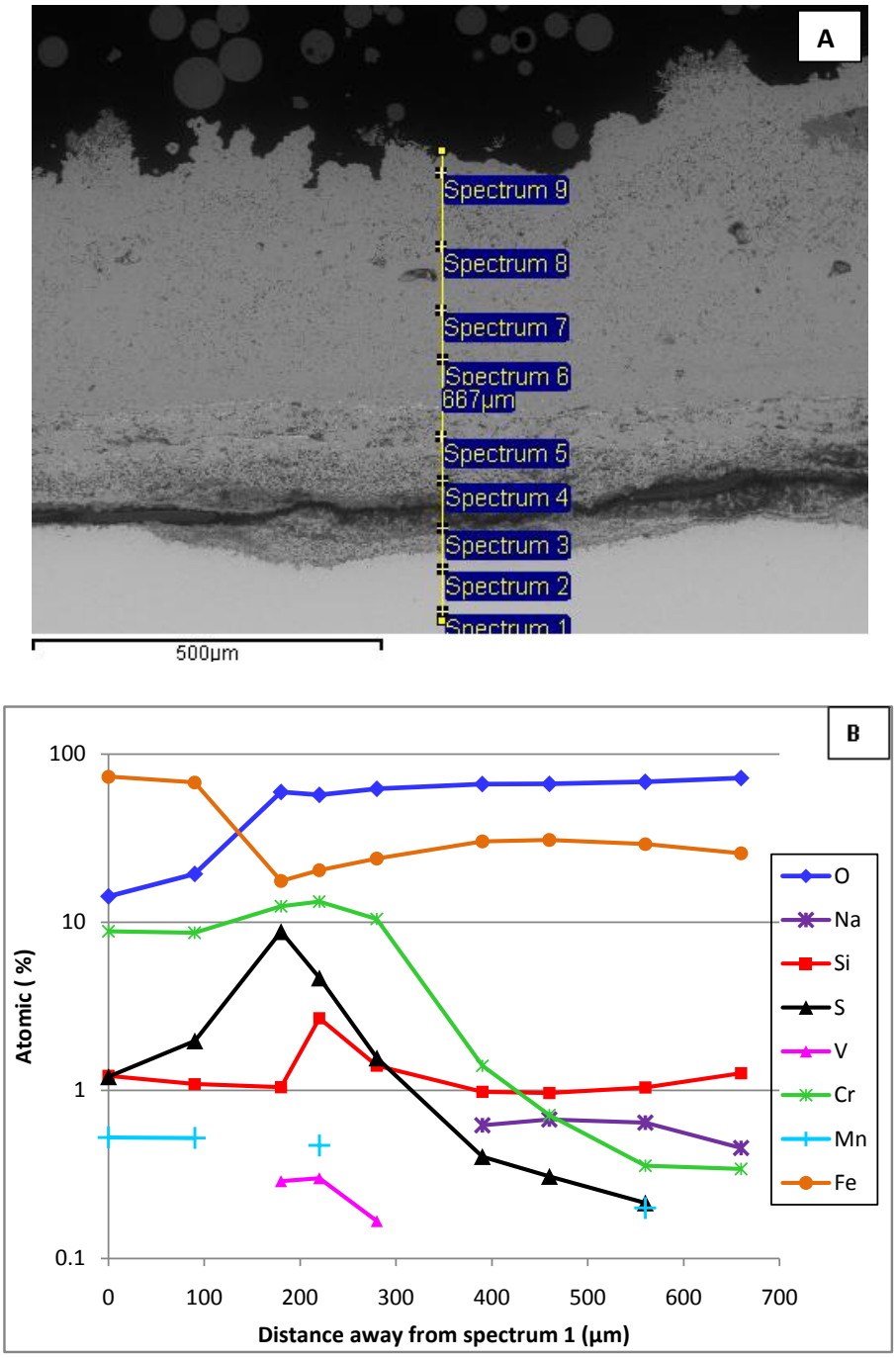

Figure 4-52: (A) BSE image and (B) EDX profile of cross-section through initially bare T92 alloy exposed to simulated oxy-fired combustion gases (with 6260 vppm SO_2/1700 vppm HCl) at 700°C for 1000 hours

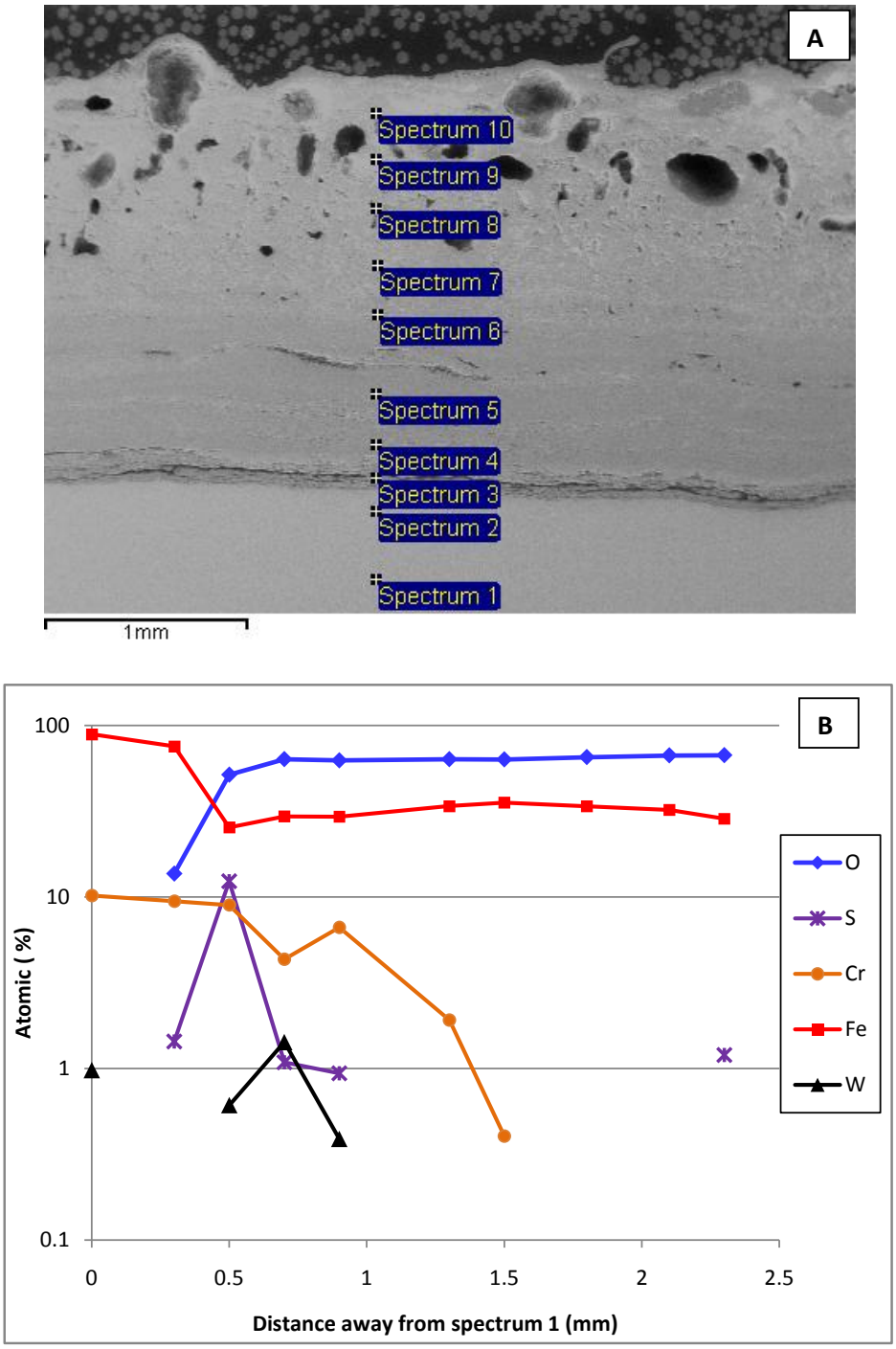

Figure 4-53: (A) BSE image and (B) EDX profile of cross-section through T92 covered in deposit D1 exposed to simulated oxy-fired combustion gases (with 6260 vppm SO_2/1700 vppm HCl) at 700°C for 1000 hours

4.4 Dimensional metrology

4.4.1 Introduction

The polished cross-sections were all measured using an image analyser to generate accurate measurements of the amount of metal remaining after the corrosion tests. These measurements were compared to the pre-exposure metal thickness data to produce distributions of the change in metal resulting from the exposures. These results are plotted as metal damage as a function of cumulative probability; this has been called 'change in metal thickness' for the purpose of this thesis (for ease of interpretation, the parameter metal loss is also used which corresponds to 'change in metal thickness' multiplied by -1) [17]. Details of the technique can be found in experimental method chapter, section 0.

4.4.2 Air-firing tests

4.4.2.1 T22

Figure 4-54 illustrates the damage distribution for alloy T22 initially bare and covered with four different deposits after 1000 hours of exposure in the simulated air-firing combustion gases at 700°C. At 50 % probability alloy T22 covered with the aggressive deposit D1 (high levels of alkali sulphates and iron oxide) shows the highest median metal loss of approx 600 μm, whereas the sample covered with deposit D3 shows the lowest metal loss of approx 100 μm. Other T22 samples with deposits D0, D2 and D4 exhibit median metal loss values between 250-350 μm. The corrosion damage on samples D0, D2 and D4 appeared to be more uniformed compared to D1 and D3.

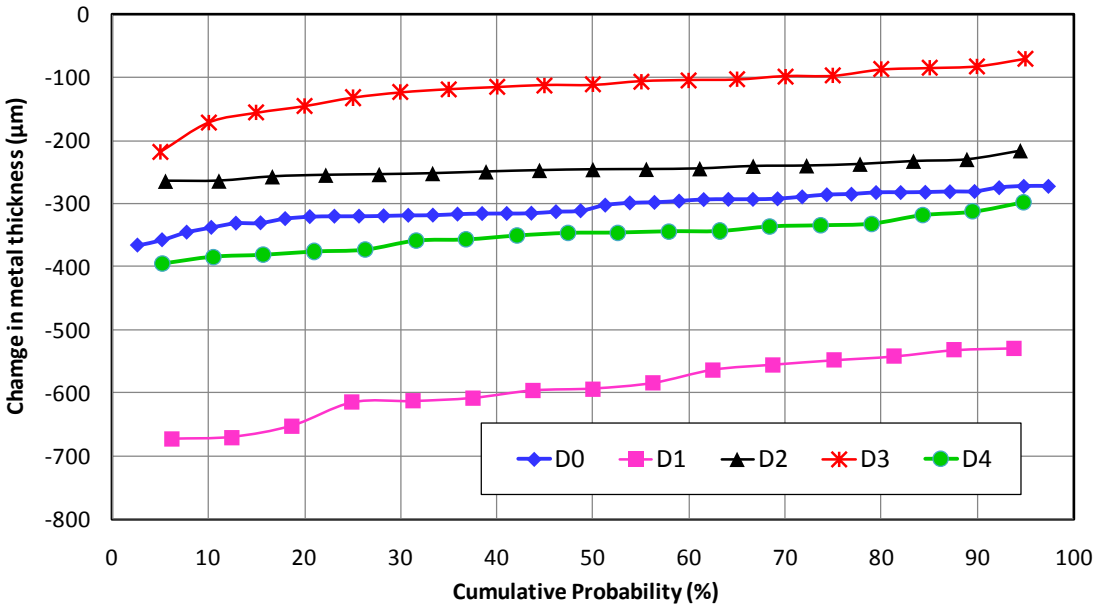

Figure 4-54: Change in metal thickness versus cumulative probability showing the behaviour of alloy T22 covered with various deposits exposed to simulated air-fired combustion gases (with 1300 vppm SO_2/400 vppm HCl) at 700°C for 1000 hours

4.4.2.2 T92

Figure 4-55 to Figure 4-57 illustrate metal loss data for alloy T92 covered with different deposits exposed to simulated air-fired combustion gases (with1300 vppm SO_2/400 vppm HCl) at 600, 650, and 700 °C for 1000 hours. At all three temperatures T92 covered with deposit D1 shows the highest metal losses with ~ 280, 500 and 850 µm of damage, respectively. Thus, the ranking follows the temperature change. Figure 4-55 shows median metal loss values for alloy T92 at 600°C covered with other deposits D2, D3 and D4 are less than 50 µm.

In Figure 4-56 at 650°C almost no median metal loss was observed for D3 sample; however, D0, D2 and D4 samples all showed significant metal loss values. At 700°C (Figure 4-57) the initially bare alloy and alloy covered with other deposits (D2 and D3) show median metal loss values in a range between ~45 to ~85 µm.

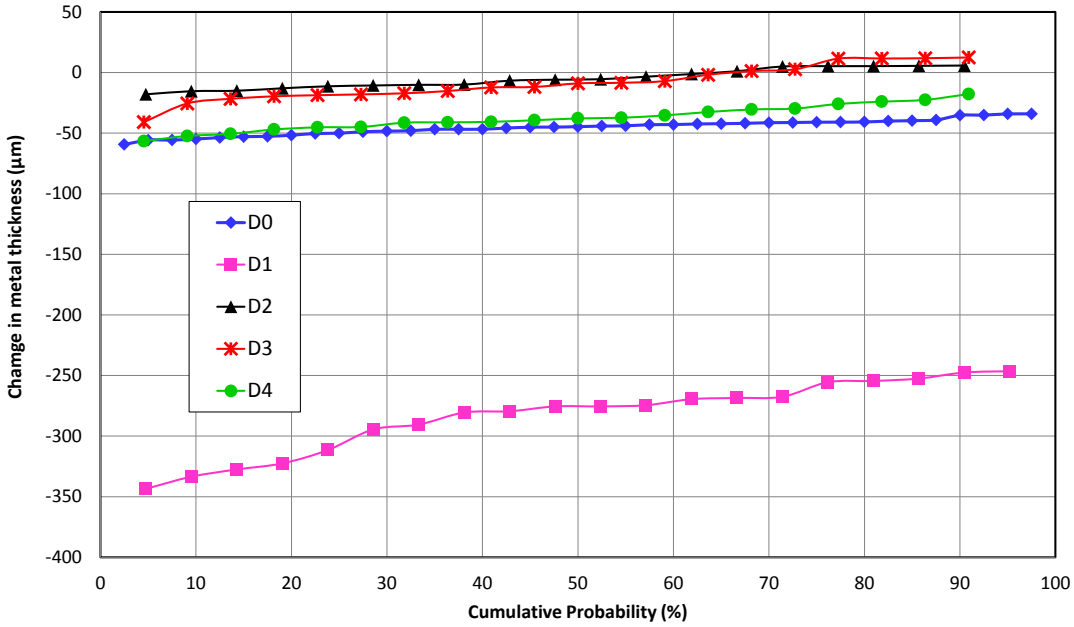

Figure 4-55: Change in metal thickness versus cumulative probability showing the behaviour of alloy T92 covered with various deposits exposed to simulated air-fired combustion gases (with 1300 vppm SO_2/400 vppm HCl) at 600°C for 1000 hours

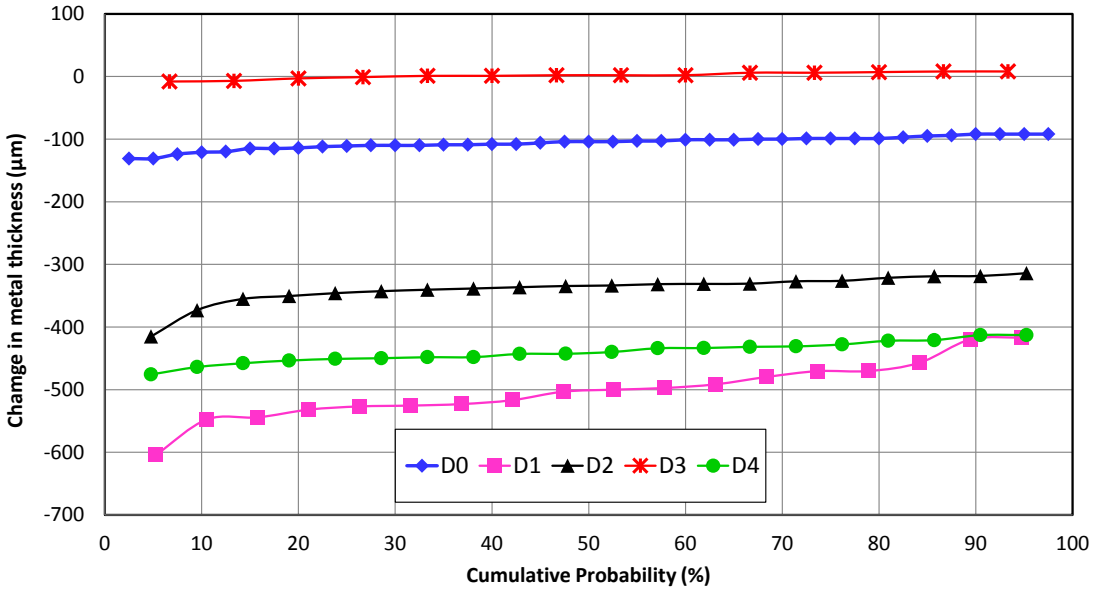

Figure 4-56: Change in metal thickness versus cumulative probability showing the behaviour of alloy T92 covered with various deposits exposed to simulated air-fired combustion gases (with 1300 vppm SO_2/400 vppm HCl) at 650°C for 1000 hours

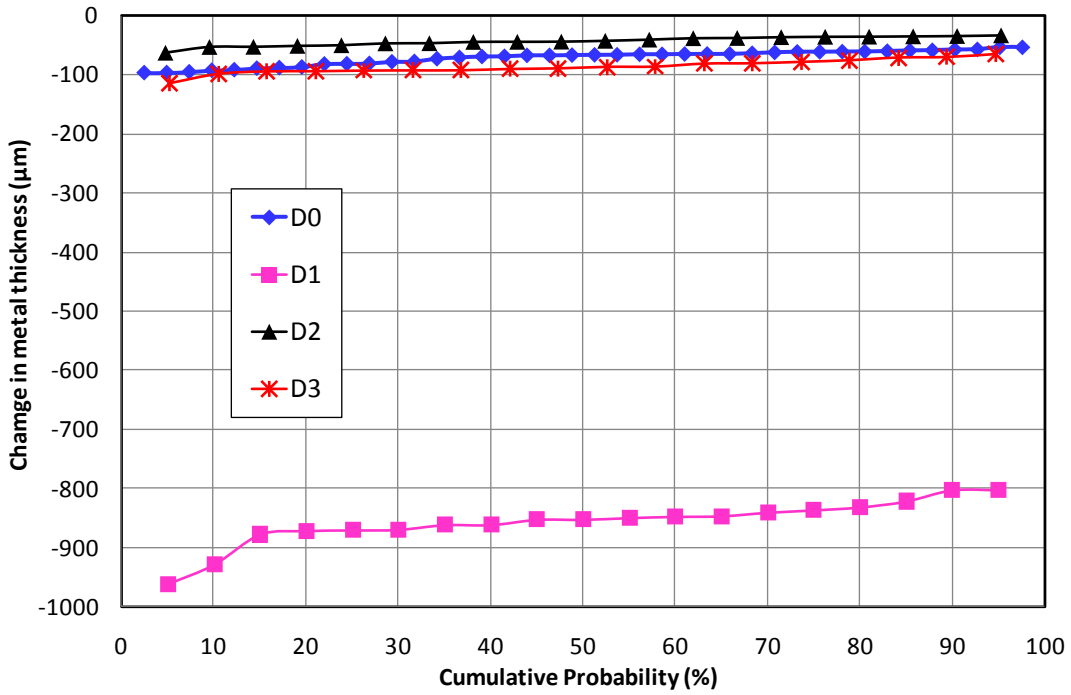

Figure 4-57: Change in metal thickness versus cumulative probability showing the behaviour of alloy T92 covered with various deposits exposed to simulated air-fired combustion gases (with 1300 vppm SO_2/400 vppm HCl) at 700°C for 1000 hours

4.4.2.3 347HFG

Figure 4-58 to Figure 4-60 show metal loss data of austenitic alloy 347HFG in the same gas environment (simulated air-fired combustion gases 1300 vppm SO_2/400 vppm HCl) at three different temperatures (600, 650 and 700°C). As expected, samples covered with deposit D1 showed significant metal loss values at all the three temperatures. In Figure 4-58 the median metal loss value for D1 sample was approx 140 µm. With a 50°C increase in temperature to 650°C (Figure 4-59) the median metal loss value increased almost 4 times to ~500 µm. However, with a further 50°C increase in temperature to 700°C (Figure 4-60) the median metal loss value decreased to approx 470 µm. Initially bare alloy samples of alloy 347HFG, follow the same trend as D1 samples at all three temperature (median metal loss increases with temperature from 600 to 650°C and then decreases with a further 50°C increase from 650 to 700°C). All the samples for alloy 347HFG (except alloy covered with deposit D1) at all three

temperatures exhibit median metal loss values less than 20 μm (within the traditional target range for superheater/reheaters).

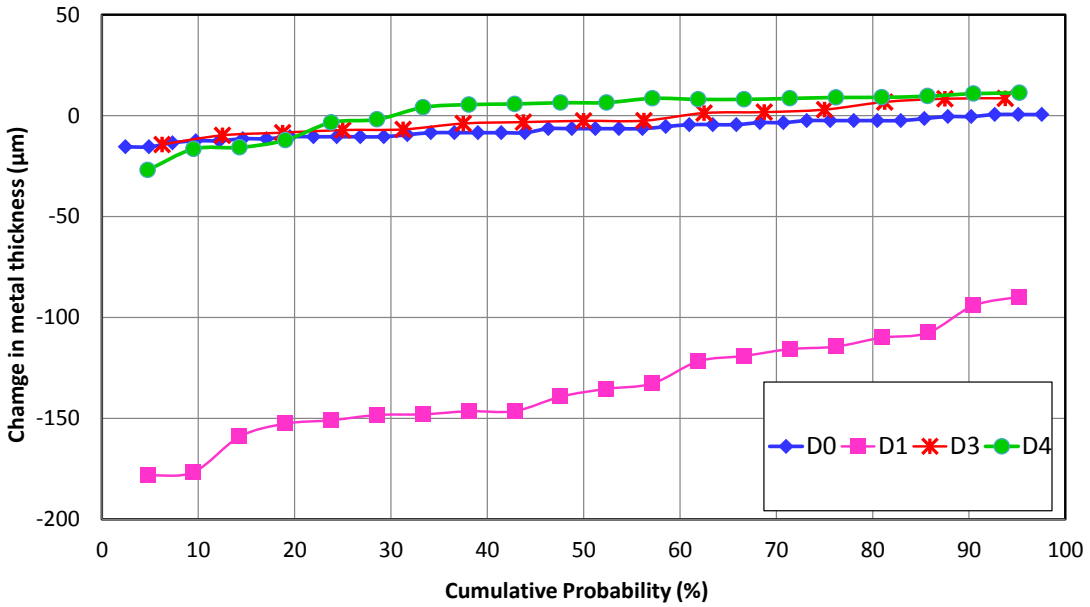

Figure 4-58: Change in metal thickness versus cumulative probability showing the behaviour of alloy 347HFG covered with various deposits exposed to simulated air-fired combustion gases (with 1300 vppm SO_2/400 vppm HCl) at 600°C for 1000 hours

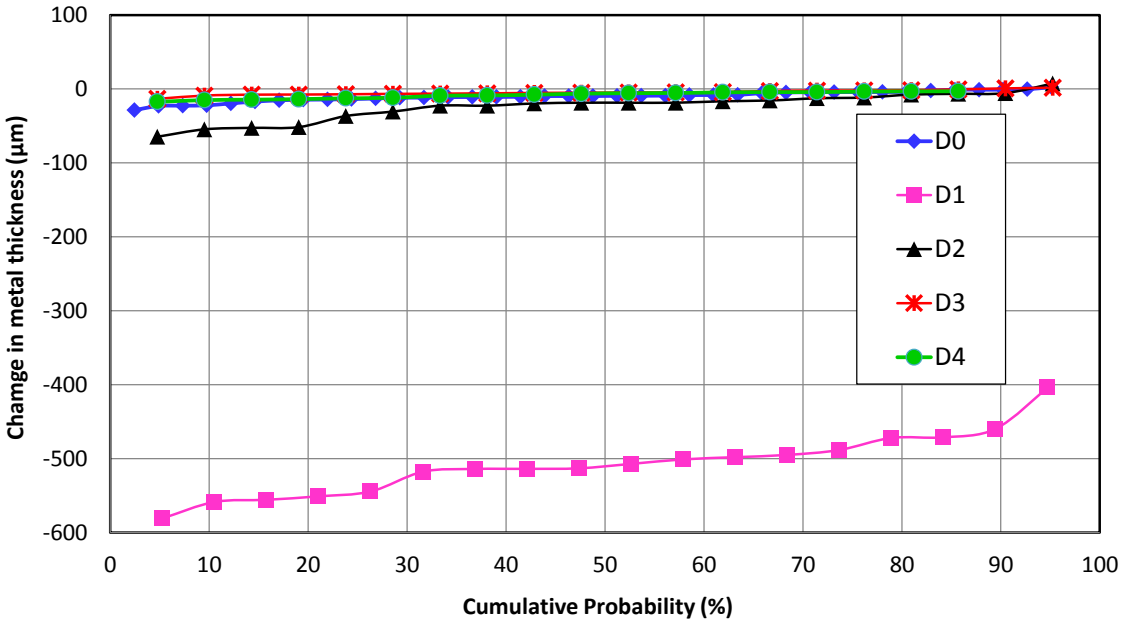

Figure 4-59: Change in metal thickness versus cumulative probability showing the behaviour of alloy 347HFG covered with various deposits exposed to simulated air-fired combustion gases (with 1300 vppm SO_2/400 vppm HCl) at 650°C for 1000 hours

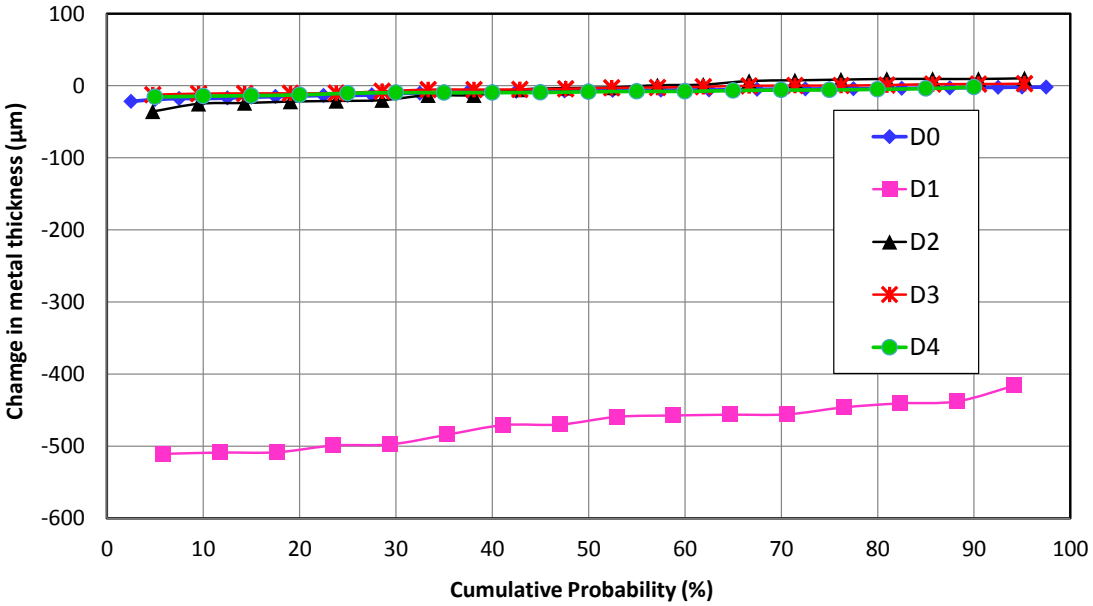

Figure 4-60: Change in metal thickness versus cumulative probability showing the behaviour of alloy 347HFG covered with various deposits exposed to simulated air-fired combustion gases (with 1300 vppm SO_2/400 vppm HCl) at 700°C for 1000 hours

4.4.2.4 HR3C

Figure 4-61 to Figure 4-63 illustrates the metal loss data of stainless steel HR3C covered with different deposits exposed to simulated air-fired combustion gases (with 1300 vppm SO_2/400 vppm HCl) for 1000 hours at 600, 650 and 700°C respectively. As expected, samples covered with deposit D1 showed the highest metal loss values at all the temperatures. In Figure 4-63, D1 sample revealed a rapid increase in the metal loss at lower probability indicates a case of localised corrosion. Comparing Figure 4-61and Figure 4-62 the median metal loss for D1 samples increased almost 10 times (from 50 to 500 µm) with the 50°C increase in exposure temperature. However Figure 4-63 revealed that with further 50-degree increase in temperature at 700°C median metal loss values for D1 sample decreased to ~ 150 µm. Such a temperature effect on the performance of alloy HR3C is also in line with mass change data (as seen in section 4.2.2.4.).

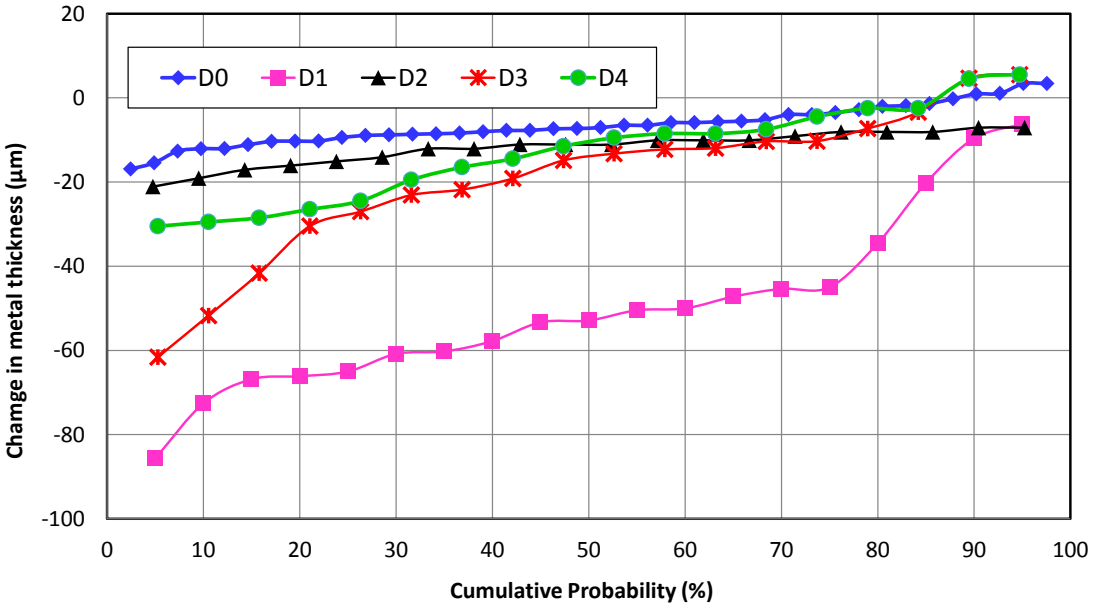

Figure 4-61: Change in metal thickness versus cumulative probability showing the behaviour of alloy HR3C covered with various deposits exposed to simulated air-fired combustion gases (with 1300 vppm SO_2/400 vppm HCl) at 600°C for 1000 hours

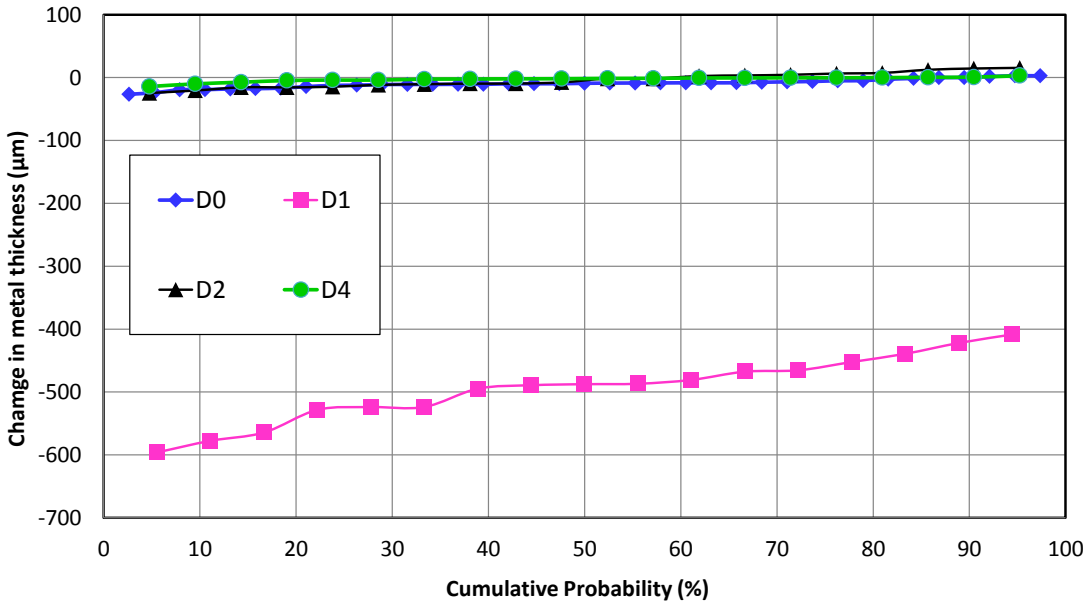

Figure 4-62: Change in metal thickness versus cumulative probability showing the behaviour of alloy HR3C covered with various deposits exposed to simulated air-fired combustion gases (with 1300 vppm SO_2/400 vppm HCl) at 650°C for 1000 hours

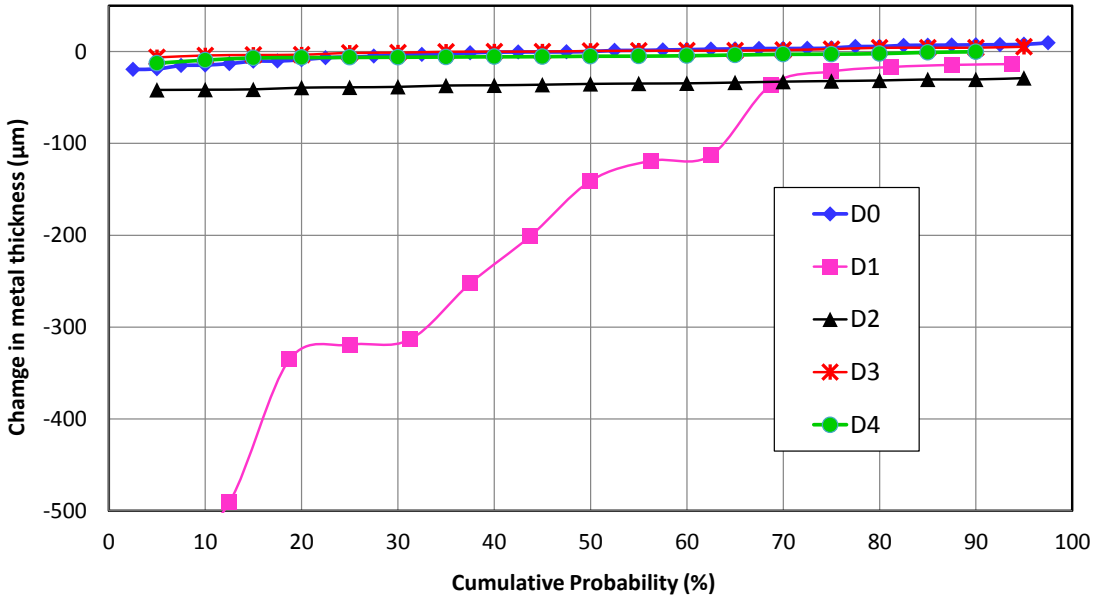

Figure 4-63: Change in metal thickness versus cumulative probability showing the behaviour of alloy HR3C covered with various deposits exposed to simulated air-fired combustion gases (with 1300 vppm SO_2/400 vppm HCl) at 700°C for 1000 hours

Alloy HR3C (D0 and D1) samples show the same effect with the increase in temperature as observed for 347HFG (D0 and D1) samples; i.e. the samples experienced higher corrosion damage at 650°C compared to 600 and 700°C. Alloy HR3C covered with other deposits (D2, D3 and D4) was the least affected material, showing the minimum metal loss in all three cases.

4.4.2.5 Alloy 625

Figure 4-64 to Figure 4-66 illustrate the metal loss data for nickel-based alloy 625 covered with different deposits in the simulated air-fired combustion gases and at different temperatures. As expected, alloy 625 covered with deposit D1 showed the highest metal loss values. In Figure 4-64 (at 600°C) the median metal loss value for the sample covered with deposit D1 was approximately 35 µm. With the increase in temperature to 650 and 700°C, the median metal loss values were also increased to ~ 250 and ~270 µm, respectively. Such behaviour of alloy 625 covered with deposit D1 is in contrast to austenitic alloys 347HFG and HR3C D1 covered samples, where with 50°C increase in temperature from 650 to 700°C caused a decrease in the median metal loss values (instead of an increase).

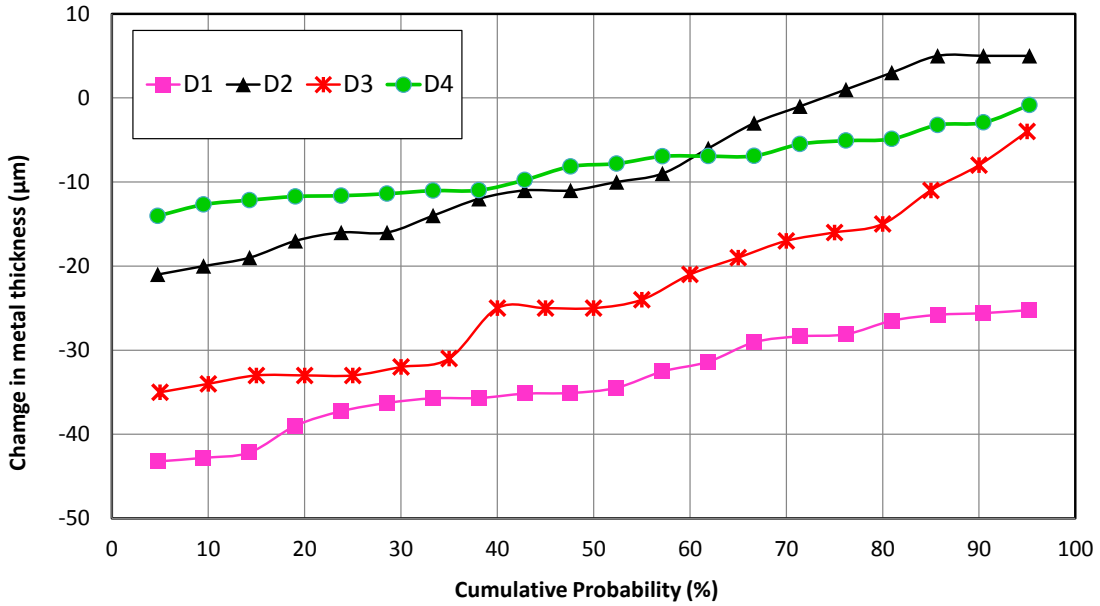

Figure 4-64: Change in metal thickness versus cumulative probability showing the behaviour of alloy 625 covered with various deposits exposed to simulated air-fired combustion gases (with 1300 vppm SO_2/400 vppm HCl) at 600°C for 1000 hours

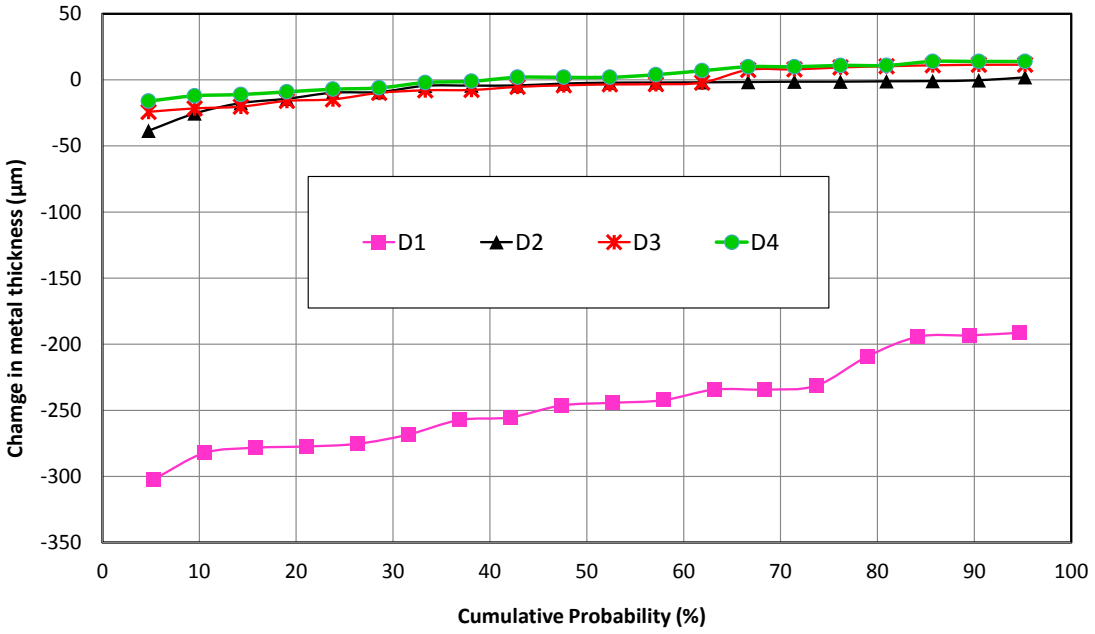

Figure 4-65: Change in metal thickness versus cumulative probability showing the behaviour of alloy 625 covered with various deposits exposed to simulated air-fired combustion gases (with 1300 vppm SO_2/400 vppm HCl) at 650°C for 1000 hours

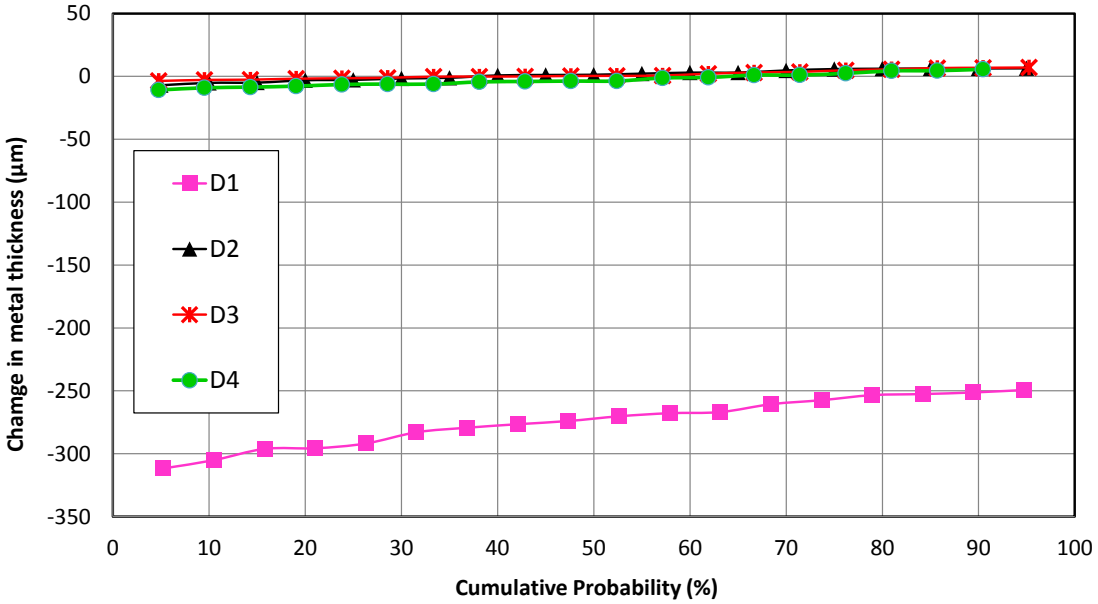

Figure 4-66: Change in metal thickness versus cumulative probability showing the behaviour of alloy 625 covered with various deposits exposed to simulated air-fired combustion gases (with 1300 vppm SO_2/400 vppm HCl) at 700°C for 1000 hours

In Figure 4-65 and Figure 4-66 alloy 625 covered with other deposit (D2, D3 and D4) did not show any significant affect; with minimal metal loss values being observed in both cases (650 and 700°C). However, at 600°C (Figure 4-64) the results showed approx 10 µm median metal loss values for alloy 625 samples covered with deposit D2 and D4.

4.4.3 Oxy-firing tests

4.4.3.1 T22

Figure 4-67 and Figure 4-68 illustrate metal loss data for ferritic alloy T22 exposed to simulated oxy-fired combustion gases (with 6260 vppm SO_2/1700 vppm HCl) for 1000 hours at 700 and 750°C respectively. In both cases all samples exhibit significant metal loss values. The performance of low chromium T22 at both temperatures suggests a severe attack of gas and deposits resulted in high corrosion damage. In Figure 4-67 at 50% probability the highest metal loss value observed was approximately 700 µm (for initially bare sample and sample covered with deposit D1). In Figure 4-68 at 750°C the highest median metal loss value observed was > 1000 µm for sample covered with deposit D4.

Another noticeable feature observed in both cases is that the corrosive effect of the aggressive deposit D1 on T22 at these temperatures is not significantly different to other deposits (D2, D3 and D4) and bare samples (D0). That is in contrast to the previous data that showed the more aggressive nature of deposit D1. The mass change data shown in Figure 4-14 and Figure 4-15 also showed this behaviour for alloy T22, with different deposits showing similar mass gains to deposit D1. The median metal loss values of each T22 sample in Figure 4-67 (oxy-firing gases) are much higher than the metal loss values of similar T22 samples in Figure 4-54 (air-fired simulation) at the same temperature.

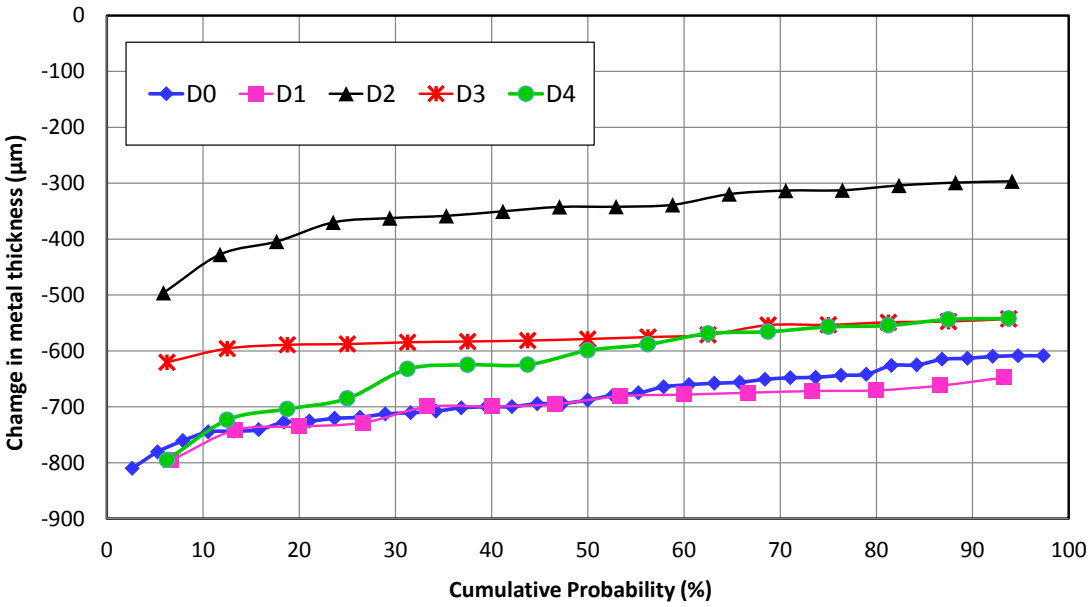

Figure 4-67: Change in metal thickness versus cumulative probability showing the behaviour of alloy T22 covered with various deposits exposed to simulated oxy-fired combustion gases (with 6260 vppm SO_2/1700 vppm HCl) at 700°C for 1000 h

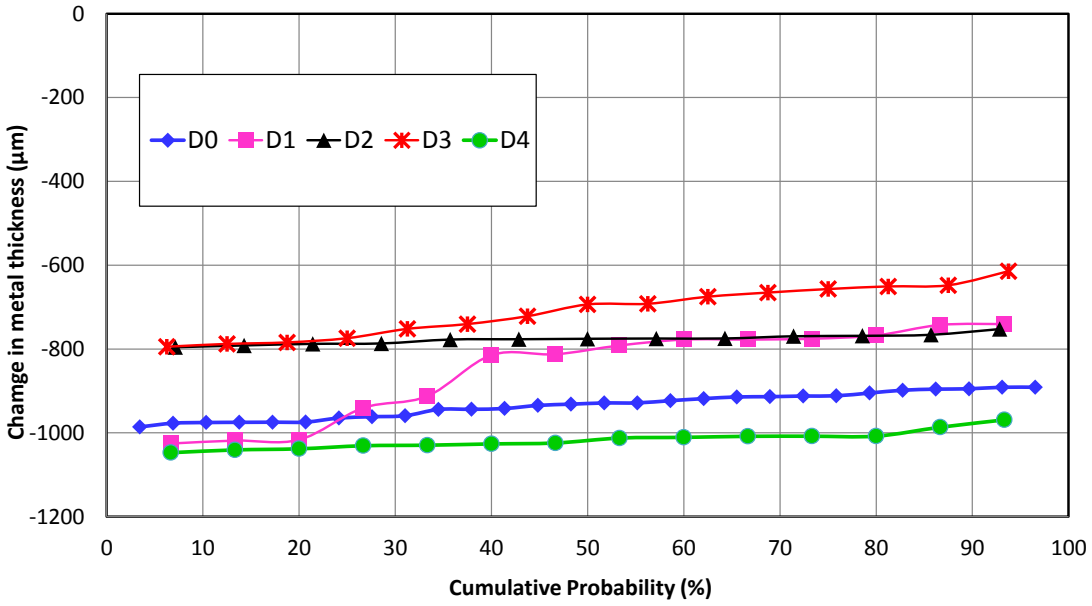

Figure 4-68: Change in metal thickness versus cumulative probability showing the behaviour of alloy T22 covered with various deposits exposed to simulated oxy-fired combustion gases (with 6260 vppm SO_2/1700 vppm HCl) at 750°C for 1000 h

4.4.3.2 T92

Data for T92 samples covered with different deposits exposed to simulated oxy-fired combustion gases (with 6260 vppm SO_2/1700 vppm HCl) for 1000 hours are given at 600°C (Figure 4-69), 650°C (Figure 4-70), 700°C (Figure 4-71), and 750°C (Figure 4-72). In Figure 4-69 an unusual behaviour was observed, with the sample covered with deposit D2 showing a high metal loss value than the sample covered with aggressive deposit D1. However, at other temperatures (650, 700 and 750°C) as expected the metal loss data for samples covered with deposit D1 was higher than their comparative T92 samples with other deposits.

Samples covered with deposit D1 showed an increasing trend with the increase in temperature up to 700°C where a rapid increase in metal loss was observed. However, at 750°C the median metal loss value for the D1covered T92 sample was lower than at 700°C. The median metal loss values for sample T92 covered with deposit D1 with a 50°C increase in temperature were found to be ~107, ~375, ~1130 and ~970 µm at 600, 650, 700 and 750°C respectively. The results also revealed that at 650, 700 and 750°C samples covered with other deposits

(D0, D2, D3 and D4) exhibited median metal loss values under or approximately 200 µm, whereas at 600°C samples with all the deposits showed median metal losses < 200 µm. It is also clear that only at 600°C did samples with deposit D4 and D3 show median metals loss values below 50 µm/1000 hours (acceptable range), whereas all the other deposits at different temperature caused corrosion damage above the acceptable range.

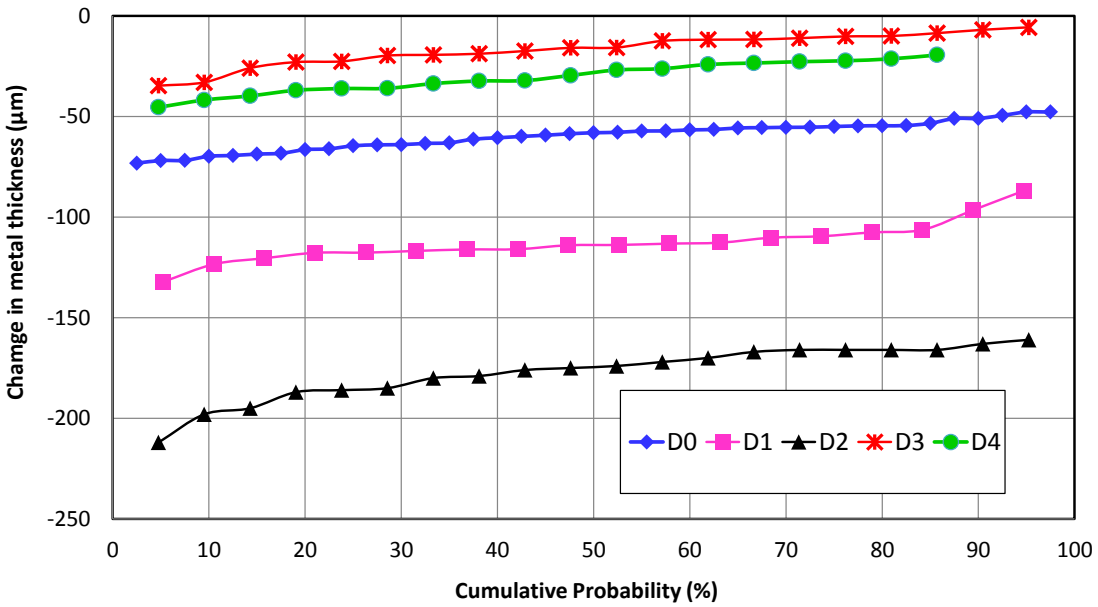

Figure 4-69: Change in metal thickness versus cumulative probability showing the behaviour of alloy T92 covered with various deposits exposed to simulated oxy-fired combustion gases (with 6260 vppm SO_2/1700 vppm HCl) at 600°C for 1000 h

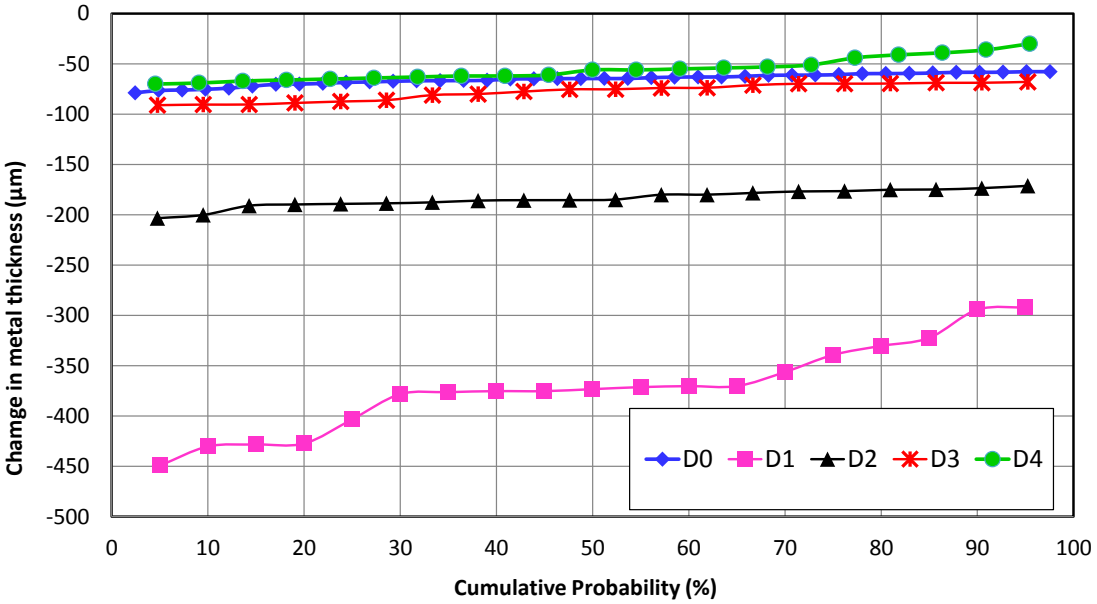

Figure 4-70: Change in metal thickness versus cumulative probability showing the behaviour of alloy T92 covered with various deposits exposed to simulated oxy-fired combustion gases (with 6260 vppm SO_2/1700 vppm HCl) at 650°C for 1000 h

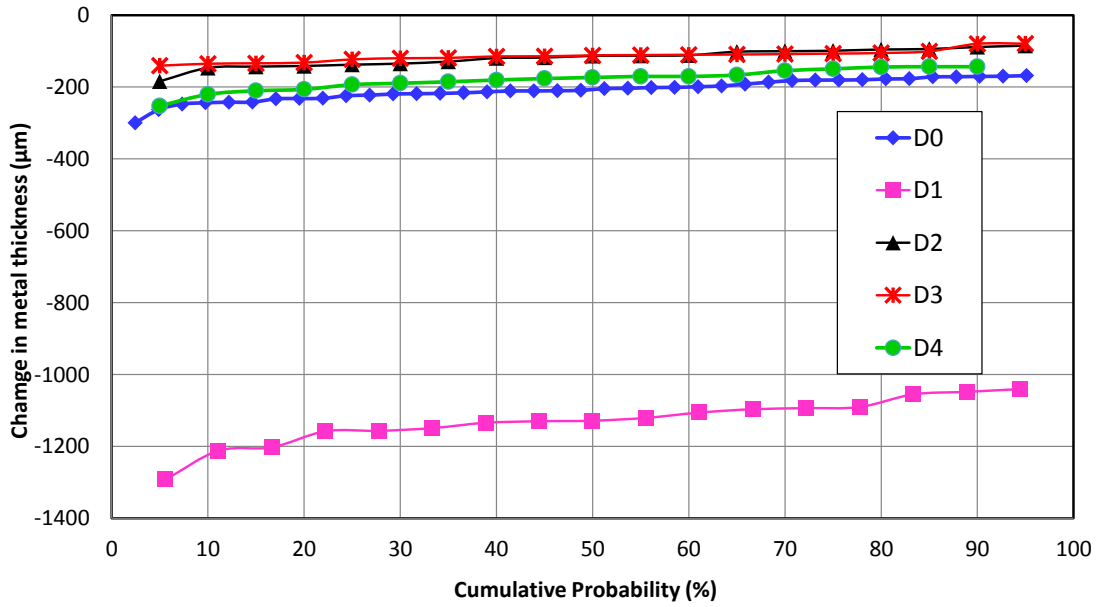

Figure 4-71: Change in metal thickness versus cumulative probability showing the behaviour of alloy T92 covered with various deposits exposed to simulated oxy-fired combustion gases (with 6260 vppm SO_2/1700 vppm HCl) at 700°C for 1000 h

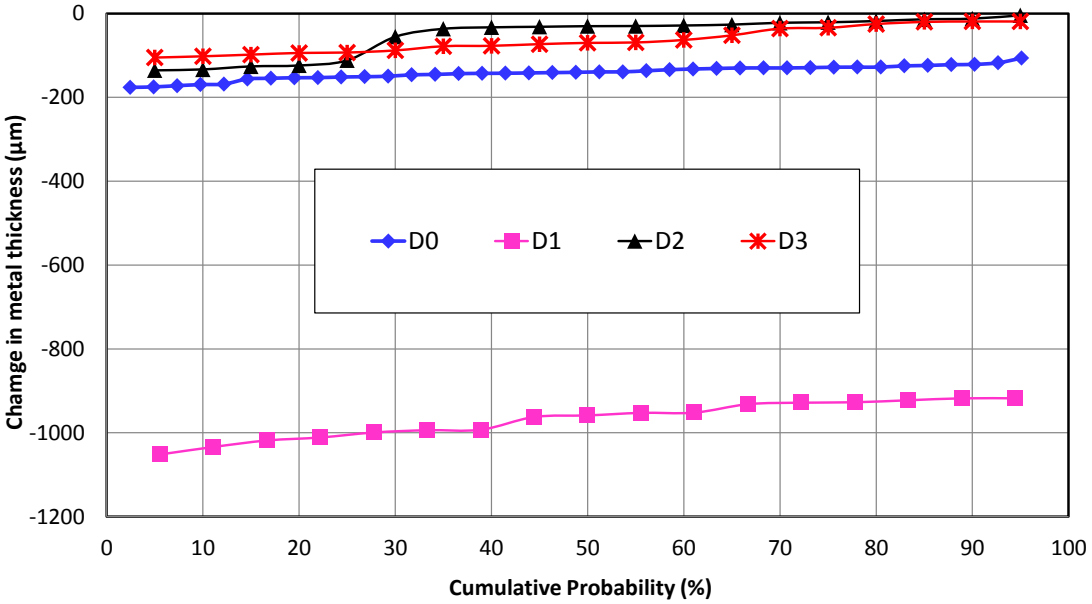

Figure 4-72: Change in metal thickness versus cumulative probability showing the behaviour of alloy T92 covered with various deposits exposed to simulated oxy-fired combustion gases (with 6260 vppm SO_2/1700 vppm HCl) at 750°C for 1000 h

4.4.3.3 347HFG

Figure 4-73 to Figure 4-76 illustrate the change in metal thickness data for alloy 347HFG at different temperatures. These results show that samples covered with deposit D1 exhibited significantly higher metal loss values. Like T92 the highest median metal loss value was also observed at 700°C (Figure 4-75); with the metal loss value being similar to T92 alloy, i.e. ~1130 µm. The median metal loss values at 600, 650 and 750 °C were found to be ~160, ~350 and ~664 µm respectively.

Initially bare 347HFG samples also followed the same trend as D1 samples; i.e. increase in metal loss values with the increase in temperature, up to 700°C and then decrease in values with a further increase in temperature to 750°C. The mass change data for alloy 347HFG (section 4.2.3.3) is also in line with these metal loss data (i.e. increasing mass gain values with the increase in temperature up to 700°C and then drop to 750°C). Figure 4-73 and Figure 4-74 show that in both cases (600 and 650°C) the 347HFG covered with other deposits (D0, D2, D3 and D4) exhibit median metal loss values less than 50 µm, whereas at 750°C (Figure 4-76) metal loss values observed were < 100 µm.

However, at 700°C (Figure 4-75) 347HFG samples covered with other deposits also showed significant metal loss values; in the range of ~200-250 µm.

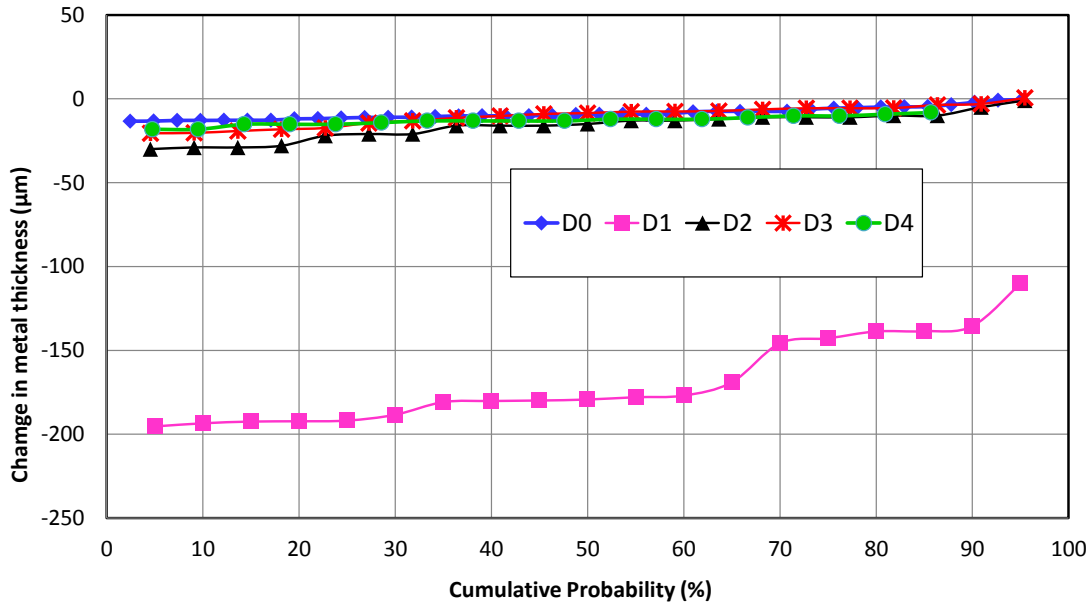

Figure 4-73: Change in metal thickness versus cumulative probability showing the behaviour of alloy 347HFG covered with various deposits exposed to simulated oxy-fired combustion gases (with 6260 vppm SO_2/1700 vppm HCl) at 600°C for 1000 h

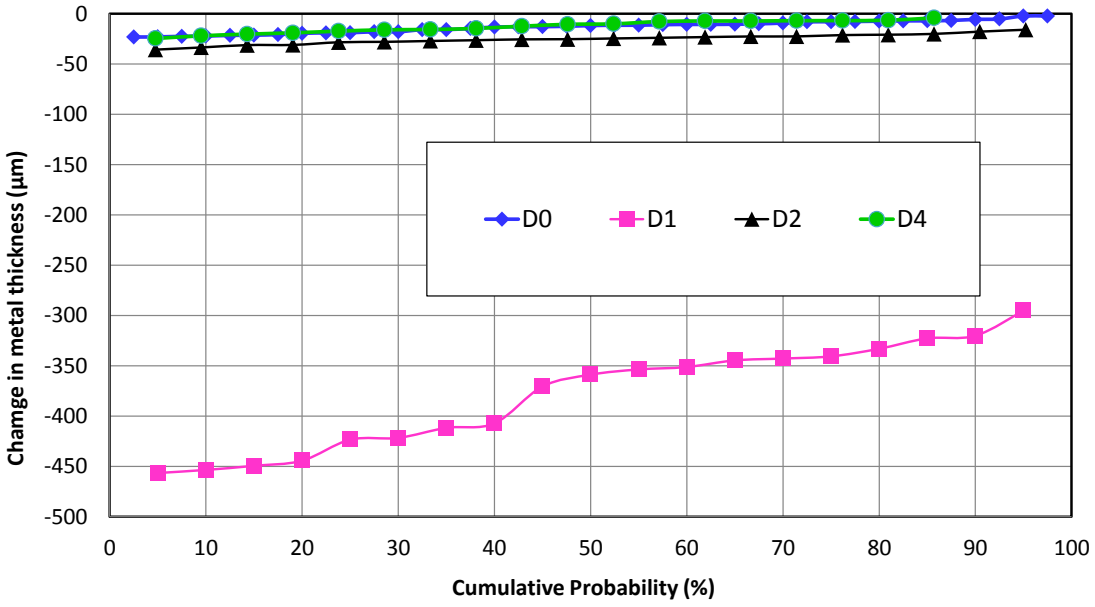

Figure 4-74: Change in metal thickness versus cumulative probability showing the behaviour of alloy 347HFG covered with various deposits exposed to simulated oxy-fired combustion gases (with 6260 vppm SO_2/1700 vppm HCl) at 650°C for 1000 h

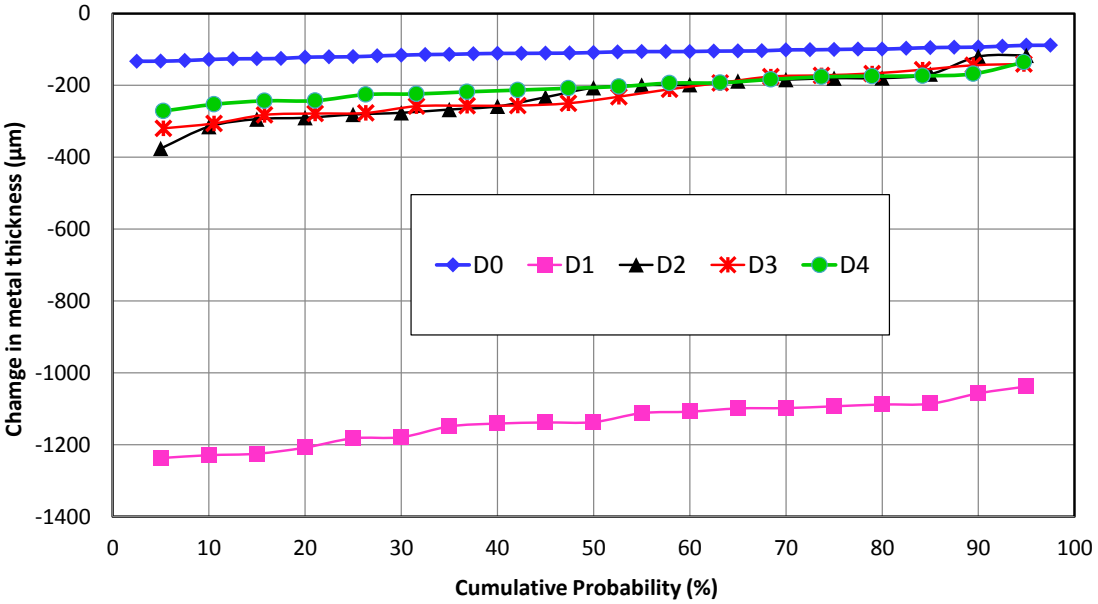

Figure 4-75: Change in metal thickness versus cumulative probability showing the behaviour of alloy 347HFG covered with various deposits exposed to simulated oxy-fired combustion gases (with 6260 vppm SO_2/1700 vppm HCl)at 700°C for 1000 h

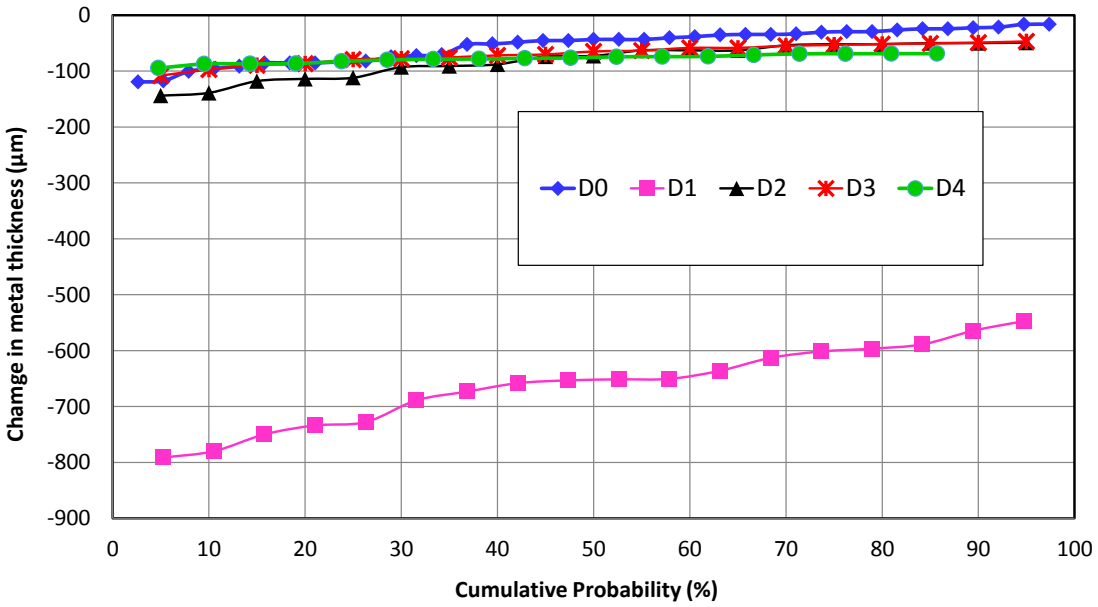

Figure 4-76: Change in metal thickness versus cumulative probability showing the behaviour of alloy 347HFG covered with various deposits exposed to simulated oxy-fired combustion gases (with 6260 vppm SO_2/1700 vppm HCl) at 750°C for 1000 h

4.4.3.4 HR3C

The results in Figure 4-77 to Figure 4-80 show the changes in metal thicknesses as functions of cumulative probability for the austenitic alloy HR3C in the same gas environment (simulated oxy-fired combustion gas) and at four different temperatures (600, 650, 700 and 750°C). As expected samples HR3C covered with (aggressive) deposit D1 show the highest corrosion damage at each temperature. The median metal loss was found to be highest at 700°C which is in line with alloy T92 and 347HFG. The mass change data for alloy HR3C D1 coated samples also exhibited their highest values at 700°C (section 4.2.3.4.).

Figure 4-79 shows that a HR3C sample covered with deposit D1 experienced median metal loss value of ~ 540 µm at 700°C. Another interesting feature observed for HR3C D1 samples is a sharp decrease in the change in metal thickness values at lower probabilities values (such behaviour was also observed for this alloy/deposit composition in air-firing conditions), suggesting localised attack on the sample surface.

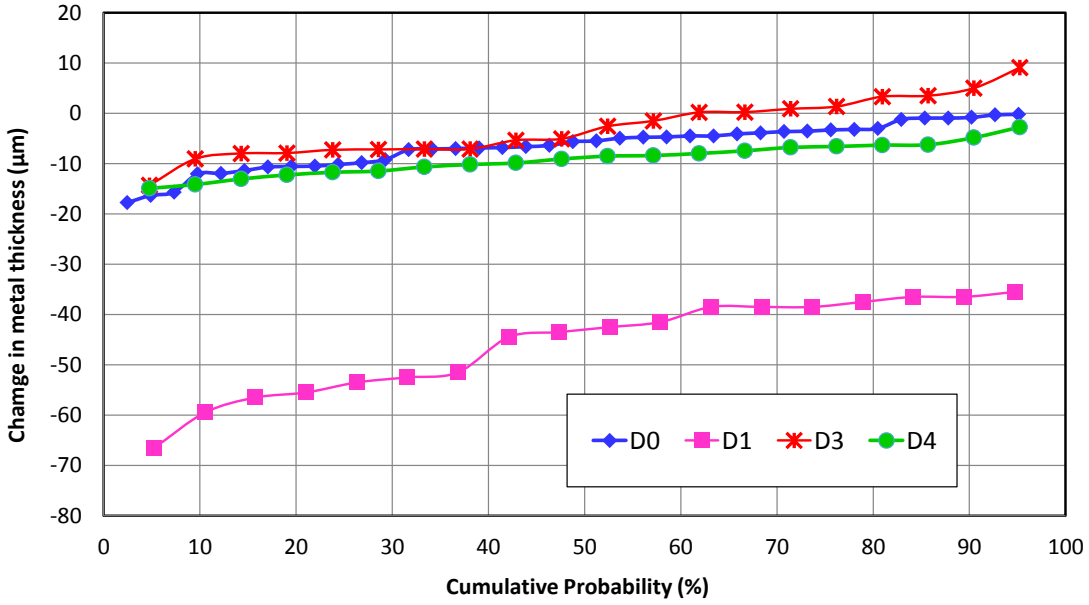

Figure 4-77: Change in metal thickness versus cumulative probability showing the behaviour of alloy HR3C covered with various deposits exposed to simulated oxy-fired combustion gases (with 6260 vppm SO_2/1700 vppm HCl) at 600°C for 1000 h

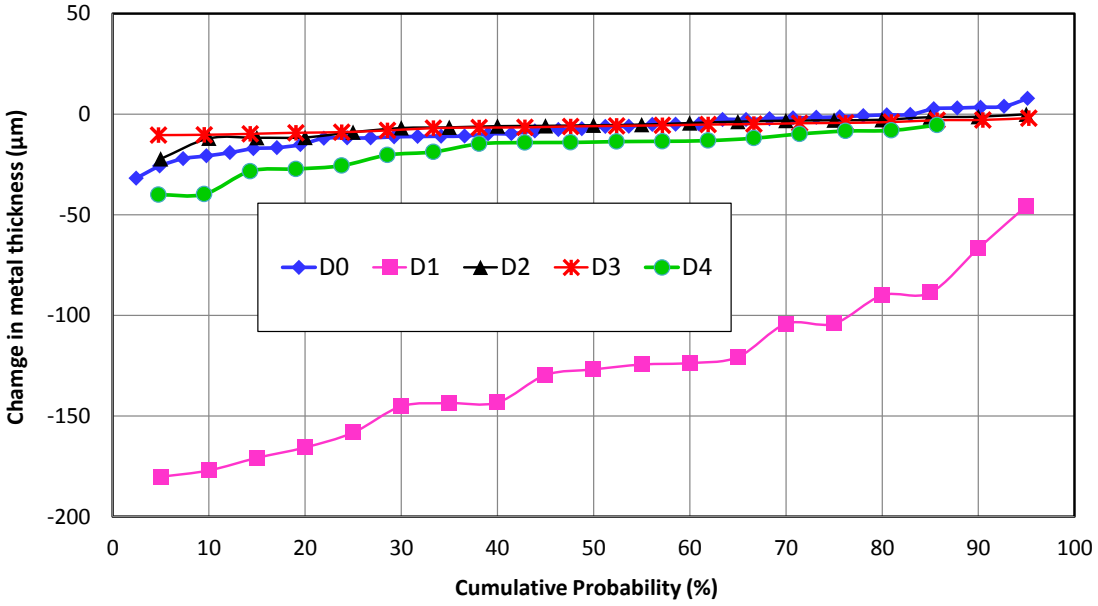

Figure 4-78: Change in metal thickness versus cumulative probability showing the behaviour of alloy HR3C covered with various deposits exposed to simulated oxy-fired combustion gases (with 6260 vppm SO_2/1700 vppm HCl)at 650°C for 1000 h

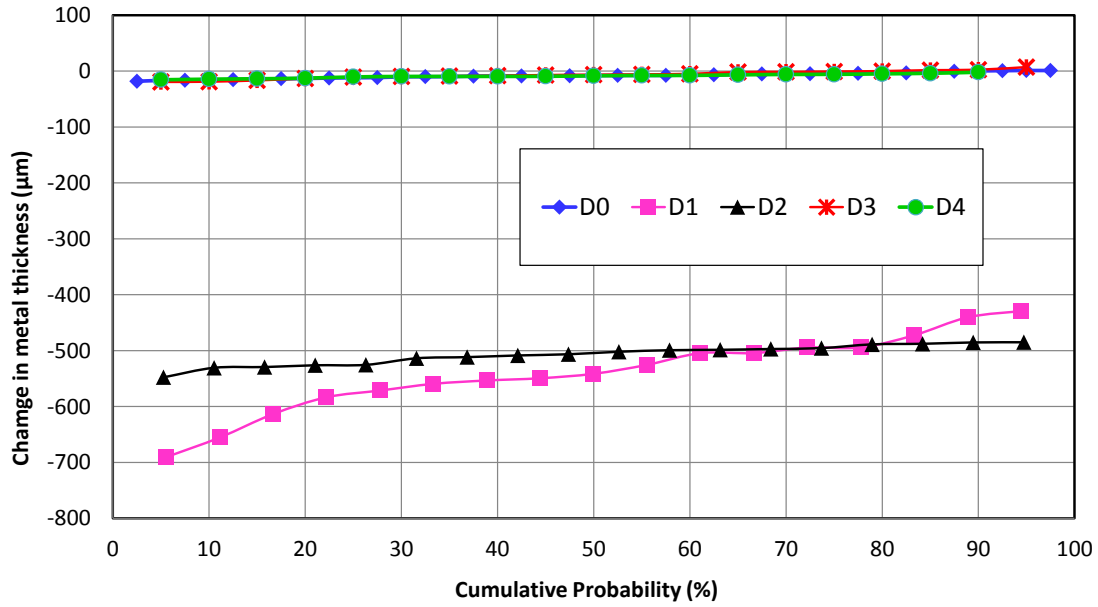

Figure 4-79: Change in metal thickness versus cumulative probability showing the behaviour of alloy HR3C covered with various deposits exposed to simulated oxy-fired combustion gases (with 6260 vppm SO_2/1700 vppm HCl)at 700°C for 1000 h

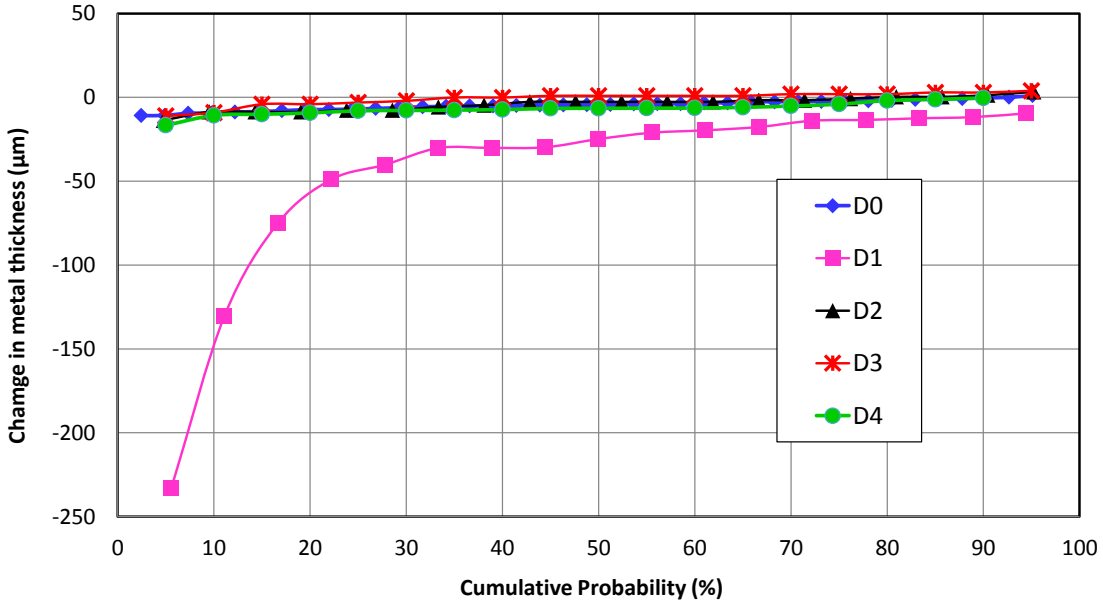

Figure 4-80: Change in metal thickness versus cumulative probability showing the behaviour of alloy HR3C covered with various deposits exposed to simulated oxy-fired combustion gases (with 6260 vppm SO_2/1700 vppm HCl) at 750°C for 1000 h

4.4.3.5 Alloy 625

Figure 4-81 to Figure 4-84 illustrate the damage distributions for alloy 625 covered with four different deposits exposed to simulated oxy-fired combustion gases (with 6260 vppm SO_2/1700 vppm HCl) at 600, 650, 700 and 750°C for 1000 hours. As expected alloy 625 samples covered with deposit D1 exhibited the highest metal loss values at all the temperatures. In Figure 4-81 alloy 625 covered with deposit D1 produced the lowest metal loss data (at approximately 33 µm) whereas at 650°C (Figure 4-82) the damaged almost doubled to 60 µm. At 700°C (Figure 4-83) the median metal loss values increased almost 8 times to ~480 µm compared to 650°C. Alloy 625 covered with deposit D1 also follows the trend observed for alloys T92, 347HFG and HR3C, with median metal loss values dropping to ~240 µm with the 50°C increase in temperature from 700 to 750°C.

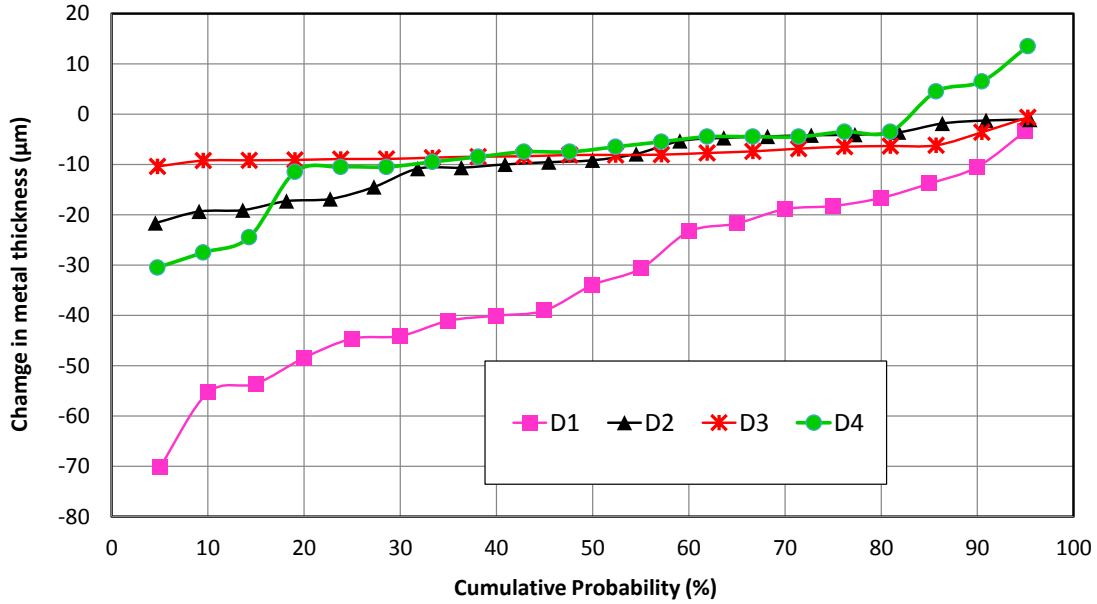

Figure 4-81: Change in metal thickness versus cumulative probability showing the behaviour of alloy 625 covered with various deposits exposed to simulated oxy-fired combustion gases (with 6260 vppm SO_2/1700 vppm HCl) at 600°C for 1000 h

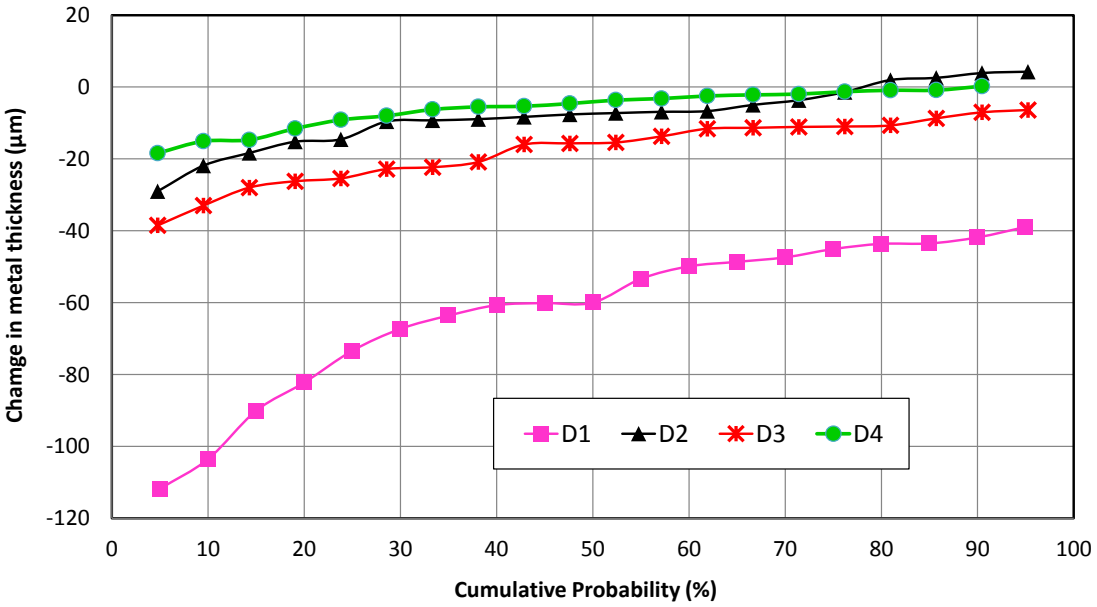

Figure 4-82: Change in metal thickness versus cumulative probability showing the behaviour of alloy 625 covered with various deposits exposed to simulated oxy-fired combustion gases (with 6260 vppm SO_2/1700 vppm HCl) at 650°C for 1000 h

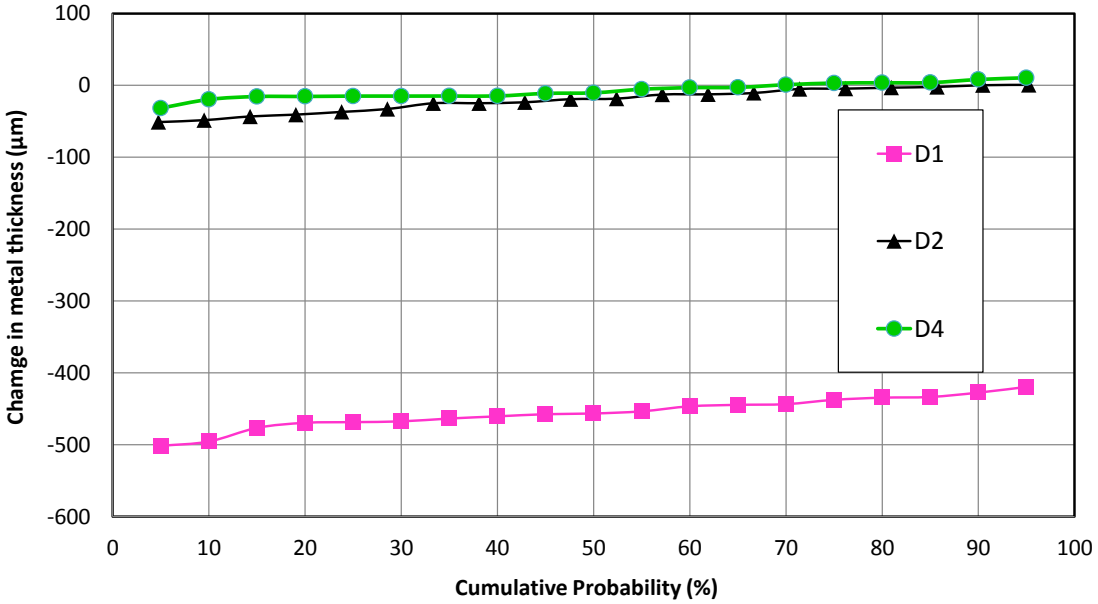

Figure 4-83: Change in metal thickness versus cumulative probability showing the behaviour of alloy 625 covered with various deposits exposed to simulated oxy-fired combustion gases (with 6260 vppm SO_2/1700 vppm HCl) at 700°C for 1000 h

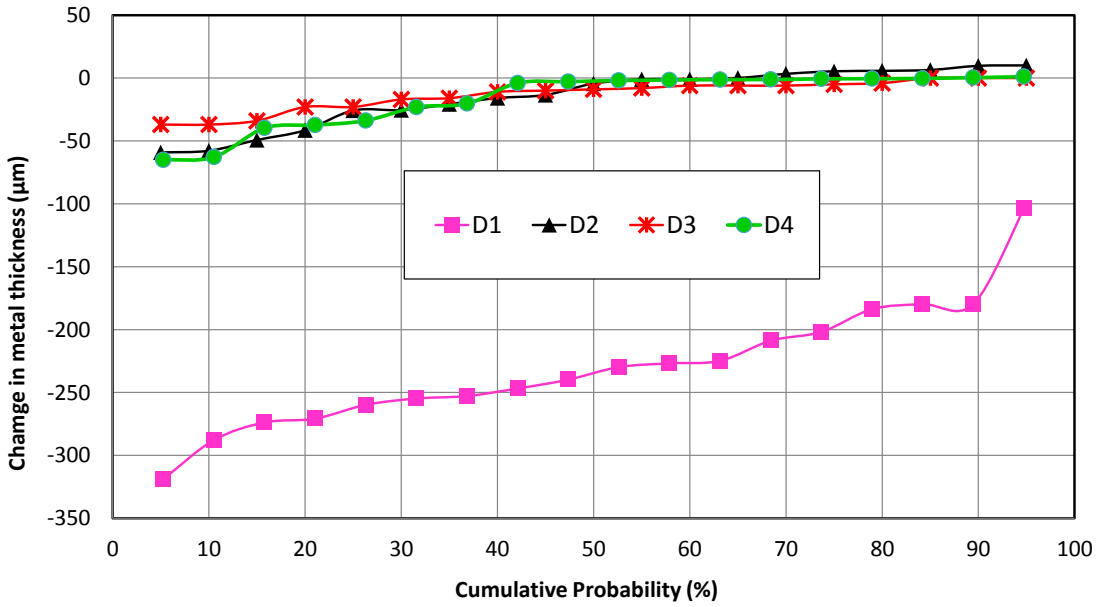

Figure 4-84: Change in metal thickness versus cumulative probability showing the behaviour of alloy 625 covered with various deposits exposed to simulated oxy-fired combustion gases (with 6260 vppm SO_2/1700 vppm HCl) at 750°C for 1000 h

4.5 XRD Analysis

4.5.1 Introduction

The clean samples, exposed bare samples or samples covered with deposits were characterised by using XRD before being mounted. The XRD technique used in the project helps in determining which compounds had formed on sample surfaces during the exposures.

4.5.2 Air-firing conditions

Figure 4-85 shows the comparison of XRD pattern for unexposed clean alloy T22 with patterns for alloy T22, bare and covered with deposit D1 exposed to air-firing conditions at 700°C for 1000 hours. In Figure 4-85 pattern (a) for clean ferritic T22 was found to be body centred cubic (bcc) (as for ferritic stainless steel 434) as expected, whereas patterns (b) and (c) revealed clear haematite phase (Fe_2O_3) peaks for the exposed samples. The haematite (Fe_2O_3) peaks are more distinctive and intense, on the exposed bare sample compared to peaks (with back ground noise) obtained from the sample exposed with deposit D1. The pattern for alloy T22 covered with deposit D1 also shows some additional peaks which were not identified.

Figure 4-86 shows the comparison of XRD pattern for unexposed clean alloy T92 with pattern for alloy T92, bare and covered with deposit D1 exposed to simulated air-fired combustion gases (with 1300vppm SO_2/400vppm HCl) at 700°C for 1000 hours. As expected pattern (a) found to be a typical iron chromium alloy with body centred cubic (bcc) crystal structure. Patterns (b) and (c) contained peaks identified as haematite (Fe_2O_3). The intensities of peaks for bare T92 exposed sample are much higher than for bare T22.

Figure 4-87 illustrates a comparison of XRD patterns for unexposed clean alloy 347HFG and bare alloy 347HFG exposed to simulated air-fired combustion gases (with 1300vppm SO_2/400vppm HCl) at 700°C for 1000 hours. In Figure 4-87 pattern (a) for austenitic 347HFG had a face centred cubic (fcc) crystal

structure (as for stainless steel 304) and haematite phase observed for exposed (bare 347HFG) alloy.

Figure 4-88 shows that XRD pattern for alloy HR3C clean (unexposed), bare and covered with deposit D1 exposed to air-firing conditions at 700°C for 1000 hours. A typical pattern (a) for fcc crystal phase for iron chromium nickel alloy (austenitic HR3C) was obtained. As observed for exposed bare T22, T92, and 347HFG, haematite phase was also detected for bare exposed HR3C. However for alloy HR3C covered with deposit D1 along with haematite phase (Fe_2O_3), peaks for chromium oxide (Cr_2O_3) and iron sulphide (Fe7S8) were also observed.

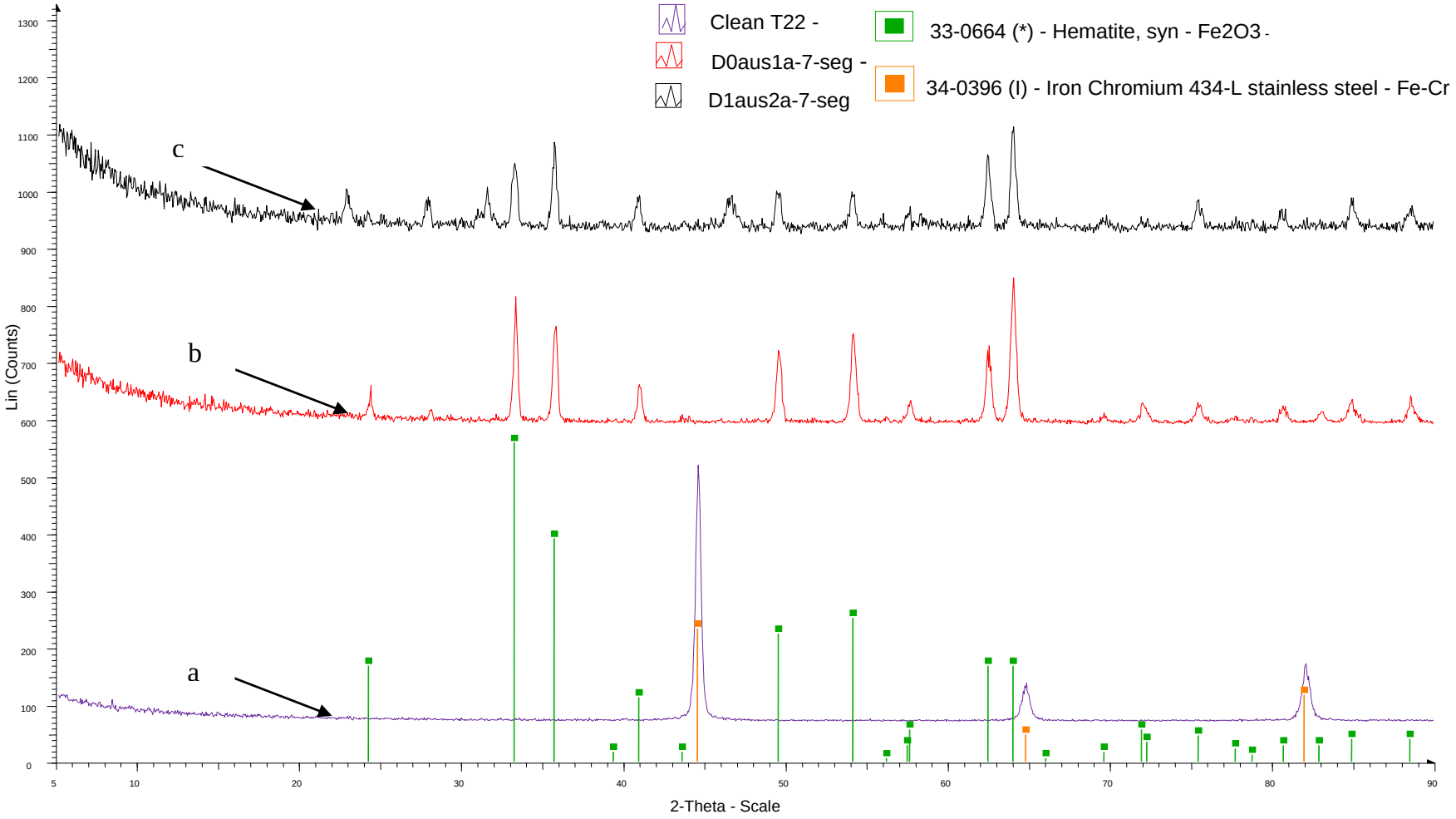

Figure 4-85: X-ray diffraction pattern of (a) unexposed bare alloy T22 (b) exposed bare alloy and (c) alloy covered with deposit D1 (1300 vppm SO_2/400 vppm HCl at 700°C for 1000 hours)

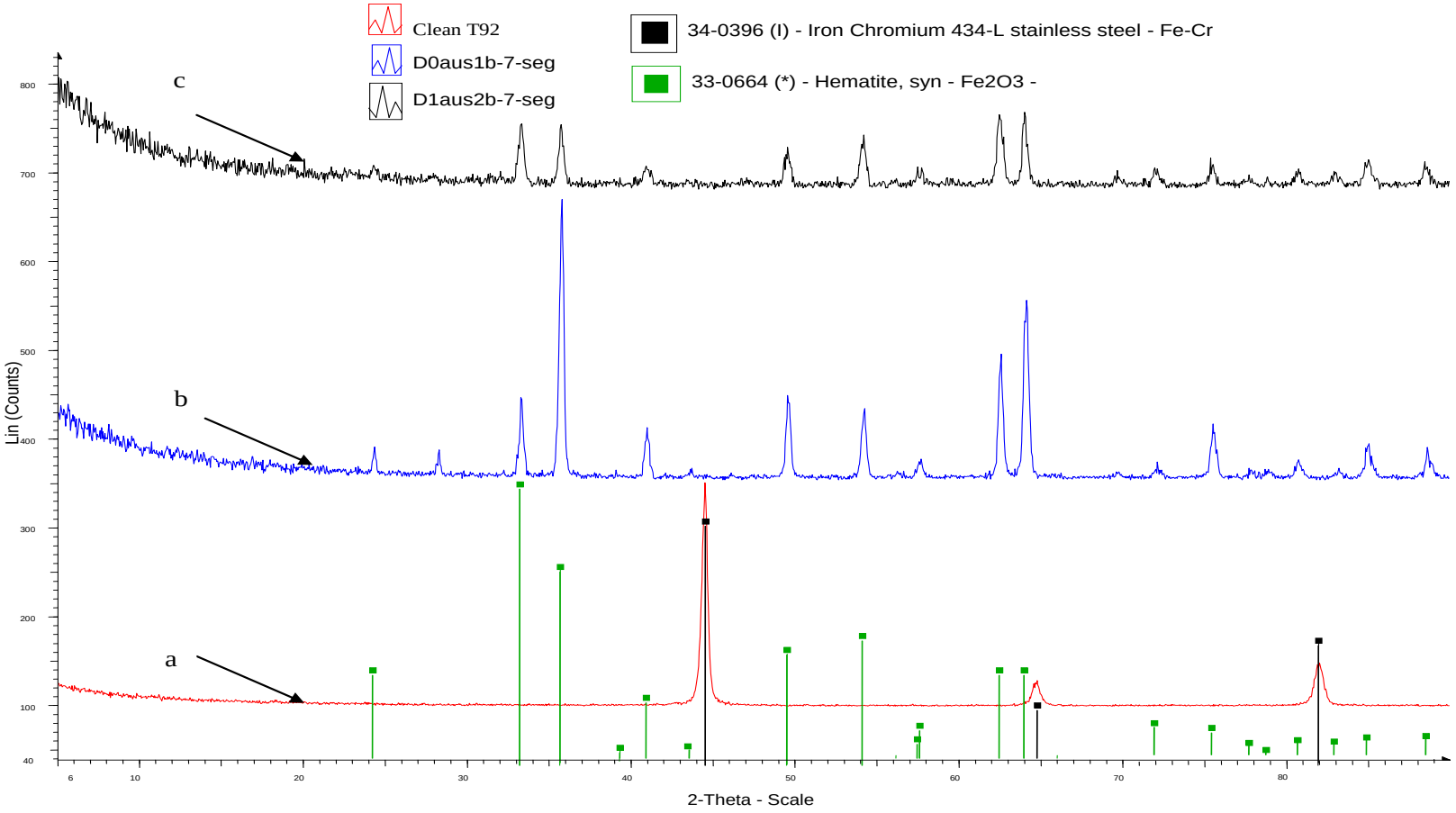

Figure 4-86: X-ray diffraction pattern of (a) unexposed bare alloyT92, (b) exposed bare alloy and (c) alloy covered with deposit D1 (1300 vppm SO_2/400 vppm HCl at 700°C for 1000 hours)

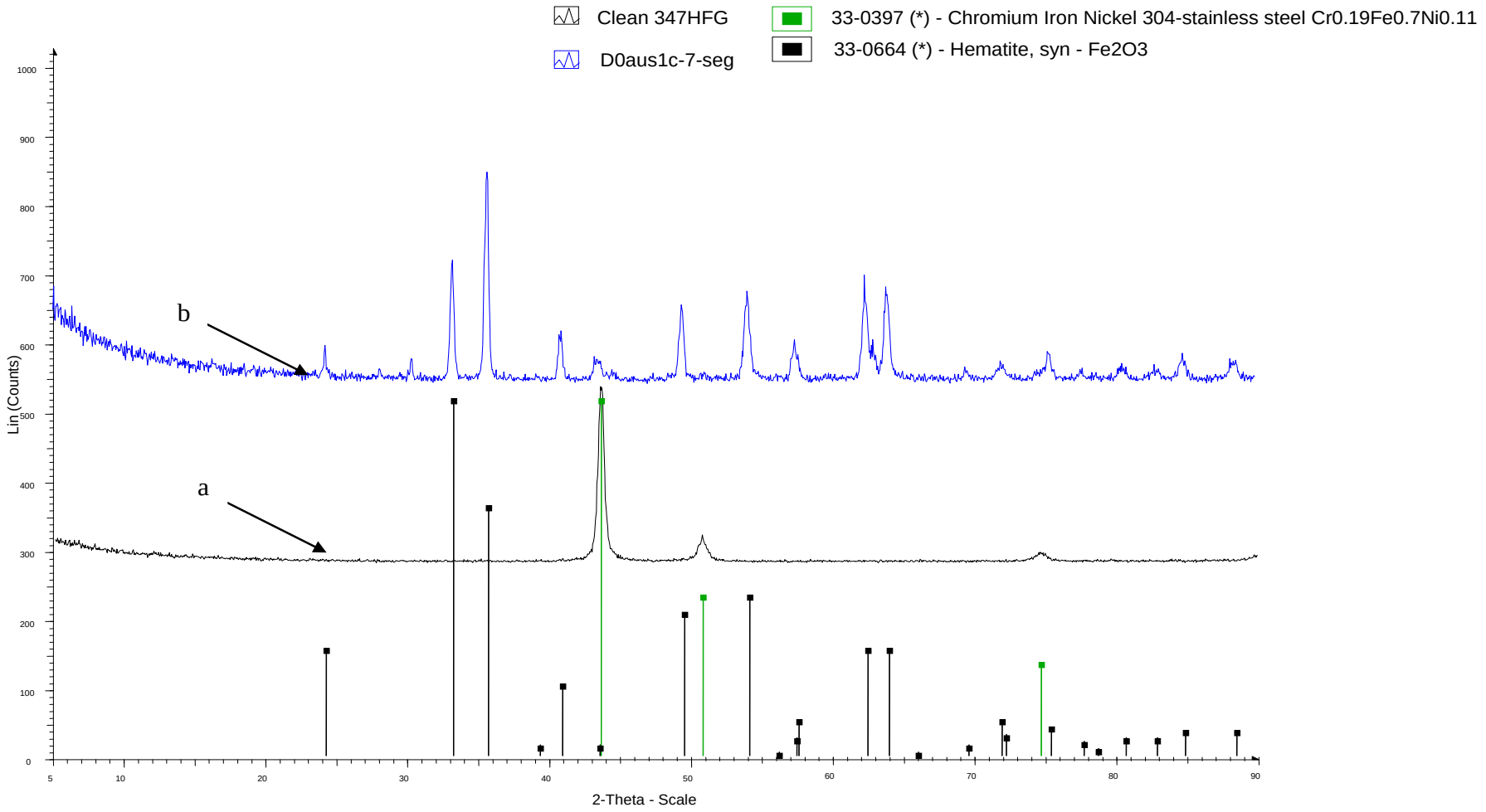

Figure 4-87: X-ray diffraction pattern of (a) unexposed clean alloy 347HFG, (b) and bare alloy 347HFG exposed to 1300 vppm SO_2/400 vppm HCl at 700°C for 1000 hours

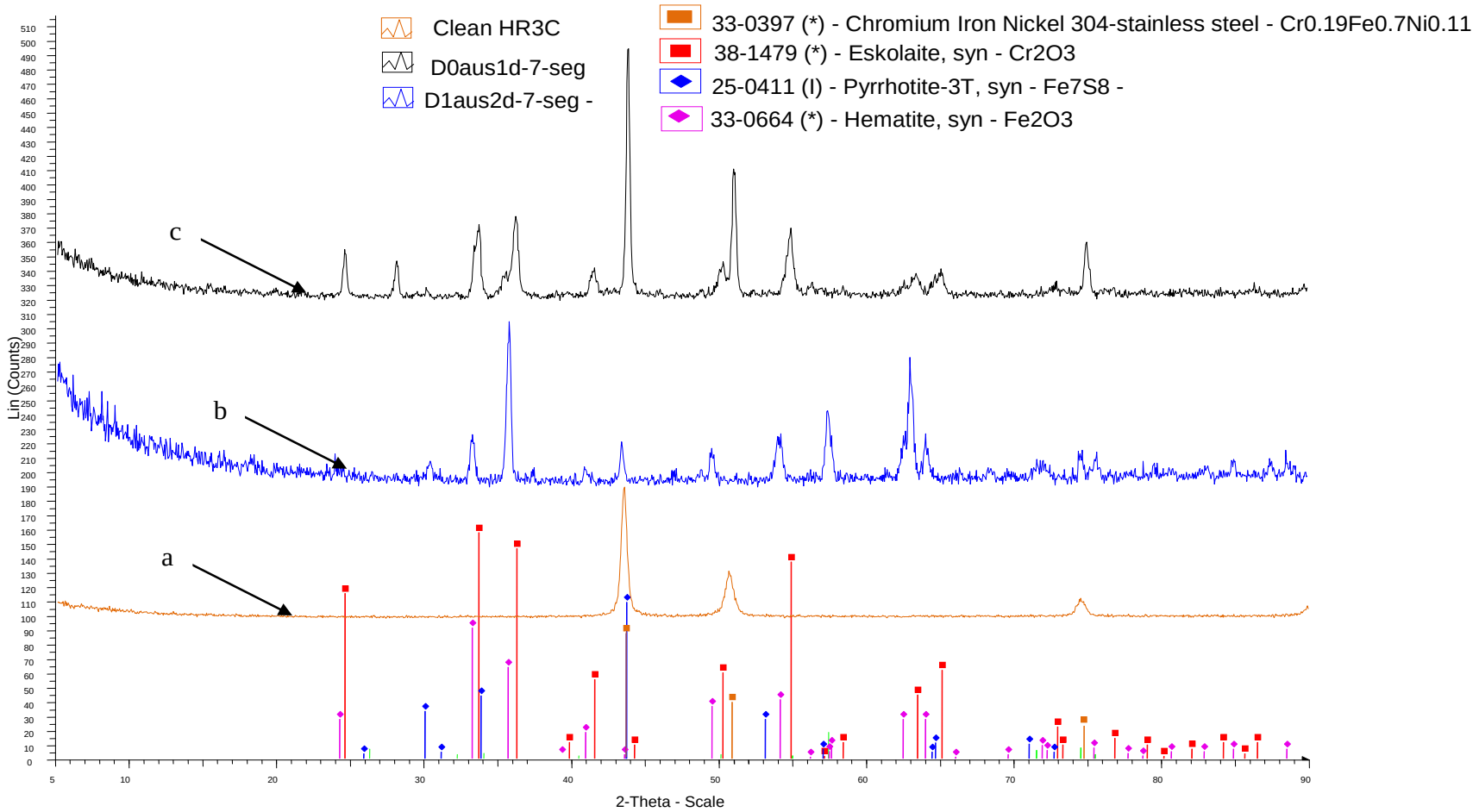

Figure 4-88: X-ray diffraction pattern of (a) unexposed bare alloy HR3C, (b) exposed bare alloy and (c) alloy covered with deposit D1 (1300 vppm SO_2/400 vppm HCl at 700°C for 1000 hours)

4.5.3 Oxy-firing conditions

Figure 4-89 illustrates XRD patterns for unexposed clean alloy T22 and for bare alloy T22, exposed to oxy-firing conditions at 750°C for 1000 hours. In Figure 4-89 pattern (a) for clean T22 alloy found to be a body centred cubic (bcc) crystal structure (as for ferritic stainless steel 434) as expected, whereas pattern (b) revealed clear haematite phase (Fe_2O_3) peaks. No other peaks for other possible compounds were observed

Figure 4-90 shows the comparison of XRD pattern for unexposed clean alloy T92 with pattern for alloy bare T92, exposed to 6260vppm SO_2/1700 vppm HCl at 750°C for 1000 hours. As expected a typical diffractogram of iron chromium alloy with bcc structure for alloy T92 was detected. Data shows distinctive peaks for haematite (Fe_2O_3) phase formed on bare exposed alloy were observed.

Figure 4-91 shows the comparison of XRD pattern for unexposed clean alloy T22 with pattern for alloy T22, bare and covered with deposit D1 exposed to 6260vppm SO_2/1700vppm HCl at 700°C for 1000 hours. As expected pattern (a) found to be a typical iron chromium alloy with body centred cubic (bcc) crystal structure. Patterns (b) (exposed bare sample) and (c) (exposed sample covered with deposit D1) contained peaks identified as haematite (Fe_2O_3). Potassium chromium sulphate [$K_3Cr(SO_4)_3$] phase was also detected for alloy T22 exposed with deposit D1.

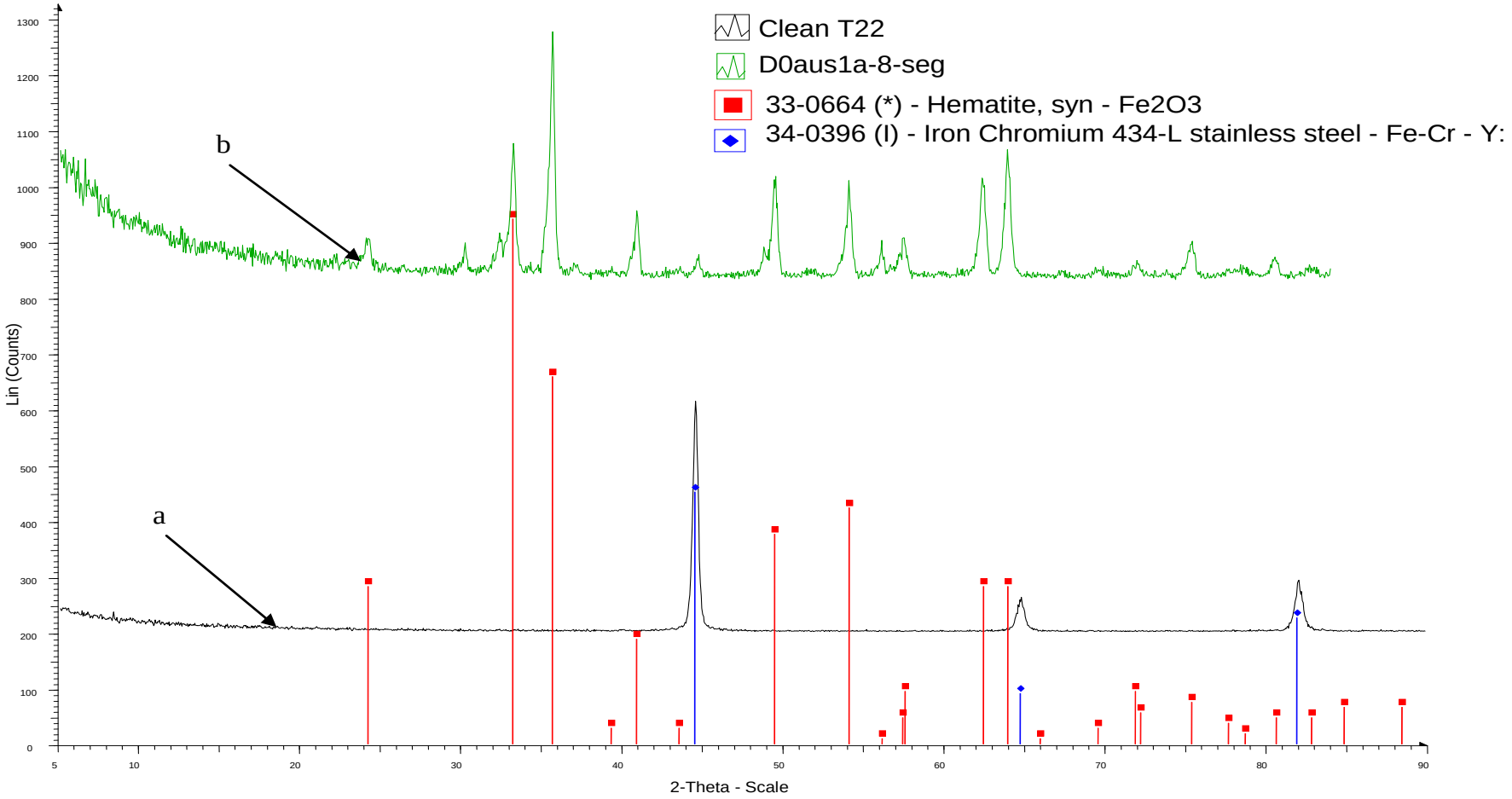

Figure 4-89: X-ray diffraction pattern of (a) bare alloy T22 unexposed and (b) exposed (b) to 6260 vppm SO_2/1700 vppm HCl at 750°C for 1000 hours

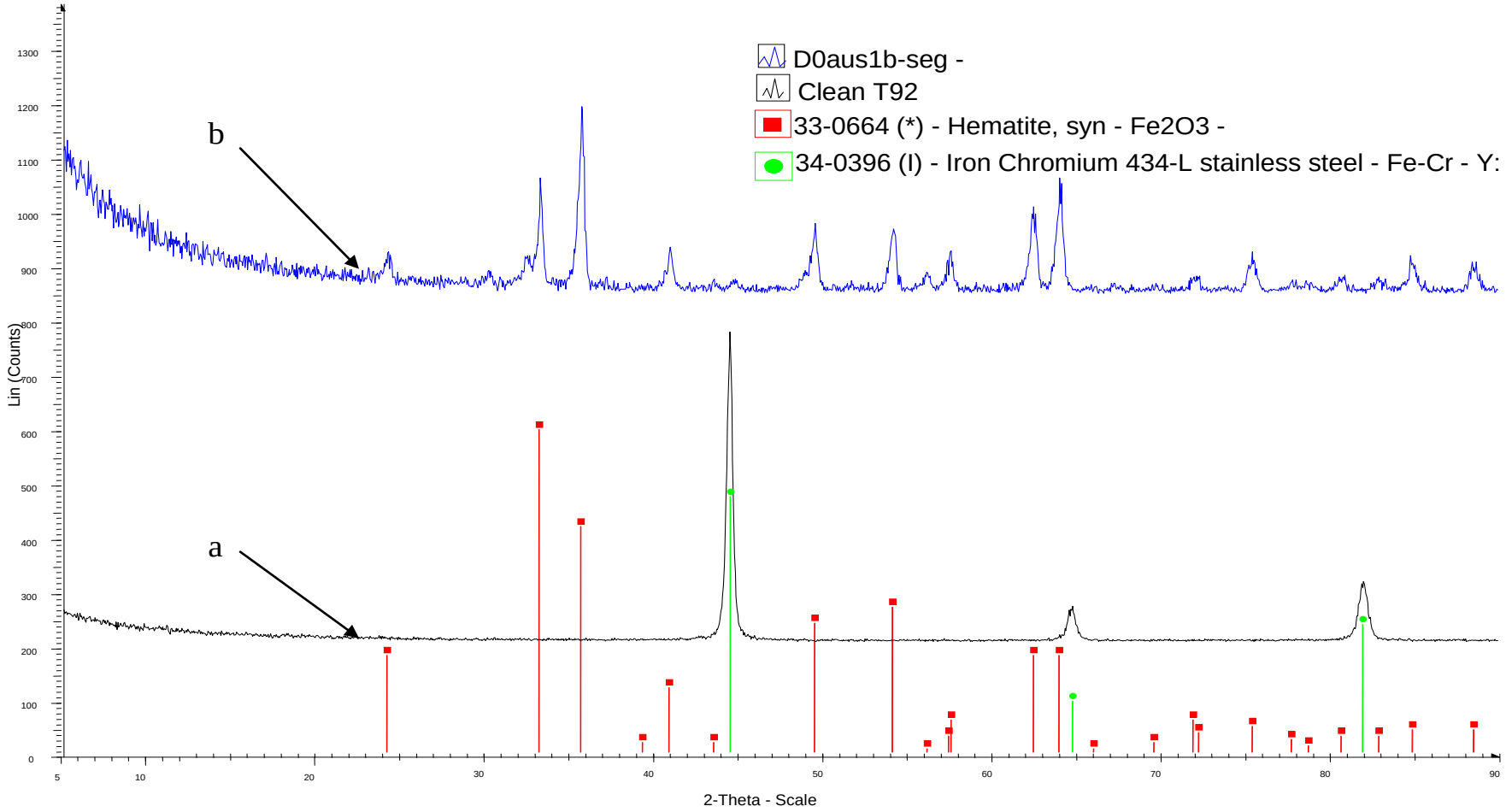

Figure 4-90: X-ray diffraction pattern of (a) bare alloy T92 unexposed and (b) exposed to 6260 vppm SO_2/1700 vppm HCl at 750°C for 1000 hours

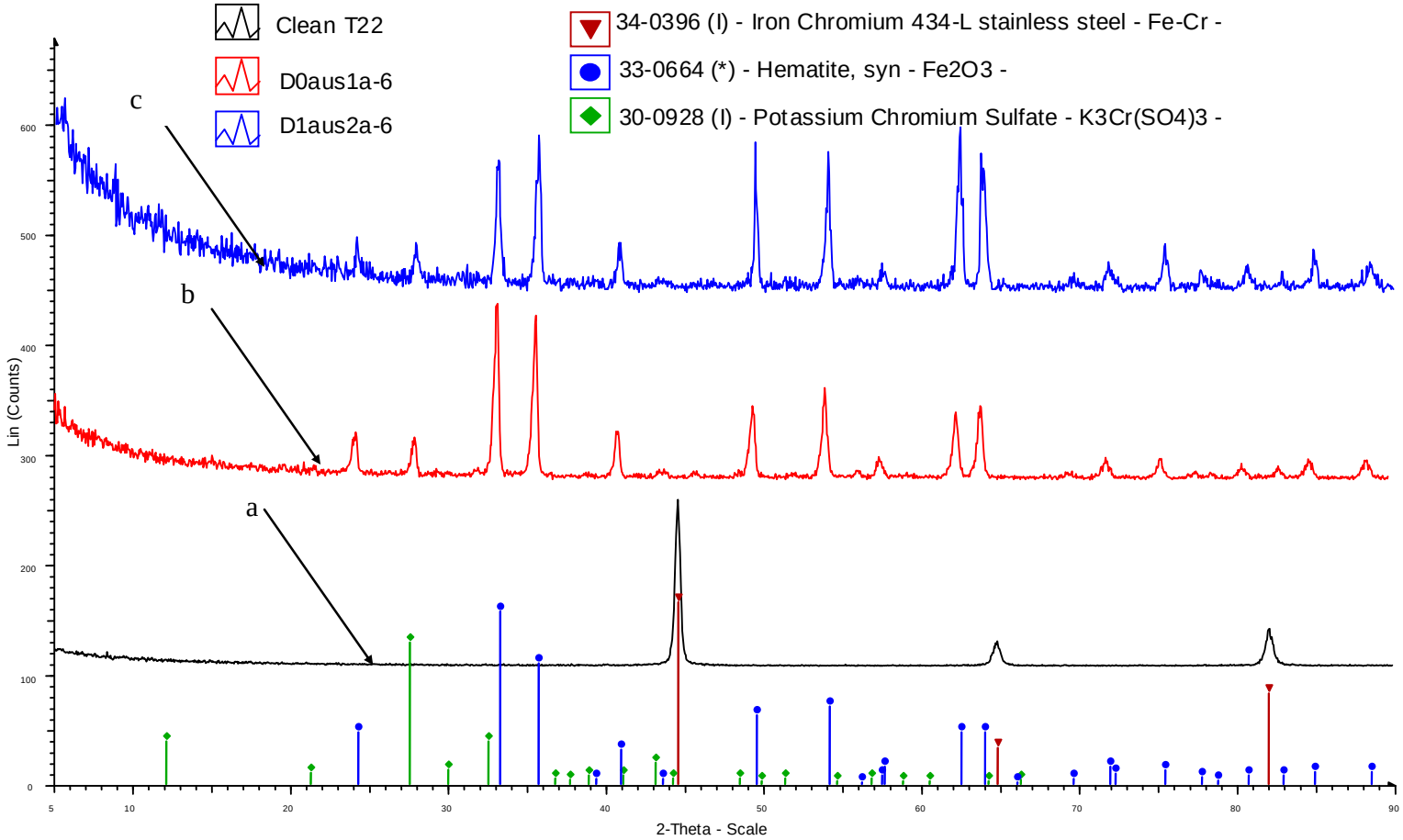

Figure 4-91: X-ray diffraction pattern of (a) alloy T22 clean unexposed, (b) bare and (c) covered with deposit D1 (6260 vppm SO_2/1700 vppm HCl at 700°C for 1000 hours)

4.6 Deposit stability test

4.6.1 Introduction

As discussed in the experimental chapter, (section 3.2.5) chemical analyses were carried out of deposits before and after the 200 hours exposure. The idea was to determine the ionic/atomic concentration of elements present in the deposits. Mainly two different (wet chemistry) techniques were used to analyse the samples; atomic spectroscopy (AS) and ion chromatography (IC).

The atomic spectroscopy technique was used to analyse atoms of potassium (K), sodium (Na), aluminium (Al) and iron (Fe), whereas Ion chromatography (IC) was used to analyse water soluble anions: chlorides (Cl^-) and sulphates (SO_4^{2-}).

4.6.2 Chemical analysis

Figure 4-92 and Figure 4-93 illustrate the analytical results obtained for deposits D1-D6 and deposits D7-D10 respectively. These data show the theoretical value (wt %) for each species in all the deposits, the amount detected for unexposed deposits and the average values for the amount detected for anions and metal atoms (from one or more test cycles) for all deposits exposed to gases simulated oxy-firing conditions at 650°C for 200 hours.

Results for deposit D1 in Figure 4-92 show that unexposed sample had higher amount of Fe but similar levels of sodium and potassium compared to the calculated value. However, for the exposed deposit, the amounts recovered for sodium and iron were very similar to the calculated amount, but lower amounts (~ 7% less than calculated value) were detected for potassium. The deposit D1 exposed sample was not analysed for anions analysis. However, anion (SO_4^{2-}) recovery from the unexposed deposit were ~ 6% higher than the calculated value.

In Figure 4-92 deposit analysis results for deposit D2 shows that detection of metals and anions for unexposed sample are in a range of ± 2 % of the

calculated value. For the exposed deposit sample, the average value of alkali metals (Na and K) and particularly SO_4^{2-} anions were found to be higher than the calculated values.

Results presented in Figure 4-92 for deposit D3 shows that low levels of K and high levels Na were detected for the unexposed deposit, whereas Al and Fe were in a range of ±4 % of the calculated values. Results for the exposed deposit D3 shows that the average value of K and Na was found to be higher than the calculated values, whereas amounts for Al and Fe correlate extremely well with calculated values. The SO_4^{2-} anion calculated values was ~6%, whereas the amount detected in the unexposed deposit was found to be 8% SO_4^{2-} and in the exposed deposit had an average of ~10%. SO_4^{2-}.

Results for deposit D4 in Figure 4-92 revealed that levels of alkali metal (Na and K) and SO_4^{2-} anion were found to be higher (almost doubled) for both unexposed and exposed deposit analysis. However levels of Cl^-, and Fe were found to be ±1% of the calculated values.

Result for deposit D5 show that the unexposed deposit D5 had a high recovery for K whereas amount for SO_4^{2-} (± 2%) is in good agreement with the calculated value. No samples were analysed for exposed deposit D5.

Results for deposit D6 in Figure 4-92 show that the unexposed sample had slightly higher amounts of Cl^- and lower levels (± 2 %) of K than the calculated values. Whereas for the exposed deposit higher K was recovered. Sample D6 was not analysed for anions (Cl^- and SO_4^{2-}).

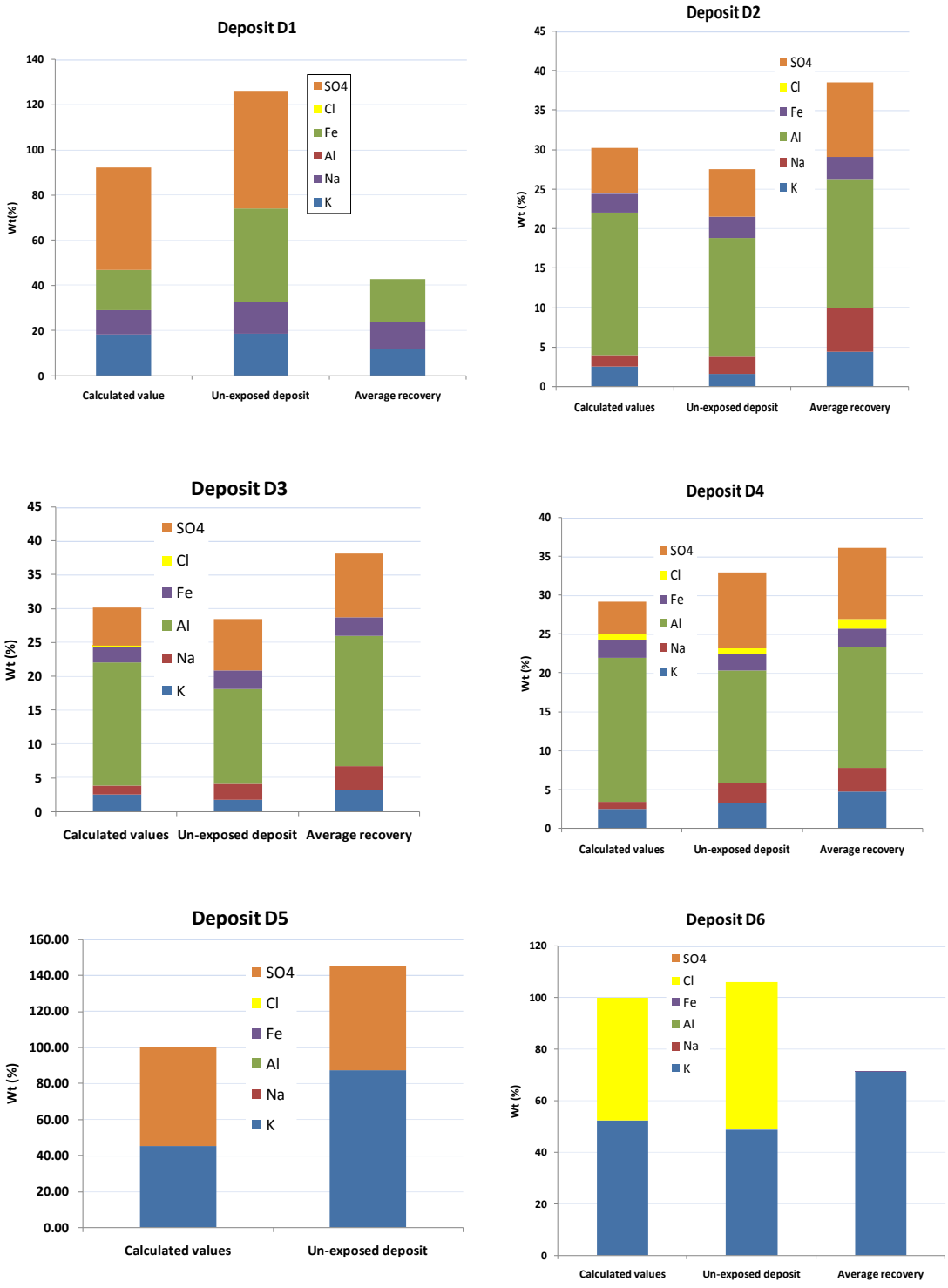

Figure 4-92: Calculated values, unexposed deposit analysis and an average value (from various cycles) of metals (Na, K, Fe and Al) and anions (Cl and SO_4) recovered from deposits D1-D6 exposed to gases simulating oxy-fired combustion for 200 hours at 650°C

In Figure 4-93 , analysis results for deposit D7 show that detection of SO_4^{2-} anions for unexposed sample are ~10 % higher than the calculated value. No exposed D7 sample was available for anion analysis as all the exposed samples were prepared for metals analysis. For the exposed deposit D7 sample, the average value of K was found to be 10% lower, whereas Fe average value was almost doubled than the calculated values. Surprisingly, low levels of Na and Al (as a result of possible contamination) were also detected in the exposed deposit D7 sample.

Results presented in Figure 4-93 for deposit D8 shows that recovery of K in both exposed and unexposed deposit D8 sample was almost ~20% lower than the calculated value. Results for SO_4^{2-} in the unexposed deposit D8 analysis show an amount increase by 8%. Exposed deposit D8 sample was not analysed for SO_4^{2-} (as all samples were used for metal analysis using atomic spectroscopy).

Results for deposit D9 in Figure 4-93 shows that in the unexposed sample the Cl^- and Fe levels detected correlate very well with the calculated values. However, the Cl^- amount detected in the exposed deposit was almost 10 times lower than the calculated value. These data show that significant amount of SO_4^{2-} ions which were initially not present in the deposit D9 (Table 3-2) were detected.

Results for deposit D10 in Figure 4-93 show that the unexposed sample had higher levels of Cl^- and K than the calculated value. For the exposed deposit a low level of K was detected, and Cl^- was not recovered but instead high amounts of SO_4^{2-} ions were detected. Atomic spectroscopy of exposed deposit D10 also found contaminants of Na (possible during the corrosion test).

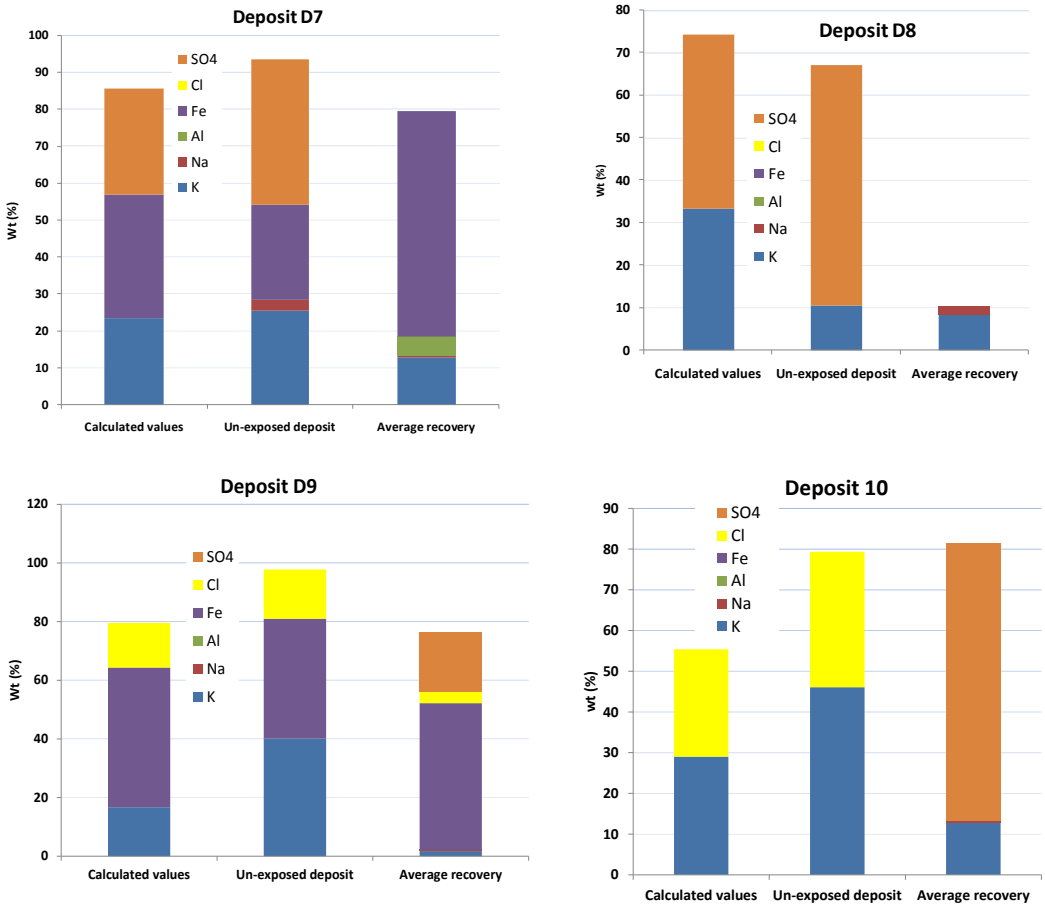

Figure 4-93: Calculated values, unexposed deposit analysis and an average value (from various cycles) of metals (Na, K, Fe and Al) and anions (Cl and SO_4) recovered from deposits D7-D10 exposed to gases simulated oxy-fired combustion for 200 hours at 650°C

4.7 High concentration salts exposure test

Three different alloys (T92, 347HFG and alloy 625) were used in the high concentration salt exposure test. The post exposure samples analysis was carried out using the same techniques (SEM/EDX, dimensional metrology, mass change data and XRD analysis) as used for the main tests.

4.7.1 Mass change data

4.7.1.1 T92

Figure 4-94 illustrates the mass change data for ferritic alloy T92 exposed to oxy-firing conditions (6260 vppm SO_2/1700 vppm HCl) for 1000 hours at 650°C. These data show that alloy T92 covered with deposit D6 shows the most aggressive effect with the highest mass gain (i.e. approximately 75 mg/cm^2) followed by alloy T92 covered with deposit D10 and then samples covered with other deposits. Alloy T92 covered with deposit D5 (deposit contain K_2SO_4 100 mol %) shows the lowest mass gain value (of approximately 24 mg/cm^2) i.e. almost three times less than the highest mass gain value (T92 covered with deposit D6).

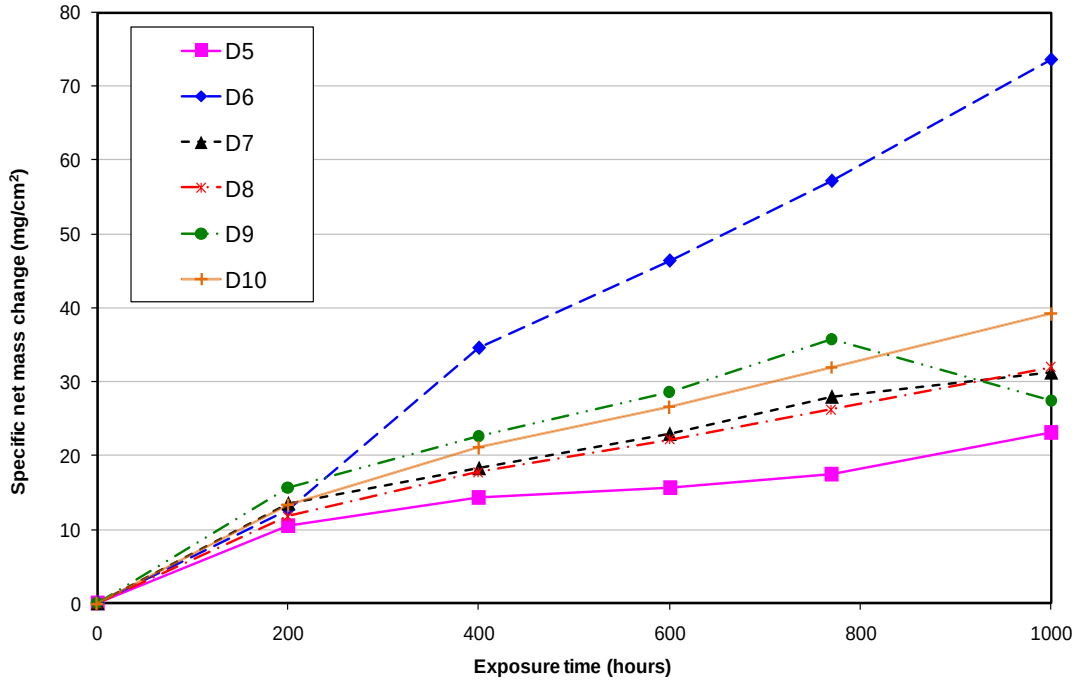

Figure 4-94: Specific net mass change data for alloys T92 covered with six high concentration salts deposits exposed to the simulated oxy-firing combustion gas for 1000 h at 650°C

4.7.1.2 347HFG

Figure 4-95 illustrates mass change data for austenitic alloy 347HFG exposed to oxy-firing conditions (6260 vppm SO_2/1700 vppm HCl) for 1000 hours at 650°C. The highest mass gain value (approximately 31 mg/cm^2) was shown by alloy 347HFG covered with deposit D10 (KCl 50 mol% - $SiO_2$50 mol%) whereas the mass gain value for alloy 347HFG covered with deposit D6 (100 % KCl) was found to be lower (approximately 21 mg/cm^2) than alloys covered with deposits D8, D9 and D10 sample. Whereas alloy 347HFG covered with deposit D7 (K_2SO_4 50 mol%-Fe_2O_3 50 mol %) gained the lowest mass of approx i.e. 4 mg/cm^2.

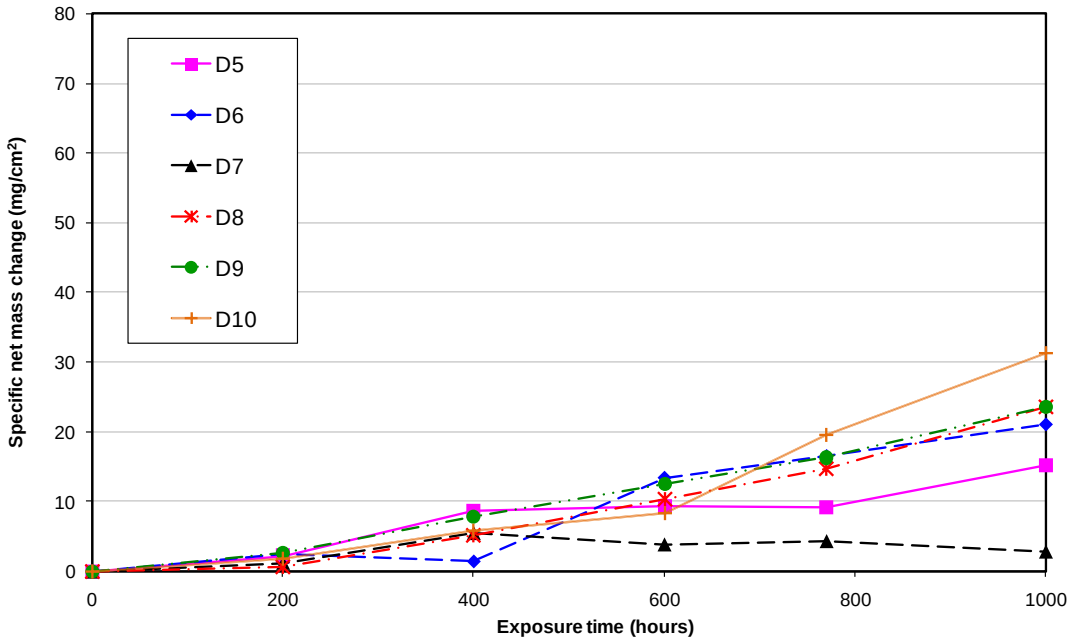

Figure 4-95: Specific net mass change data for alloys 347HFG covered with six high concentration salts deposits exposed to the simulated oxy-firing combustion gas for 1000 h at 650°C

4.7.1.3 Alloy 625

Figure 4-96 illustrates the mass change data for nickel based alloys 625 covered with high concentration salt deposits (D5-D10) exposed oxy-firing conditions (6260 vppm SO_2/1700 vppm HCl) for 1000 hours at 650°C. The sample covered with deposit D6 showed significant mass gain value (approximately 46 mg/cm^2). The mass gain values for other sample alloys covered with deposits (D5, D7-D10) were in the range of 13-16 mg/cm^2.

A noticeable feature for alloy 625 with deposit D6 was the higher mass gain value i.e. more than two times mass gain value compared to alloy 347HFG with the same deposit in the same conditions, such high mass gain value was also observed for alloy T92 with deposit D6.

Another key feature noticed for all the alloys (T92, 347HFG and alloy 625) was the effect of deposits that contained KCl (D6, D9 and D10) was more significant in terms of mass gain values than deposits containing K_2SO_4 (D5, D7 and D8).

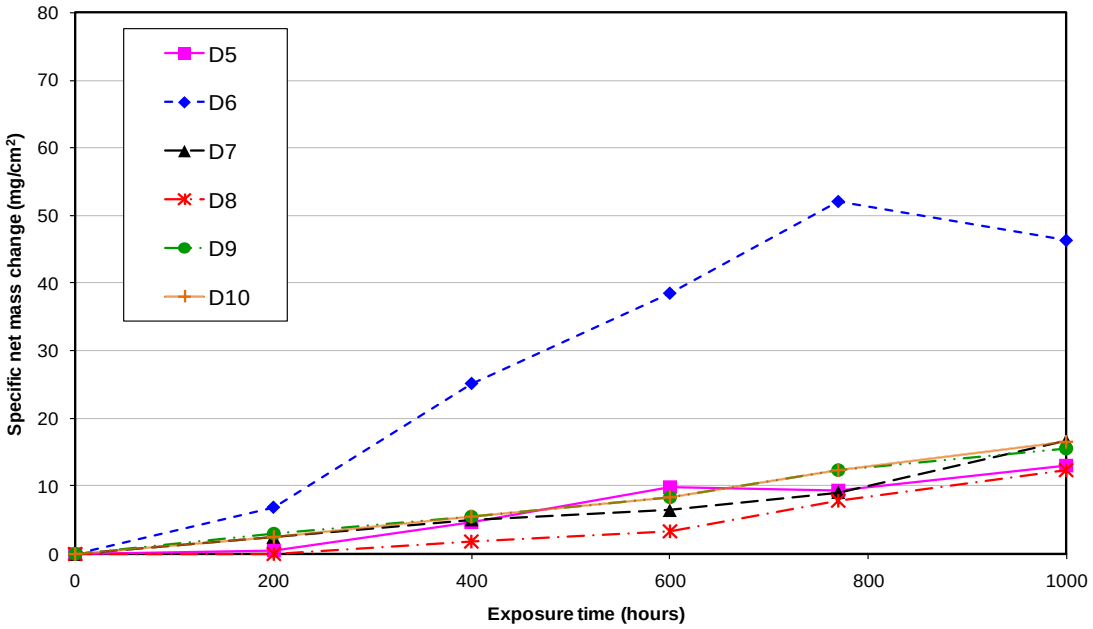

Figure 4-96: Specific net mass change data for alloys 625 covered with six high concentration salts deposits exposed to the simulated oxy-firing combustion gas for 1000 h at 650°C

4.7.2 SEM/EDX

4.7.2.1 Scales Thickness

Figure 4-97 illustrates the cross-sections through the scales formed on ferritc T92, austenitic 347HFG and alloy 625 covered with deposit D5 and D6 after exposure for 1000 hours at 650°C. The scales on alloy T92 are much more compact with both deposits D5 and D6. The scales formed on alloy 347HFG are thinner and not as uniformed compared to alloy T92 which is also in agreement with mass change data.

Alloy 625 covered with deposit D5 and D6 shows the scale as having been damaged during the preparation but having numerous voids. Alloy 625 covered with deposit D6 showed significant scale thickness. Such corrosion damage of this alloy is also in line with mass change data.

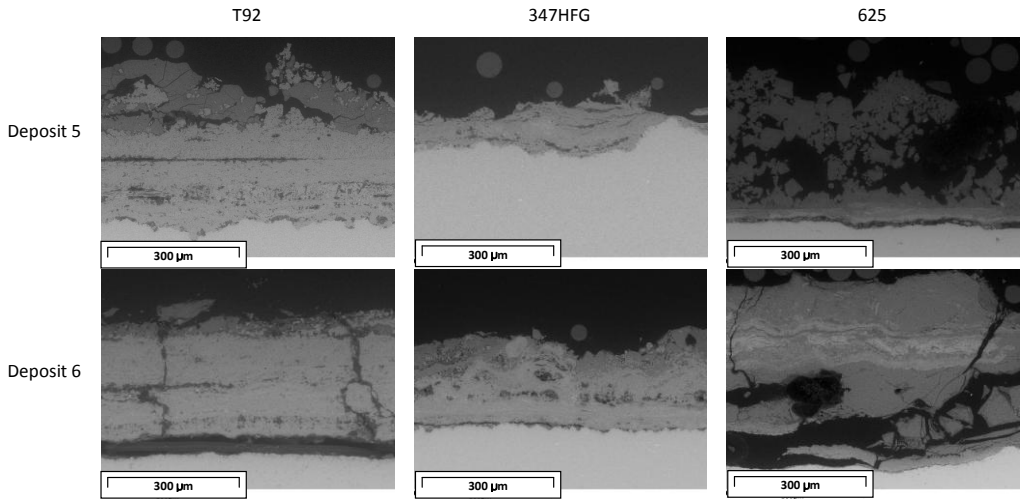

Figure 4-97: BSE images of cross-sectioned scales on T92, 347HFG and alloy 625 covered with deposit D5 and D6 exposed to 6260 vppm SO_2/1700 vppm HCl at 650 °C for 1000 hours

4.7.2.2 EDX Mapping

Figure 4-98 shows EDX mapping of alloyT92 covered with deposit D5 exposed to simulated oxy-fired combustion gas at 650°C for 1000 hours. Aggressive nature of deposit D5 (100% KCl) on alloy T92 with thick scale being formed are clearly shown. The BSE image shows distinctive multi-layers of oxides and deposit. The EDX maps illustrate the distribution of oxygen throughout the oxide/sulphide/deposit. Iron is in the upper region of the oxide. Chromium is detected in the spinel oxide layer close to the alloy. Potassium is concentrated towards the surface of the oxide/deposit mix layers. Sulphur shows a concentration distribution that similar to the potassium, but in addition, there is a further concentration in patches at the alloy/oxide interface.

Figure 4-99 shows EDX mapping of alloy 347HFG covered with deposit D6 exposed to simulated oxy-fired combustion gas at 650°C for 1000 hours. The mapping shows oxygen is distributed throughout the scale (oxide/deposit mix). Fe is also present in the scale but richer in the scale upper region, deposit oxide interface and in the alloy as expected. The iron level is depleted where chromium is present in a layer closer to the alloy. Sulphur is detected beneath the chromium layer and more significantly at the scale/deposit mix surface along with alkali metal (potassium).

Figure 4-100 presents a BSE image and EDX maps for an alloy 625 cross-section exposed with deposit D6 to 6260 vppm SO_2/1700 vppm HCl at 650°C for 1000 hours. Data shows uniform distribution of oxygen all over the scale. Chromium is rich at the metal scale interface, however multi- layers of chromium were also detected in the outer regions of the scale/deposit mix. Ni is located mainly in the alloy but a significant amount is clearly observed in the centre of scale. Sulphur along with potassium are distributed very abundantly in the scale suggesting penetration through the scale/deposit. Moreover low levels of manganese were also detected in the same locations as chromium.

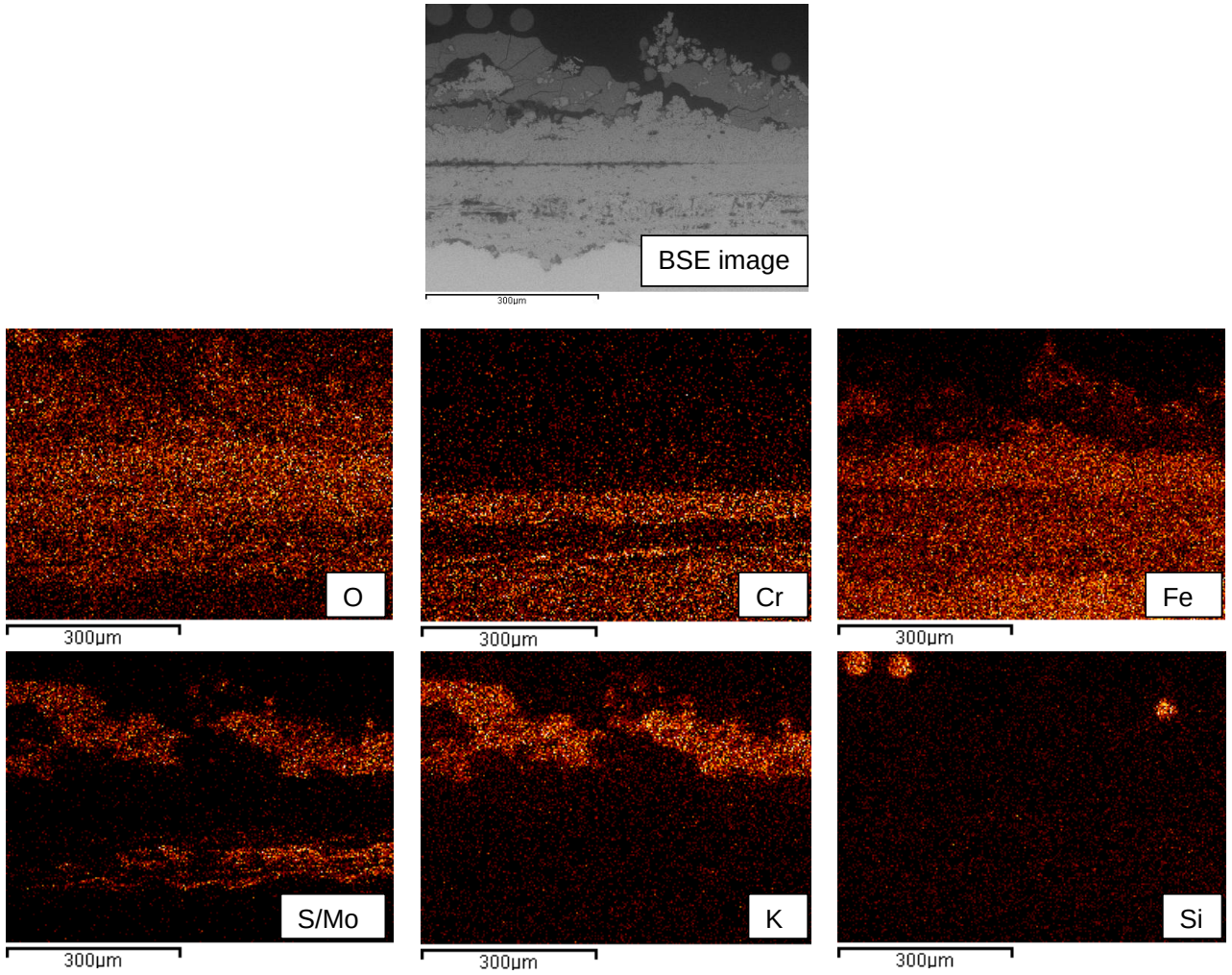

Figure 4-98: BSE image and x-ray maps of alloy T92 covered with deposit D5 exposed to simulated oxy-fired combustion gases (with 6260 vppm SO_2/1700 vppm HCl) at 650°C for 1000 hours

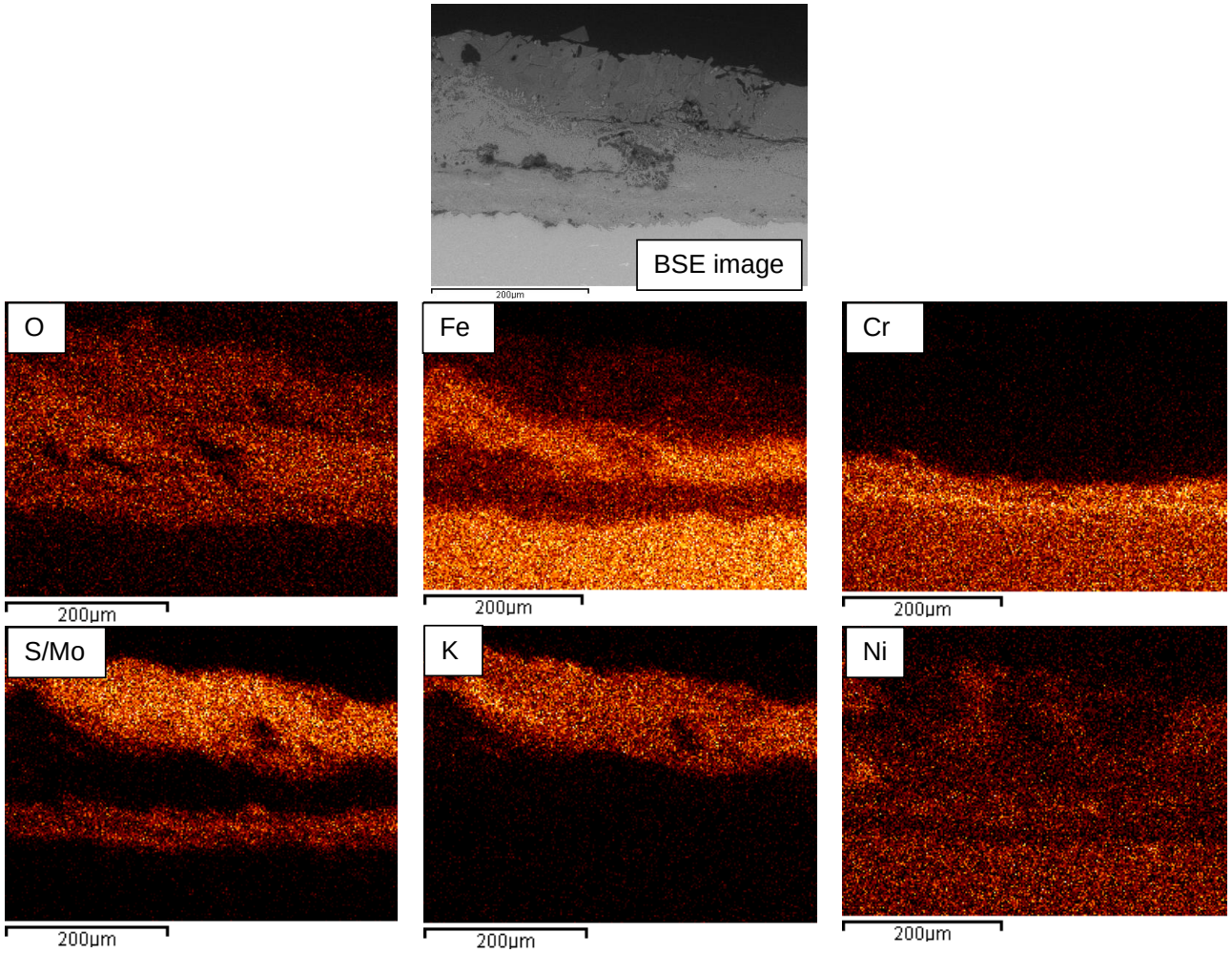

Figure 4-99: BSE image and x-ray maps of alloy 347HFG covered with deposit D6 exposed to simulated oxy-fired combustion gases (with 6260 vppm SO_2/1700 vppm HCl) at 650°C for 1000 hours

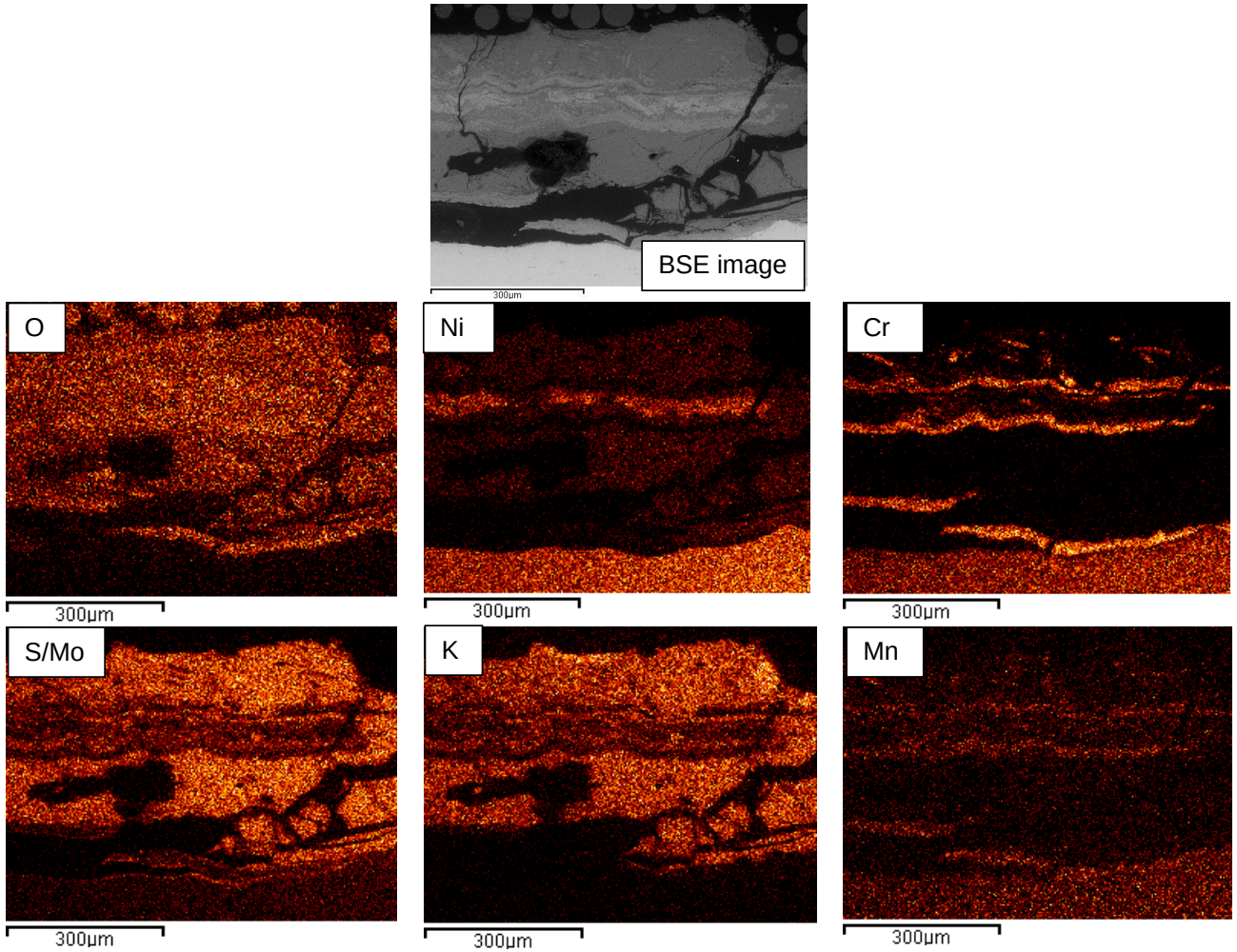

Figure 4-100: BSE image and x-ray maps of alloy 625 covered with deposit D6 exposed to simulated oxy-fired combustion gases (with 6260 vppm SO_2/1700 vppm HCl) at 650°C for 1000 hours

4.7.2.3 EDX Profile

Figure 4-101 illustrates a BSE image and EDX profile for an alloy T92 cross-section exposed with deposit D5 to 6260 vppm SO_2/1700 vppm HCl at 650°C for 1000 hours. The result shows continuous depletion of iron and chromium moving away from the alloy. Silicon is present in between spectrum 3 and 7 (mainly in scale).The detection of high level of oxygen value at spectrum 3 indicates analysis in oxide layer. Low levels of sulphur were detected along the entire line scan, however the highest concentration was located at spectrum 4. suggest sulphur attack. Significant levels of tungsten was also detected at spectrum 1 and 3 (alloy and spinel region). The line scan showed high levels of potassium at the outer region in-between spectrum 6-9 where deposit/scale reactions are occurring.

Figure 4-102 illustrates a BSE image and EDX profile for an alloy 347HFG cross-section exposed with deposit D6 to 6260 vppm SO_2/1700 vppm HCl at 650°C for 1000 hours. The result shows an increasing trend of oxygen between spectrum 1 and 10. Iron depleted up to spectrum 4, however then increased from spectrum 4 to 6 and then depleted again. Chromium highest concentration at spectrum 4 suggesting presence of iron-chromium rich oxide, Nickel shows mixture of upward and downward trend. Sulphur significant concentration was found at spectrum 3. Manganese was detected between spectrum 1 and 6 whereas increasing trend for potassium as moving away from the base metal was observed.

Figure 4-103 presents a BSE image and EDX profile for an alloy 625 cross-section exposed with deposit D6 to 6260 vppm SO_2/1700 vppm HCl at 650°C for 1000 hours. A gradual depletion of iron and chromium level are observed at points moving away from the base metal, however at spectrum 7 a rapid increase was observed. Nickel, a main constituent of alloy 625, also shows a depletion initially, however on moving away from the base metal between spectrum 3 and 6 the nickel concentration stabilised. Within the scale the nickel concentration was highest at spectrum 7. High levels of sulphur and potassium were detected between spectrum 4 and 5.

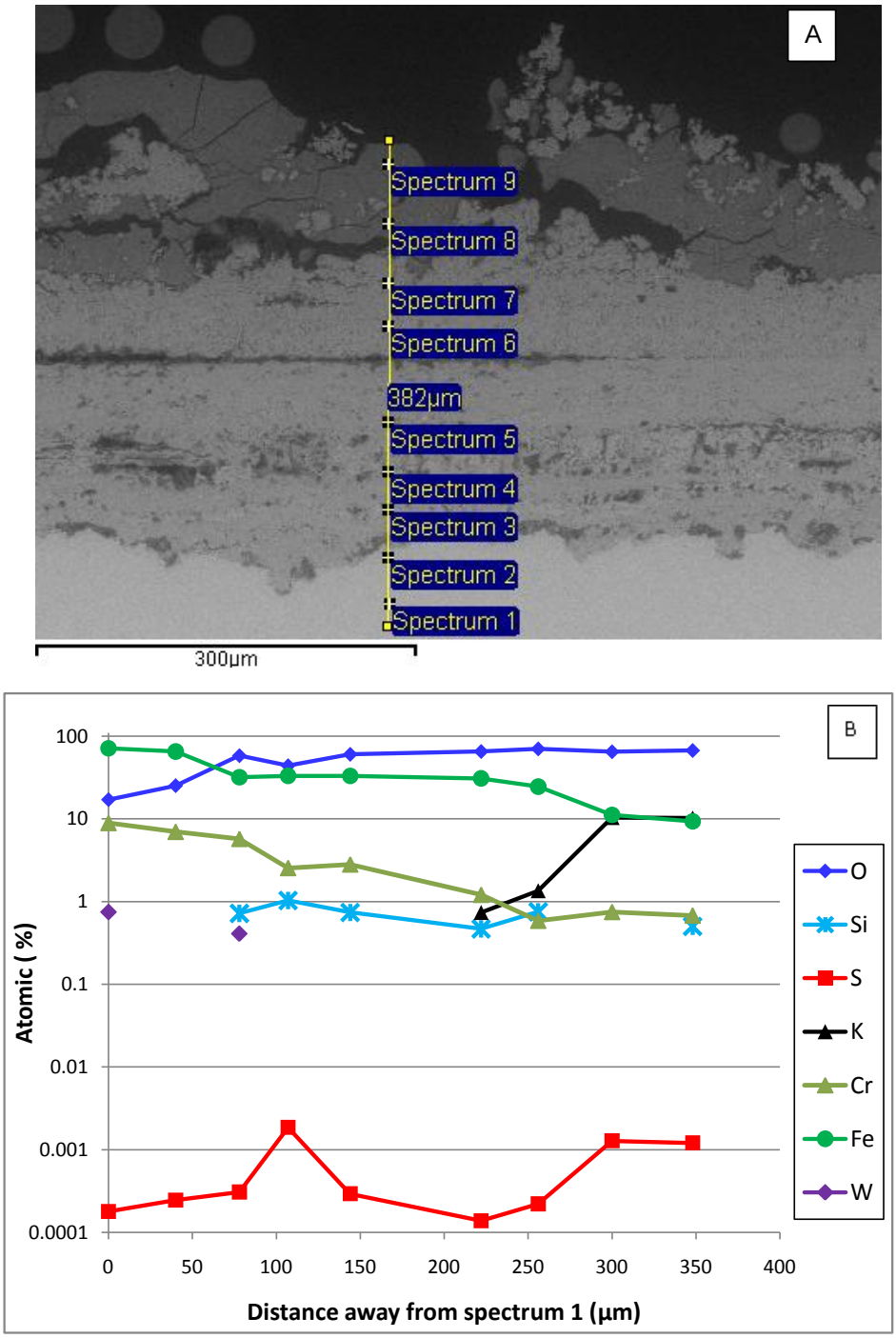

Figure 4-101: BSE image (A) and EDX profile (B) of cross-section alloy T92 covered with deposit D5 exposed to simulated oxy-fired combustion gases (with 6260 vppm SO_2/1700 vppm HCl) at 650°C for 1000 hours

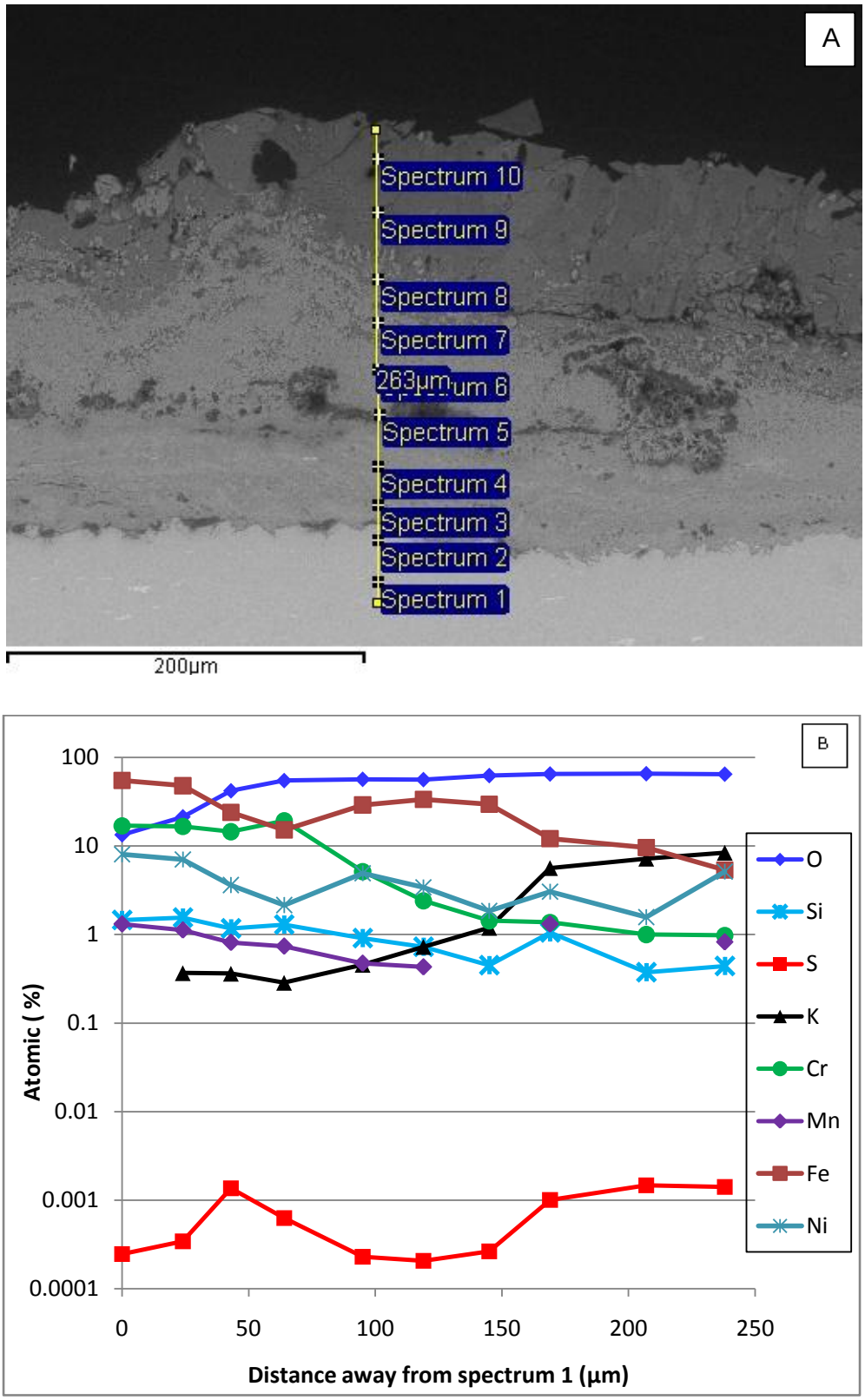

Figure 4-102: BSE image (A) and EDX profile (B) of cross-section alloy 347HFG covered with deposit D6 exposed to simulated oxy-fired combustion gases (with 6260 vppm SO_2/1700 vppm HCl) at 650°C for 1000 hours

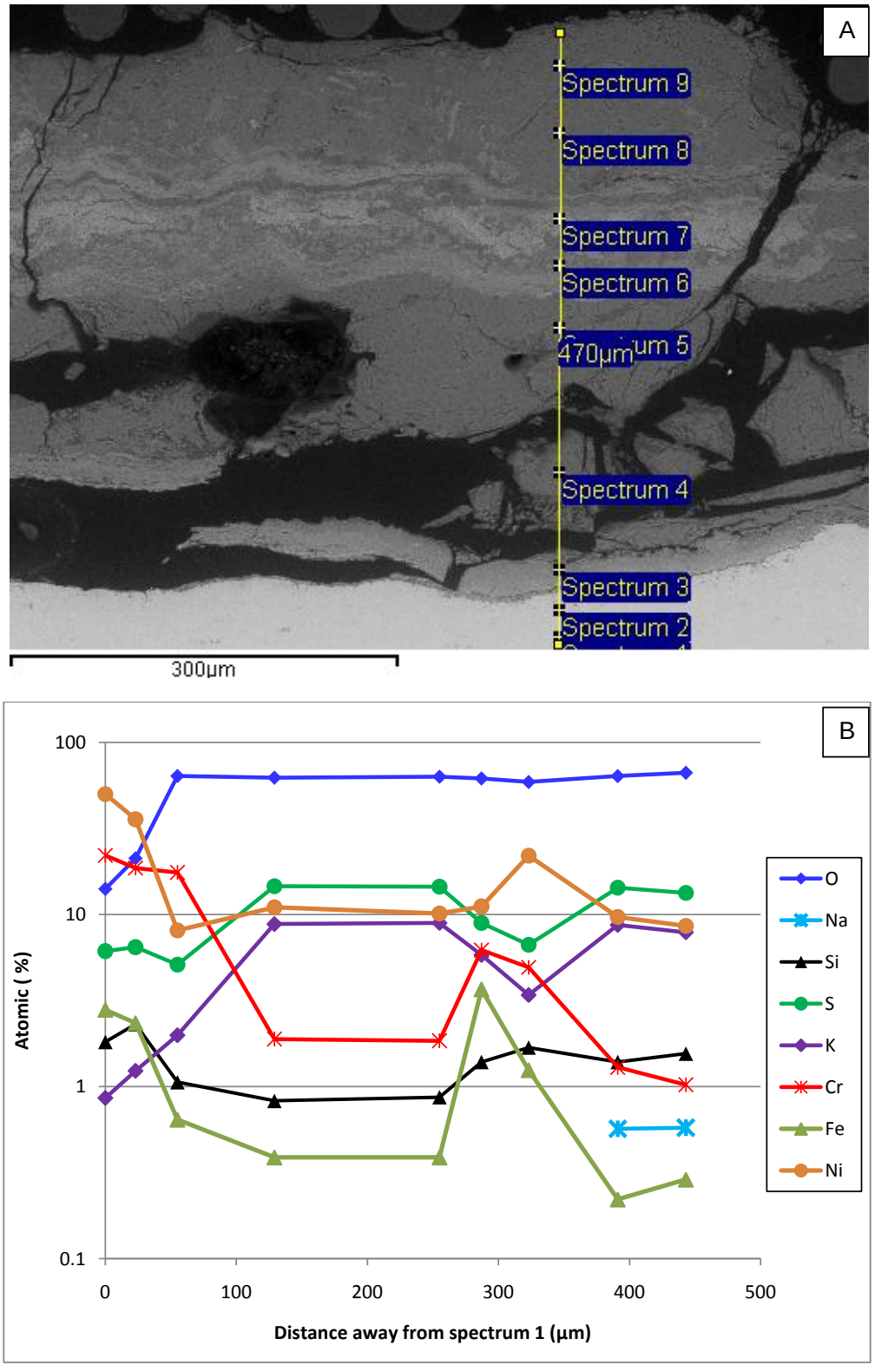

Figure 4-103: BSE image (A) and EDX profile (B) of cross-section alloy 625 covered with deposit D6 exposed to simulated oxy-fired combustion gases (with 6260 vppm SO_2/1700 vppm HCl) at 650°C for 1000 hours

4.7.3 Dimensional Metrology

4.7.3.1 T92

Figure 4-104 illustrates the metal loss data for ferritic alloy T92 exposed to oxy-firing conditions (6260 vppm SO_2/1700 vppm HCl) for 1000 hours at 650°C. These data show that at 50% probability the highest metal loss value observed was approximately 160 µm i.e.(for sample alloy covered with deposit D6, 100%KCl), which is also in line with mass change data. The lowest metal loss value observed was approximately 45 µm for alloy T92 covered with deposit D8. For alloys T92 covered with other deposits (D6, D7, D9 and D10), metal loss values were in range of 80-100 µm

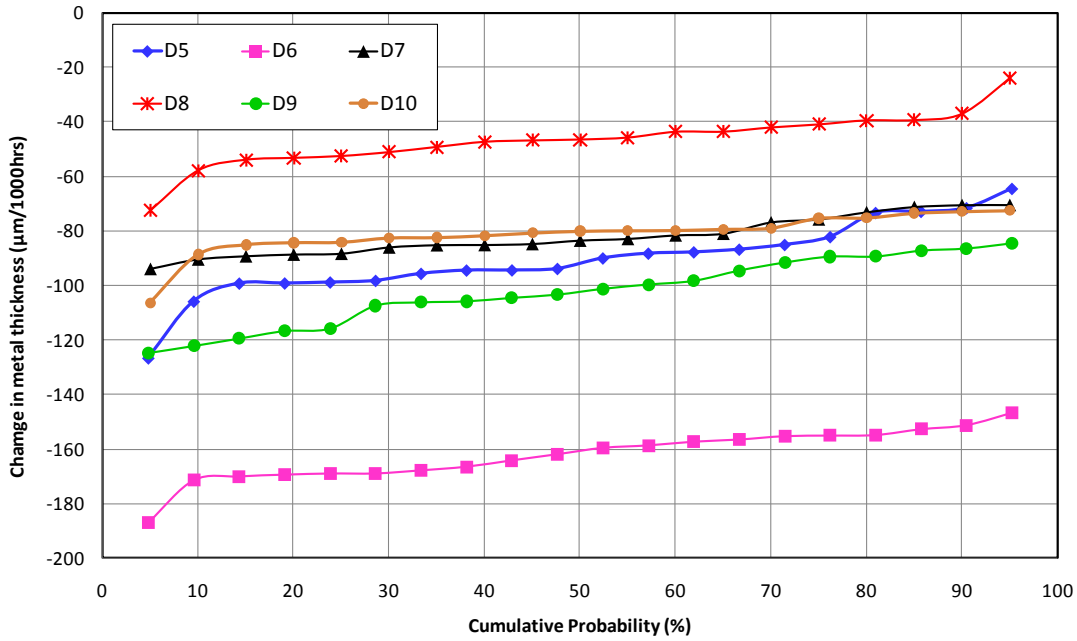

Figure 4-104: Change in metal thickness versus cumulative probability showing the behaviour of alloy T92 covered with various high concentration salt deposits exposed to simulated oxy-fired combustion gas at 650°C for 1000 h

4.7.3.2 347HFG

Figure 4-105 shows metal loss data for austenitic alloy 347HFG exposed to oxy-firing conditions (6260 vppm SO_2/1700 vppm HCl) for 1000 hours at 650°C. As shown in previous results, deposit D6 demonstrated aggressive behaviour and the sample covered with deposit D6 exhibit the highest metal loss value of

approximately 270 µm. Surprisingly metal loss value for alloy 347HFG is almost 100 µm more than metal loss shown by alloy T92 covered with the same deposit D6 in the same conditions. Alloys covered with deposits (D5, D7 and D9) exhibit median metal loss values ~140µm whereas alloys covered with deposit D8 and D10 showed median metal loss values as 80µm and 65µm respectively. Another interesting feature observed for alloy 347HFG samples is a decrease in change in metal thickness at lower probabilities values (such behaviour was also observed previous data for austenitic alloys covered with deposit D1), suggesting localised attack on the sample surface.

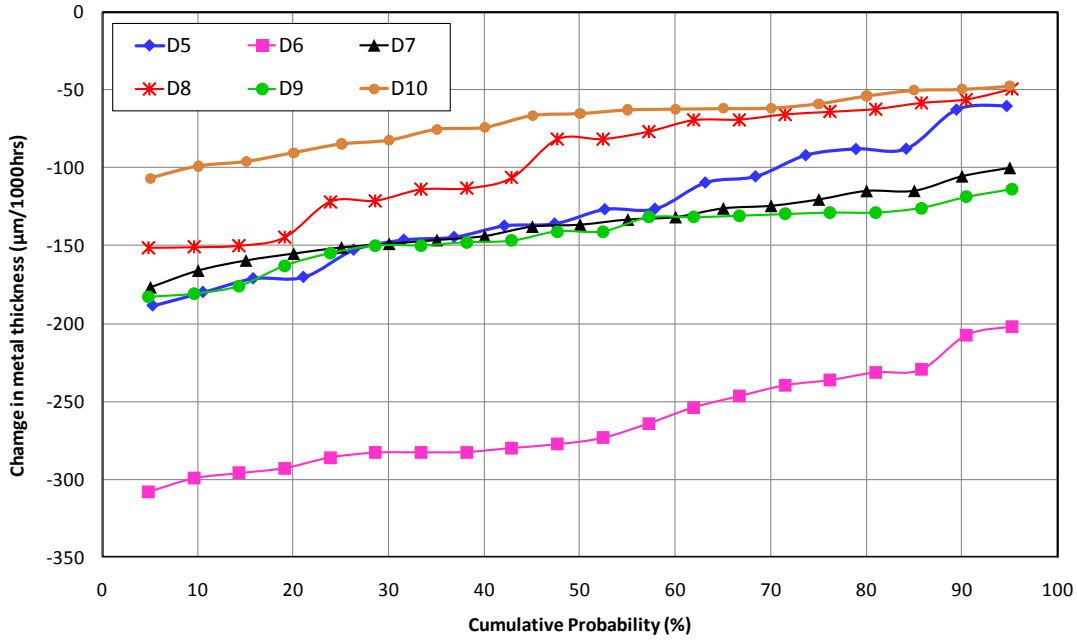

Figure 4-105: Change in metal thickness versus cumulative probability showing the behaviour of alloy 347HFG covered with various high concentration salt deposits exposed to simulated oxy-fired combustion gas at 650°C for 1000 h

4.7.3.3 Alloy 625

The results in Figure 4-106 show the change in metal thickness as a function of cumulative probability for alloy 625 exposed to oxy-firing conditions (6260 vppm SO_2/1700 vppm HCl) for 1000 hours at 650°C. As expected deposit D6 caused the highest metal loss value (~96µm) followed by deposit D5.

Alloy 625 covered with deposit D6 (100% KCl) exhibit median metal loss values (~95 µm) which is approximately three times less than metal loss value compared to alloy 347HFG covered with deposit D6 (100% KCl) and in agreement with mass change data where difference in mass gain values between these alloys (with deposit D6) is also approximately 3 times. Alloys 625 covered with other deposits (D7-D10) exhibit metal loss values below 22 µm.

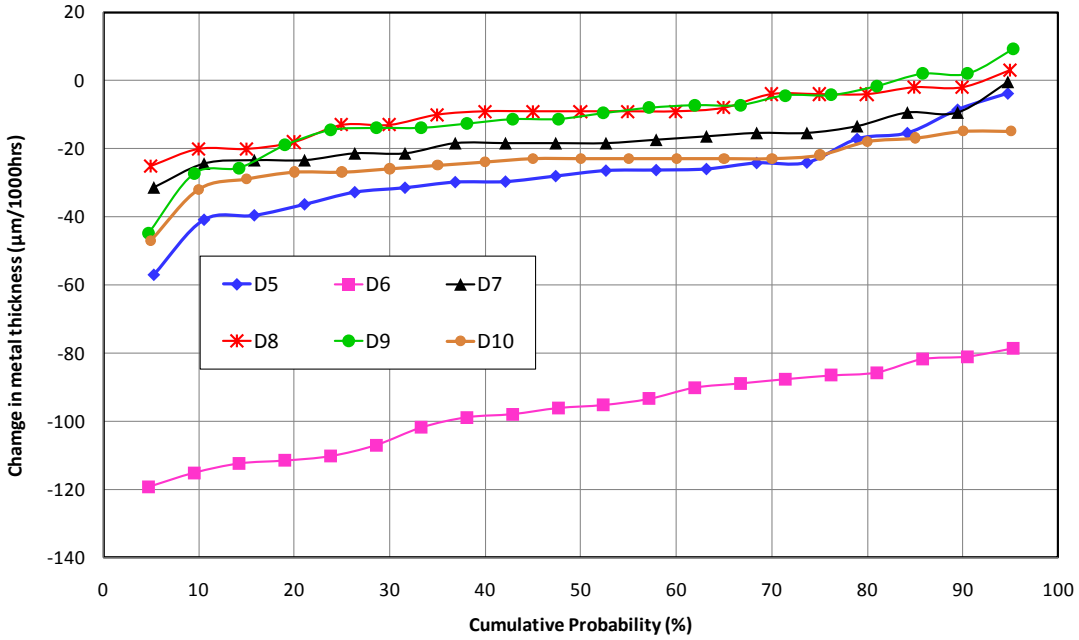

Figure 4-106: Change in metal thickness versus cumulative probability showing the behaviour of alloy 625 covered with various high concentration salt deposits exposed to simulated oxy-fired combustion gas at 650°C for 1000 h

4.7.4 XRD analysis

Figure 4-107 shows that XRD pattern for alloy T92 covered with deposit D5 exposed to 6260vppm SO_2/1700vppm HCl at 650°C for 1000 hours. The distinctive peak of $K_3Fe\ (SO_4)_3$ was clearly observed. Peaks of haematite (Fe_2O_3) are also present. The intensity for $K_3Fe\ (SO_4)_3$ was much higher. EDX analysis of this sample also showed higher levels of potassium, iron and sulphur in the outer region of the scale.

Figure 4-108 presents the XRD pattern for alloy 347HFG covered with deposit D5 exposed to 6260vppm SO_2/1700vppm HCl at 650°C for 1000 hours. Peaks observed for crystalline phases were hematite (Fe_2O_3), potassium sulphate (K_2SO_4) and potassium chromium oxide (K_3CrO_4). Peaks for haematite were more distinctive and intense. Alkali iron tri-sulphate was not detected

Figure 4-109 presents the XRD pattern for alloy 625 covered with deposit D5 exposed to 6260vppm SO_2/1700vppm HCl at 650°C for 1000 hours. The pattern shown peaks of potassium nickel tri-sulphate [$K_2Ni_2(SO_4)_3$]. No other crystalline phases were detected.

Figure 4-110 shows the XRD pattern for alloy T92 covered with deposit D6 exposed to 6260vppm SO_2/1700vppm HCl at 650°C for 1000 hours. Data shows distinctive peaks for alkali iron tri-sulphates [$K_3Fe\ (SO_4)_3$]. Deposit D6 had a high level of KCl salt (100 mol%), however XRD data did not find any KCl. The XRD pattern also revealed presence of a mixed oxide ($Cr_{1.3}Fe_{0.7}O_3$).

Figure 4-111 presents the XRD pattern for alloy 347HFG covered with deposit D6 exposed to 6260vppm SO_2/1700vppm HCl at 650°C for 1000 hours. This XRD pattern shows the presence of crystalline phases of alkali iron tri-sulphate and iron chromium oxide. The phases found for austenitic alloy 347HFG with deposit D6 shown in Figure 4-111 are identical to the phases found for alloy T92 with the same deposit (D6) as presented in Figure 4-110. Another noticeable feature for alloy 347HFG was not being able to detect alkali iron tri-sulphates when covered with deposit D5 (high levels of K_2SO_4), however when

covered with deposit D6 (KCl 100 mol%) it successfully formed alkali iron tri-sulphate crystals.

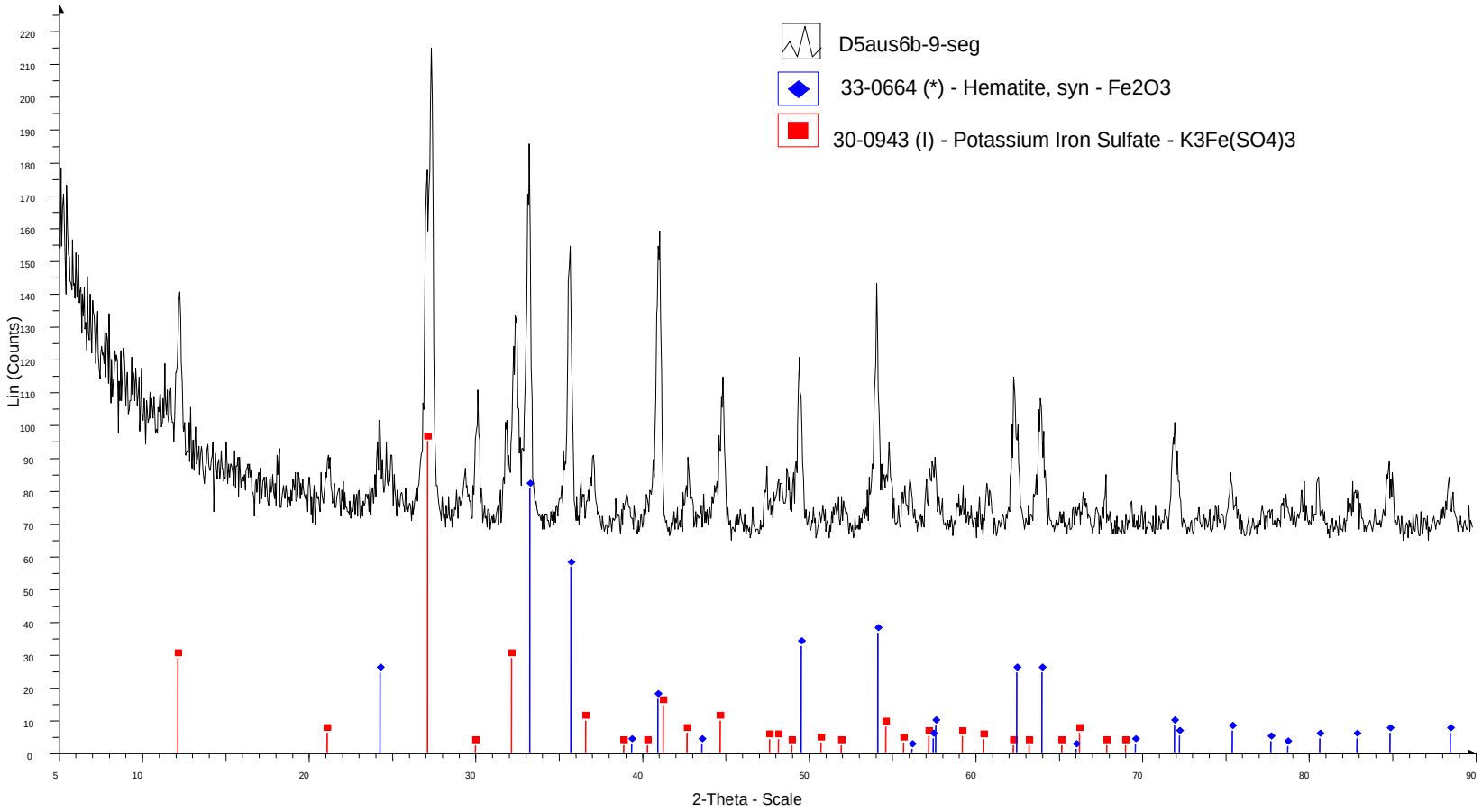

Figure 4-107: X-ray diffraction pattern of alloy T92 covered with deposit D5 exposed to simulated oxy-fired combustion gases (with 6260 vppm SO_2/1700 vppm HCl) at 650°C for 1000 hours

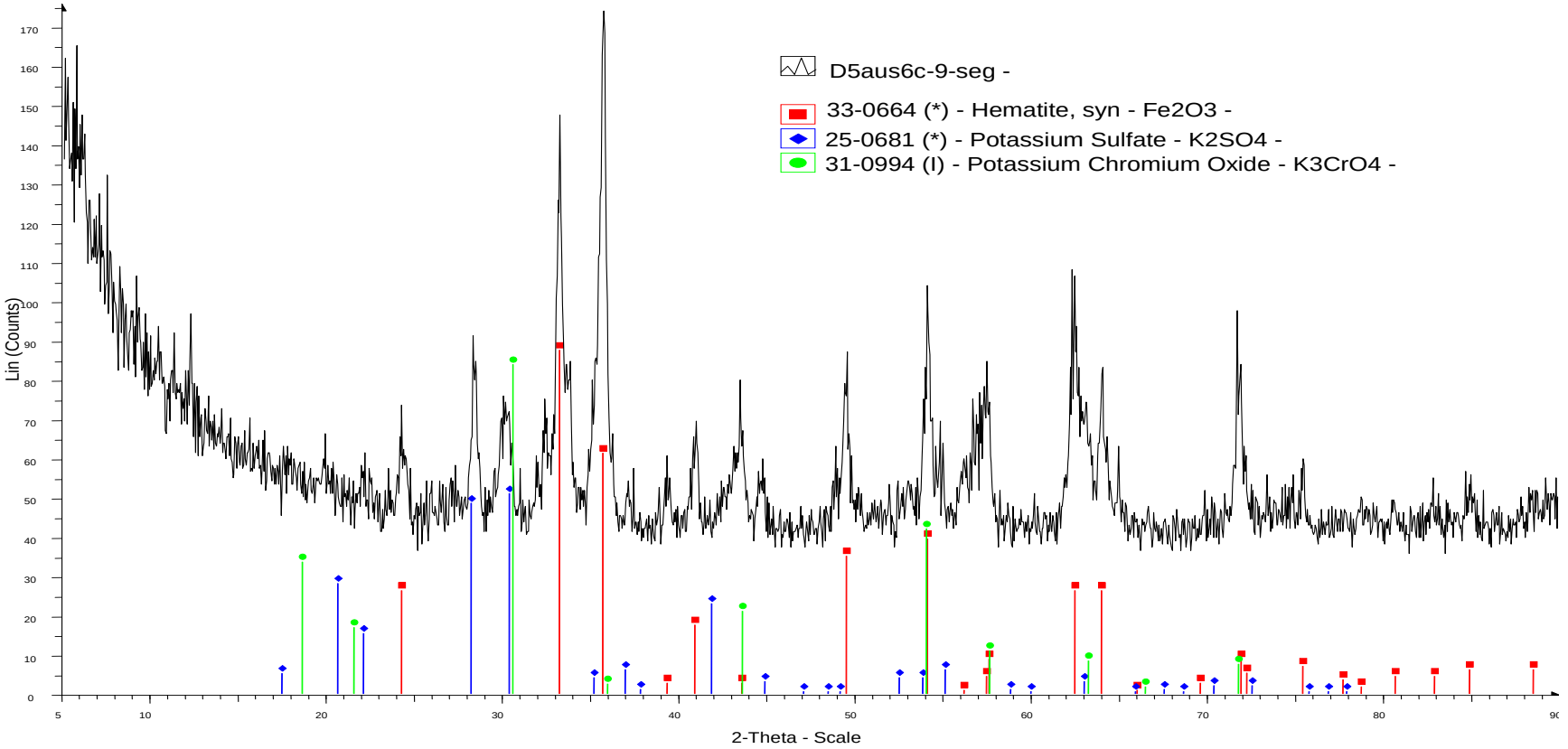

Figure 4-108: X-ray diffraction pattern of alloy 347HFG covered with deposit D5 exposed to simulated oxy-fired combustion gases (with 6260 vppm SO_2/1700 vppm HCl) at 650°C for 1000 hours

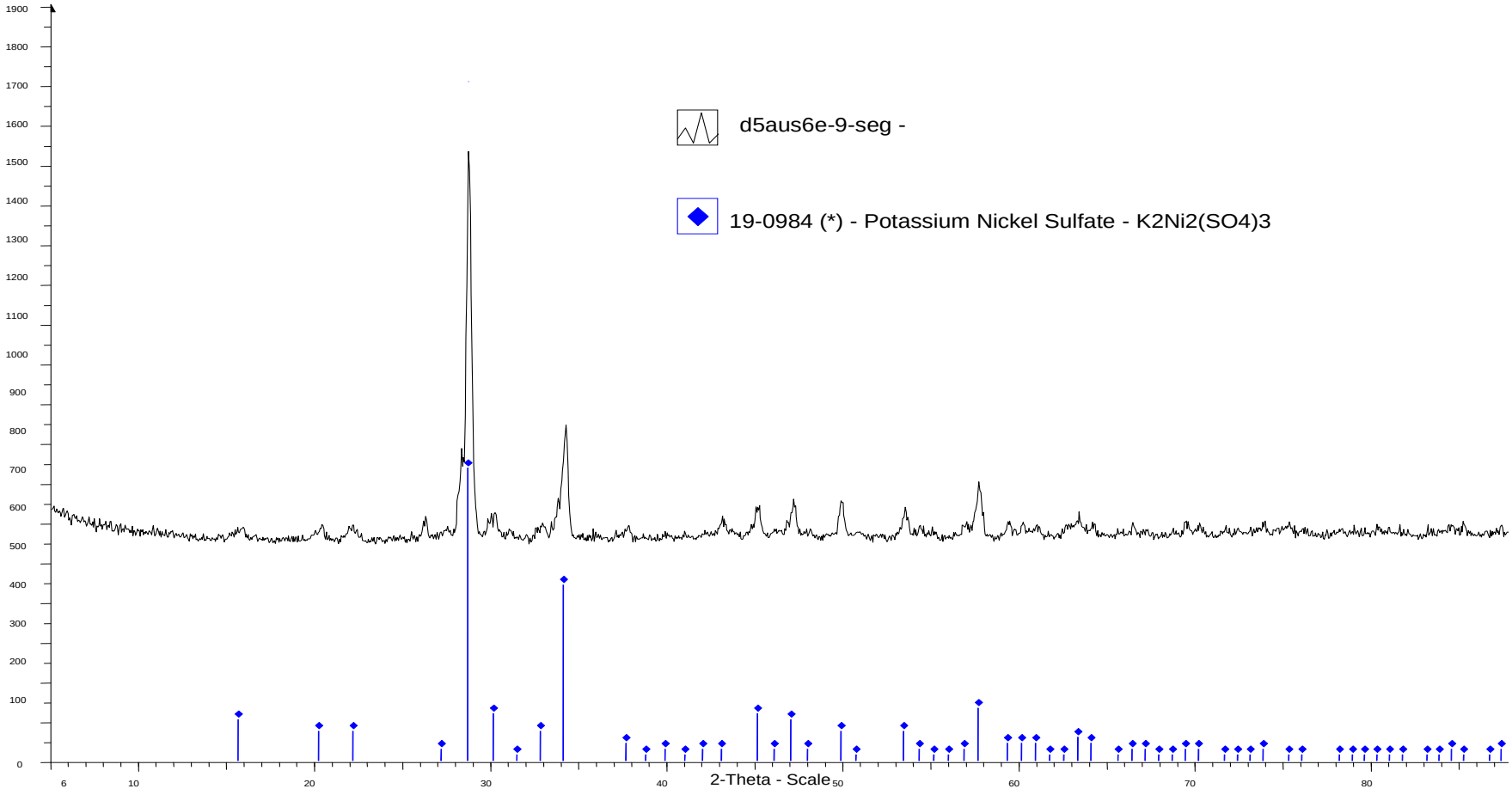

Figure 4-109: X-ray diffraction pattern of alloy 625 covered with deposit D5 exposed to simulated oxy-fired combustion gases (with 6260 vppm SO_2/1700 vppm HCl) at 650°C for 1000 hours

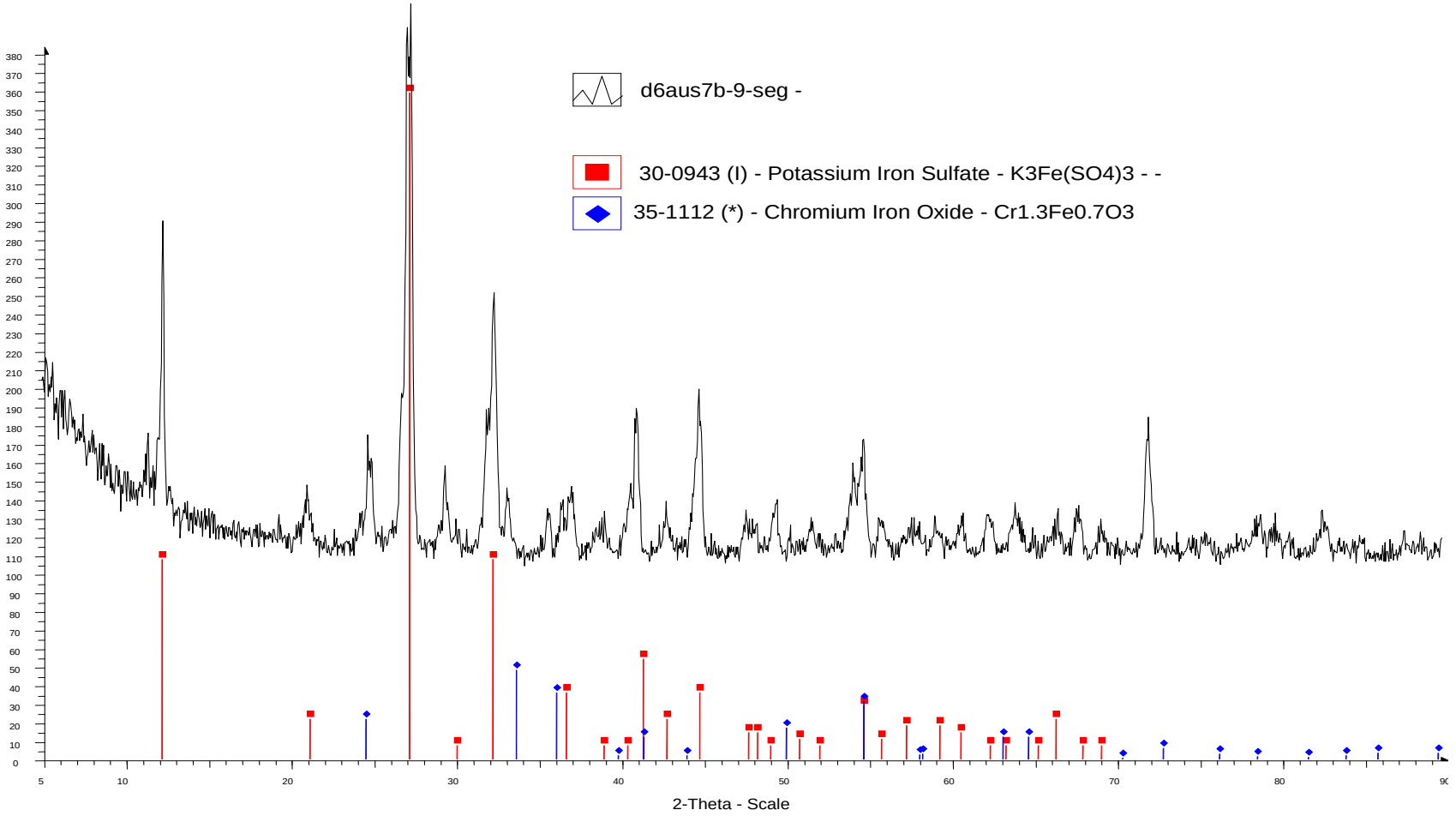

Figure 4-110: X-ray diffraction pattern of alloyT92 covered with deposit D6 exposed to simulated oxy-fired combustion gases (with 6260 vppm SO_2/1700 vppm HCl) at 650°C for 1000 hours

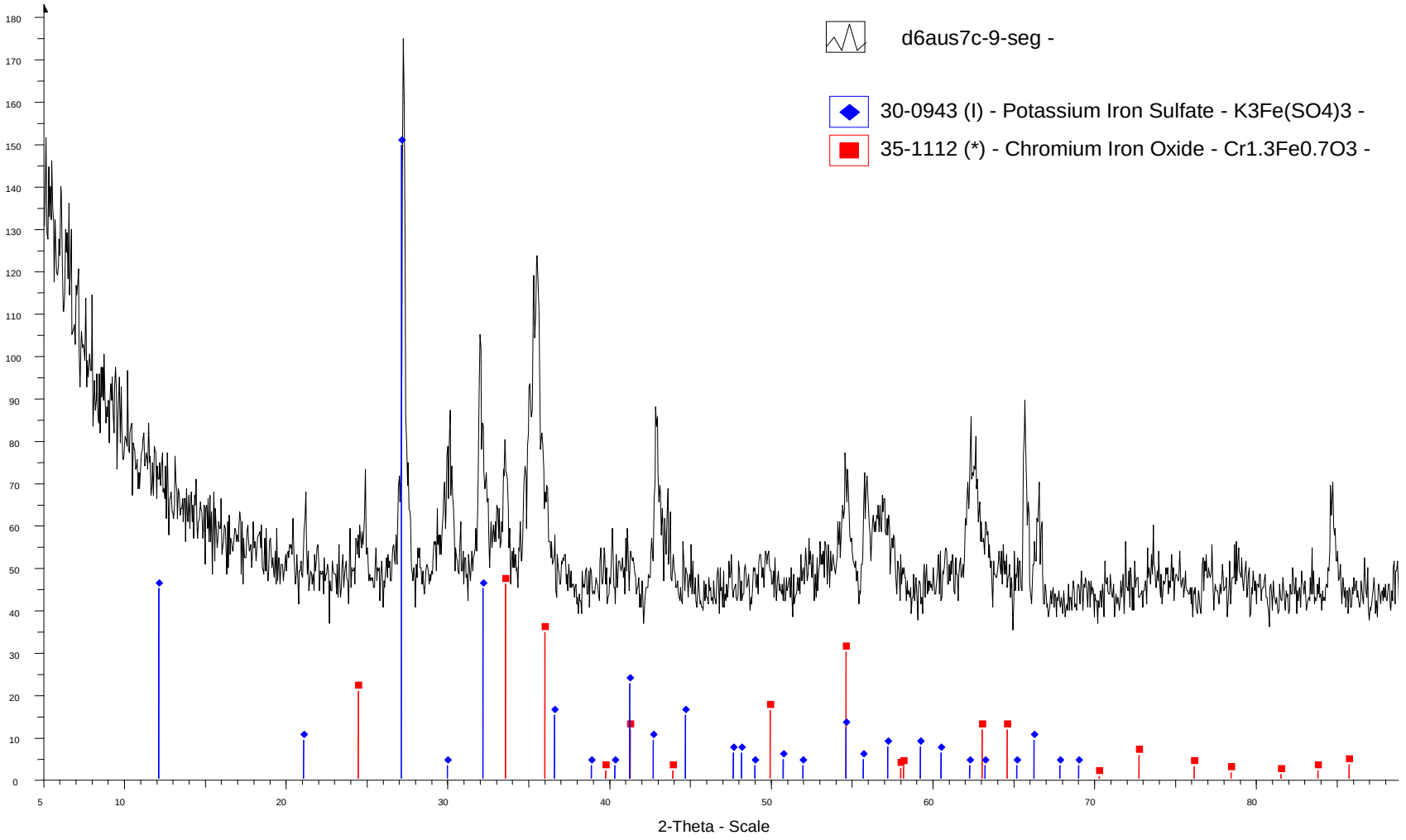

Figure 4-111: X-ray diffraction pattern of alloy347HFG covered with deposit D6 exposed to simulated oxy-fired combustion gases (with 6260 vppm SO_2/1700 vppm HCl) at 650°C for 1000 hours

4.8 Reproducibility

Test number 6 was carried out to find out the repeatability of the samples performance. The test conditions were kept same as test number 5 as mentioned in Table 3-4. A repeat test was quite important to establish the information that the results can be reproduced but is rarely carried out for fireside corrosion due to cost and time. The difference in results between test 5 and 6 could be due to various reason

- Handling errors.
- Balance errors
- Preparation errors
- Dimensional measurements errors

The above mentioned sources of error can affect results from mass change data, SEMEDX analysis and dimensional metrology.

4.8.1 Mass change data

Figure 4-112 illustrates the mass change data of the alloys covered with deposit D4 in oxy-firing conditions at 700°C. These results show the comparison of mass change data of the original test (test 5) and repeat test (test 6). Figure 4-112 (A) is the comparison of ferritic T22 and T92 alloys. The mass gain values in test 5 are slightly higher than values in test 6. This change in behaviour of an alloy in test 6 could be a result of (one or more) errors.

Table 4-1: Comparison of mass change and surface area of alloys covered with deposit D4 in test 5 and 6.

	Test 5	Test 6		Test 5	Test 6	
Alloys	Mass change values	Mass change values	± % mass change	Surface area	Surface area	± % surface area
	(mg/cm^2)	(mg/cm^2)	%	cm^2	cm^2	%
T22-D4	190.8	154.1	19.2	6.21	6.07	2.2
T92-D4	69.1	41.2	40.3	7.20	7.18	0.3
HR3C-D4	2.5	1.2	51.1	6.46	6.45	0.2
625-D4	1.3	1.6	17.9	6.32	6.29	0.5

The samples dimensions (surface area) also could be a reason of mass difference. The mass gain for alloy T22 in test 5 is approx 19% more than the mass gain in test 6. These results show that ferritc alloys are the only ones to exhibit a significant corrosion effect in both tests. Figure 4-112(B) demonstrates that alloy 625 gained approximately 17% higher mass in test 6. The austenitic (HR3C and 347HFG) and nickel based alloy (625) have all shown relatively little corrosion, with a small mass gain observed, but a scatter in behaviour throughout the test. Table 4-1 lists the mass change values and surface area (prior to exposure) of various alloys covered with deposit D4.

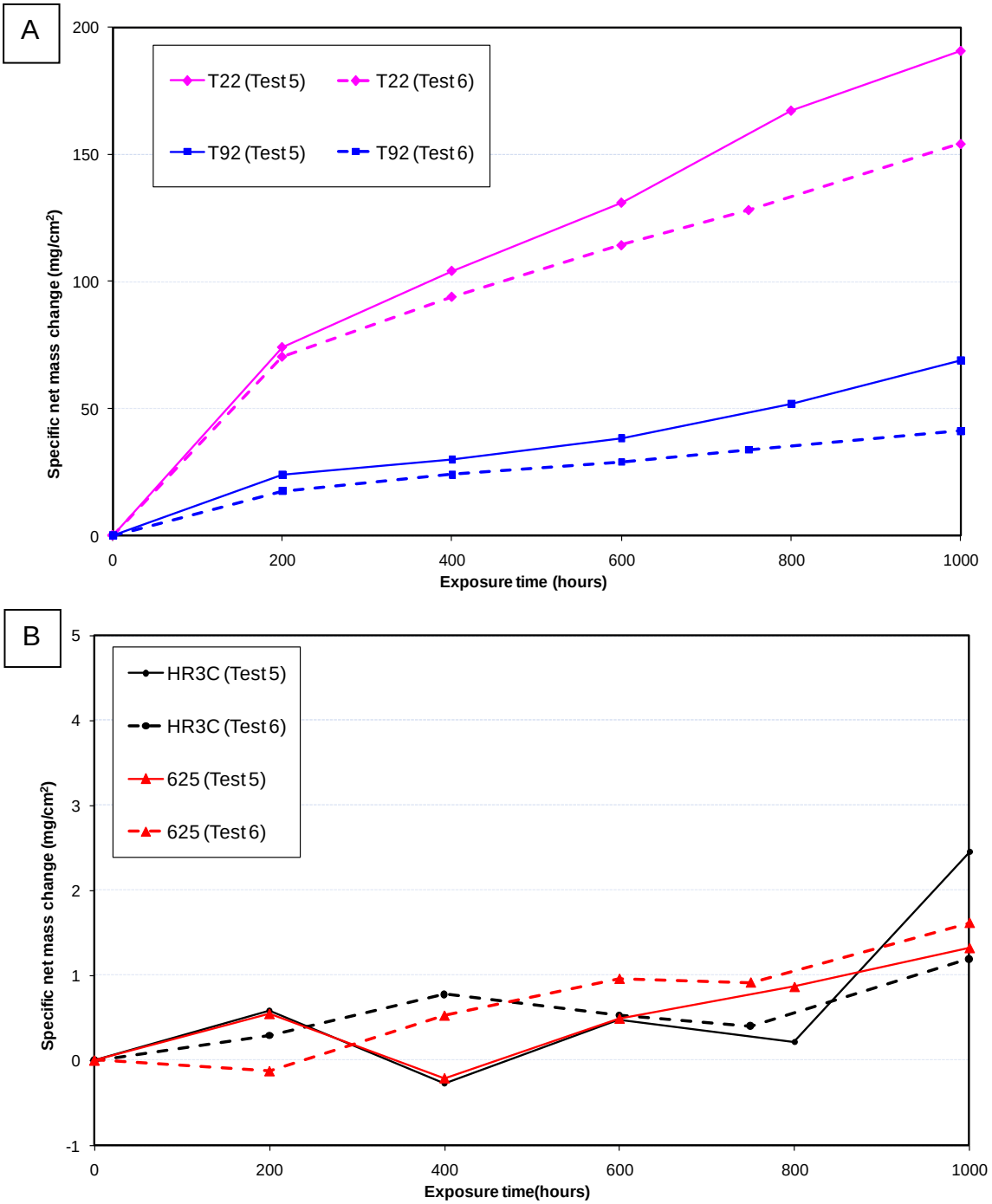

Figure 4-112: Comparison of mass change data of reproducibility test of alloys (A)T22 and T92 and (B) HR3C and alloy 625 samples covered with deposit D4 exposed to simulated oxy-fired combustion gas(with 6260 vppm SO_2/1700 vppm HCl) at 700°C for1000 hours

4.8.2 Scale thickness

Figure 4-113 illustrates the cross-sections of the scales formed on initially bare ferritic T92 and austenitic HR3C alloys after exposure for 1000 hours at 700°C in test 5 and test 6. The scale formed on bare T92 in test 5 was ~ 35% thicker compared to that formed on bare alloy T92 in test 6. The scale on bare HR3C in test 5 was also found to be thicker compared to scale formed on bare HR3C in test 6. Mass change data was also higher in test 5 compared to mass gain values for alloy in test 6. Such differences in scale thicknesses in the reproducibility test could be due to different sources of error as mentioned before. Scales spalling during handling is also possible.

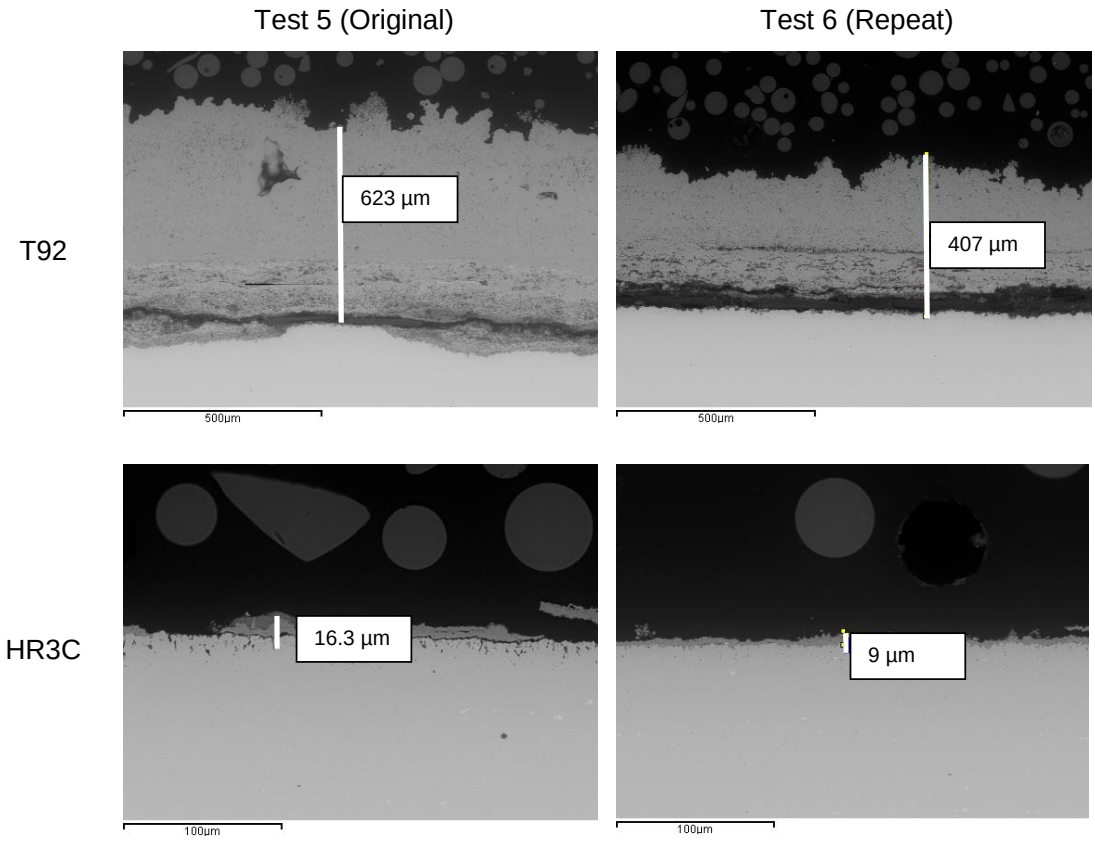

Figure 4-113: BSE images of cross-sectioned scales on bare T92 and HR3C exposed to gases simulating oxy-fired combustion at 700°C for 1000 hours

4.8.3 Dimensional Metrology

Figure 4-114 illustrates the change in metal versus cumulative probability data for alloy HR3C (bare and covered with deposit D1 and D4) and alloy T92

(covered with deposit D1) exposed to gases simulating oxy-fired combustion at 700°C for 1000 hours. These results show the comparison of change in metal data between the original test (test 5) and repeat test (test 6). Figure 4-114 (A) shows that the change in metal value at 50% probability for bare alloy HR3C in test 5 was ~6.6 µm, whereas in the repeat test (test 6) it was found to be ~5.4 µm. Data also shows that change in metal values at 50% probability for alloy HR3C when covered with deposit D4 in test 5 and test 6 were found to be ~13 and ~10 µm respectively. The change in metal values for alloy HR3C both, bare or covered with deposit D4, were higher (by ~18 and 21% respectively) in test 5 (original test) than observed in test 6 (repeat test).

Figure 4-114(B) is a comparison of change in metal data for alloys T92 and HR3C covered with deposit D1 in tests 5 and 6. Theses results show that the, median metal loss values observed in test 5 were slightly higher (by ~12 and 22% respectively) than values obtained for metal loss values in test 6.

Median metal loss values are listed in Table 4-2. These differences between tests 5 and 6 (i.e. higher values observed for mass change, metal loss and scale thicknesses) for both T92 and HR3C could be due to number of different reasons. However, any particular reasons for low values observed in test 6 could not be predicted but likely to be a combination of different source of errors.

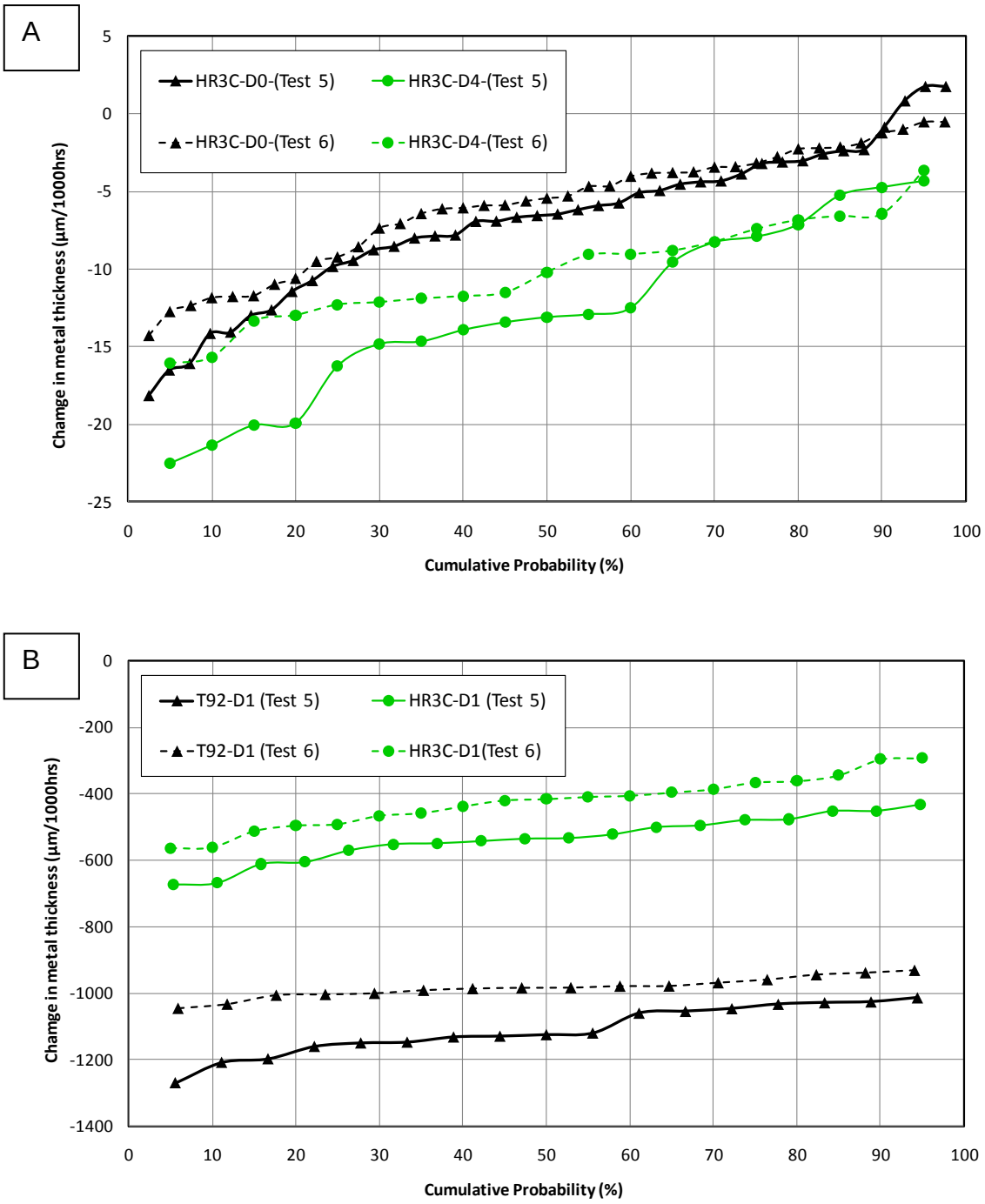

Figure 4-114: Comparison of change in metal of reproducibility test of alloys (A) HR3C bare and covered with deposit 4 (B) T92 and HR3C covered with deposit D1 exposed to simulated oxy-fired combustion gases(with 6260 vppm SO_2/1700 vppm HCl at 700°C for1000 hours

Table 4-2: Comparison of change in metal and surface area of alloys T92 covered with deposit D1 and HR3C bare and covered with deposit D1 and D4 in test 5 and 6.

	Test 5	Test 6		Test 5	Test 6	
Alloys	Change in metal	Change in metal	± % metal loss	surface area	surface area	± % surface area
	(µm)	(µm)	%	(µm)	(µm)	%
T92 -D1	1125.0	983.0	12.6	7.21	7.20	0.1
HR3C-D0	6.6	5.4	18.2	6.44	6.45	0.2
HR3C-D1	534.0	415.0	22.3	6.44	6.44	0.0
HR3C-D4	13.1	10.2	21.9	6.46	6.45	0.2

5 DISCUSSION

5.1 Introduction

Due to the involvement of many variables, fireside corrosion of heat-exchangers within a typical conventional power plant boiler is a very complex process. It is likely that the fireside corrosion rates of superheaters/reheaters will increase due to changes in fuel types and their firing methodologies, as well as steam pressure and temperature. In this chapter, the results of the study of different variables on the corrosion performance of the candidate superheater/reheater alloys will be discussed. Results from test number 9 (deposit stability and materials exposure to simplified deposit compositions) will also be discussed. And finally statistical analysis will be included to finish this chapter. The different variables can be summarised as:

- Temperature
- Alloy compositions
- Deposit compositions

5.2 Temperature effect

Power plants with higher steam temperatures and pressures are going to have to play a significant role in increasing power generation efficiency. The power generation industry used steam temperatures of 540-560°C for decades due to the poor performance of alloys at higher temperatures. The fireside corrosion tests carried out in this PhD thesis have been targeted at four different temperatures (600, 650, 700 and 750°C) to simulate metal temperatures anticipated in future power plants.

5.2.1 Air-firing conditions

Alloys were studied at three different temperature in simulated air-fired combustion gases; 600, 650 and 700°C. Figure 5-1(A) and Figure 5-1(B) summarise the specific net mass change values after 1000 hours exposure

(presented in section 4.2.2) for initially bare alloys and alloys covered with deposit D1, respectively. Ferritic steel T92, initially bare or covered with deposit D1, showed the highest mass gain values compared to the austenitic and nickel-based alloys. The highest mass gain values for all the bare alloys were observed at 650°C. However, for alloys covered with deposit D1 the peak mass gain values were at, different temperatures: for alloys 625 and HR3C this was at 650; whereas for alloys T92 and 347HFG this was at 700°C. Another noticeable feature is that the alloys are more sensitive to increases in temperature when covered with deposit D1 than when initially bare.

The mass change data results in Figure 5-1(B) (for alloy 625 and HR3C) bear a resemblance to the well-known 'bell shaped' curve, often reported for fireside corrosion [9; 28; 32; 60; 63; 131]. These data can be compared with a graph from the literature [132] shown in Figure 5-2, where the peak mass gain values were observed at ~ 650°C. However, it should be noted that gas and alloy compositions in both cases (in this PhD study and example shown in Figure 5-2) were different. The mechanisms involved in fireside corrosion which causes such a downward trend above ~ 650-670°C are well documented in the literature, (section 2.4.3.1.) and further discussed in section 5.4.1. Unfortunately a test was not carried out at 750°C for this gas composition, so it is not known whether 347HFG shows the expected downward trend, but with a peak temperature similar to that reported in Figure 5-2.

Figure 5-1 (A) revealed that the mass change data for the initially bare samples also attained bell shaped curve. However, the gas induced damage mechanisms do not involve the formation of corrosive compounds (alkali iron tri-sulphates), but are due to the well-known temperature dependence of SO_2/SO_3 reactions and the relative rates of sulphidation and oxidation reactions [133].

A

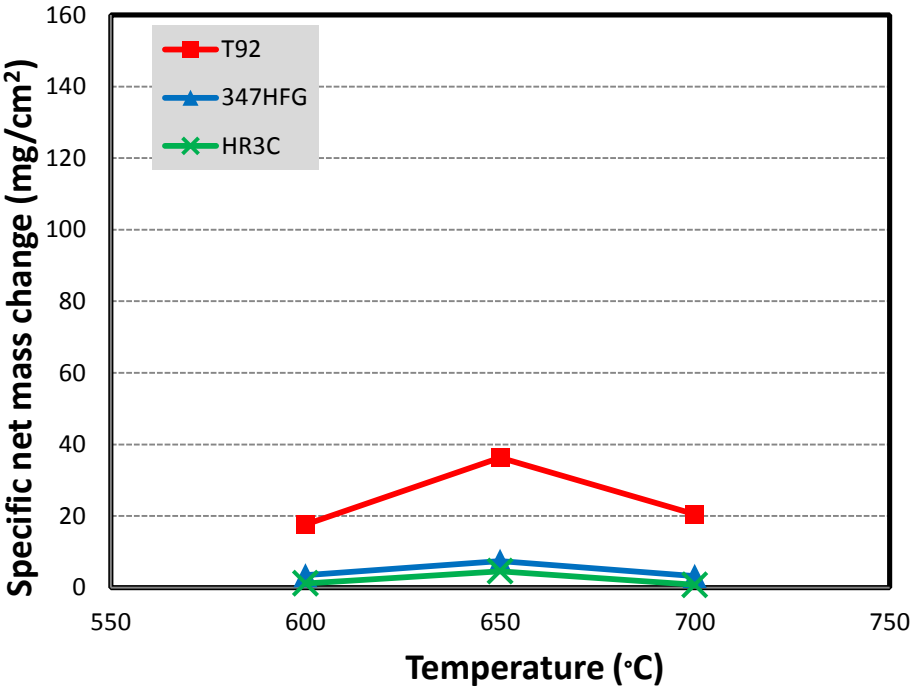

B

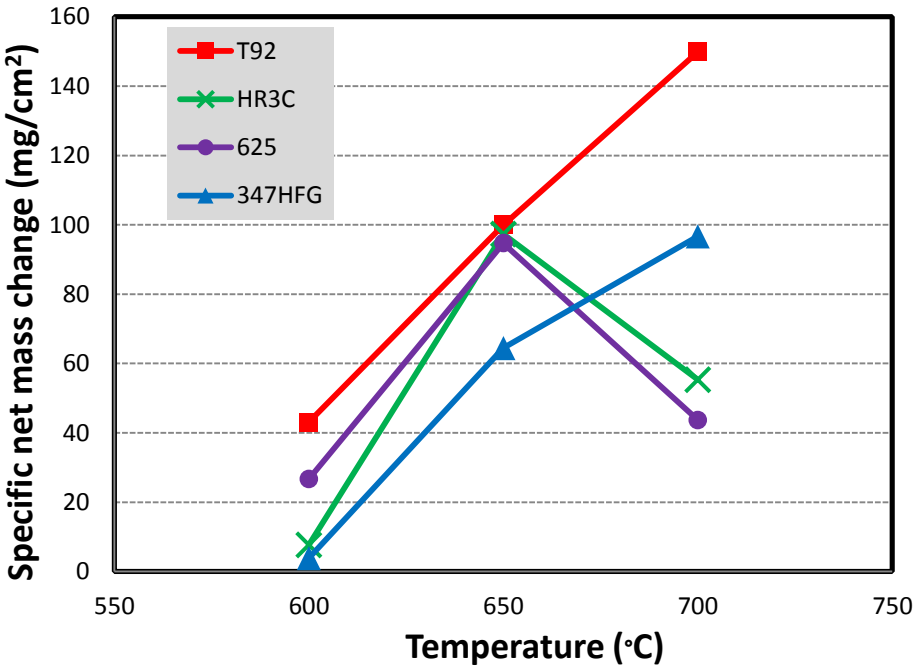

Figure 5-1: Effect of temperature on mass change data for alloys (A) bare and (B) covered with deposit D1 exposed to simulated air-fired combustion gases (with 1300 vppm SO_2/400 vppm HCl for 1000 hours

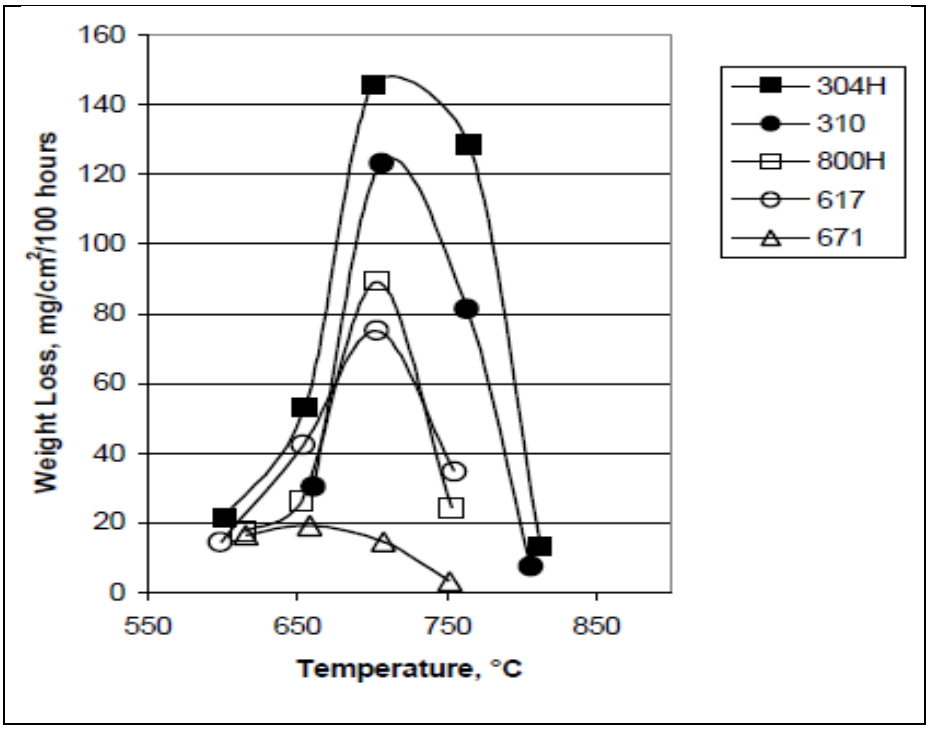

Figure 5-2: An example of a 'Bell shaped' curved of fireside corrosion dependence upon temperature for superheater materials [132]

Figure 5-3 illustrates the effect of temperature on the scale thicknesses of the initially bare alloys. The images of alloy scale thicknesses shown in Figure 4-36 clearly show the thick oxide scale formation at a 650°C followed by decline at 700°C. Scale thickness values observed for these alloys are in line with a trend that is the inverse of alloy chromium content.

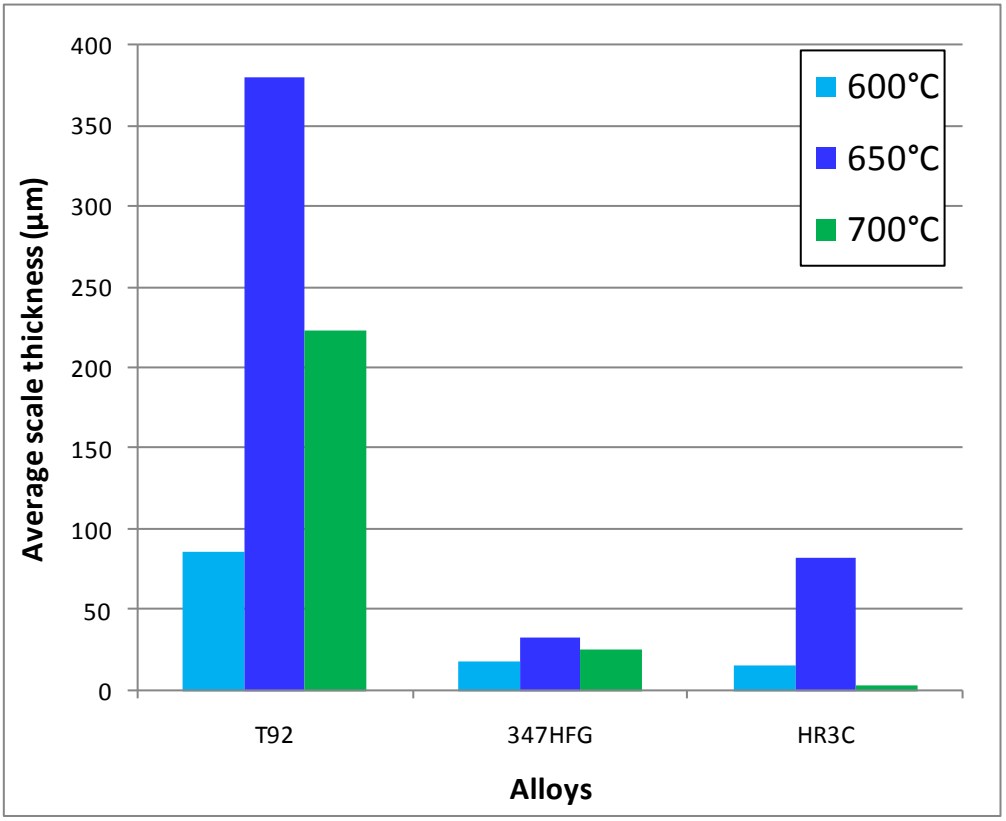

Figure 5-3: Effect of temperature on scale thickness produced in simulated air-fired combustion gases for initially bare alloys at 600, 650 and 700°C for 1000 hours

Figure 5-4 shows change in metal data for alloy T92 in simulated air-fired combustion gases after 1000 hours at the three temperatures. These data clearly show that with 50°C increase in temperature from 600 to 650°C, metal loss values increase. However, with a further 50°C increase to 700°C, the metal loss values decrease. These results and trends are in good agreement with mass change and scale thickness data obtained for the same alloys.

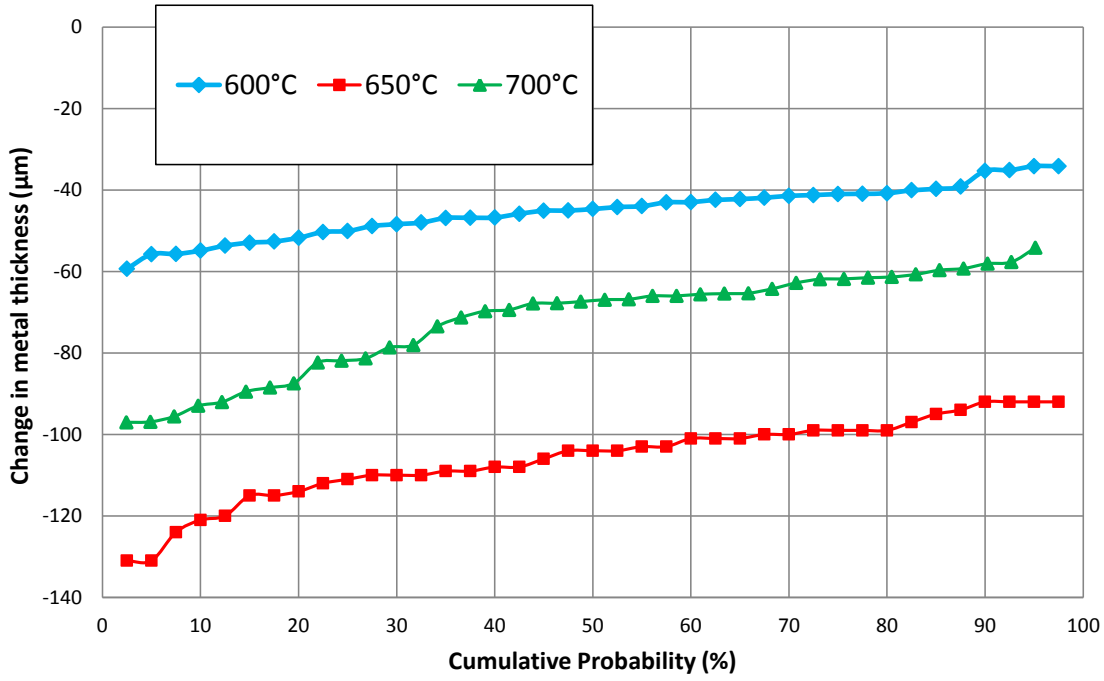

Figure 5-4: Change in metal thickness versus cumulative probability showing the behaviour of bare alloy T92 exposed simulated air-fired combustion gases (with 1300 vppm SO_2/400 vppm HCl) at different temperatures for 1000 hours

Figure 5-5(A) and Figure 5-5(B) shows the effect of temperature on median corrosion damage to alloys T92, 347HFG and HR3C (bare and covered with deposit D1 respectively) after exposure in the simulated air-fired combustion gases for 1000 hours. Figure 5-5(A) reveals that ferritc alloy T92 exhibits higher corrosion damage than the austenitic alloys (347HFG and HR3C) at all three temperatures. It also reveals that the corrosion damage to initially bare T92 alloy significantly increases at 650°C; whereas bare austenitic alloys (347HFG and HR3C) shows little increase in corrosion damage. However, a further 50°C increase to 700°C reduces the corrosion damage for all bare alloys. These metal loss data for bare samples also resemble bell-shaped curves, in line with the mass change and scale thickness results.

Figure 5-5(B) shows the corrosion damage for the alloys covered with deposit D1 in simulated air-fired gases. All the alloys show increased corrosion damage with a 50°C increase in the temperature from 600 to 650°C. However with further 50°C increase to 700°C, all the alloys except T92 experience lower

corrosion damage than observed at 650°C. A few interesting points to be noticed in the corrosion damage results for samples covered with deposit D1 are:

- Corrosion damage went up by ~ 75 % with every 50°C for alloy T92 (280 µm at 600°C, 505 µm at 650°C and 855 µm at 700°C)
- At 650°C corrosion damage values for austenitic alloys 347HFG and HR3C are very similar to ferritic alloy T92. i.e. 505 µm ±15
- At 650 and 700°C, all alloys show corrosion damage values higher than 100 µm (i.e. much higher from traditional values of superheaters 40-50 µm /1000 hours [17])

The trend of corrosion damage with temperature for alloy T92 covered with deposit D1 is also in line with mass change and scale thickness data (Figure 4-37 BSE image of sample cross-section shows thick and dense scale formed at 700°C). Corrosion damage results for HR3C and 347HFG are also in good agreement with scales morphologies (Figure 4-37 showed thick scales developed on both austenitic alloys at 650°C). Such an effect of temperature on corrosion rates was also reported by Bankiewicz et.al [134], with an increase in corrosion damage with increase in temperature, and higher corrosion damage observed for low chromium alloy when compared to higher chromium alloys. However the temperature range (350-600°C) for their studies was lower than the temperatures used for this present study (600-700°C).

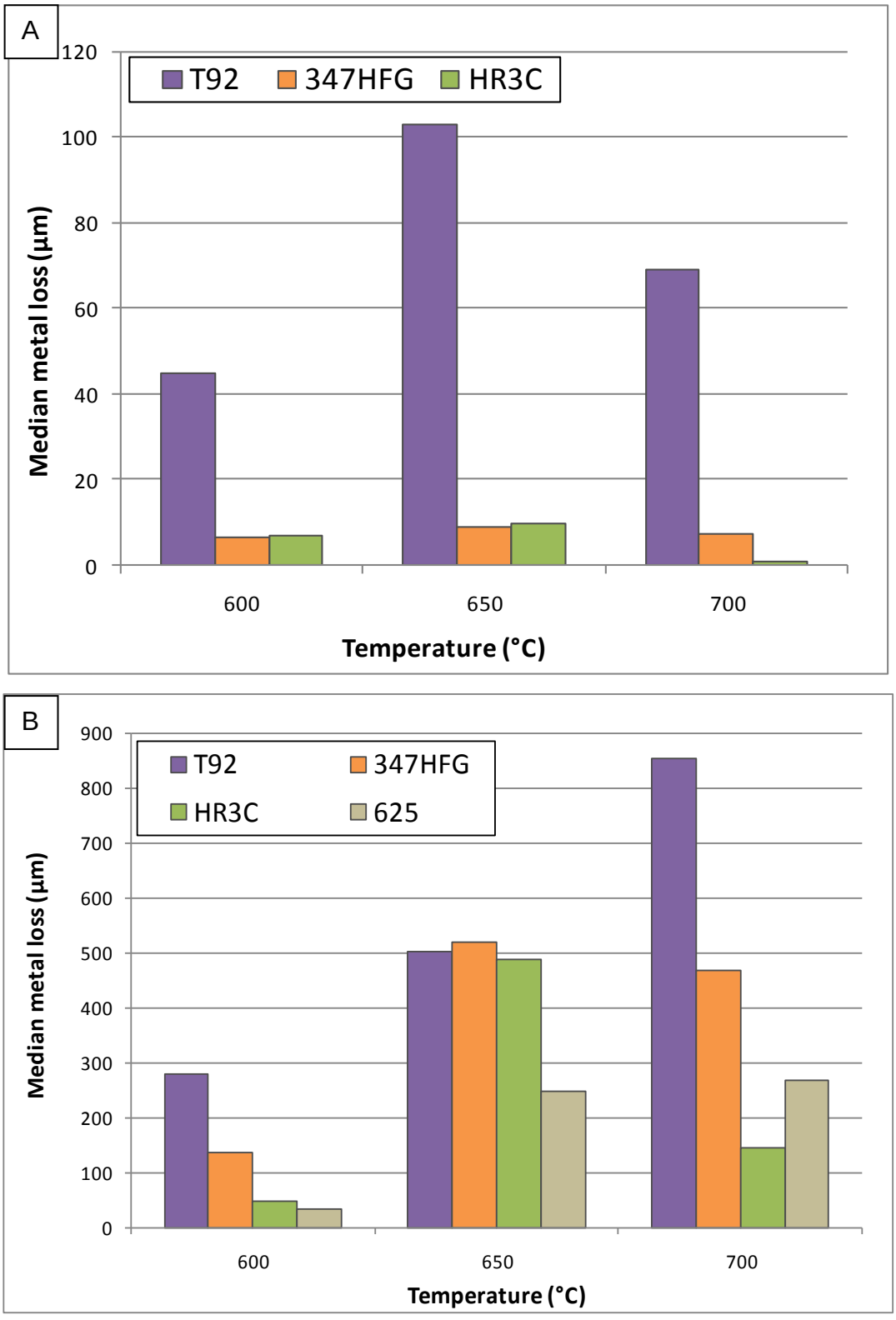

Figure 5-5: Effect of temperature on median metal loss damage for (A) bare alloys and (B) alloy covered with deposit D1 after 1000 hours exposure in the simulated air-fired combustion gases

5.2.2 Oxy-firing conditions

Figure 5-6 summarises the effect of temperature on mass change values of alloys bare and covered with deposit D1 at the four temperatures (600, 650, 700 and 750°C) after 1000 hours of exposure in oxy-fired combustion gases. Such mass changes are the combined effect of the reaction of the alloys (and deposits for samples covered with deposit D1) with the surrounding gases, and can include scale growth, deposit/scale spallation, deposit evaporation, etc.

The result in Figure 5-6(A) shows ferritic alloy T22 had the highest mass change value. The mass gain values for alloys T92 and 347HFG were in the order as 700 > 650 > 600°C, such temperatures effect, on alloys mass gain values (in air-fired conditions) has been reported in the literature [60; 65]. Thus, the ranking follows the temperature change. Similarly the results in Figure 5-6(B), for alloys T92, 347HFG, HR3C and 625 covered with deposit D1, also show an increasing mass gain trend with increase in temperature in an order as 700 > 650 > 600°C. However, with a further increase to 750°C for both, (initially bare alloys or alloys covered with deposit D1) the data show less mass gain, with only alloy T22 (bare or covered with deposit D1) showing further mass gains. The results shown in Figure 5-6 are a fine representation of the well-known ‘bell shaped curve’ and can be compared with work reported by different researchers showing the changes in fireside corrosion damage of various alloys with increases in temperatures [9; 28; 32; 60; 63; 64; 87].

The increase in mass gain values with the increase in temperature were expected, i.e. the materials showed a typical behaviour (high reaction rates with an increase in temperature). However, the reduced mass gain values observed at 750°C in both cases are for different reasons. For bare samples, the decrease in corrosion rates at 750°C is due to the SO_2/SO_3 reaction. Whereas for samples covered with deposit D1, reduced mass gain values at 750°C revealed a typical fireside corrosion behaviour of superheaters (mainly due to the instability of the corrosive compound alkali-iron tri-sulphate). The composition of deposit D1 (Table 3-2) was intended to ease the formation of

alkali-iron tri-sulphates, which are believed to be one of the possible causes of fireside corrosion damage to materials under superheater/reheater operating conditions [17; 32; 60; 63].

There is no data available in the literature which matches the conditions of this study (simulated oxy-fired gases from the combustion of coal and biomass) to compare the data generated. However, a recent work by Pirón Abellán et al. [117] in high levels of CO_2/H_2O (in absence of O_2) shows the effect of temperature (from 550-700°C). Tests were carried out on bare steel (9-12% Cr) samples shows mass change data was similar to this study i.e. increase in mass gain values with increase in temperature and then further reduced mass gain values with increase in temperature (bell-shaped curve). The mass change data for low chromium alloy 13CrMo44 (1% Cr) is also in good agreement for low chromium alloy T22 in this PhD study, which shows an increase in the mass gain value with temperature.

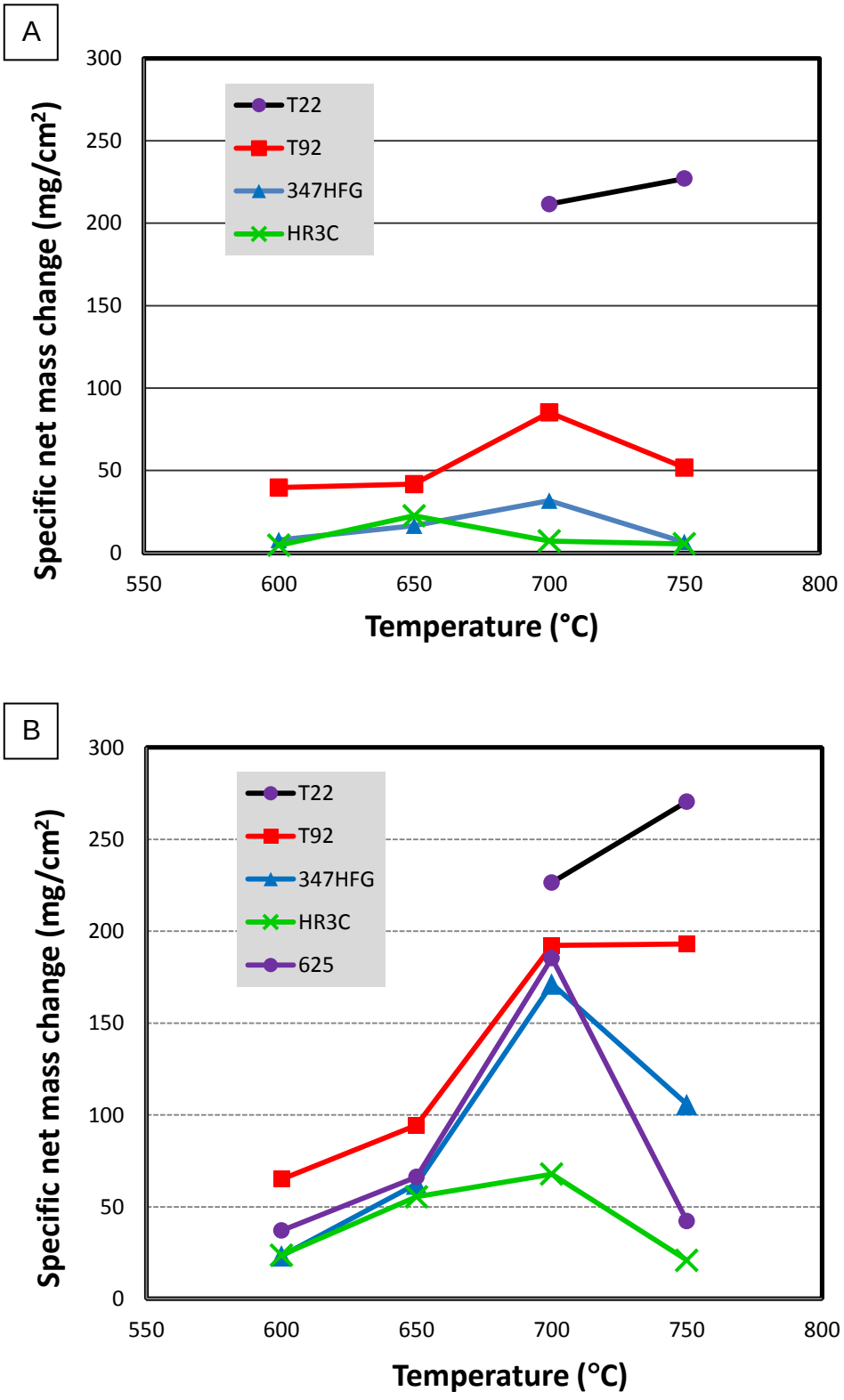

Figure 5-6: Effect of temperature on mass change data for alloys (A) initially bare and (B) covered with deposit D1 exposed to simulated oxy-fired combustion gases (with 6260 vppm SO_2/1700 vppm HCl) for 1000 hours

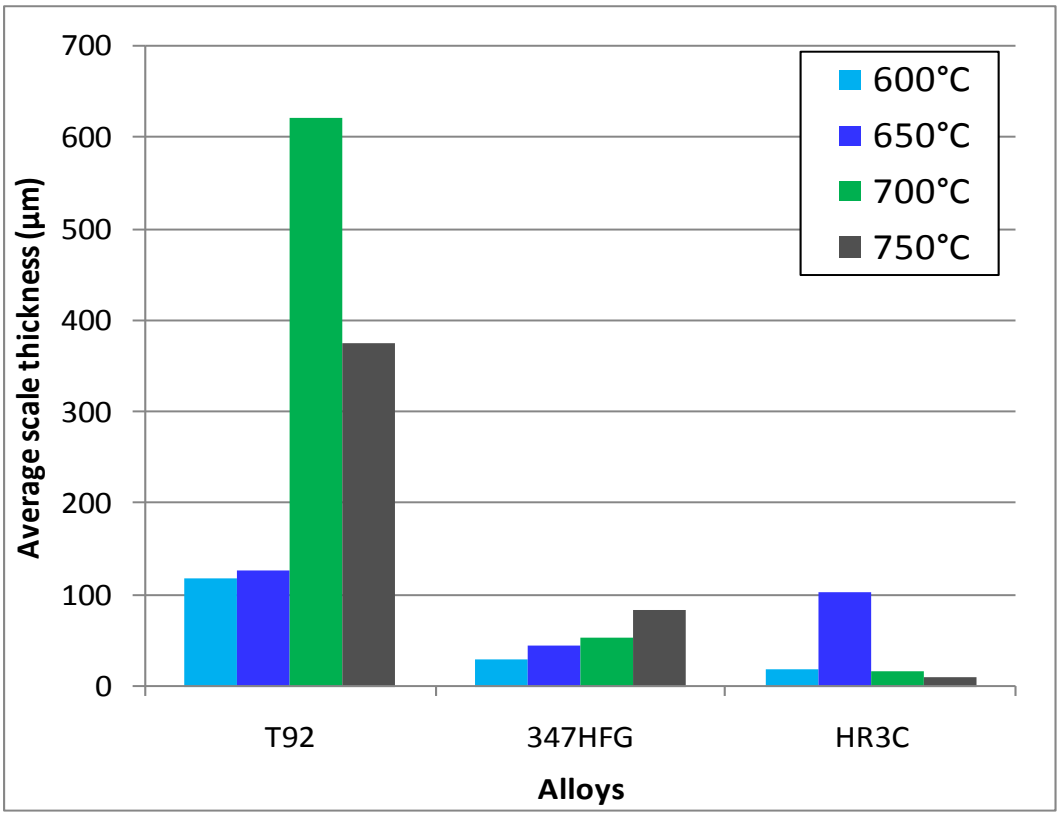

Figure 5-7: Effect of temperature on scale thickness produced in simulated oxy-fired combustion gases on bare alloys at 600, 650 and 700°C for 1000 hours

Figure 5-7 illustrates the effect of temperature on the thickness of scale grow on initially bare alloys. Alloy T92 showed thick scales developed with the increase in temperature to 700°C and then decline to 750°C, which is also consistent with mass change data. Alloy 347HFG scale thicknesses increased with temperature; i.e. in contrast to mass change data, where the peak mass gain value was observed at 700°C followed by a decline at 750°C. Scale thickness results for alloy HR3C in Figure 5-7 are also in line with mass change data; i.e. highest mass gain value and thickest scale was observed at 650°C followed by decreased in values. However, scale thicknesses do not necessarily correlate with mass change data; mainly due to scale spalation (as discussed under section 3.3.2.). The effect of temperature on corrosion damage is also very obvious in the BSE images for alloys cross-section shown in Figure 4-39 where extent of internal damage on 347HFG increases with temperature, with limited damage visible after 1000 hours at 650 ºC, but much more extensive damage being found after 1000 hours at 700 ºC.

Figure 5-8 shows dimensional metrology data for alloy T92 covered with deposit D1 in oxy-firing condition after 1000 hours at four different temperatures. These data show that with a 50°C increase in temperature, more than double the change in metal value was observed. However at the highest temperature of 750°C change in metal value decreased compared to the 700°C data but still higher than observed at 650°C. These data is also in good agreement with scale morphology results shown in Figure 4-40

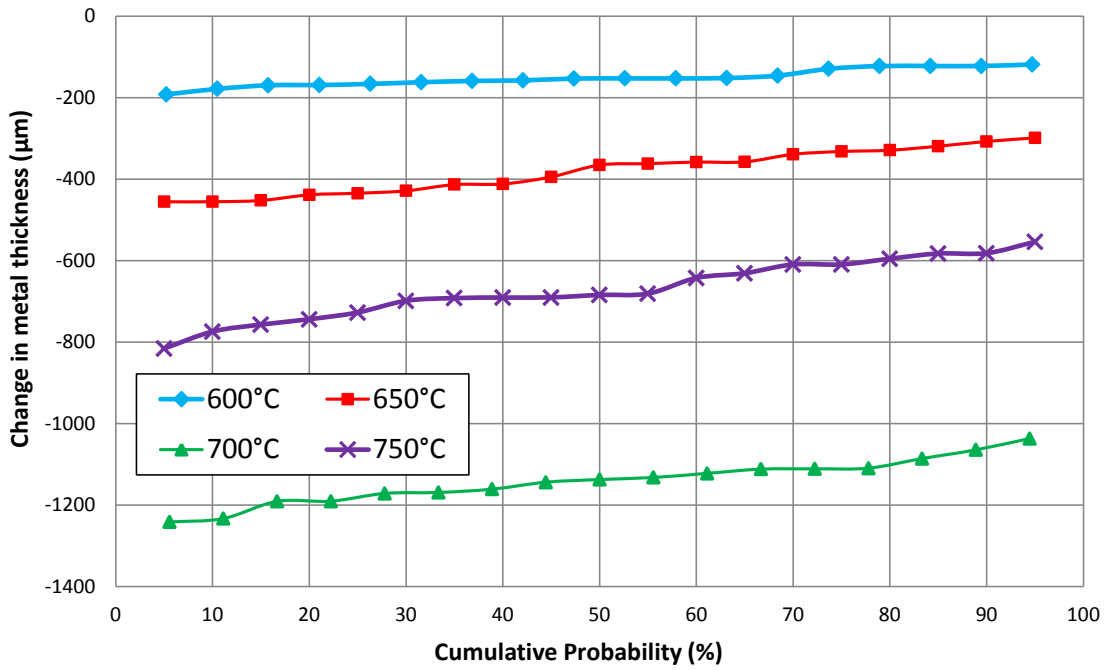

Figure 5-8: Change in metal thickness versus cumulative probability showing the behaviour of bare alloy 347HFG covered with deposit D1 exposed to simulated oxy-fired combustion gases (with 6260 vppm SO_2/1700 vppm HCl) at different temperatures for 1000 hours

Figure 5-9(A) and Figure 5-9(B) summarise the effect of temperature on metal loss of initially bare alloys and alloys covered with deposit D1 at the four temperatures (600, 650, 700 and 750°C) after 1000 hours of exposure in simulated oxy-fired combustion gases. The data generated in this study for the bare samples are consistent with a combined oxidation and sulphidation mechanism at lower temperatures moving towards oxidation alone at the highest exposure temperature. Such a change in balance between these

degradation mechanisms with a change in temperature is well known [133]. In the particular gas environment used in these tests there is quite a high level of SO_x and, at the lower temperatures in this test programme, the SO_3/SO_2 balance is expected to favour SO_3, whereas at the highest temperature it is expected to favour SO_2. The rate of combined oxidation/sulphidation is expected to be higher than for oxidation alone, and so is the expected peak in the damage levels as a function of temperature. Figure 5-9 (A) clearly shows increasing trend of corrosion damage with increase in temperature up to 700°C followed by a decline at 750°C. The highest median metal loss values for bare alloys T92 and 347HFG observed at 700°C are also consistent with mass change data.

The results shown in Figure 5-9(B) revealed that the samples exposed to the gaseous atmosphere covered with the applied surface deposit D1 showed considerably more damage than those exposed to just the gaseous environment. In all cases the damage exceeded the usual target of 40-50 µm/1000 hours for superheater/reheater materials in coal-fired power systems. However, it should be noted that this was intended to be an accelerated exposure test with the deposit composition targeted at enabling the formation of the complex alkali-iron tri-sulphate compounds. It has been frequently reported that the formation of such complex molten compounds is responsible for fireside corrosion on superheaters/reheaters [32; 135]. These compounds need to be stabilised by SO_3 and melt at much lower temperatures than alkali sulphates (e.g. 1/1 molar ratio $(Na/K)_3Fe(SO_4)_3$ has a melting point of ~550 °C) [32]. The higher SO_X level in the simulated oxy-fired combustion gas environment used in these tests would be expected to stabilise such compounds at higher temperatures than in traditional combustion gases.

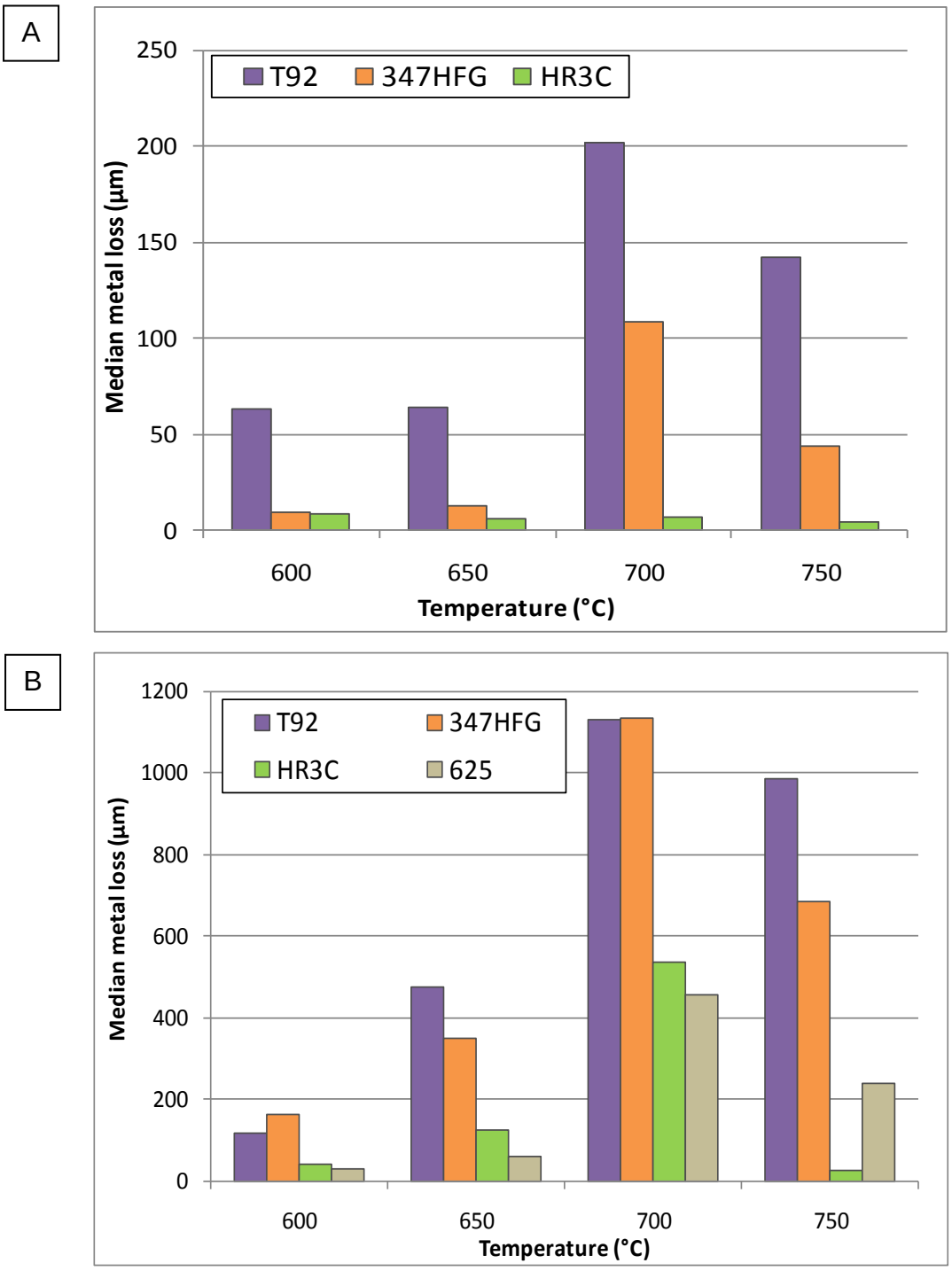

Figure 5-9: Effect of temperature on the median metal loss damage for (A) initially bare alloys and (B) alloy covered with deposit D1 after 1000 hours exposure in the gases simulated oxy-fired combustion gases

Under these gas and deposit conditions, the corrosion rates were found to increase with temperature up to 700 ºC followed by decrease in corrosion rate (Figure 5-9); this is consistent with the frequently reported bell-shaped curve for fireside corrosion in air-fired power plants by several researchers [32; 60; 63]

but with peak shifted to higher temperature. As long ago as 1980 work carried out by Raask.et.al [81] reported that fireside corrosion behaviour of superheater tubes in coal/air fired power plant followed a bell-shaped curve as shown in Figure 5-10.

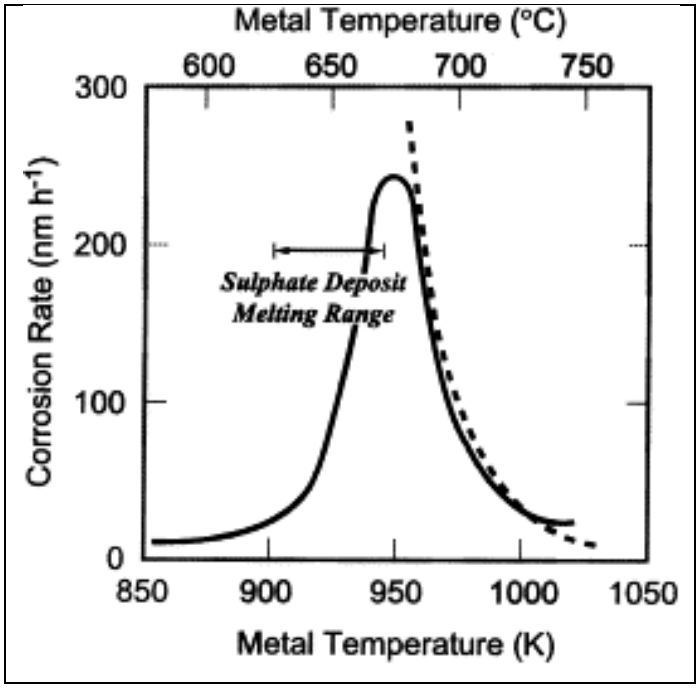

Figure 5-10: An example of 'Bell shaped' curve corrosion temperature relationship for superheater tubes in coal-fired boilers. The dotted line is a theoretical prediction [81]

5.3 Alloy composition effect

Ferritic, austenitic and nickel-based alloys are all candidates materials for heat exchangers in advanced power plants and are useful for different reasons (durability, heat transfer, strength, thermal coefficient) and for use in at different locations in the plants. The nominal elemental compositions were given in Table 3-1.

5.3.1 Air firing conditions

Figure 5-11 illustrates mass change data for alloys of different chromium level ~2% (T22), ~9% (T92), ~18% (T347HFG), and ~25% (HR3C) exposed to simulated air-fired combustion gases (with 1300 vppm SO_2/400 vppm HCl) for

1000 hours at 700°C. As expected the low chromium alloy T22 (failed to form significant protective layer) gained the highest mass values followed by T92, 347HFG and with the least mass gain values for HR3C.

The oxidation/sulphidation behaviour of chromia former alloys is well defined in the literature [26; 28]. Similar mass gain trends to Figure 5-11 are explained by Birks.et.al [26] by the low chromium alloy forming external scale rapidly (where thickness of internal scale is negligible). According to literature [26] Fe_2O_3 and Cr_2O_3 formed and further react to form spinels. It is also suggested that by increasing the Cr content the Fe^{2+} ion mobility is gradually blocked by $FeCr_2O_4$ islands and caused wustite layer become thinner and magnetite thicker, however with even more addition in Cr content, mixed spinel are produced such as Fe $(Fe, Cr)_2O_4$, and it appears that Fe become more mobile than Cr ions, and on longer exposures iron oxides are present at the outer surface of the scale through inner mixed spinel layers (if oxidation reaction is controlled by diffusion mechanism).

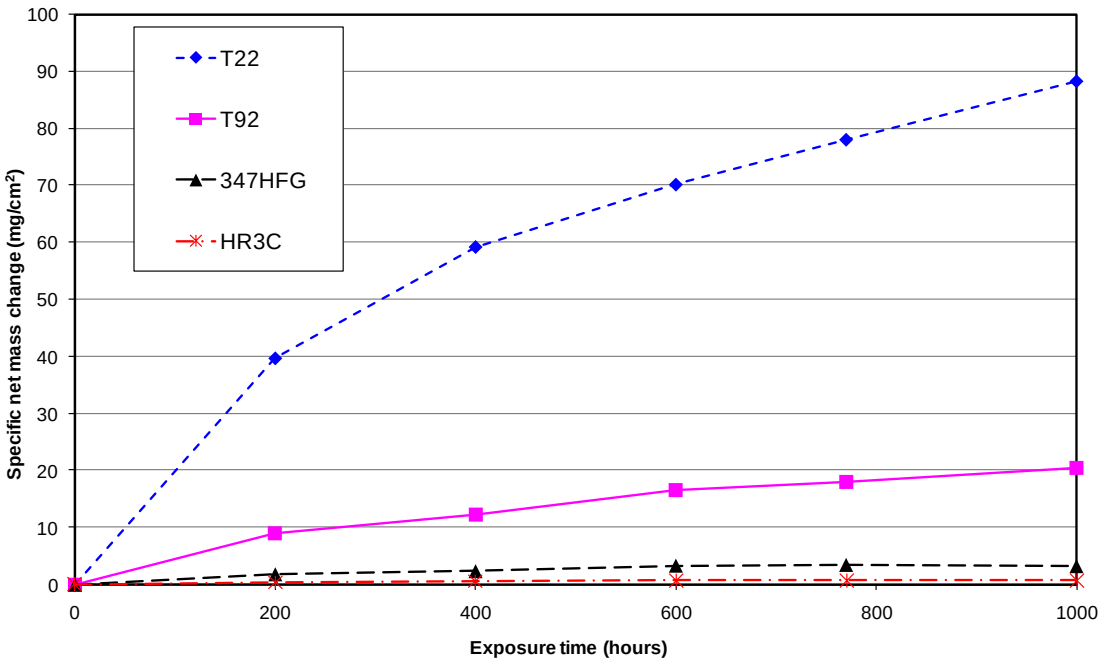

Figure 5-11: Mass change data of bare alloys samples exposed to simulated air-fired combustion gases(with1300 vppm SO_2/400vppm HCl) at 700°C for1000 hours

Figure 5-12 is a representation of Figure 5-1(A), so the effect of alloying elements (particularly Cr) on mass change data can be clarified. Figure 5-12 clearly shows that with increase in Cr content the specific net mass change data decreases in all three cases (600, 650 and 700°C). Mass gain values of initially bare alloy T92 are much higher than 347HFG (18% Cr) HR3C (25%Cr). Along with high levels of Cr in austenitic alloys (347HFG and HR3C), Ni is another element present in austenitic alloys. However, literature [27] shows that Cr content in both ferritic and austenitic alloys play a more significant role in the fireside corrosion protection of steels. The roles of other elements (such as nickel, molybdenum or titanium) are not as well explained as for Cr [27].

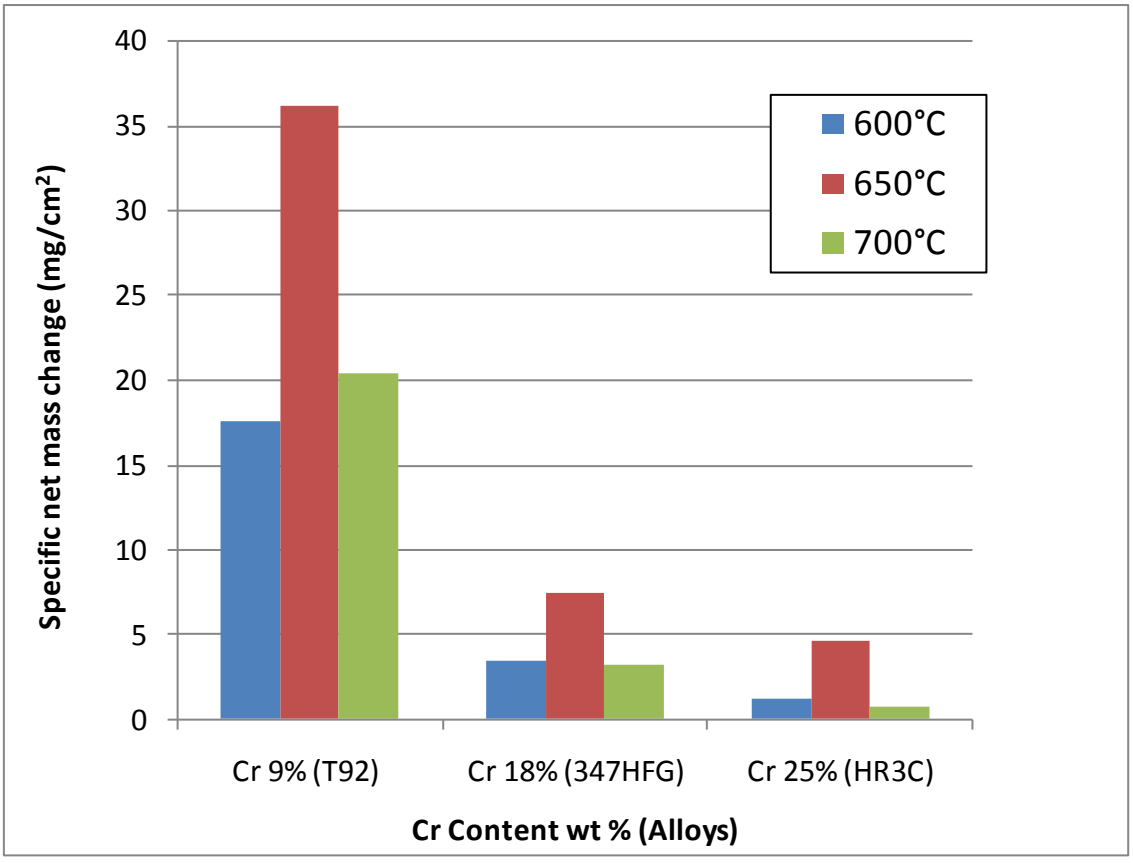

Figure 5-12: Effect of alloying elements on mass change data for bare alloys T92, 347HFG and HR3C exposed to simulated air-fired combustion gases(with 1300 vppm SO_2/400 vppm HCl for1000 hours at 600, 650 and 650°C.

Examples of surface morphology development on different alloys (exposed to gases simulating air-firing conditions) were presented in section 4.3.2.1. The results clearly show the different scale morphology on low and high chromium

alloys. Figure 5-13 is another example showing the effect of alloying element on scale growth. Results shows that, after 1000 hours of exposure to simulated air-fired combustion gases at 650°C, the scales developed on the surface of high chromium alloys (HR3C) are not adherent and spalled off (the high Cr level formed the protective scale and inhibited the formation of thicker magnetite and mixed Iron and chromium spinels). In contrast scales formed on low chromium alloy (T92) are comparatively thick and adhere to the surface. These data confirm the role of alloy Cr level in the protection of superheaters/reheaters from oxidation/sulphidation.

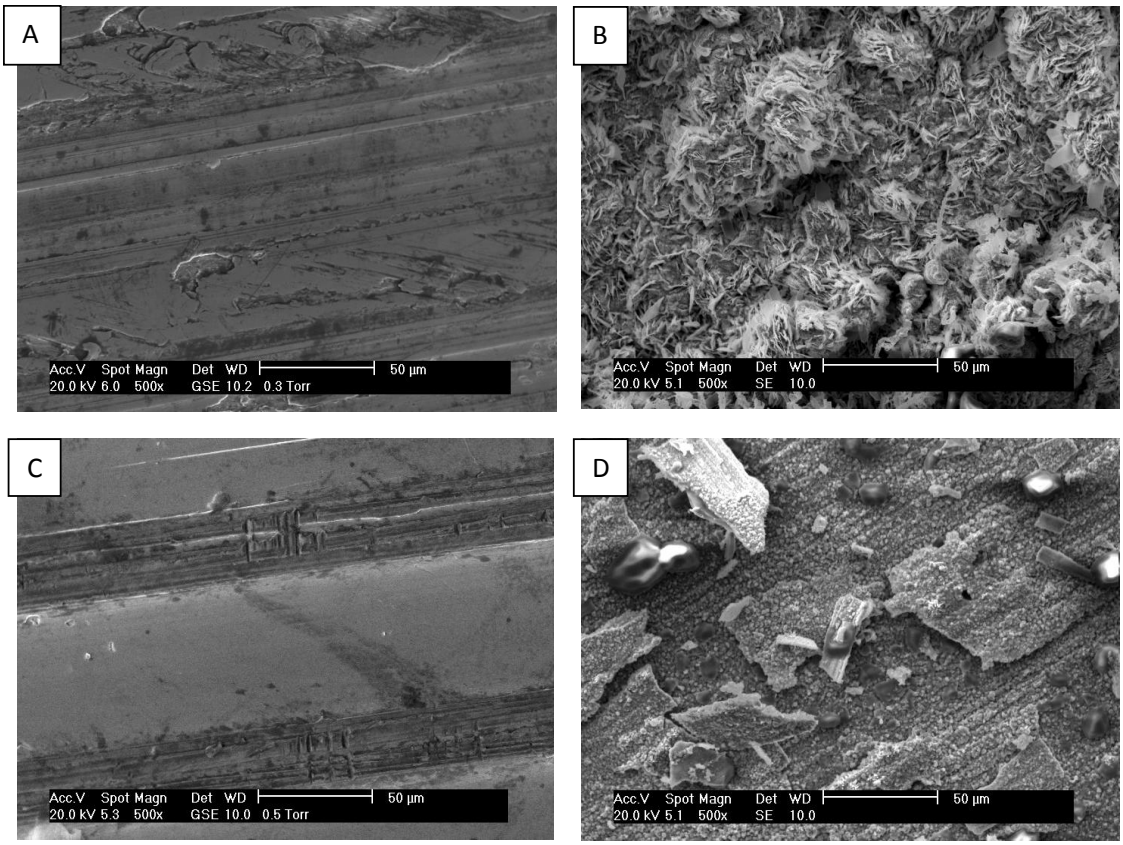

Figure 5-13: SEM images of bare alloy T92 prior (A) after 1000 hours (B) and alloy HR3C prior (C) after 1000 hours (D) exposed to simulated air-fired combustion gases (with 1300 vppm SO_2/400 vppm HCl) at 650°C.

BSE images of cross-section scales on bare alloys samples (T92, 347HFG and HR3C) exposed to gases simulated air-firing condition at different temperatures were presented in Figure 4-36. These results show (as expected) thick scale developed on low chromium alloy (T92) compared to thin scale formation on

high chromium alloy (347HFG and HR3C). However, Figure 5-14 in this section highlights an interesting issue observed for high chromium alloys; i.e. internal damage. Internal damage for high chromium alloys (such as 347HFG) is also reported by Montgomery.et.al. [65]. Furthermore it suggests that austenitic alloys can show inhibition of thick scale formation but on the other hand still experience severe internal damage (a concern from the mechanical properties view point-such as creep and fatigue for high pressure steam system).

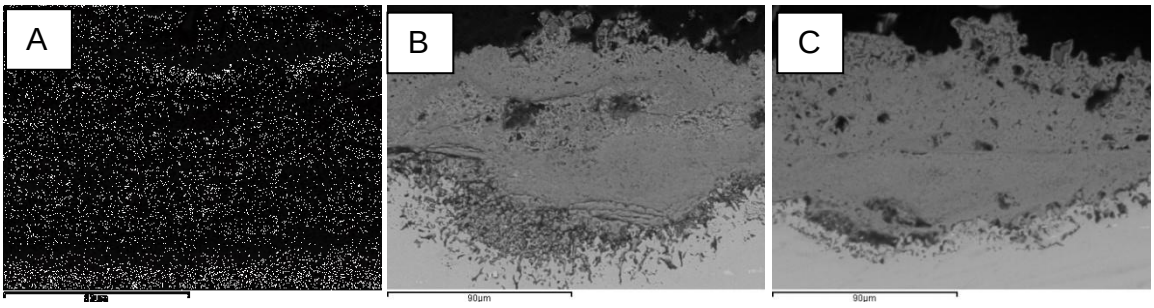

Figure 5-14: BSE image of bare alloys T92 (A)HR3C (B) and 47HFG (C) cross-sections exposed to 1300 vppm SO_2/400 vppm HCl at 650°C for 1000 hour

In the previous chapter, (sections 4.3.4 and 4.3.5) EDX maps and elemental profiles were given for selected T92 and HR3C sample cross-sections. These data help understand elemental distribution in the scale formed on low and high chromium alloys and the effect of alloying element on oxidation/sulphidation corrosion. Table 5-1 presents the quantification of the main elements (at %), as detected by energy dispersive x-ray analysis, of a bare alloy T92 exposed to simulated air-fired combustion gases at 600°C for 1000 hours. Detailed maps and elemental profile are shown in Figure 4-42 and Figure 4-48 respectively.

Table 5-1 lists the elements detected by EDX analysis. At spectrum 3, chromium was found with high concentration that is where it should have a possible presence of protective iron chromium spinel because at the same point iron level decreased and oxygen increased. At spectrum 3, Cl was also detected shows possible Cl compound such as $FeCl_2$ or $CrCl_2$. The high concentration of sulphur at spectrum 2 shows a possible sulphur penetration through the iron and chromium rich oxide layers.

The result shows the role of chromium to form protective layer, and Fe ions being more mobile and passing through the chromium rich layer to form the outer most layer of iron oxide. Tungsten (which is added into alloy T92 as a substitute for molybdenum used in T91 [73]) is also concentrated at spectrum 3. However both tungsten and manganese are detected up to spectrum 4 and spectrum 7 (Fe, Cr spinel) respectively and are absent in outer iron rich oxides.

Table 5-1: Elements (at %) detected by EDX analysis of bare alloy T92 exposed to simulated air-fired combustion gases(with 1300vppm SO_2/400 vppm HCl) at 600°C for 1000 hours

Element	Spectrum 1	Spectrum 2	Spectrum 3	Spectrum 4	Spectrum 5	Spectrum 6	Spectrum 7	Spectrum 8	Spectrum 9	Spectrum 10
	at %	at %	at %	at %	at %	at %	at %	at %	at %	at %
O	17.8	24.5	51.9	43.3	51.7	55.6	60.2	52.9	58.5	66.0
Si	3.9	4.4	6.1	10.4	3.7	3.4	4.6	6.3	4.0	8.5
S	0.0	0.6	0.4	0.4	0.4	0.0	0.0	0.0	0.3	0.4
Cl	0.0	0.0	0.2	0.0	0.0	0.0	0.0	0.0	0.0	0.3
Cr	8.5	8.7	13.2	8.5	6.8	6.4	1.7	1.6	1.3	1.3
Mn	0.4	0.4	0.3	0.4	0.0	0.0	0.0	0.0	0.0	0.0
Fe	65.7	58.6	25.2	34.3	34.6	31.8	31.5	36.5	33.6	20.3
W	0.5	0.5	0.6	0.2	0.5	0.4	0.1	0.0	0.0	0.0

Table 5-2 presents data for bare alloy HR3C exposed to simulated air-fired combustion gases at 650°C for 1000 hours (maps and elemental profiles are given in Figure 4-44 and Figure 4-50 respectively). At spectrum 6, chromium was found with high concentration likely to be a protective chromia layer, or presence of iron chromium spinel is also possible because at the same point oxygen level were amplified and iron level less significant. The high nickel presence in spectra 7 and 10 indicate possible nickel compound. The result also show the flux of chromium through nickel rich layer and further supports the Fe ions movement through the chromium rich layer to form the outer most possible haematite.

High concentrations of sulphur are detected at spectra 4 and 5. As listed in Table 5-2 the levels of sulphur found in highly alloyed material (HR3C) are higher by several orders of magnitude if compared with sulphur levels detected for ferritic alloy (T92) listed in Table 5-1. At the same spectra (3 and 4) listed in

Table 5-2 internal damage is very significant (shown in relevant maps) indicating sulphidation mechanism (diffusion or intergranular) and risk for alloy with high nickel content in sulphidising environment. Literatures also report such Ni behaviour in sulphur rich environment [60; 136]. The results indicate the significance of Cr and Cr/Ni levels in the alloy material.

Table 5-2: Elements (at %) detected by EDX analysis of bare alloy HR3C exposed to simulated air-fired combustion gases (with 1300vppm SO_2/400 vppm HCl) at 650°C for 1000 hours

Element	Spectrum 1	Spectrum 2	Spectrum 3	Spectrum 4	Spectrum 5	Spectrum 6	Spectrum 7	Spectrum 8	Spectrum 9	Spectrum 10
	at%	at%	at%	at%	at%	at%	at%	at%	at%	at%
O	11.0	9.9	17.5	47.5	54.4	64.7	56.6	63.9	65.2	61.7
S	0.0	0.0	1.9	3.0	7.3	1.3	1.2	2.4	0.7	0.8
K	0.0	0.0	0.0	0.0	0.0	0.0	0.0	1.3	0.0	0.3
Cr	24.6	24.6	14.5	18.4	17.1	24.5	15.8	9.1	4.6	3.7
Mn	1.0	1.5	0.9	0.0	0.0	0.0	0.9	1.6	0.4	0.0
Fe	45.1	44.1	44.4	18.6	8.9	5.5	13.4	12.1	23.5	20.4
Ni	15.6	16.8	17.7	7.8	3.6	1.8	7.4	5.6	1.6	8.1

Figure 5-15(A) and Figure 5-15(B) present the possible order of different metal oxides or sulphides in the scale formed on initially bare alloys T92 and HR3C respectively.

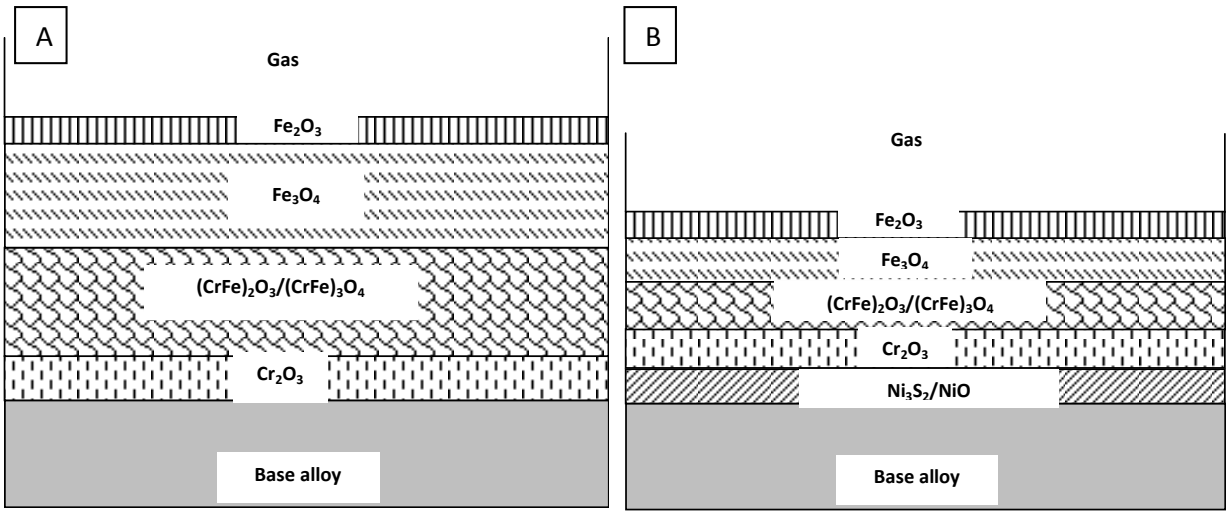

Figure 5-15: Possible scales on bare alloys (A) T92 and HR3C (B) and exposed to simulated air-fired combustion gases (with 1300vppm SO_2/400vppm HCl at 600 and 650°C for 1000 hours

Figure 5-16 shows dimensional metrology data for bare alloy T22, T92, 347HFG and HR3C exposed to simulated air-fired combustion gases for 1000 hours at

700°C. As expected the level of corrosion damage decreases with increase in Cr level. From the data the performance of the materials under these conditions may be ranked as (most damage to least): T22 > T92 > 347HFG > HR3C. The dimensional metrology data shows in Figure 5-16 is in good agreement with mass change data in Figure 5-12 and scale thickness shown in Figure 4-36.

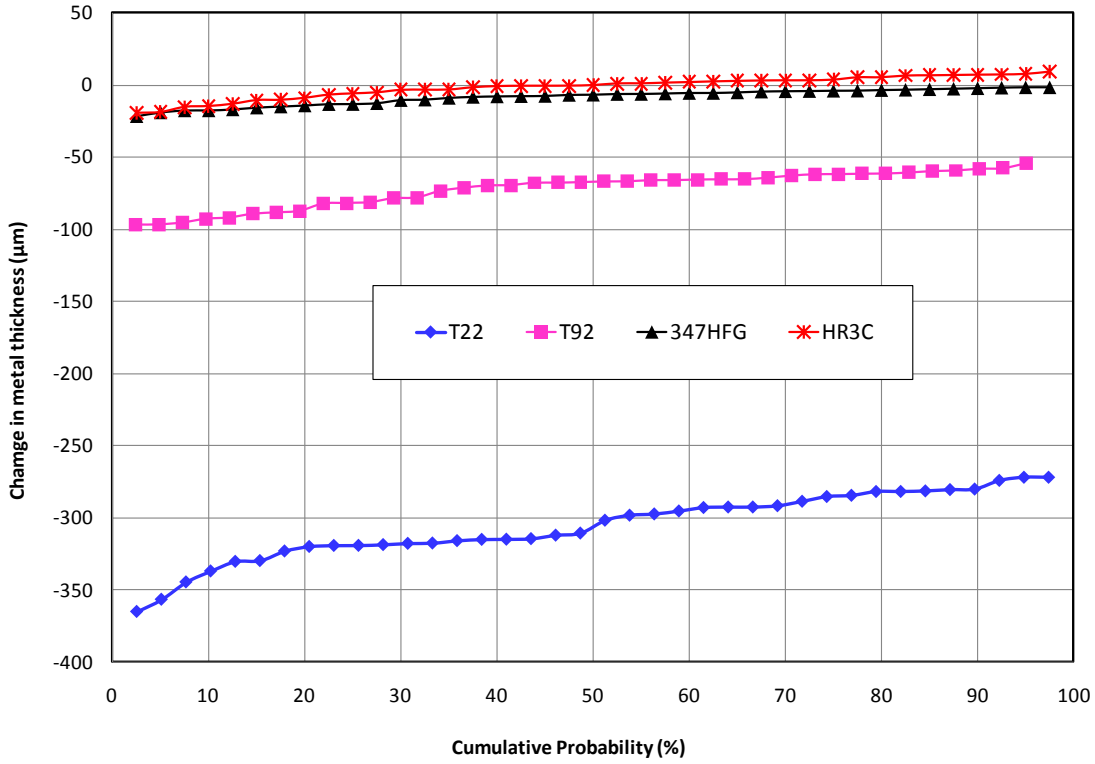

Figure 5-16: Change in metal thickness versus cumulative probability showing the behaviour of different bare alloys exposed to simulated air-fired combustion gas at 700°C for 1000 hours

Figure 5-17 is a representation of data from Figure 5-5(A) in order to illustrate the effect of chromium content on metal loss data. The results shown are for bare alloys T22, T92, 347HFG and HR3C exposed to simulated air fired combustion gases at 700°C for 1000 hours. These median metal loss data are consistent with the mass change and scale thickness data.

XRD data presented in section 4.5.2 for bare alloys T22, T92 and 347HFG exposed to air-firing condition at 700°C for 1000 hours does not revealed any significant information, which can be useful to highlight the alloying effect. Alloy

T22, T92 and 347HFG showed presence of only haematite whereas HR3C XRD data shows presence of Fe_2O_3, Cr_2O_3 and Fe_7S_8. It indicates that scale formed on high alloy material is thinner and enable detection of other compounds on the sample surface.

Overall the results for bare alloys (ferritic and austenitic) show that the low alloy material exhibit more damage than highly alloyed materials. This is consistent with the Cr contents of these alloys; i.e. lowest chromium correlates to the highest corrosion damage, with the 18 and 25 wt. % Cr in 347HFG and HR3C respectively being high enough to form protective chromium rich scales particularly at 600 and 650 ºC, whereas the 2 and 9 wt. % Cr of T22 and T92 respectively results in less protective multi-layered scales. In agreement with trends reported in the literature [32], EDX mapping shows these multi-layered scales consist of an innermost layer of an Fe-Cr spinel oxide (that also incorporates sulphides), a central magnetite layer, and an outer haematite layer that also contains S rich zones. In contrast, the breakdown of the protective oxide scales on HR3C is shown by sulphur penetration through these scales to form internal sulphides, especially Ni-rich sulphides (again in line with trends reported in the literature [32]).

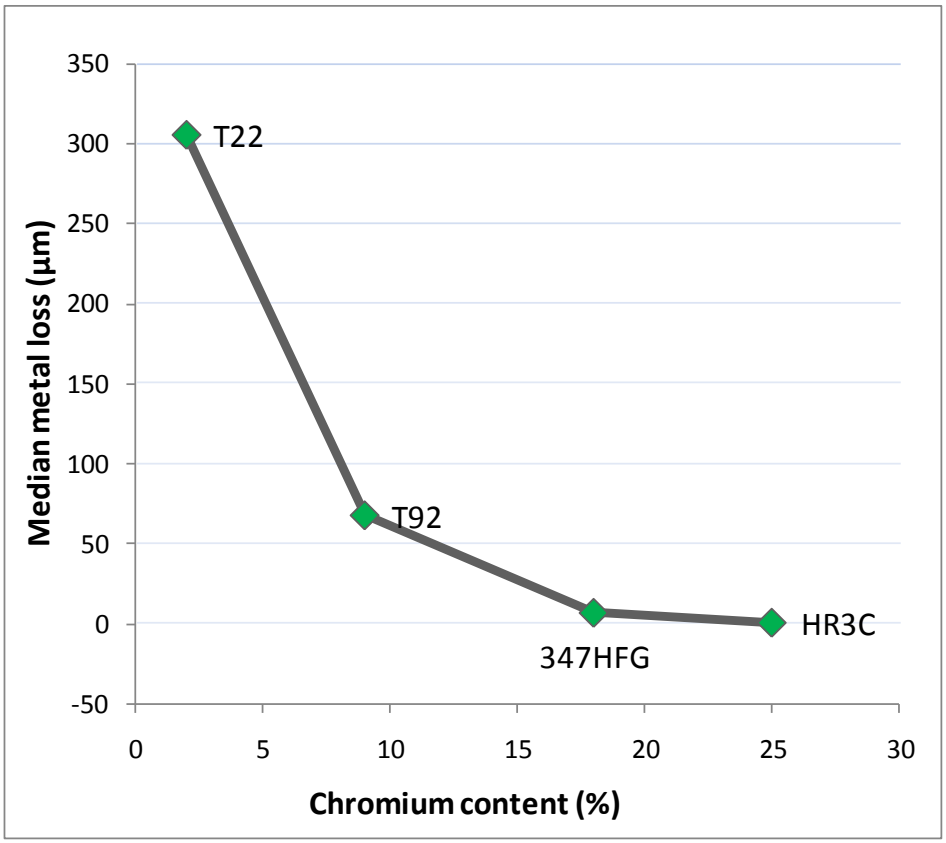

Figure 5-17: Effect of alloying elements on the median metal loss damage for bare alloy T22, T92, 347HFG and HR3C after 1000 hours exposure in the gases simulating air-fired conditions at 700°C

As a result of these different attack mechanisms, the metal losses measured for the ferritic and austenitic alloys were significantly different. For T22 and T92 at all exposure temperatures, the metal losses exceeded the 40-50 µm/1000 hours target that has traditionally been used for superheaters/reheaters in power plants (section 4.4.2). However, for 347HFG the damage levels at 600 and 650ºC were below this target, though at 700ºC the target was clearly exceeded in terms of metal loss and far exceeded in terms of good metal loss (i.e. taking internal damage into account).

However, it should be noted that results presented in section 5.3.1 only shows data from bare samples results so the effect of alloying element particularly Cr an Ni can be highlighted. The consequences are different when alloys are covered with deposits and exposed at different temperatures; this will be discussed in section.5.4.

5.3.2 Oxy-firing conditions

Figure 5-18 illustrates the mass change data of all five alloys (used in this PhD project) covered with deposit D1 exposed to simulated oxy-fired combustion gases at 750°C for 1000 hours. As expected the low chromium alloy T22 showed the highest mass gain values, followed by T92. The austenitic alloys 347HFG and HR3C gained less mass compared to the ferritic alloys. Alloy 625 with deposit D1 shows aggressive corrosion damage and higher corrosion damage levels than HR3C. Such behaviour of nickel-based alloy when covered with deposit D1 was also noticed in other tests performed.

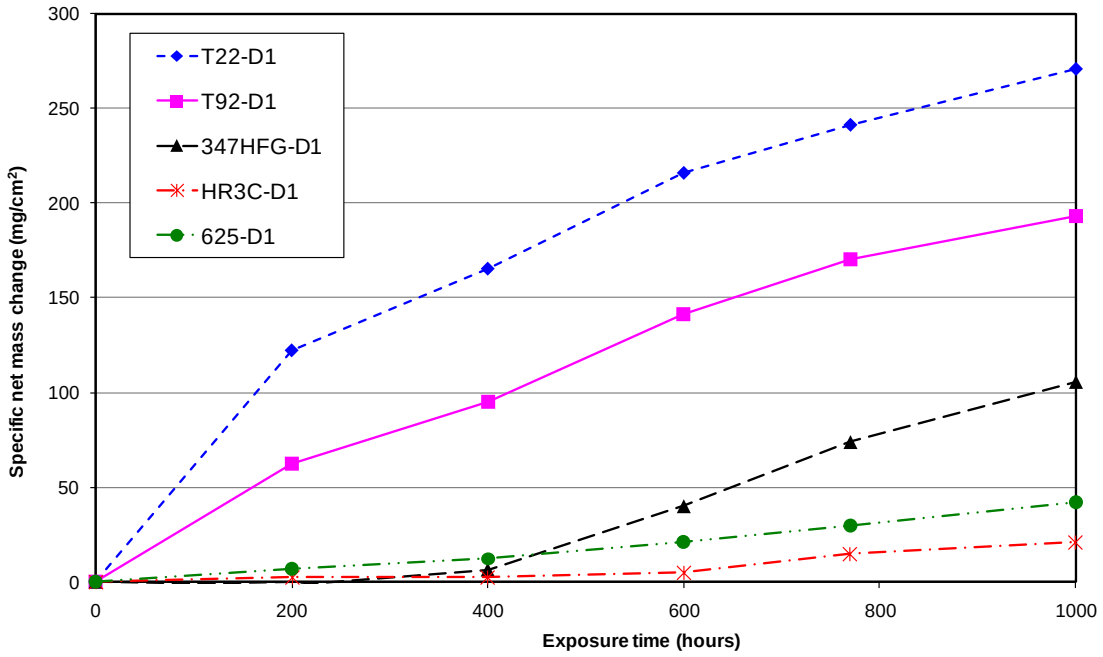

Figure 5-18: Mass change data of alloys samples covered with deposit D1 exposed to simulated oxy-fired combustion gases (with 6260 vppm SO_2/1700 vppm HCl) at 750°C for1000 hours

All alloys show a combination of parabolic and linear kinetic behaviours. The mass gain of low chromium alloy T22 is almost 10 times more than the mass gain by austenitic alloy HR3C. This type of behaviour of low chromium alloys in coal [60], biomass [97] or coal and biomass co-firing [96] in air-fired conditions is well documented.

Figure 5-19 is a representation of data shown in Figure 5-6 (B), so the effect of alloying element on mass change can be explained. These data show the mass gain values of various alloys covered with deposit D1 at 700 and 750°C after 1000 hours exposure in simulated oxy-fired combustion gases. These results are in good agreement with previous research (in air-fired conditions) [60; 109] that showed, low chromium alloy (T22) exhibited the highest mass gain compared to T92 and austenitic alloys 347HFG and HR3C at both temperatures (700 and 750°C). And more recently work by Covino and co-workers [123] also found such alloying effect on mass change values in oxy-fired conditions. The data showed that at both temperatures Ni-based alloys attained higher mass values than HR3C or 347HFG at 700°C.

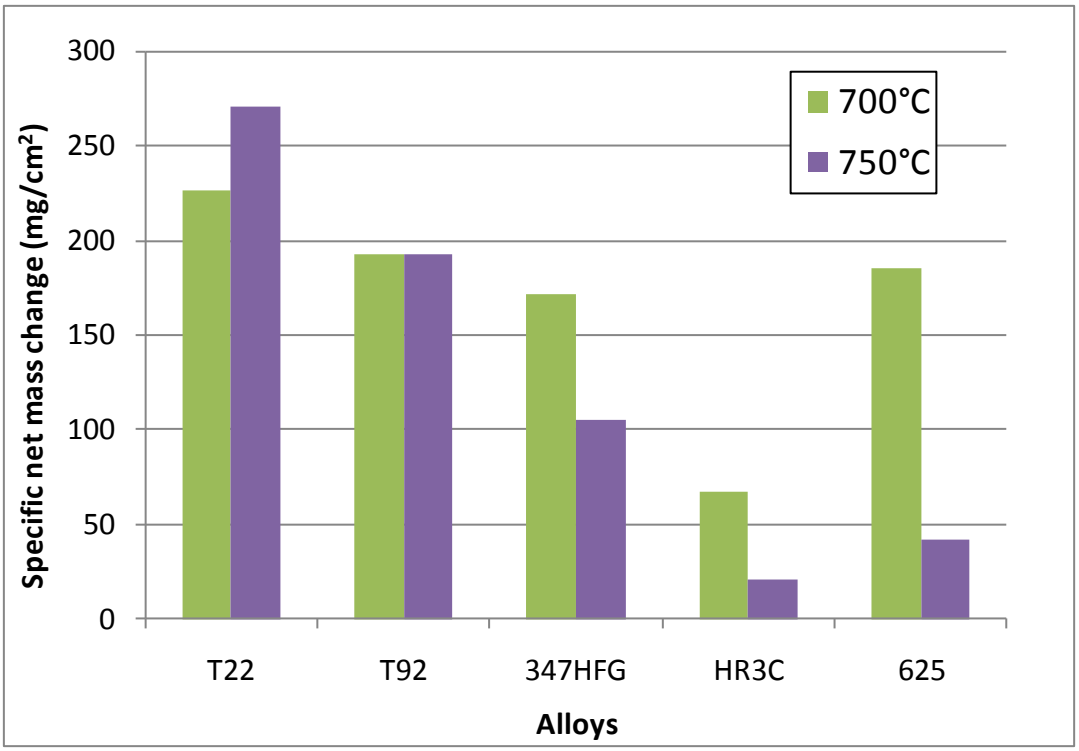

Figure 5-19: Effect of alloying elements on mass change data for alloys T92, 347HFG and HR3C covered with deposit D1 exposed to simulated oxy-fired combustion gases (with 6260 vppm SO_2/1700 vppm HCl) for1000 hours at 700 and 750°C.

In addition to Figure 4-34 and Figure 4-35, Figure 5-20 is another example illustrating the alloying effect on fireside corrosion. Figure 5-20 illustrates the development of surface morphology of alloy T92 and 347HFG exposed to simulated oxy-fired combustion gas condition at 650°C for 1000 hours. The

surface analysis was carried out before exposure and after 600 and 1000 hours exposure. The results show a dense growth was formed on ferritic alloy (T92) and crystalline type growth on the austenitic alloys (HR3C), as expected with the increase in chromium content. The scale layer on alloy T22 seems more porous compared to austenitic alloy HR3C. Such behaviour of ferritic and austenitic alloys was consistently observed at other temperatures in both air-fired and oxy-fired combustion gases. During the morphological studies EDX mapping was also carried out on both bare alloys; in addition to S and Cl, traces of K were detected on the surface indicating limited vapour phase transport of alkali contaminants had occurred during the course of the exposures [17].

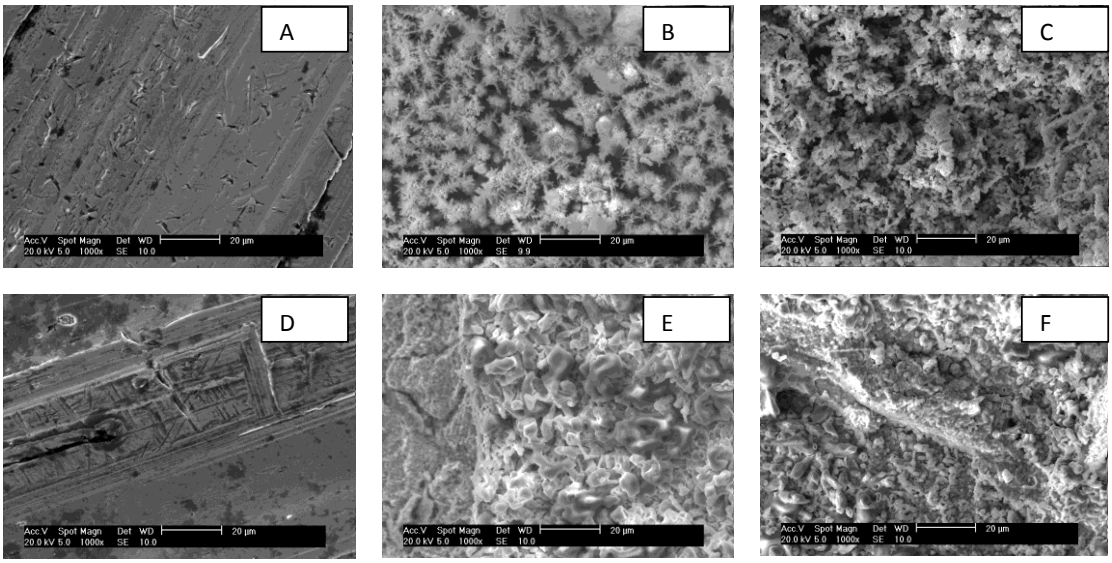

Figure 5-20: SEM images of bare alloy T92 (A) prior (B) 500 hours and (C) 1000 hours and alloy 347HFG (D) prior (E) 500 hours and (F) 1000 hours exposed to the simulated oxy-fired combustion gas at 650°C

Figure 4-39 presents the scale morphologies from initially bare T92, 347HFG and HR3C at four different temperatures. Figure 5-21 is a representation of Figure 4-39 data to illustrate the alloying effect on scale growth. The micrographs are cross-sections of the scales formed on initially bare ferritic and austenitic alloys after exposure at 600°C for 1000 hours in simulated oxy-fired combustion gases. These results show that much thicker scales were formed on T92, with progressively thinner scales being formed on 347HFG and HR3C, and that the scales formed on T92 and 347HFG are also clearly multi-layered. These results are in line with the expected trend in scale development for these

alloys as a result of their different compositions (Table 3-1) [26; 133]. These data show that by increasing the chromium level from 9% (T92) to 18% (347HFG) the scale thickness reduces by a factor of approximately four. The scale formed on HR3C is approximately half the thickness of that formed on 347HFG, as a result of the higher Ni and Cr content of HR3C compared to 347HFG. Henderson and co-worker [97] carried out exposures of T92 and higher chromium alloys in a 105 MW air biomass fired power plant with average metal temperature at 580 °C; these results also showed that the high chromium levels caused a similar reduction in scale growth. The presence of three different scale layers on alloy T92 is expected for this relatively low Cr alloy at 600 °C, with the scale layers being (innermost to outermost): Fe–Cr spinel, magnetite and haematite [17].

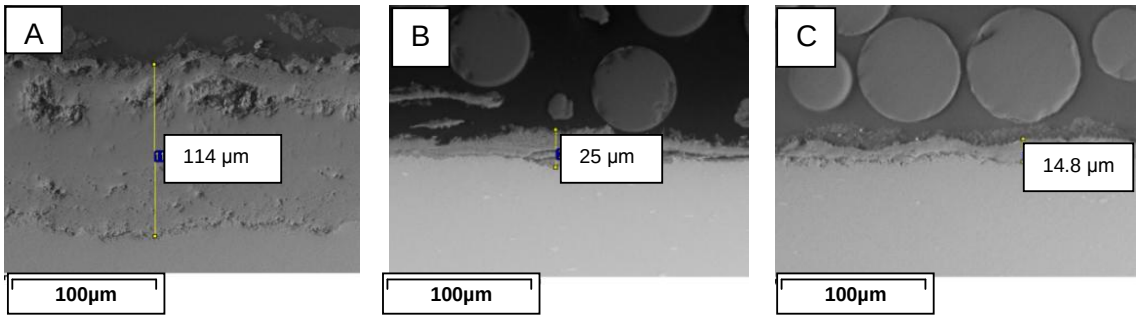

Figure 5-21: BSE images of cross-section scales onT92, 347HFG, and HR3C alloys covered with deposit D4 exposed to simulated oxy-fired combustion gases(with 6260 vppmSO_2/1700 HCl) for 1000 hours at 600°C

XRD data presented in section 4.5.3 for bare alloys T22 and T92, exposed to oxy-firing gases at 700 and 750°C reveal the presence of haematite. No other compounds were detected. XRD results suggest formation of thick scales of iron oxide on ferritic alloys, which is also in line with mass change data, scale morphology results from SEM and dimensional metrology data.

Alloy composition has also an effect on metal loss. Figure 5-22 presents the metal loss data of bare alloys exposed to simulated oxy-fired combustion gas at 650°C for 1000 hours. As expected the metal loss for alloys was found in an order from high to low corrosion as follows T22 > T92 > 347HFG > HR3C. As noticed in mass change and scale thickness results, T22 was found to be the most sensitive alloy with the highest metal loss value (i.e. at 50% probability

almost 700µm) after 1000 hours exposure; comparatively alloy HR3C found to be least affected alloy.

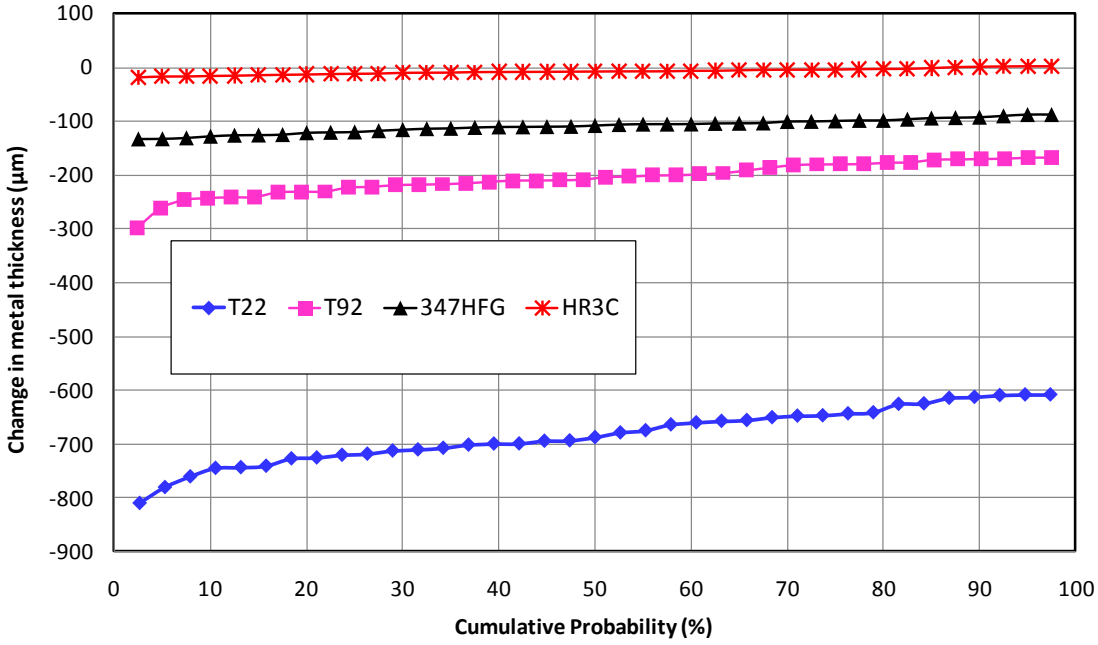

Figure 5-22: Change in metal thickness versus cumulative probability showing the behaviour of different bare alloys exposed to oxy-firing gas at 700°C for 1000 hours

Figure 5-23 is a representation of median metal loss data (at 700°C) shown in Figure 5-9(A) so that the alloying effect on metal loss can be clearly understood. As expected, corrosion damage was the inverse of the alloy chromium content (i.e. with the highest damage being associated with the lowest alloy chromium content, ~2 % Cr in T22).

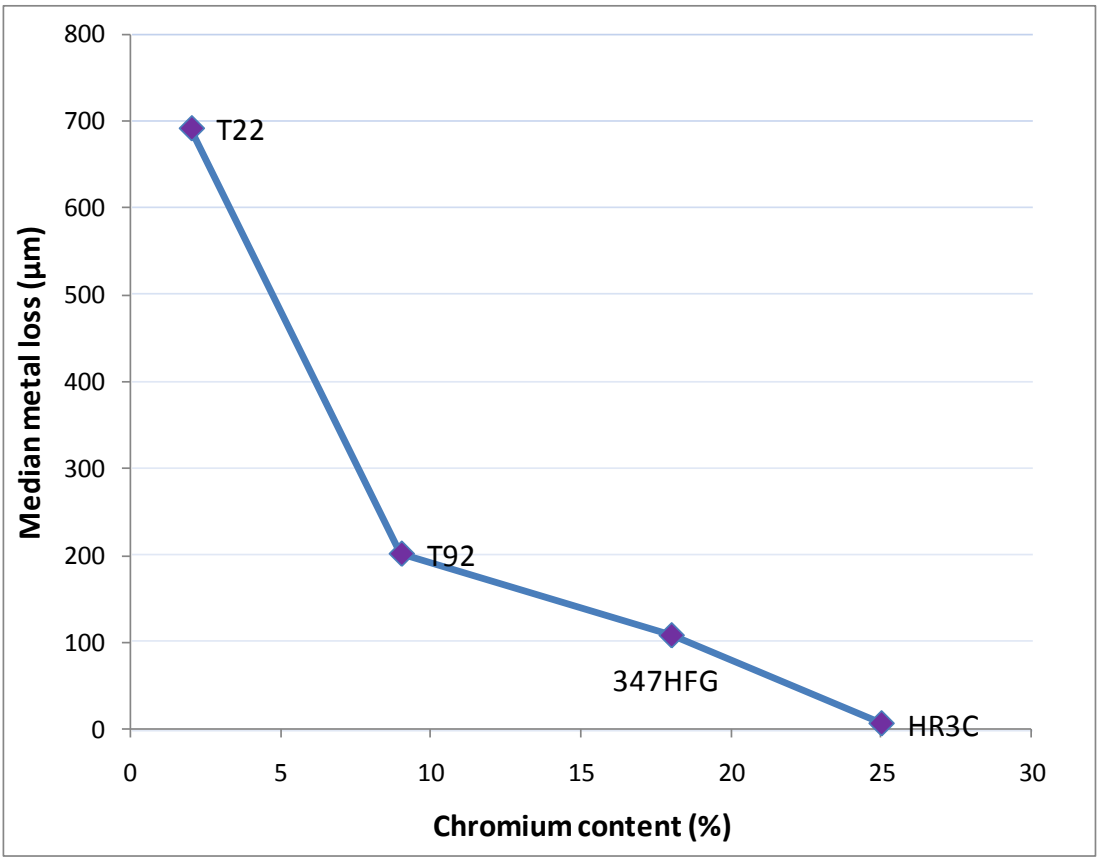

Figure 5-23: Effect of alloying elements on the median metal loss damage for bare alloy T22, T92, 347HFG and HR3C after 1000 hours exposure in the gases simulating oxy-fired conditions at 700°C

The metal loss data for all alloys in oxy-firing conditions at all the temperature presented in section 4.4.3 can be summarised as:

- Figure 4-43 Ferritic alloy T22, (Cr content ~2%), bare or covered with any deposits, at all temperatures exceeded the 40-50 µm/1000 hour targets that has traditionally been used for superheaters/reheaters in power plants.
- Figure 4-43Ferritic alloy T92, (Cr content ~9%), bare or covered with any deposits, at all temperatures also exceeded traditional fireside corrosion values for superheaters, except at 600°C where samples covered with deposit D3 and D4 exhibit corrosion damage below 40 µm/1000 hours.
- Austenitic steel 347HFG (Cr content ~18 %) samples (bare or covered with any deposits) at 700 and 750°C showed substantial corrosion damage, however at 600 and 650°C corrosion damage was below the

acceptable range of 40-50 µm/1000, except for samples covered with deposit D1.

- The damage levels for high alloying material HR3C were relatively low at all temperatures, reflecting its high Cr (~25%) and Ni content (~20%).
- Overall dimensional metrology results revealed that nickel-based alloy 625 was the most corrosion resistant alloy if compared with iron based alloys (T22, T92, 347HFG and HR3C), however with deposit D1 in a temperature range of 650-750°C, corrosion damage was higher than 40 µm/1000 hours.

Dimensional metrology results produced for alloys of different Cr level at different temperatures in either air or oxy-fired combustion gases show the significance of alloying materials in fireside corrosion testing. Results (from SEM/EDX) highlight the role of Cr in particular in formation of protective scales as a barrier against corrosive environments.

Corrosion damage data generated in this PhD show the effect of Cr content in resisting oxidation/sulphidation plus fireside corrosion. This is in good agreement with results reported by other researchers showing the performance of different alloys in coal [60; 75], biomass [97], bio-fuel [86] or co-firing [96] coal and biomass or waste [137] flue gas environments.

5.3.3 Nickel alloy behaviour

Nickel-based alloys are being considered as candidate materials in advanced power plants due to their higher strength at higher temperatures. However results presented for mass change data for alloy 625 covered with deposit D1 in both air and oxy-firing condition [in Figure 5-1(B) and Figure 5-6(B)] show high mass gain values.

Some results from SEM scale morphology of samples cross-section (Figure 4-37 and Figure 4-40) also showed that alloy 625 was found to form a thicker inner and outer scale layer than on the austenitic alloys. Such findings are in contrast to dimensional metrology (results showed alloy 625 had the lowest

corrosion damage). It could be the Ni reaction with alkali sulphate and gases formed complex compounds with a high quantity fine particles, which may not corrode the material. Such nickel-alloy behaviour was suggested by Natesan et al. [60] with sticky deposits being more adherent to the nickel-based-alloy substrates and oxides than ferritics. However, alloy 625 covered with other deposits (D2, D3 and D4) show very thin scale formation compared to austenitic alloys. Deposit D1 has >7 times the initial sulphate content of deposits D2, D3 and D4.

Figure 5-24 demonstrates the different appearances developed on the sample surfaces of nickel-based alloy 625 and austenitic alloy HR3C. The morphology for HR3C shows that shinny scales are adherent to its surface, whereas green/ yellowish complex compounds (high quantities of such residue was also found in the crucible) formed on alloy 625 are dusty, dry and easily removable. The scales on HR3C are nodular and showed lateral scale growth, whereas the morphology for alloy 625 shows cracks formed in residual deposits (through to the sample surface) as revealed in Figure 5-24.

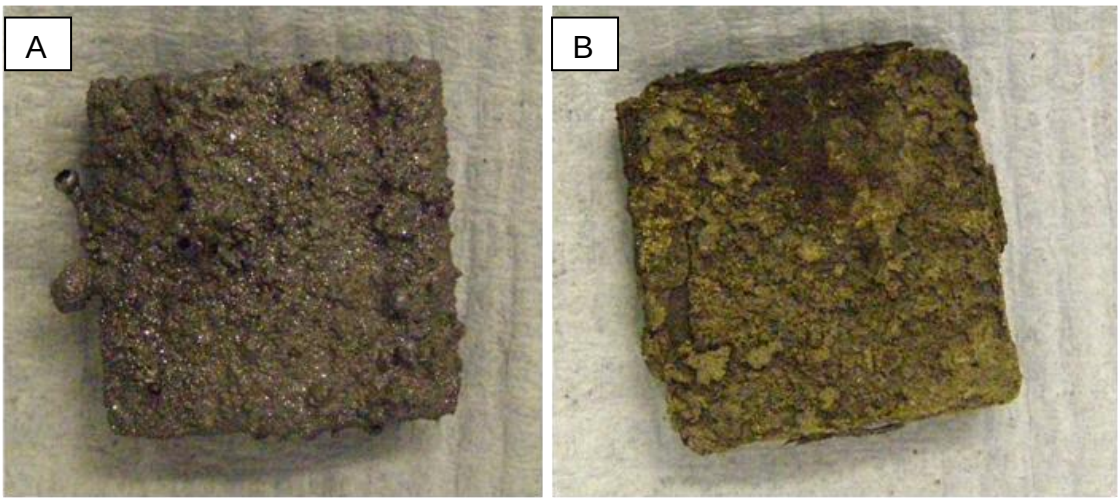

Figure 5-24: (A) high alloyed material HR3C (B) and nickel based alloy 625 after 1000 hours exposure to gases simulating oxy-fired combustion at 700°C

5.4 Deposit effect

Deposits on the heat exchanger surfaces play a fundamental role in fireside corrosion. In a conventional coal-fired boiler the deposits on

superheaters/reheaters are mainly fly ash and salt compounds (that can include alkali, sulphur, and chlorides depending on the fuel). The flue gas chemical composition, particularly the SO_x, HCl reactions with the deposits and scales, can alter the deposit chemistry and as a result a complex corrosion product can be formed such as, alkali iron tri-sulphates. Fireside corrosion is believed to involve a variation on type II hot corrosion [28; 50; 51] in which a complex corrosion product is formed with a lower melting point than the original deposit, triggering further corrosion. In this PhD thesis mainly four synthetic deposits (i.e. D1, D2, D3 and D4) were used (deposits D5-D10, with higher % of salts were only used in one test) on different samples of each of the candidate materials. These deposits were prepared with different compositions to simulate the deposits anticipated on superheaters/reheaters. The details of deposits formation such as alkali iron tri-sulphate (and reaction mechanisms involved) are given in literature review, section 2.4.3.

5.4.1 Air firing conditions

Figure 5-25 summarise the effect of all the different deposit compositions on alloys (T92, 347HFG, HR3C and alloy 625) in terms of specific net mass change data after exposure in the simulated air-fired combustion gas at 600, 650 and 700°C. These data show that deposit D1 has the most severe corrosion effect on the alloy surfaces at all temperatures, which is not unexpected since it corresponds to the most aggressive deposit found in air-fired plant environments [32].

The composition of deposit D1 (Table 3-2) was intended to ease the formation of alkali iron trisulphates, which are believed to be one of the possible causes of fireside corrosion damage to materials under superheater/reheater operating conditions [32].The other deposits all contained alkali and iron compounds in the same ratio as for D1, but at lower concentrations (effectively resulting in a reduced deposition flux of these species). The data in Figure 5-25 shows deposits D2, D3 and D4 (diluted versions of deposit D1), are not as corrosive as

D1; samples at all the temperatures covered with these deposits (D2, D3 and D4) showed low mass gains.

Figure 5-25(A) illustrates the mass gain values for all the alloys covered with these more realistic deposits (D2, D3 or D4) at 600°C, were ~10mg/cm^2 or below, indicating some mass losses (negative values i.e. possibly due to spalation during the heat exposure or sample handling procedures). With deposit D1 at 600°C, alloy T92 gained significant mass i.e. ~45 mg/cm^2, followed by alloy 625 with ~25 mg/cm^2, whereas austenitic alloys 347HFG and HR3C showed mass gained values less than 10 mg/cm^2.

In Figure 5-25(B), specific net mass gain data at 650°C, showed (as expected) deposit D1 was the most aggressive deposit with alloys. Samples covered with deposit D1 gaining the most mass i.e. in a range of 65-100 mg/cm^2. Alloy T92 covered with deposit D4 showed substantial mass gain value, however all the other mass change data (for all samples covered with deposit D2-D4) showed mass gain values of ~15 mg/cm^2 or less.

At 700°C the mass gain values shown in Figure 5-25(C) for all the alloys covered with deposit D1 were found to be in a range of 45-150 mg/cm^2; alloy T92 gained the highest mass and alloy 625 gained the lowest. Alloy T92 samples with other deposits showed mass gain values of approximately 20 mg/cm^2, whereas almost no mass gain values were observed for other alloys 347HFG, HR3C and alloy 625 covered with deposits D2-D4.

Mass change data for most of the initially bare alloys [i.e. covered with no deposit (D0)] were higher than for the same alloys covered with deposits D2-D4 at all the temperatures.

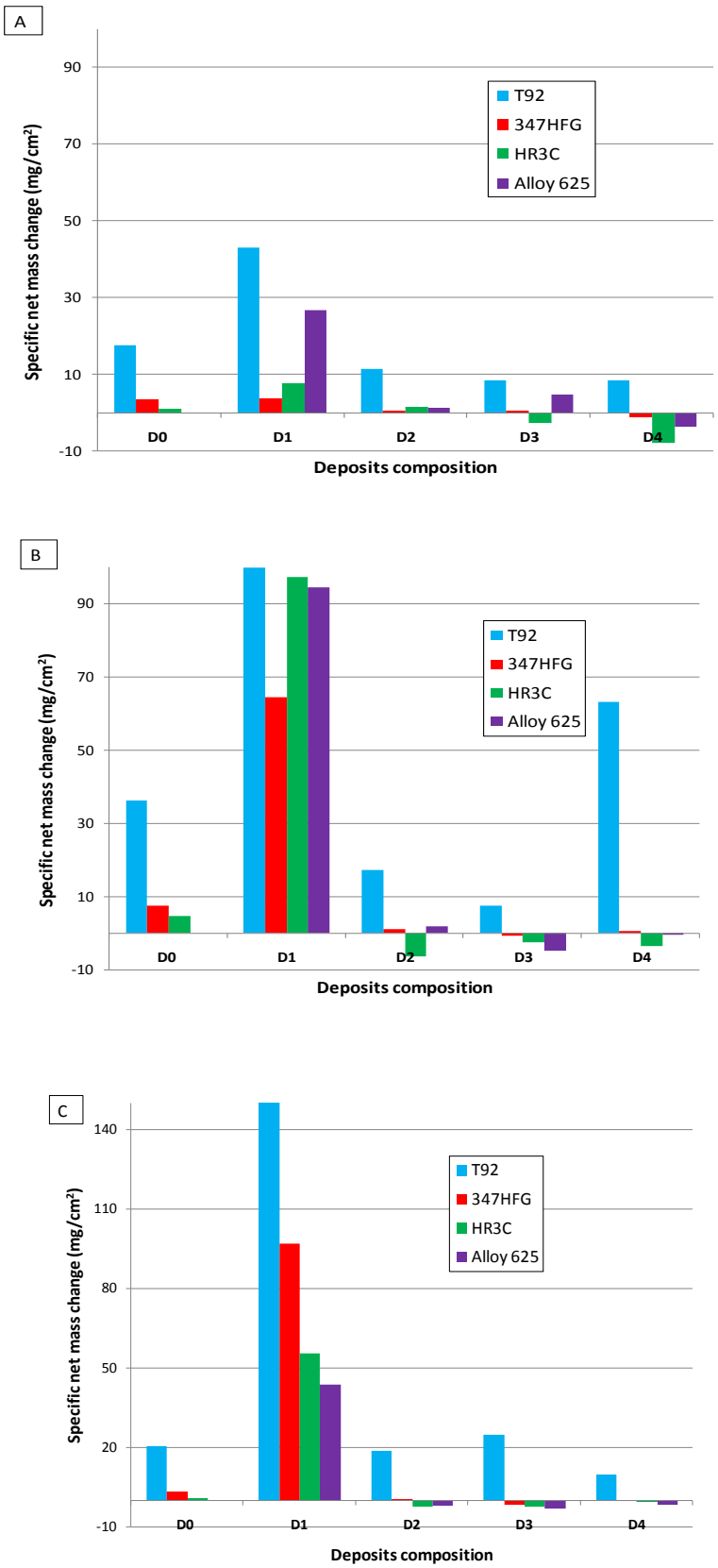

Figure 5-25: Effect of various deposits on mass change for alloys exposed to gas simulating air-fired conditions at (A) 600, (B) 650 and (C) 700°C for 1000 hours

Figure 5-26 summarises the effect of all the different deposit compositions on alloys (T92, 347HFG, HR3C and alloy 625) in terms of median metal loss data after exposure in the simulated air-firing conditions at 600, 650 and 700°C. As discussed before in the experimental methods chapter, the composition used for deposit D1 has frequently been used in screening tests for fireside corrosion of superheaters/reheaters in traditional air-fired combustion systems. As it is not diluted by other components present in real boiler deposits (e.g. alumina-silicates, etc), it usually generates accelerated fireside corrosion conditions.

At all temperatures, deposit D1 was found to be the most damaging deposit. The effect of deposit D1 on metal loss data for all the alloys at all the temperatures is in good agreement with the mass change data. Figure 5-26(A) shows median metal loss values for samples of T92, 347HFG, HR3C and alloy 625 at 600°C. For samples covered with deposit D1 at 600°C, alloy T92 exhibited the highest median metal loss value (~280 µm), followed by 347HFG (~140 µm), HR3C (~50 µm), and alloy 625 (~35 µm). All other samples covered with deposit D2, D3 and D4 show median metal loss values below 20 µm, except alloy T92 with deposit D4 which showed a median metal loss value of approximately 40 µm.

Figure 5-26(B) reveals that at 650°C, the median metal loss values for alloys T92, 347HFG and HR3C covered with deposit D1 were very similar, i.e. 505 µm ±15. Alloy T92 covered with deposit D2 and D4 at 650°C showed substantial median metal loss values of ~340 µm and ~440 µm respectively. All other alloys (347HFG, HR3C and alloy 625) covered with deposit D2, D3 or D4 showed minimal damage, i.e. maximum ~25 µm.

Figure 5-26(C) shows median metal loss data for various alloys at 700°C. For alloys covered with deposit D1, alloy T92 was found to be the most affected (with a median metal loss value of ~850 µm), whereas austenitic alloy HR3C was found to be the least damaged alloy, (with a median metals loss value of ~140 µm). All other samples (T92, 347HFG, HR3C and alloy 625) covered with

deposits (D2, D3 and D4) showed median metal loss values of ~45 µm or less (except alloy T92 with deposit D3 showed a median metal loss value of 85 µm).

The median metal loss data from samples covered with deposit D1 exceed the traditional targets for metal loss for all the alloys at all the temperatures, particularly at 650 and 700°C. It should be noted that although the deposits D2, D3, D4 and bare surfaces show the less corrosion damage (compared with deposit D1), for T92 under these exposure conditions these levels of damage are still above the traditional target level of ~40–50 µm/1000 hours exposure for superheater/reheater materials [17; 62].

Another noticeable feature which highlights the deposit effect, is that the corrosion damage of the two more realistic deposits for coal-fired systems (D2 and D3) are at relatively low levels. D4 (representing a higher level of biomass co-firing) showed a higher level of damage, but still much lower than that found for the deposit D1 (which is commonly used in screening trials). As discussed in literature review chapter, such effect of deposit D4 (Table 3-2), indicates the role of Cl in fireside corrosion.

In this PhD study the corrosion damage observed, particularly with deposit D1 (designed to ease the formation of alkali iron tri-sulphates), suggests the following reaction mechanism

i. Alkali sulphates (Na_2SO_4 and K_2SO_4) with iron oxide (constituent in deposit D1) in the presence of SO_3 leads to development of $(Na/K)_3Fe(SO_4)_3$ as:

$$Fe_2O_3+3SO_3 = Fe_2(SO_4)_3 \quad \textbf{(5-1)}$$

$$3(Na/K)_2SO_4 + Fe_2(SO_4)_3 + 3SO_3 = 2(Na/K)_3Fe(SO_4)_3 \quad \textbf{(5-2)}$$

ii. The protective chromia or iron-chromium spinel dissolved by molten deposit constituents (combined gas and deposit induced damage)

iii. Molten SO_4 reacts with the metal (where M = Fe, Cr or Ni) as

$$3M + SO_4^{2-} = M_3O_4 + S^{2-} \quad \textbf{(5-3)}$$

Where sulphides react with available oxygen and produce sulphur

$$2MS + O_2 = 2MO + S_2 \quad \textbf{(5-4)}$$

Literature [63; 138] reports two possibilities of the resulted sulphur are:

a. Sulphur react with excess oxygen and form SO_2 which further form SO_3 to produce more alkali iron tri sulphate [63]
b. Sulphur produced, further penetrated into the alloy surface [138].

EDX mapping results presented in section 4.3.4, for samples covered with deposit D1 showed significant presence of sulphur (as sulphides) beneath the chromium rich oxide and in some cases (347HFG) also detected within the grain boundaries.

The possible series of mechanisms presented above is also reported by Srivastava.et.al [84]. Several other researchers [32; 60] also suggested that the presence of alkali iron trisulphate in a molten form is a cause of corrosion in these conditions. Details of alkali iron tri-sulphates and other deposits formed on the heat exchanger surface of coal–fired boiler and their related reaction mechanisms were explained in the literature review chapter.

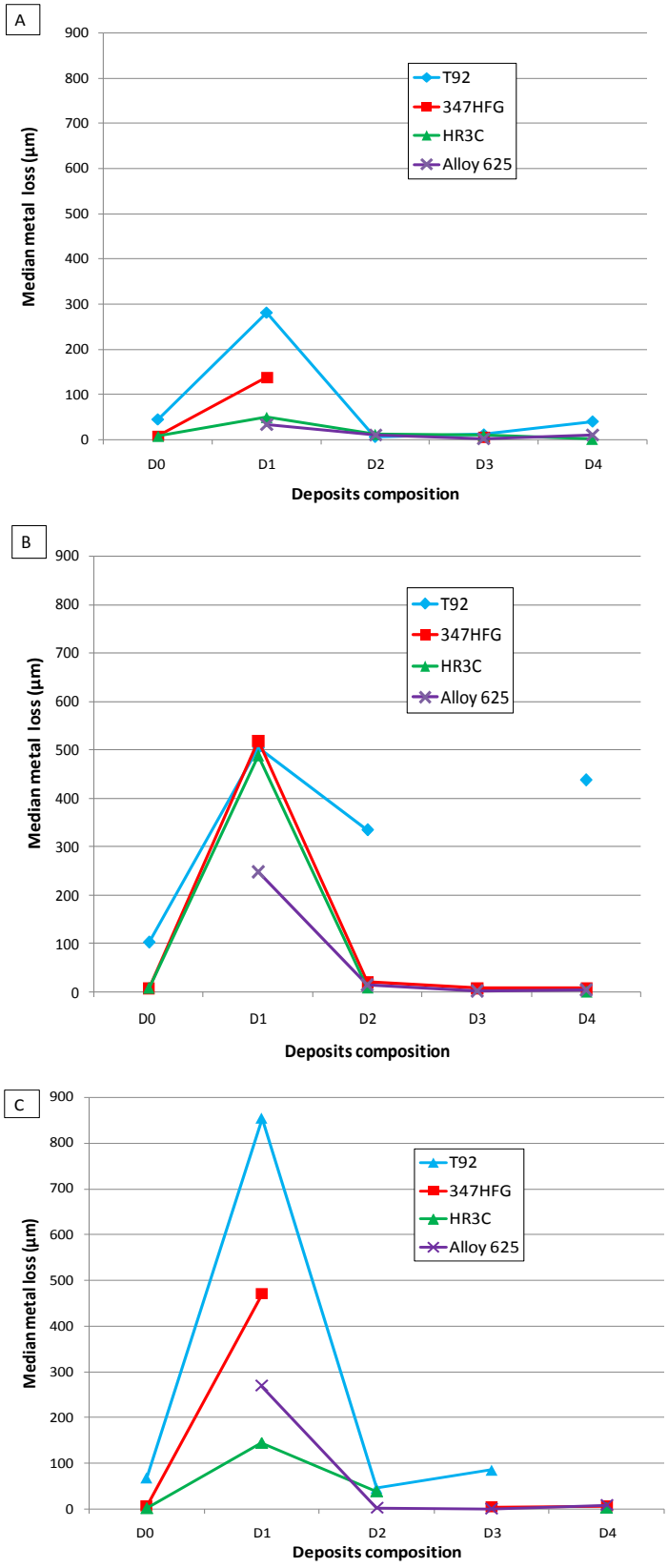

Figure 5-26: Effect of various deposits on metal loss for the alloys exposed to gases simulating air-fired combustion at (A) 600, (B) 650 and (C) 700°C for 1000 hours

5.4.2 Oxy-firing conditions

Figure 5-27 summarises the effect of all the different deposit compositions on alloys T92, 347HFG, HR3C and alloy 625 in terms of specific net mass change data after exposure in the simulated oxy-fired combustion gases at 600, 650 700 and 750°C. The most aggressive deposit was found to be D1, which caused the formation of thick layers of scale/deposit; this deposit had the highest concentration of alkali sulphate/iron oxide in it. Deposit D2 had the same ratio between these deposit components, but diluted by a clay mineral (kaolinite); the effect was to greatly reduce the amount of damage to the material. Deposit D3 (adding 1% KCl to the deposit mix) produced similar results to deposit D2. Deposit D4 (with 5% KCl) produced more damage than D2 and D3, but less than that observed with D1. Increased corrosion damage due to high levels of KCl in deposits has often been reported previously, and has been related to the formation of volatile metal chloride species (e.g. [65; 99]).

Figure 5-27(A) and Figure 5-27(B) presents mass change data for alloys T92, 347HFG, HR3C and alloy 625 exposed to simulated oxy-fired combustion gases at 600 and 650°C respectively. These data show that at both temperatures samples covered with deposit D1 gained the higher masses (as expected). Alloy T92, bare D0 or covered with deposits (D1-D4), at both temperatures (600 and 650°C), gained the higher mass values compared to other alloys (347HFG, HR3C and 625). At 600°C alloy T92 covered with deposits D2-D3 gain approximately 20 mg/cm^2 ±5, whereas all other alloys (347HFG, HR3C and alloy 625) covered with deposits D2-D4 show mass gain values < 10 mg/cm^2.

Similarly at 650°C samples covered with deposit D1 gained significant mass. Alloy T92 covered with deposit D1 gained ~90 mg/cm^2, whereas other alloys' mass gain values were in a range of 55-65 mg/cm^2. Alloy T92 covered with deposit D2-D4 gained 33 mg/cm^2 ±3 whereas other alloys (347HFG, HR3C and alloy 625) covered with deposits D2 –D4 showed mass gain values in range of 9-19 mg/cm^2.

In Figure 5-27(C), specific net mass gain data at 700°C, showed no surprise; as expected, alloy samples covered with deposit D1 gained high mass values. Alloy T92 covered with deposit D1 gained the highest mass of ~190 mg/cm^2 , whereas the higher alloyed HR3C with deposit D1, gained the lowest mass of ~70 mg/cm^2. Alloys T92 and 347HFG covered with deposit D2-D4 show significant mass change, whereas alloy HR3C and 625 with the same deposits showed barely any mass gains.

Figure 5-27(D) illustrates mass change data for alloys at 750°C. These data show that mass gain value for alloy T92 covered with deposit D1 was the highest (~190 mg/cm^2), whereas mass gain values for alloy T92 covered with other deposits D2-D4 show mass values of approximately 40 mg/cm^2 ±5. Other alloys (347HFG, HR3C and alloy 625) covered with deposit D2-D4 showed much lower mass gain values.

Figure 5-27 reveals that alloy T92 samples covered with deposit D2-D4 at all the temperatures (600-750°C) gained less mass than initially bare T92 samples. However, initially bare samples for the austenitic alloys (347HFG and HR3C) showed mass gain values are either higher or lower than austenitic alloys (347HFG and HR3C) covered with deposit D2-D4 at all the temperatures (600-750°C).

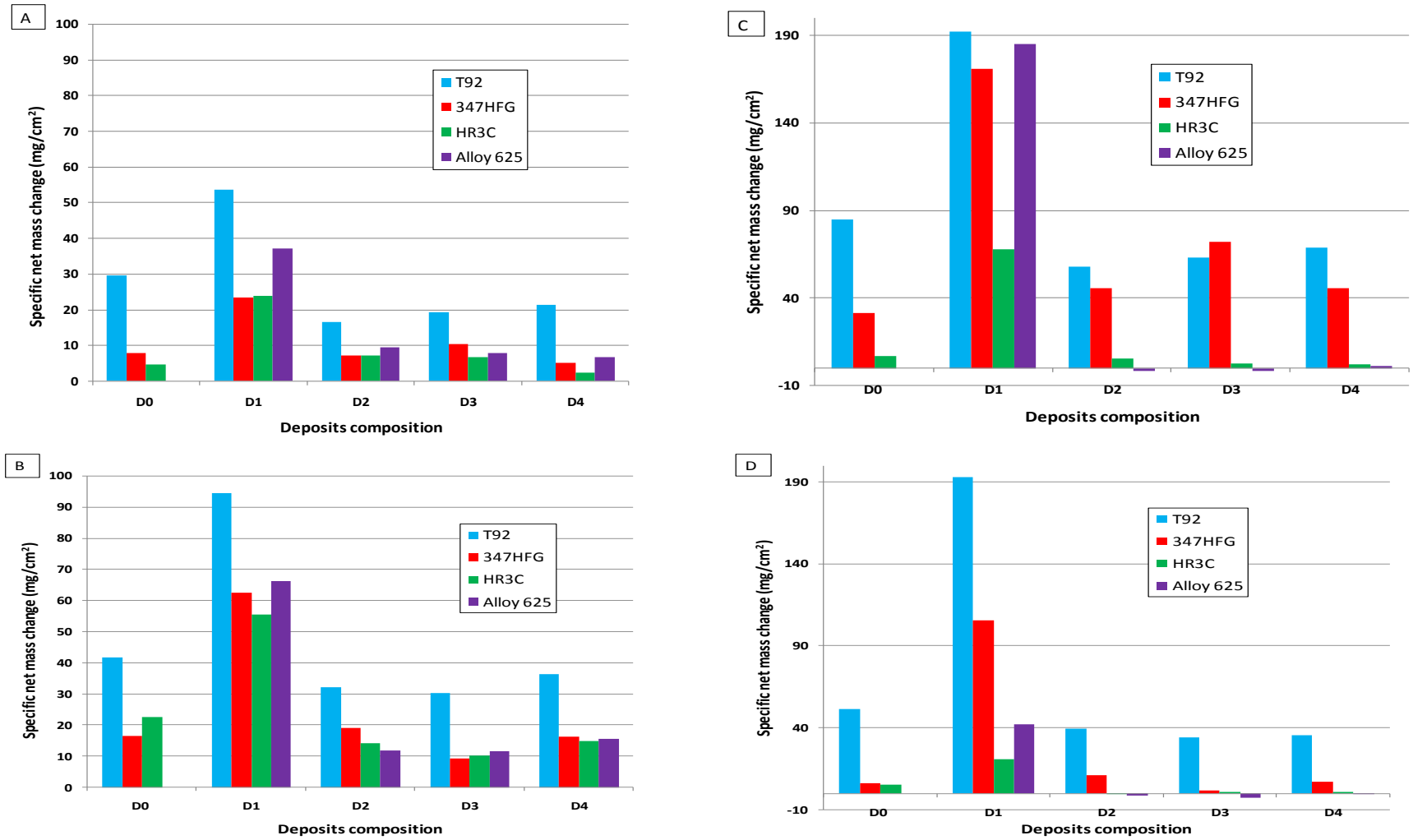

Figure 5-27: Effect of various deposits on mass change for various alloys exposed to gas simulating oxy-fired combustion at (A) 600, (B) 650 , (C)700 and (D) 750°C for 1000 hours

Figure 5-28 summarise the effect of all the different deposit compositions on alloys T92, 347HFG, HR3C and alloy 625 in terms of median metal loss data after exposure in the simulated oxy-fired combustion gases at 600, 650 700 and 750°C. The deposits in the current study have compositions that range from sulphate to sulphate/chloride mixes and so are expected to show fireside corrosion damage as a result of either sulphate or mixed sulphate and chloride related mechanisms (depending on the detailed compositions).

Figure 5-28(A) shows that alloy T92 exhibited a high metal loss value when covered with deposit D2, which was unexpected (i.e. the only sample with deposit other than deposit D1 that shows high metal loss). Alloys 347HFG, HR3C and alloy 625 show expected results with high median metal loss values when samples are covered with deposit D1 (also in agreement with mass change data). Median metal loss data for alloy T92 with deposit D3 and D4 and alloys 347HFG, HR3C and alloy 625 covered with deposit D2-D4 show values less than 35µm.

Figure 5-28(B) shows median metal loss data for the alloys at 650°C. These results show that (as expected) low chromium alloy T92 covered with deposit D1 was the most damaged alloy, with a median metal loss value of ~375 µm. Nickel-based alloy 625 with deposit D1 was found to be the least damaged alloy, with a median metal loss value of ~60 µm. T92 samples covered with deposits D2, D3 and D4 showed significant median metal loss values of ~185 µm ~75 µm and ~55 µm respectively. All other samples (347HFG, HR3C and alloy 625) covered with other deposits (D2, D3 and D4) exhibited median metal loss values of ~22 µm or less.

Figure 5-28(C) summarises the median metal loss data for alloys covered with deposits at 700°C. In oxy-firing conditions 700°C was found to be the most critical temperature with median metal loss values being the highest for all the alloys compare to the other temperatures. As expected, deposit D1 was found to be extremely corrosive at this temperature and all the alloys suffered high metal losses (in line with mass change data). Ferritic T92 and austenitic

347HFG had almost the same metal loss value of ~1135 µm. The median metal loss values observed for HR3C and alloy 625 covered with deposit D1 were 540 µm and 455 µm respectively. Samples covered with more realistic deposits (D2-D4) also showed substantial metal losses; alloy 347HFG covered with deposit D2-D4 showed higher metal loss values than ferritic T92 at 700°C. Alloy HR3C showed significant metal losses when covered with deposit D2, in fact higher metal loss than any of the other alloys (T92, 347HFG and alloy 625) covered with the same deposit (D2).

Figure 5-28(D) presents the median metal loss data for alloys T92, 347HFG, HR3C and alloy 625 covered with deposits D1-D4 exposed to simulated oxy-fired combustion gases at 750°C. For all the alloys, the most aggressive deposit was found to be deposit D1 (in agreement with the mass change data). Alloy T92 covered with deposit D1 showed the highest metal loss (~975 µm) followed by 347HFG (~660 µm) then alloy 625 (~345 µm) and finally HR3C (~30 µm). Alloy T92 and 347HFG covered with deposit D2-D4 exhibited metal loss values in a range of 50-70 µm, whereas alloy HR3C and alloy 625 median metal loss values were found to be 10 µm or less.

It can be clearly seen from the data that medial metal loss values for samples covered with deposit D1 at all the temperatures showed considerably more damage than those samples covered with other deposits (D2-D4) or exposed to gas only (D0). In addition, as discussed earlier the decrease in metal loss value with the same deposit at the highest temperature (750°C), compared with the values observed at 700°C gives a characteristic 'bell-shaped' curve. This was expected from the literature (available for fireside corrosion in air-fired conditions) [9; 32; 57; 60; 63; 67; 68] i.e. due to formation of molten complex compounds (alkali iron tri-sulphates).

These compounds are stabilised by SO_3 and melt at a lower temperature than alkali sulphates (e.g. $K_3Fe(SO_4)_3$ ~618 °C) [32; 63]. A low metal loss value for all the alloys covered with any deposits at 750°C could be due to the instability of these corrosive compounds (due to a reduction in SO_3 levels with increasing

temperature). Fireside corrosion rates have been reported to be at their highest between 650-670°C [28; 60; 63] for air-fired conditions. However, results in this PhD study in oxy-fired conditions suggest that the peak is higher, at over 700°C.

Some notable exceptions from median metal loss data in oxy-firing conditions are as follows:

- T92 and 347HFG covered with deposit D1 at 700 °C showed similar levels of rapid fireside corrosion damage
- Alloy 625 covered with deposit D1 at 750°C showed more damage than HR3C, whereas 347HFG covered with deposit D1 showed more damaged than T92 at 600°C
- With deposit D1, the low chromium steel, T92, showed the highest levels of damage at three test temperatures (650, 700 and 750°C). However, 347HFG also showed relatively high levels of damage (even matching T92 at 700 °C), indicating that its 18 weight % Cr content was not sufficient to generate more protective scales when covered with deposit D1
- HR3C and alloy 625 covered with deposit D1 showed lower damage levels but these were still higher than the 40-50 µm target levels at 650 and 700 °C for both alloys, and 750 °C for alloy 625. This suggests that the nickel-based alloy 625 may have difficulties coping with the more aggressive fireside corrosion conditions experienced at high operating temperatures

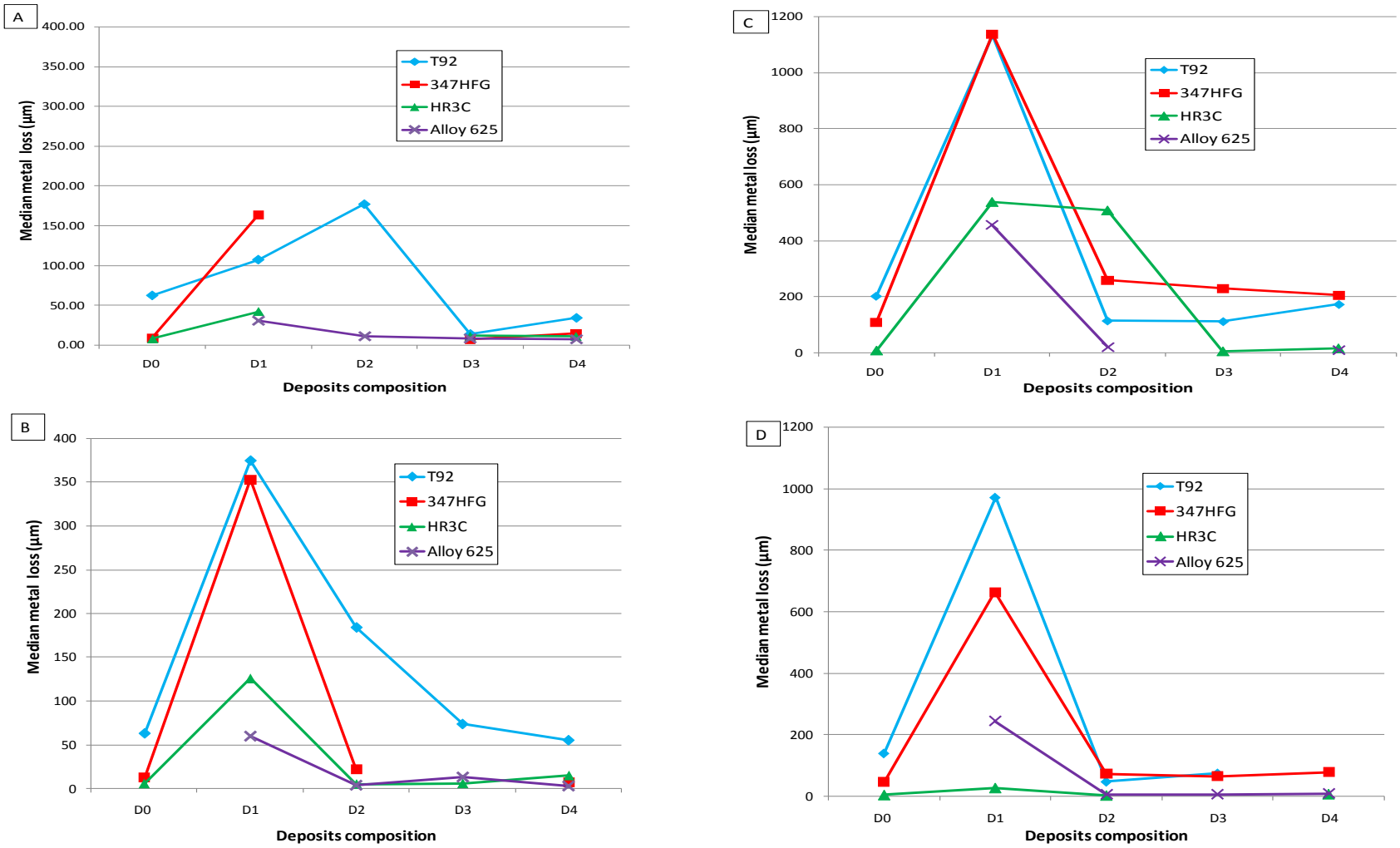

Figure 5-28: Effect of various deposits on metal loss for various alloys exposed to gas simulating oxy-fired combustion at (A) 600, (B) 650, (C) 700 and (D) 750°C for 1000 hours

5.5 Air and Oxy-firing summary

Oxy-firing technology is a demanding research area and requires further analysis and a lot more laboratory-based experimental data before its practical applications in the power plants are possible. In oxy-firing conditions (with hot flue gas recycle after the particle removal system), the reduced N_2 in the combusted gas stream combined with flue gas recycling increases the level of other gases (such as CO_2, H_2O) and corrosives gases (such as HCl and SO_2).

In this PhD project, as discussed earlier, tests were designed to target gas compositions (Table 3-3) that represent those produced using a UK coal co-fired with 20 weight % cereal co-product (CCP) in both firing conditions (air-firing [102] and oxy-firing).

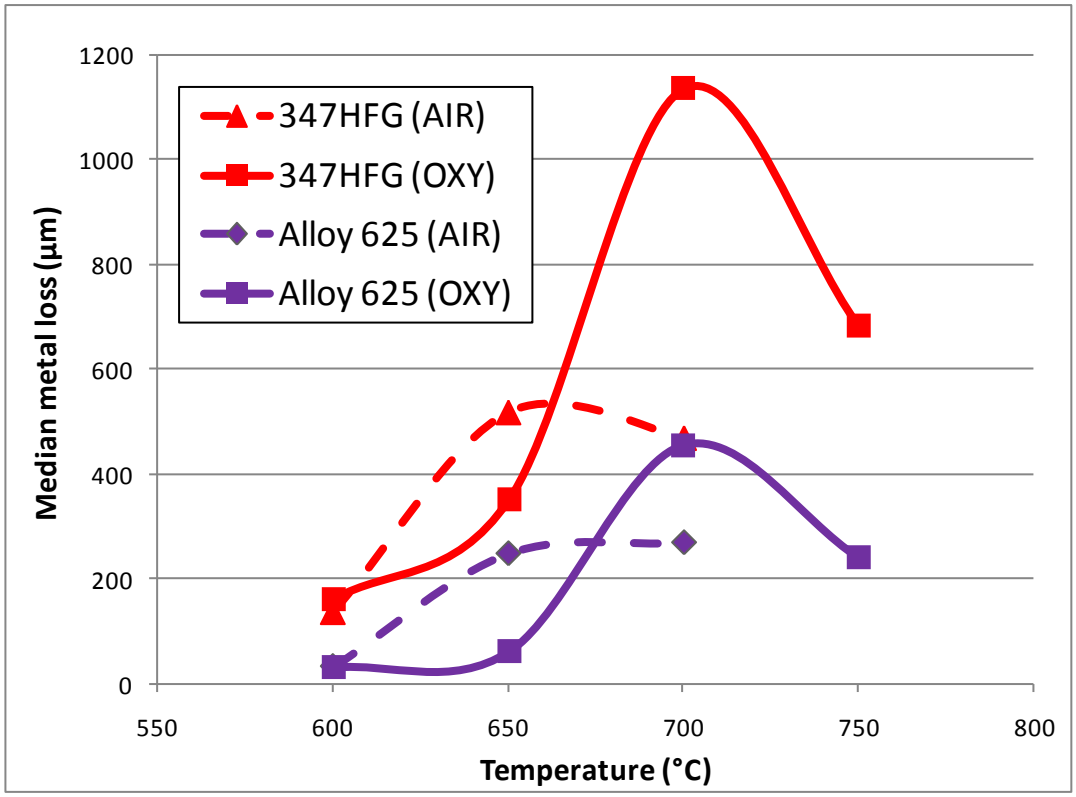

Figure 5-29: Effect of firing conditions on median metal loss damage for alloy 347HFG and 625 covered with deposit D1 after 1000 hours exposure over the temperature range from 600 to 750°C

Results in both firing conditions have been presented and discussed in previous sections. However, in this section an example is presented in Figure 5-29, so

the air and oxy-firing conditions can be compared in terms of median metal loss for alloys. Several researchers, such as Bordenet [22], Vitalis [20] and Jordal et al [21] predicted that higher corrosion damage would be observed in the oxy-firing conditions due to the more corrosive environment (i.e. higher concentrations of HCl, SO_2, CO_2 and moisture than air-firing).

The reaction mechanisms in a mixed gas environment are always difficult to predict and the presence of deposits on the alloy surface make it even more difficult. At 700°C the higher metal losses and higher mass gain values in oxy–firing gas conditions (0.63% SO_2 levels) as seen in results section, indicate the possibility of substantial formation of metal sulphates or sulphides in scales compared to air-firing condition (0.13% SO_2 levels). However, results at 650°C show median metal loss values are higher in air than oxy-fired conditions, so the formation of molten corrosive compounds in higher SO_x gas could be in transition and not fully reactive until then temperature reaches 700°C. The differences between air and oxy-fired gases at 650°C are, however, small compared to the peak values obtained in oxy-firing gases at 700°C.

5.6 Deposit stability test

Researchers involved in fireside corrosion of superheater/reheater tubes or hot corrosion of gas turbines blades, are sometimes interested in finding the changes in deposit composition during the course of their exposure. A deposit stability investigation was carried out as a small part of this PhD thesis.

The key species believed to be the main constituents of deposits formed on superheater/reheater tubes (such as potassium, sodium, iron, aluminium, sulphates and chloride) were the focus of this deposit stability test. Table 5-3 listed the atom/ions recovered from various deposits after exposure to simulated oxy-fired combustion gas (with 6260 vppm SO_2/1700 vppm HCl) at 650°C for 200 hours.

Table 5-3: Anions/atomic % recovery from various deposits after 200 hours exposure to simulated oxy-fired combustion gas (with 6260 vppm SO_2/1700 vppm HCl) at 650°C

Deposit	K (%)	Na (%)	Fe (%)	Al (%)	SO_4 (%)	Cl (%)
D1	-6.3	+1	+1.4	N/A	N/A	N/A
D2	+1.9	+4.0	+0.5	-1.7	+3.8	0
D3	+0.7	+2.2	+0.3	+1.1	+3.8	0
D4	+2.3	+2.1	-0.1	-3.0	+5.0	+0.5
D5	N/A	N/A	N/A	N/A	N/A	N/A
D6	+18	N/A	N/A	N/A	N/A	N/A
D7	-10.6	+0.6	+27.6	+5.1	N/A	N/A
D8	-24	+2.2	N/A	N/A	N/A	N/A
D9	-15	+0.5	+2.4	N/A	+20.3	-11.3
D10	-16.2	+0.6	N/A	N/A	+68	-26.4

N/A = where samples were not available for analysis.

NOTE: Table shows absolute percentage difference between calculated and recovery values

In Table 5-3 values for deposit D1 shows low recovery of K, whereas Fe and Na value are slightly higher than calculated values. K_2SO_4 and Na_2SO_4 (Table 3-2) have high melting points (1069 and 884°C respectively). Literature [82] shows, although their (Na-K sulphates) binary system has a lowest melting points of ~ 832°C, the presence of iron forms a ternary sulphate system which reduces the melting point to as low as 550°C (as listed in Table 5-4 and also shown in the diagram in Figure 5-30). The deposit D1 at test temperature 650°C should be a melt if stabilised by SO_3 from the gas stream which solidifies on cooling. The lower recovery for K could be due to transport of K into the gas stream as KOH [101].

Results for deposit D2 and D3 in Table 5-3 shows recovery for SO_4^{2-} ions suggesting, the high stability of alkali sulphates. Alkali metals (Na and K) for both deposit (D2 and D3) were also higher than the calculated values. Aluminium, one of the constituent of kaolin (mp=~1750°C) was also detected for both deposits (D2 and D3).

Table 5-4: Melting points for ternary sulphate mixtures [82]

Nominal composition w/o $Fe_2(SO_4)_3$	Melting point	Phases identified by X-ray diffraction
5.0	806	$KNaSO_4 + Na_2SO_4 + [Fe_2O_3]$
15.0	550	$KNaSO_4 + (Na, K)_3Fe(SO_4)_3 +$ hydrated salts $+ [Fe_2O_3]$
25.0	546	$KNaSO_4 + (Na, K)_3Fe(SO_4)_3 +$ hydrated salts $+ [Fe_2O_3]$
50.0	540	$(Na, K)_3Fe(SO_4)_3 +$ hydrated salts $+ [Fe_2O_3]$

In Table 5-3 results for deposit D4 show a good recovery of SO_4^{2-} and Cl^-. Deposit D4 initially contained 5 mol% of KCl salt, but at the test temperature (650°C) Cl was expected to be evaporated but in fact was detected, at slightly higher levels than the calculated value. Deposit D6 (KCl 100%) was analysed for metal only and the data in Table 5-3 show a significant yield of K. It would have been ideal to analyse deposit D6 sample for anions (Cl^- and SO_4^{2-}) to see the expected depletion of Cl^- and presence of SO_4^{2-}, but unfortunately this was not possible due to the unavailability of a sample for anion analysis by ion chromatography (IC).

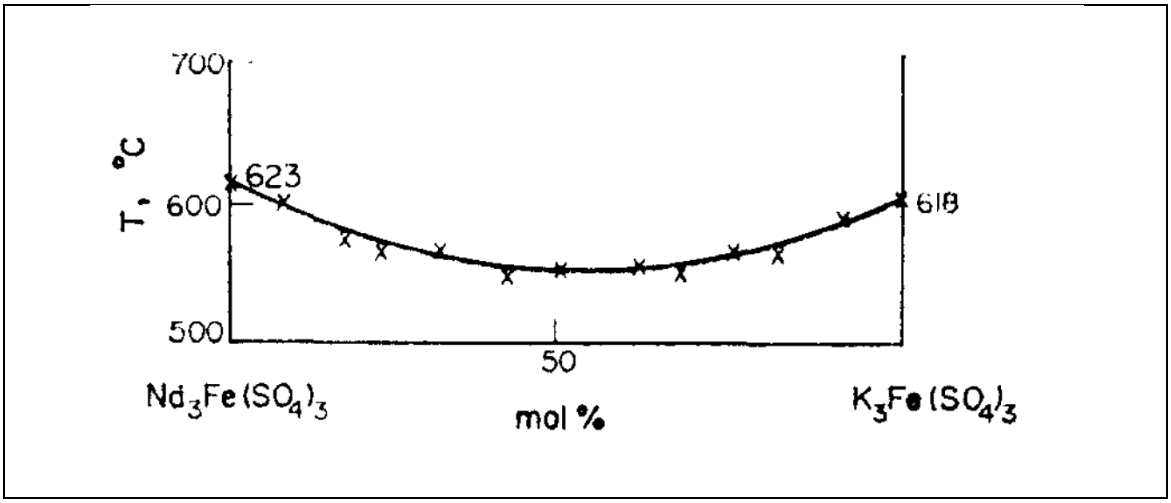

Figure 5-30: $Na_3Fe(SO4)_3$-$K_3Fe(SO4)_3$ system[82]

Similarly samples for deposit D7 and D8 were also not available for anions analysis (metals analysis required the different technique of atomic spectroscopy). However, results (for deposits D7 and D8) revealed significant loss of K and good recovery of Fe (for deposit D7).

Results for deposits D9 and D10 are the most interesting in this deposit stability test. Both deposits contain 50 mol % KCl in the initial deposit composition. However IC anion analyses showed a high depletion in Cl levels for deposit D9 and absolutely no detection for Cl in deposit D10. Moreover both deposits showed higher levels of SO_4^{2-} (20% and 68% for deposit D9 and D10 respectively). XRD analyses for these deposit were not carried out to confirm what products were formed, however results from the D6 corrosion exposure test (section 4.7.4) show that, alloy T92, 347HFG and 625 covered with 100 mol% KCl (deposit D6) formed alkali Fe/Ni tri sulphates with no sign of chlorides.

5.7 High concentration salts exposure test

The role of sulphates and chlorides (present in the deposits) as the key driving forces in the fireside corrosion of superheaters/reheaters is well known [32]. The levels of sulphur and chlorine in the fuel coal or biomass (likely to be chlorides, sulphates, SO_x or HCl after combustion) are very important for the heat exchanger lifetimes. The four synthetic deposits (D1-D4) which were

mainly used for this PhD thesis (tests 1-8) contain comparatively more sulphates than chlorides. In the last test, the deposit compositions were deliberately planned (Table 3-2) so that the effect of chlorides versus sulphates on alloys corrosion rates could be compared.

Figure 5-31 summarises some mass change data presented in the results chapter (section 4.7.1.) These data show mass changes for three alloy (T92, 347HFG and alloy 625) covered with 100 % K_2SO_4 (deposit D5) and 100% KCl (deposit D5). It can be clearly seen that low chromium alloy (T92) covered with deposit D5 and D6, as expected gained higher mass values compared to other alloys (347HFG and 625). Another important feature to be noticed is the substantial mass gain values of each alloys covered with deposit D6 (100 % KCl) compared to alloys covered with deposit D5 (100% K_2SO_4).

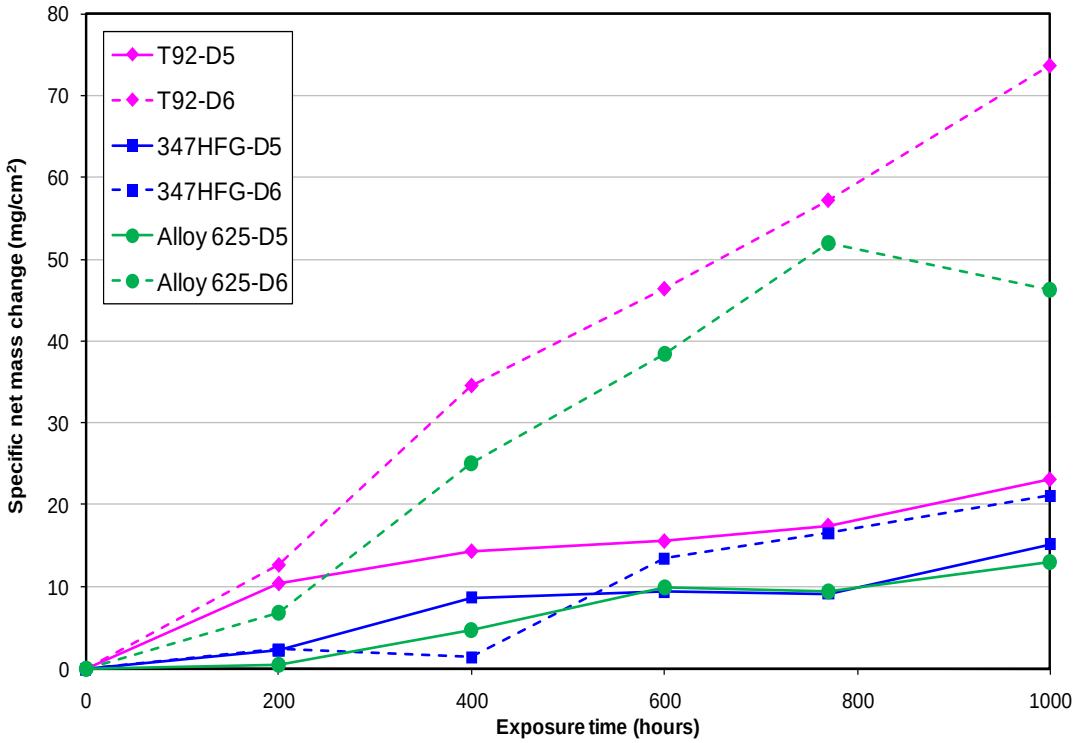

Figure 5-31: Specific net mass change data for alloys T92, 347HFG and 625 covered with deposits D5 and D6 exposed to the simulated oxy-firing combustion gas for 1000 h at 650°C

Such high mass gain values for an alloy covered with chlorides than alloy with sulphates shows a similar trend to work carried out by Johansson and co-

workers [66] who showed high mass gain values for alloy covered with KCl salt (in Figure 5-32). However, it should be noted that test conditions, such as temperature, alloy and gas compositions were different to the environment set for this PhD study.

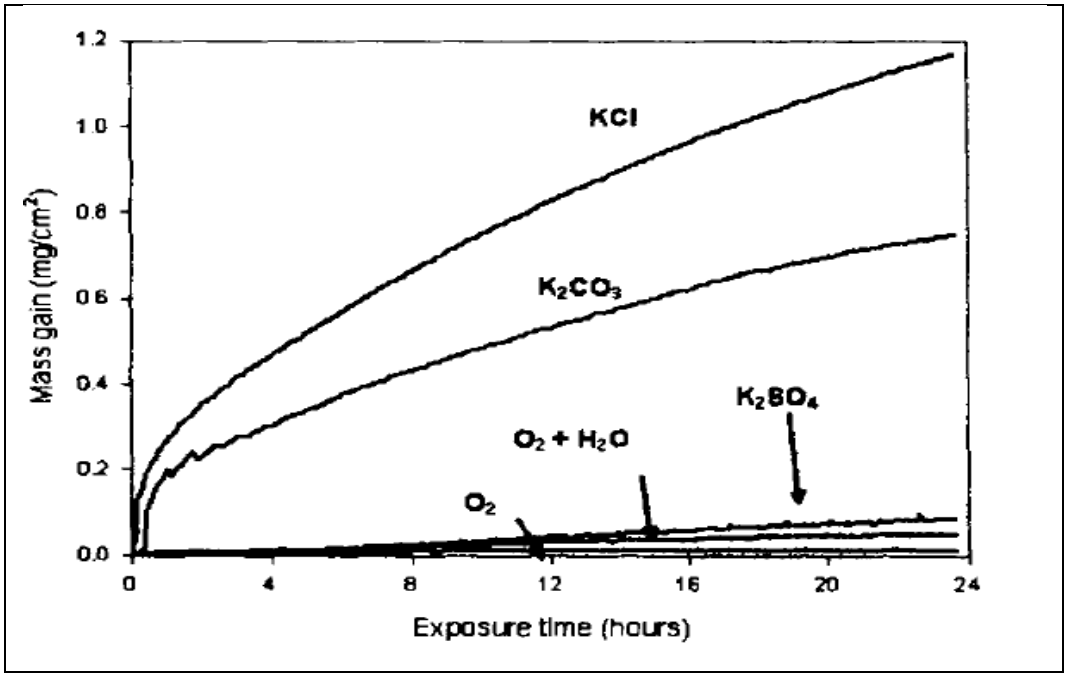

Figure 5-32: Mass change data for alloy 304L steel bare (exposed to O_2+ 40% H_2O and dry O_2) and covered with 0.1mg/cm^2 of KCl, K_2CO_3 and K_2SO_4.exposed at to O_2+ 40% H_2O at 600°C. [66]

Several researchers [66; 139] have reported that in boiler flue gas environments, alkali chlorides in the deposits are replaced by alkali sulphates, and suggested the following reactions:

$$KCl+SO_2+\frac{1}{2}O_2(g) + H_2O(g) = K_2SO_4 + 2HCl(g) \quad \textbf{(5-5)}$$

$$2KCl + SO_2\,(g) + O_2(g) = K_2SO_4 + Cl_2(g) \quad \textbf{(5-6)}$$

Thermodynamic calculations in a fireside corrosion environment also show that a formation of sulphates are favoured and indicates that corrosion damage can be reduced by adding sulphur in the system [66; 105].

The metal loss data for all three alloys (T92, 347HFG and 625), covered with high concentration of salts (Table 3-2) has been presented in section 4.7.3.

Figure 5-33 shows median metals loss data for alloys T92, 347HFG and 625 covered with deposit D5, D6, D7 and D9 so that the effects of Cl^- and SO_4^{2-} on different alloy corrosion damage can be observed. Data shows that all alloys covered with 100% KCl salt experienced higher metal loss value than alloys covered with 100% K_2SO_4. Median metal loss results for alloys covered deposits 7 and 9 show that alloy T92 and 347HFG had higher corrosion damage with deposit D9 (higher chlorides), whereas alloy 625 had higher damage with deposit D7 (higher sulphates). Another interesting feature noticed, was the higher damage observed for austenitic alloy 347HFG (~18% chromium) than T92 (~9% chromium) with all four deposits (D5, D6, D7, and D9). Median metal loss data indicates that the high chromium level in alloy 347HFG reacts to produce chlorides; such rapid reaction of alloys with higher chromium contents compared to low chromium alloys with chlorides has been reported by several researchers [66; 77; 106].

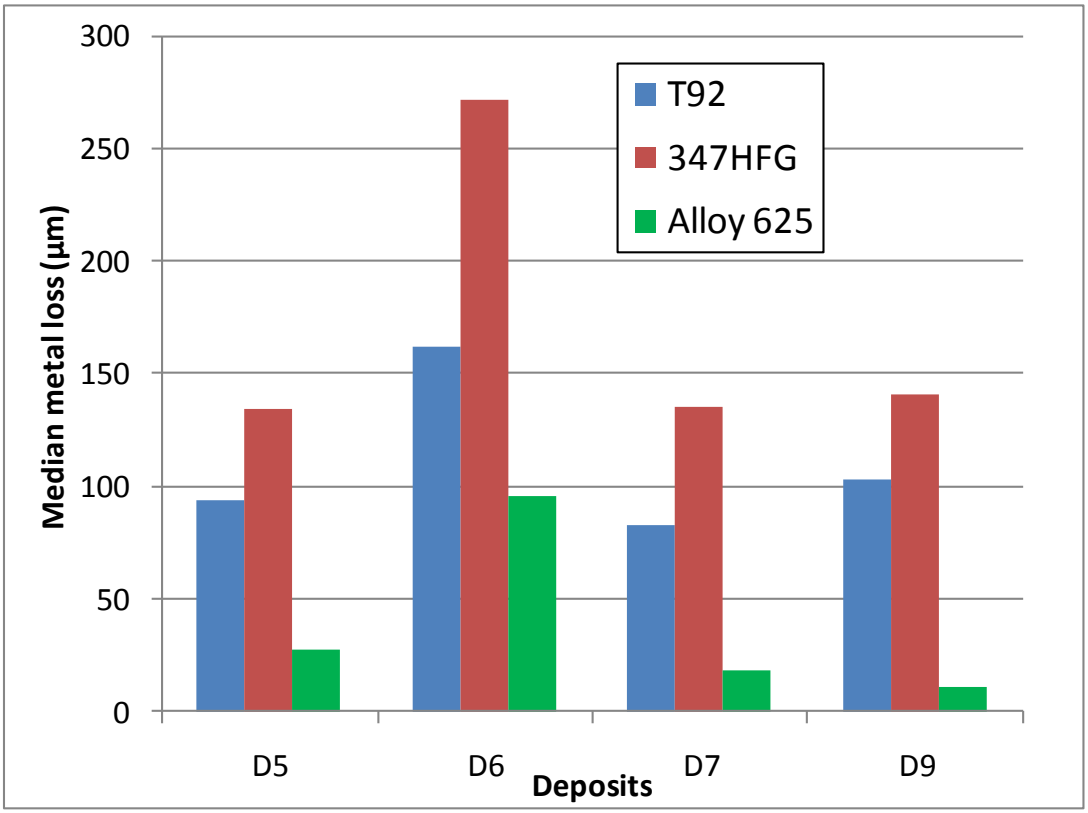

Figure 5-33: Median metal loss data for alloys T92, 347HFG and 625 covered with deposit D5, D6, D7 and D9 in simulated oxy-fires combustion gases at 650°C after 1000 hours.

Figure 5-34 shows the stabilities of different metals (Cr, Ni and Fe) oxides and chlorides at different partial pressures of oxygen and chlorine. It is clearly shown that at higher and lower pCl_2, Cr forms $CrCl_3$ and $CrCl_2$ respectively. Cr also forms chlorides at lower pCl_2 chlorides than iron and nickel.

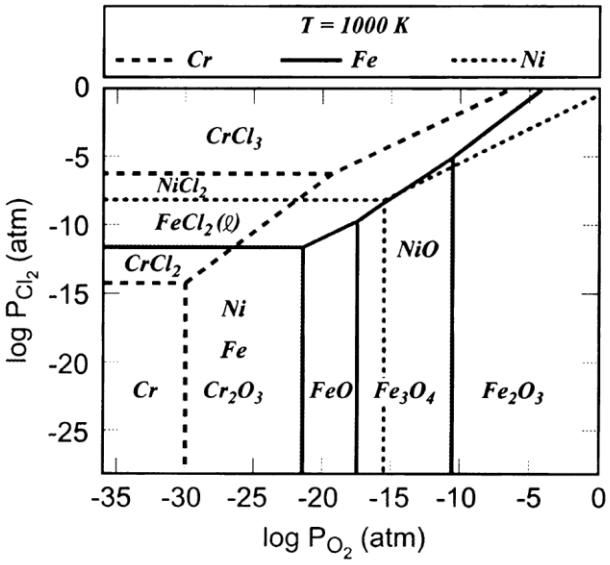

Figure 5-34: Stability diagram for Cr/Fe/Ni-O-Cl at 727°C [139]

The reaction mechanisms shown in equation (5-5) and (5-6) are well known and reported in several publications [65; 66; 139]. These show that alkali chloride salts present on the heat exchanger surface in SO_2 oxidising gas favour the formation of sulphates and the release of Cl_2 and/or HCl gases. If there is insufficient sulphur (low SO_2 in the environment) to react with the chlorides then they will remain on the metal surface and cause rapid corrosion. Nielsen.et.al [139] presents an extensive work by Karlsson and co-workers [140], of the reaction between KCl and metals (Fe, Cr and their oxides). In their work they observed a reaction between KCl and Fe_2O_3 (or Fe) in the gas (1:1 mixture of SO_2 and O_2) at temperature 310°C with rate increases up to 500°C. The corrosion product was analysed and found to be $K_3Fe(SO_4)_3$ and no $FeCl_3$. It was believed that corrosion was caused by liquid $FeCl_3$ ($FeCl_3$ absence could be due to reaction with SO_2 and O_2 equation(5-8]) and proposed the following mechanisms which could be a case in this PhD study for alloys covered with high levels of KCl (deposit D6, D9 and D10).

Fe_2O_3+ 6KCl + $3SO_2(g)$ + $\frac{3}{2}O_2(g)$ = $2FeCl_3$ (s, l, g) + $3K_2SO_4$ **(5-7)**

$2FeCl_3(s, l, g) + 3SO_2(g) + 3O_2(g) = Fe_2(SO_4)_3(s) + 3Cl_2(g)$ **(5-8)**

And by combining both equations:

$2Fe_2O_3 + 12KCl + 12SO_2(g) + 9O_2(g) = 4K_3Fe(SO_4)_3(s) + 6Cl_2(g)$ **(5-9)**

XRD analysis, after exposure for the alloys covered with deposit D6 (100% KCl) showed the presence of sulphate crystals (alkali iron tri-sulphates) in good agreement with the reported work data [139].

5.8 Alloys life prediction modelling

The selection of suitable alloys for the superheater /reheater materials in novel conditions such as oxy-firing environment is one of the power generation industry's main interests. Using experimental data to generate mathematical fireside corrosion models will play a crucial role to achieve such targets. This PhD course has provided sufficient data sets which could be used for the development of such models (i.e. five different alloys in air and oxy-firing conditions with different deposits in the temperature range of 600-750°C)

An Arrhenius equation was used (5-10) to determine the activation energy for alloys

$$k = A \exp\ -\frac{Q}{RT} \quad \textbf{(5-10)}$$

Further simplifying the equation

$$lnk = lnA - \frac{Q}{R} \cdot \frac{1}{T} \quad \textbf{(5-11)}$$

Where

lnk = natural log of corrosion damage (μm)

lnA = natural log of constant A

Q= Activation energy (J/mol)

T = temperature (K)

R = gas constant ($J/mol.K$)

Activation energy was calculated

The first step was to simply take the natural log of corrosion damage (k) values for alloys of interest, followed by fitting the regression line to the data lnk versus $1/T$. The slope = (-Q/R) was used to calculate activation energy Q, where R = 8.314 KJ/mol. The y-intercepts gives a lnA constant value. However it should be noted that the activation energy calculated in this modelling work considers, only the upward trend for the corrosion curves. From the results it was clear that alloys corrosion behaviours showed a well-known 'bell shaped' curves. Additional equations with more data sets are needed to define the downwards trends and give a wider range fireside corrosion model. The activation energy 'Q' and constant 'lnA' values were further plotted against alloy types as shown in Figure 5-35 for alloys 347HFG and 625 covered with deposit D1, in both air and oxy-firing environments.

Figure 5-35 shows that that are higher activation energies and lnA values in air-firing conditions for both alloys compared to oxy-firing conditions and suggested that higher activation energies are required when the environment is less corrosive. In contrast low activation energy (Q) values for oxy-firing data, suggested alloys required lower activation energy for corrosion to occur in the oxy-firing gas environment.

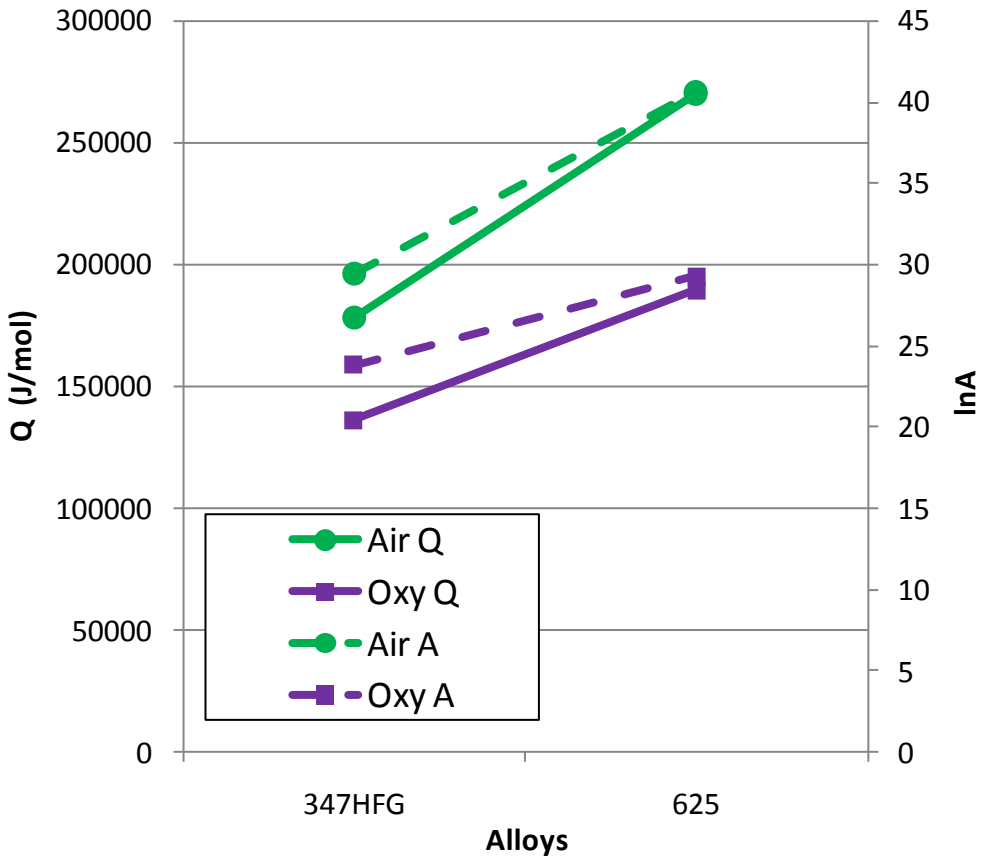

Figure 5-35: Model shows activation energy and constant values for alloy 347HFG and 625 in simulated air and oxy-firing combustion gas plus deposit D1.

Similarly higher activation energies values for alloy 625 in both firing conditions indicates that, high levels of chromium and nickel in the alloy 625 required higher activation energy for corrosion to occur. Figure 5-35 is a simple approach towards fireside corrosion modelling of upward slope of bell shaped curve. As discussed earlier more data are needed to define downwards slope of these curves.

6 CONCLUSIONS

Fireside corrosion of superheater/reheater tubes is a major concern for the operation of advanced power plants (using high levels of biomass co-fired with coal, oxy-firing system and advanced steam conditions). This PhD study was focused on gaining a better understanding of materials performance in the conditions future power plants will have to face. A series of fireside corrosion tests were carried out in a temperature range of 600-750 °C for 1000 h using the well-established deposit recoat test method. The tests were targeted at simulating the corrosive environments on the surfaces of superheaters/reheaters in power plants operating with air-firing or oxy-firing (with hot flue gas recycling) of fuel mixes (biomass and coal).The conclusions drawn from the overall work are as follows:

- The trend in corrosion damage with temperature for alloy covered with deposits in both firing conditions shows a bell-shaped curve, which is characteristic of superheater fireside corrosion damage, with the highest damage levels generally being observed at 700°C for oxy-firing test and at 650°C for air-firing test. This shift in peak corrosion damage in oxy-firing environment from 650°C (in air-firing) to 700°C was due to the higher levels of SO_x gases which stabilised the corrosive compounds; particularly alkali iron tri-sulphates
- The mass change data results show that under most exposure (for both air and oxy-firing) conditions the fireside corrosion performance of the materials can be ranked inversely to their chromium contents. However when alloys covered with deposit D1, alloy 625 gained higher mass values than austenitic alloys (347HFG and HR3C) in most cases
- The dimensional metal loss dataset generated form a good basis for the development of quantitative models of alloy fireside corrosion performance in these exposure conditions

- The ranking of alloys in terms of metal damage was generally (highest to lowest): T22 > T92 > 347HFG > HR3C > 625. However, there were notable exceptions when samples were covered with deposit D1:
    - In oxy-firing conditions, at 700°C, alloys T92 and 347HFG showed similar levels of rapid fireside corrosion damage
    - In oxy-firing at 750°C, alloy 625, showed more damage than HR3C
    - In air-firing conditions, at 650°C alloys T92, 347HFG and HR3C showed similar level of damage
    - In air-firing at 700°C nickel based alloy 625 showed higher corrosion damage than alloy HR3C
- Amongst all the deposits, deposit D1 was found to be the most aggressive deposit for all the alloys, in both (air and oxy) firing conditions
- Surface morphology of alloys distinguishes ferritic and austenitic alloys. Scales formed on ferritic alloys were generally more dense and adherent to the surface whereas scales formed on austenitic alloys were thin and flakey /crystalline in structure
- SEM images of cross-sections through bare 347HFG and HR3C in both (air and oxy) firing conditions showed internal corrosion attack. Another significant observation for alloys covered with deposit was generally a uniform corrosion for ferritic alloys whereas localised and pitting type attack for high alloyed material was observed
- EDX mapping of ferritc and austenitic alloys in both (air and oxy) firing conditions, shows mixed oxidation/sulphidation or fireside corrosion mechanisms. EDX maps and elemental profiles of ferritic and austenitic alloys: reveals NiS precipitates in the internal damage zones in austenitic steels; and S rich zone close to spinel/metal interface in ferritic steels
- Deposit stability shows reasonable recovery for alkali metal (sodium and potassium), aluminium and iron. However, chlorides were either replaced by sulphates or recovered at low levels
- The high concentration salt exposure test reveals:

  - Deposits containing high levels of KCl (i.e. D6, D9 and D10), painted on alloys demonstrated higher corrosion damage than the comparative deposits with higher K_2SO_4 concentration (D5, D7 and D8) painted on samples
  - Alloy 347HFG suffered higher corrosion damage than alloy T92 suggesting a higher affinity of Cr towards chlorine.
  - Most alloys covered with high concentration deposits (100% K_2SO_4 or 100% KCl) after exposure showed evidence of complex alkali iron tri-sulphates, responsible for severe fireside corrosion of superheaters/reheaters

- In the reproducibility test, the mass change, scale thickness and metal loss values for alloys were found to be slightly lower than the original test. However, considering the number of variables, duration and intensive manual handling involved in the fireside corrosion testing, this repeat test showed fair reproducibility
- An example of an initial corrosion damage model for the upward slope of a 'bell-shaped' curve has been presented as an opening for further development of fireside corrosion models (in which downward trend could also be included)

7 RECOMMENDATIONS FOR FURTHER RESEARCH

Towards the end of this PhD thesis several ideas emerged. Some major recommendations for further work are as follows:

- The highest corrosion damage in oxy-firing tests was observed at 700°C followed by a decrease in corrosion to 750°C. One or more tests in the temperature range between 700 and 750°C should be carried out so the peak corrosion temperature can be established and more data generated for the downward trend for fireside corrosion models. A similar approach should be applied for the air-fired environments.
- In all the fireside corrosion tests, the remaining deposits in the crucibles that had fallen off from the samples during or after the tests were collected in sealed plastic bags and stored in a desiccator. It is highly recommended that these deposits should be characterised using XRD/SEM analysis.
- For the determination of deposit stability, only one test was carried out, which produced limited number of samples and, due to different methods of analysis for metals (K, Na, Al and Fe) and anions (SO_4^{2-} and Cl^-), not all the samples could be analysed. It is suggested that more tests should be carried out, that should provide enough samples for analysis by both AS for metals and IC for anions; such data will be very useful in the understanding for corrosion mechanisms as well as deposit stabilities.
- KCl salt ratio in realistic deposits (D2-D4) should be increased to help simulate higher ratio of biomass in co-firing power plants
- In oxy-firing conditions, the alloys carburisation, and formation of carbides is an outstanding question. In-depth analysis should be carried out to observe any carbide present in polished cross-sections.

REFERENCES

[1] *International Energy Agency IEA, World Energy Outlook,* (2010).

[2] Stringer, J. (2004), "High temperature corrosion issues in energy-releated systems", *Materials Research,* vol. 7, no. 1, pp. 1-19.

[3] Oakey, J. E., Pinder, L. W., Vanstone, R., Henderson, M. and Osgerby, S. (2003), *Review of Status of Advanced Materials for Power Generation,* COAL R224, DTI/Pub URN 02/1509.

[4] *DECC; Statistical Report "UK climate change sustainable development indicator: 2010 greenhouse gas emissions, provisional figures and 2009 greenhouse gas emissions, final figures byfuel type and end-user",* (2011).

[5] *Annual Report and Financial Statements; Doosan Babcock Energy,* (2008), .

[6] Dechamps, P. (2006), "The EU Research Strategy Towards Zero Emission Fossil Fuel Power Plants", in Lecomte-Beckers, J., Carton, M., Schubert, F., et al (eds.), *Materials for Advanced Power Engineering 2006,* (Forschungszentrum Jülich GmbH 2006), pp. 25-40.

[7] Farley, M. (2007), "Clean Coal Technologies for Power Generation", in Strang, A., Banks, W.,M., McColvin, G.,M., et al (eds.), *Parsons 2007: Power Generation in an Era of Climate Change,* (IoM Communications, 2007), pp. 335-342.

[8] Shingledecker, J. P. and Wright, I. G. (2006), "Evaluation of the Materials Technology Required for a 760°C Power Steam Boiler", in Lecomte-Beckers, J., Carton, M., Schubert, F., et al (eds.), *Materials for Advanced Power Engineering 2006,* (Forschungszentrum Jülich GmbH, 2006), pp. 107-119.

[9] Simms, N. J., Kilgallon, P. J. and Oakey, J. E. (2007), "Fireside issues in advanced power generation systems", *Energy Materials: Materials Science and Engineering for Energy Systems,* vol. 2, no. 3, pp. 154-160.

[10] Syed, A. U., Hussain, T., Simms, N. J. and Oakey, J. E. ((Accepted)), "Microscopy of Fireside Corrosion on Superheater Materials for Advanced Power Plants", *Materials at High Temperatures.*

[11] Abou-elazm, A. S., El Mahallawi, I., Abdel-karim, R. and Rashad, R. (2009), "Failure investigation of secondary super-heater tubes in a power boiler", *Engineering Failure Analysis,* vol. 16, no. 1, pp. 433-448.

[12] *Advanced Power Plant Using High Efficiency Boiler/Turbine,* (2006), DTI/Pub URN 06/655, BEST PRACTICE BROCHURE, CARBON ABATEMENT TECHNOLOGIES PROGRAMME.

[13] Otter, N. (2007), *BCURA Robens coal science lecture.*

[14] Li, L., Duan, Y., Cao, Y., Chu, P., Carty, R. and Pan, W. -. (2007), "Field corrosion tests for a low chromium steel carried out at superheater area of a utility boiler with three coals containing different chlorine contents", *Fuel Processing Technology,* vol. 88, no. 4, pp. 387-392.

[15] MacCarthy, J. and Choudrie, S. (2010), *UK Greenhouse Gas Inventory: National Statistics User Guide,* AEA Technology plc.

[16] Bordenet, B. (2008), "Influence of novel cycle concepts on the high-temperature corrosion of power plants", *Materials and Corrosion,* vol. 59, no. 5, pp. 361-366.

[17] Syed, A. U., Simms, N. J. and Oakey, J. E. (2011), "Fireside corrosion of superheaters: Effects of air and oxy-firing of coal and biomass", *Fuel,* vol. In Press.

[18] Skea, J. and Ekins, P. (2009), *Making the transition to a secure and low-carbon energy system,* S3097.

[19] Khan, A. A., de Jong, W., Jansens, P. J. and Spliethoff, H. (2009), "Biomass combustion in fluidized bed boilers: Potential problems and remedies", *Fuel Processing Technology,* vol. 90, no. 1, pp. 21-50.

[20] Vitalis, B. (2007), "Overview of oxy-combustion technology for utility coal-fired boilers", pp. 968.

[21] Jordal, K., Anheden, M., Yan, J. and Strömberg, L. (2004), "Oxyfuel combustion for coal-fired Power Generation with CO_2 Capture - Opportunities and Challenges", *Proceedings of GHGT-7, 7th International Conference on Greenhouse Gas Control Technologies.*

[22] Bordenet, B. and Kluger, F. (2008), "Thermodynamic modelling of the corrosive deposits in oxy-fuel fired boilers", Vol. 595-598 PART 1, pp. 261.

[23] Koch, G. H., Brongers, M. P. H., Thompson, N. G., Virmani, Y. P. and Payer, J. H. (2002), *Corrosion costs and preventive strategies in the United States,* U.S. Dept of Transportation.

[24] Montgomery, M., Henderson, P., Davis, C. and Karlsson, A. (2005), "In-situ Fireside Corrosion Testing of Superheater Materials with Coal, Wood and Straw Fuels for Conventional and Advanced Steam Temperatures", *VGB PowerTech,* vol. 6, pp. 50-53.

[25] Gleeson, B. (2009), "Oxidations of Metals: Editorial", *Oxidation of Metals,* vol. 71, no. 1-2, pp. 1-3.

[26] Birks, N., Meier, G. H. and Pettit, F. S. (2006), *Introduction to the high-temperature oxidation of metals,* 2nd ed, Cambridge University Press, Cambridge, UK.

[27] Lai, Y. G. (1990), *High Temperature Corrosion of Engineering Alloys,* ASM International.

[28] Khanna, A. S. (2002), *Introduction to high temperature oxidation and corrosion,* ASM International, Materials Park, OH.

[29] Wright, I. G., Schütze, M., Paterson, S. R., Tortorellia, P. F. and and Dooley, R. B. (2004), "Progress in prediction and control of oxide scale exfoliation on superheater and reheater alloys", *Proc. Fourth International Conference on Boiler Tube and HRSG Tube Failures and Inspections,* 2-5 November, SanDiego C.A, .

[30] Slattery, J. C., Peng, K. -., Gadalla, A. M. and Gadalla, N. (1995), "Analysis of iron oxidation at high temperatures", *Industrial & Engineering Chemistry Research,* vol. 34, no. 10, pp. 3405-3410.

[31] Kubaschewski, O. and Hopkins, B. E. (eds.) (1962), *Oxidation of Metals and Alloys,* 2nd ed, Butterworth and Co Ltd, London.

[32] Stringer, J. and Wright, I. G. (1995), "Current limitations of high-temperature alloys in practical applications", *Oxidation of Metals,* vol. 44, no. 1-2, pp. 265-308.

[33] Atkins, P. W. (ed.) (1998), *Physical Chemistry,* 6th ed, Oxford University Press.

[34] NASA (2011), *Thermodynamics*, available at: http://www.grc.nasa.gov/WWW/k-12/airplane/thermo.html (accessed 1 June 2010).

[35] Cottrell, A. (ed.) (1995), *An Introduction to Metallurgy,* 2nd ed, The Institute of Materials, London.

[36] Stephenson, D., (2009), *High temperature oxidation and corrosion*, Cranfield University.

[37] Brady, J. H.,J (ed.) (1988), *Fundamentals of chemistry,* 2nd ed, Wiley.

[38] University of Cambridge (2009), *Dissemination of IT for the Promotion of Materials Science (DoITPoMS)*, available at:

http://www.doitpoms.ac.uk/tlplib/ellingham_diagrams/ellingham.php (accessed Febuary, 11).

[39] Getman, R. B., Xu, Y. and Schneider, W. F. (2008), "Thermodynamics of environment-dependent oxygen chemisorption on Pt(111)", *Journal of Physical Chemistry C,* vol. 112, no. 26, pp. 9559-9572.

[40] Wikepedia, *Ellingham diagram*, available at: http://en.wikipedia.org/wiki/Ellingham_diagram (accessed June 09).

[41] Andersson, J., Helander, T., Höglund, L., Shi, P. and Sundman, B. (2002), "Thermo-Calc & DICTRA, computational tools for materials science", *Calphad,* vol. 26, no. 2, pp. 273-312.

[42] Huang, Z., Conway, P. P., Thomson, R. C., Dinsdale, A. T. and Robinson, J. A. J. (2008), "A computational interface for thermodynamic calculations software MTDATA", *Calphad,* vol. 32, no. 1, pp. 129-134.

[43] Ashby, M. F. and Jones, D. R. H. (2006), *Engineering Materials 2: An Introduction to Microstructures, Processing and Design,* Elsevier Science & Technology.

[44] Stott, F. H. (1987), "The protective action of oxide scales in gaseous environments at high temperature", *Reports on Progress in Physics,* vol. 50, no. 7, pp. 861-913.

[45] Kofstad, P. (1988), *High temperature corrosion,* 2nd ed, Elsevier Applied Science, Barking.

[46] Talbot, D. and Talbot, J. (1997), *Corrosion science and technology,* CRC Press, Boca Raton, Fl.

[47] Fontana, M. G. and Greene, N. D. (1978), *Corrosion engineering,* 2d ed, McGraw-Hill, New York.

[48] Trethewey, K. R. and Chamberlain, J. (eds.) (1995), *Corrosion for Science and Engineering,* 2nd ed, Addison Wesley Longman Limited, England.

[49] Cahn, R. W., Haasen, P., Kramer, E. J. and Schütze, M. (2000), *Corrosion and environmental degradation,* Wiley-VCH, Weinheim.

[50] Coleman, K. (2008), *Fireside corrosion in biomass combustion plants* (Ph.D thesis), Cranfield University.

[51] Spiegel, M., Thonnsssen, F. and Schraven, P. (2011), "Corrorisks of nickel bases allloys in morden 700°C power plants", Vol. Paper 1065, 5-8th Sep, .

[52] Wikepedia (2009), *High temperature corrosion*, available at: http://en.wikipedia.org/wiki/High_temperature_corrosion (accessed May/19).

[53] Sidhu, T. S., Prakash, S. and Agrawal, R. D. (2006), "Hot corrosion studies of HVOF NiCrBSi and Stellite-6 coatings on a Ni-based superalloy in an actual industrial environment of a coal fired boiler", *Surface and Coatings Technology,* vol. 201, no. 3-4, pp. 1602-1612.

[54] Nicholls, J. R., Simms, N. J. and Encinas-Oropesa, A. (2007), "Modelling hot corrosion in industrial gas turbines", *Materials at High Temperatures.Vol.24,* vol. 24, no. 3, pp. 149-162.

[55] Otero, E., Pardo, A., Merino, C., Perez, F. J., Utrilla, M. V. and Del Peso, J. L. (1997), "Corrosion behaviour of IN-800 alloy in waste incineration: hot corrosion by molten chlorides", *FE, Ferrous alloys; SP, Superalloys*.

[56] Scully, J. C. (1990), *The fundamentals of corrosion,* 3rd ed, Pergamon, Oxford.

[57] Stringer, J. (1983), "High-temperature corrosion problems in steam boilers", Vol. 83-5, pp. 1.

[58] Nicholls, J. R., Simms, N. J., Chan, W. Y. and Evans, H. E. (2002), "Smart overlay coatings - Concept and practice", *Surface and Coatings Technology,* vol. 149, no. 2-3, pp. 236-244.

[59] Simms, N.J., Encinas-Oropesa, A. and Nicholls, J.R., (2004), *Development of hot corrosion on coated single crystal superalloys*.

[60] Natesan, K. and Park, J. H. (2007), "Fireside and steamside corrosion of alloys for USC plants", *International Journal of Hydrogen Energy,* vol. 32, no. 16, pp. 3689-3697.

[61] Shamanna, S. and Schobert, H. H. (1997), "Fireside corrosion of selected alloys by ash recovered from coal-water slurry combustion", *Fuel Processing Technology,* vol. 53, no. 1-2, pp. 133-156.

[62] Syed, A. U., Simms, N. J. and Oakey, J. E. (2010), "Fireside corrosion of superheaters/reheaters in advanced power plants", *9th Liege Conference: Materials for Advanced Power Engineering, 2*7-29 September, Belgium, pp. 976-985.

[63] Reid, W. T. (1971), *External corosion and deposits:boilers and gas turbines,* Elsevier, New York.

[64] Meadowcroft, D. B. (1987), "High temperature corrosion of alloys and coatings in oil-and coal-fired boilers", *Materials science and engineering,* vol. 88, pp. 313-320.

[65] Montgomery, M., Vilhelmsen, T. and Jensen, S. A. (2008), "Potential high temperature corrosion problems due to co-firing of biomass and fossil fuels", *Materials and Corrosion.Vol.59,* vol. 59, no. 10, pp. 783-793.

[66] Johansson, L., Svensson, J., Skog, E., Pettersson, J., Pettersson, C., Folkeson, N., Asteman, H., Jonsson, T. and Halvarsson, M. (2007), "Critical Corrosion Phenomena on Superheaters in Biomass and Waste-Fired Boilers", *Journal of Iron and Steel Research, International,* vol. 14, no. 5, Supplement 1, pp. 35-39.

[67] Bryers, R. W. (1996), "Fireside slagging, fouling, and high-temperature corrosion of heat-transfer surface due to impurities in steam-raising fuels", *Progress in Energy and Combustion Science,* vol. 22, no. 1, pp. 29-120.

[68] Davis, C. J. and Pinder, L. W. (2004), *The effect of co-firing biomass with coal on the fireside corrosion of boiler materials,* COAL R267 DTI/Pub URN 04/1795.

[69] Wright, I. G., Price, C. W. and Herchenroeder, R. B. (1978), EPRI-FP-557, Electric Power Research Institute report, Palo Alto, CA.

[70] James, P. J. and Pinder, L. W. (1997), "The impact of coal chlorine on the fireside corrosion behaviour of boiler tubing: A UK perspective", *Corrosion,* no. 133.

[71] Shim, H., Valentine, J. R., Davis, K., Seo, S. and Kim, T. (2008), "Development of fireside waterwall corrosion correlations using pilot-scale test furnace", *Fuel,* vol. 87, no. 15-16, pp. 3353-3361.

[72] Kalivodová, J., Baxter, D., Schütze, M. and Rohr, V. (2008), "Corrosion behaviour of boiler steels, coatings and welds in flue gas environments", *Materials and Corrosion,* vol. 59, no. 5, pp. 367-373.

[73] Viswanathan, R. and Bakker, W. (2001), "Materials for ultrasupercritical coal power plants - boiler materials: Part 1", *Journal of Materials Engineering and Performance,* vol. 10, no. 1, pp. 81-95.

[74] Zhao, S., Xie, X., Smith, G. D. and Patel, S. J. (2005), "The corrosion of INCONEL alloy 740 in simulated environments for pulverized coal-fired boiler", *Materials Chemistry and Physics,* vol. 90, no. 2-3, pp. 275-281.

[75] Viswanathan, R. and Bakker, W. (2000), "Materials for Boilers in Ultra Supercritical Power Plants", *2000 International Joint Power Generation Conference,* 23-26 July, Miami Beach, Florida, .

[76] Holmes, D. R. (1968), "New corrosion-resistant high temperature heat exchanger materials", *Corrosion Science,* vol. 8, no. 8, pp. 603-622.

[77] Airiskallio, E., Nurmi, E., Heinonen, M. H., Väyrynen, I. J., Kokko, K., Ropo, M., Punkkinen, M. P. J., Pitkänen, H., Alatalo, M., Kollár, J., Johansson, B. and Vitos, L. (2010), "High temperature oxidation of Fe–Al and Fe–Cr–Al alloys: The role of Cr as a chemically active element", *Corrosion Science,* vol. 52, no. 10, pp. 3394-3404.

[78] Masuyama, F. (2001), "History of power plants and progress in heat resistant steels", *ISIJ International,* vol. 41, no. 6, pp. 612-625.

[79] F. Masuyama (1999), *New developments in steels for power generation boilers in Advanced Heat Resistant Steels for Power Generation,* IOM Communications Ltd., London.

[80] Encinas-Oropesa, A. (2005), *A study of Hot Corrosion of single crystal superalloys and Platinum-Aluminide coatings* (PhD thesis), Cranfield University, .

[81] Cutler, A. J. B. and Raask, E. (1981), "External corrosion in coal-fired boilers: Assessment from laboratory data", *Corrosion Science,* vol. 21, no. 11, pp. 789-800.

[82] Hendry, A. and Lees, D. J. (1980), "Corrosion of austenitic steels in molten sulphate deposits", *Corrosion Science,* vol. 20, no. 3, pp. 383-404.

[83] Reid, W. T., Corey, R. C. and Cross, B. J. (1945), "External corrosion of furnace wall tubes: Part I - History and occurrence", *Trans.ASME,* vol. 67, pp. 279-288.

[84] Srivastava, S. C., Godiwalla, K. M. and Banerjee, M. K. (1997), "Fuel ash corrosion of boiler and superheater tubes", *Journal of Materials Science (UK),* vol. 32, no. 4, pp. 835-849.

[85] Folkeson, N., Johansson, L. -. and Svensson, J. -. (2007), "Initial stages of the HCl-induced high-temperature corrosion of alloy 310", *Journal of the Electrochemical Society,* vol. 154, no. 9, pp. C515-C521.

[86] Uusitalo, M. A., Vuoristo, P. M. J. and Mäntylä, T. A. (2004), "High temperature corrosion of coatings and boiler steels below chlorine-containing salt deposits", *Corrosion Science,* vol. 46, no. 6, pp. 1311-1331.

[87] Ahila, S. and R, I. (1992), "Fire-side corrosion of superheaters and reheaters in coal fired boilers", *Tool & Alloy Steels,* vol. 26, no. 2-3.

[88] Grabke, H. J., Reese, E. and Spiegel, M. (1995), "The effects of chlorides, hydrogen chloride, and sulfur dioxide in the oxidation of steels below deposits", *Corrosion Science,* vol. 37, no. 7, pp. 1023-1043.

[89] Li, L., Duan, Y., Cao, Y., Chu, P., Carty, R. and Pan, W. (2007), "Field corrosion tests for a low chromium steel carried out at superheater area of a utility boiler with three coals containing different chlorine contents", *Fuel Processing Technology,* vol. 88, no. 4, pp. 387-392.

[90] Stringer, J. (1993), "High temperature corrosion in practical systems", *J. Phys. IV France,* vol. 3, pp. 43-61.

[91] Kalivodova, J., Baxter, D., Schu□tze, M. and Rohr, V. (2005), "Gaseous corrosion of alloys and novel coatings in simulated environments for coal, waste and biomass boilers", *Materials and Corrosion,* vol. 56, no. 12, pp. 882-889.

[92] *Draft code of practice for discontinuous corrosion testing in high temperature gaseous atmospheres,* (2000), EC project SMT4-CT95-2001, TESTCORR. UK: ERA Technology.

[93] Corey, R. C., Cross, B. J. and Reid, W. T. (1945), *Trans. ASME,* vol. 67, pp. 289.

[94] Laux, S., Grusha, J. and Tillman, D. (2011), *Co-firing of Biomass and Opportunity Fuels in Low NOx Burners*, available at: http://www.fwc.com/publications/tech_papers/powgen/pdfs/clrw_bio.pdf (accessed Sep).

[95] Baxter, L. (2005), "Biomass-coal co-combustion: opportunity for affordable renewable energy", *Fuel,* vol. 84, no. 10, pp. 1295-1302.

[96] Simms, N. J., Kilgallon, P. J. and Oakey, J. E. (2007), "Degradation of heat exchanger materials under biomass co-firing conditions", *Materials at High Temperatures,* vol. 24, no. 4, pp. 333-342.

[97] Henderson, P., Szakalos, P., Pettersson, R., Anderson, C. and Hogberg, J. (2006), "Reducing superheater corrosion in wood-fired boilers", *Materials and Corrosion,* vol. 57, no. 2, pp. 128-134.

[98] Jappe Frandsen, F. (2005), "Utilizing biomass and waste for power production—a decade of contributing to the understanding, interpretation and analysis of deposits and corrosion products", *Fuel,* vol. 84, no. 10, pp. 1277-1294.

[99] Michelsen, H. P., Frandsen, F., Dam-Johansen, K. and Larsen, O. H. (1998), "Deposition and high temperature corrosion in a 10 MW straw fired boiler", *Fuel Processing Technology,* vol. 54, no. 1-3, pp. 95-108.

[100] Baxter, L. L., Miles, T. R., Miles, T. R., Jenkins, B. M., Milne, T., Dayton, D., Bryers, R. W. and Oden, L. L. (1998), "The behavior of

inorganic material in biomass-fired power boilers: field and laboratory experiences", *Fuel Processing Technology,* vol. 54, no. 1-3, pp. 47-78.

[101] Nielsen, H. P., Baxter, L. L., Sclippab, G., Morey, C., Frandsen, F. J. and Dam-Johansen, K. (2000), "Deposition of potassium salts on heat transfer surfaces in straw-fired boilers: A pilot-scale study", *Fuel,* vol. 79, no. 2, pp. 131-139.

[102] Simms, N. J., Kilgallon, P. J. and Oakey, J. E. (2006), "Heat Exchanger Corrosion in Biomass and Coal Co-fired Power Plants", in J Lecomte-Becker et al (ed.), *Materials for Advanced Power Engineering 2006,* 18-20 Sept. 2006, Liege, Belgium, pp. 1513.

[103] Aho, M., Gil, A., Taipale, R., Vainikka, P. and Vesala, H. (2008), "A pilot-scale fireside deposit study of co-firing Cynara with two coals in a fluidised bed", *Fuel,* vol. 87, pp. 58-69.

[104] Kilgallon, P. J., Oakey, J. E. and Simms, N. J. (2005), "Modelling Corrosion in Biomass-Fired Power Plants", Vol. 05318.

[105] Pettersson, C., Pettersson, J., Asteman, H., Svensson, J. -. and Johansson, L. -. (2006), "KCl-induced high temperature corrosion of the austenitic Fe–Cr–Ni alloys 304L and Sanicro 28 at 600 °C", *Corrosion Science,* vol. 48, no. 6, pp. 1368-1378.

[106] Pettersson, J., Svensson, J. -. and Johansson, L. -. (2009), "KCl-induced corrosion of a 304-type austenitic stainless steel in O 2 and in O2 + H2O environment: The influence of temperature", *Oxidation of Metals,* vol. 72, no. 3-4, pp. 159-177.

[107] Pettersson, J., Folkeson, N., Johansson, L. -. and Svensson, J. -. (2011), "The Effects of KCl, K2SO4 and K2CO3 on the High Temperature Corrosion of a 304-Type Austenitic Stainless Steel", *Oxidation of Metals,* pp. 1-17.

[108] Van Lith, S. C., Frandsen, F. J., Montgomery, M., Vilhelmsen, T. and Jensen, S. A. (2009), "Lab-scale investigation of deposit-induced chlorine corrosion of superheater materials under simulated biomass-firing conditions. Part 1: Exposure at 560°C", *Energy and Fuels,* vol. 23, no. 7, pp. 3457-3468.

[109] Montgomery, M., Karlsson, A. and Larsen, O. H. (2002), "Field test corrosion experiments in Denmark with biomass fuels Part 1: Straw-firing", *Materials and Corrosion,* vol. 53, pp. 121-131.

[110] Zheng, Y., Jensen, P. A., Jensen, A. D., Sander, B. and Junker, H. (2007), "Ash transformation during co-firing coal and straw", *Fuel,* vol. 86, no. 7-8, pp. 1008-1020.

[111] Regional Biomass Energy Program (2009), *Biomass co-firing in existing power plants*, available at: http://www.earthscape.org/r1/ES17359/DOE_Biomass.pdf. (accessed May/27).

[112] Stanger, R. and Wall, T. (2010), "Sulphur impacts during pulverised coal combustion in oxy-fuel technology for carbon capture and storage", *Progress in Energy and Combustion Science*.

[113] Buhre, B. J. P., Elliott, L. K., Sheng, C. D., Gupta, R. P. and Wall, T. F. (2005), "Oxy-fuel combustion technology for coal-fired power generation", *Progress in Energy and Combustion Science,* vol. 31, no. 4, pp. 283-307.

[114] Hadjipaschalis, I., Kourtis, G. and Poullikkas, A. (2009), "Assessment of oxyfuel power generation technologies", *Renewable and Sustainable Energy Reviews,* vol. 13, no. 9, pp. 2637-2644.

[115] Kakaras, E., Koumanakos, A., Doukelis, A., Giannakopoulos, D. and Vorrias, I. (2007), "Oxyfuel boiler design in a lignite-fired power plant", *Fuel,* vol. 86, no. 14, pp. 2144-2150.

[116] Rathnam, R. K., Elliott, L. K., Wall, T. F., Liu, Y. and Moghtaderi, B. (2009), "Differences in reactivity of pulverised coal in air (O2/N2) and oxy-fuel (O2/CO2) conditions", *Fuel Processing Technology,* vol. 90, no. 6, pp. 797-802.

[117] Pirón Abellán, J., Olszewski, T., Penkalla, H. J., Meier, G. H., Singheiser, L. and Quadakkers, W. J. (2009), "Scale formation mechanisms of martensitic steels in high CO 2/H2O-containing gases simulating oxyfuel environments", *Materials at High Temperatures,* vol. 26, no. 1, pp. 63-72.

[118] Zheng, X. G. and Young, D. J. (1994), "High temperature corrosion of pure chromium in CO-CO2-SO2-N2 atmospheres", *Corrosion Science,* vol. 36, no. 12, pp. 1999-2015.

[119] Huenert, D. and Kranzmann, A. (2011), "Impact of oxyfuel atmospheres H2O/CO2/O2 and H2O/CO2 on the oxidation of ferritic–martensitic and austenitic steels", *Corrosion Science,* vol. 53, no. 6, pp. 2306-2317.

[120] Kranzmann, A., Neddemeyer, T., Ruhl, A. S., Huenert, D., Bettge, D., Oder, G. and Neumann, R. S. "The challenge in understanding the corrosion mechanisms under oxyfuel combustion conditions", *International Journal of Greenhouse Gas Control,* vol. In Press, Corrected Proof.

[121] Gheno, T., Monceau, D., Zhang, J. and Young, D. J. (2011), "Carburisation of ferritic Fe–Cr alloys by low carbon activity gases", *Corrosion Science,* vol. 53, no. 9, pp. 2767-2777.

[122] Ochs, T. L., Oryshchyn, D. B., Gross, D., Patrick, B., Dogan, C. and Summers, C. (2004), *Oxy-fuel Combustion Systems for Pollution Free Coal Fired Power Generation*.

[123] Covino Jr., B.S., Matthes, S.A. and Bullard, S.J., (2008), *Effect of oxyfuel combustion on superheater corrosion*.

[124] Davis, C. (2011), "Pilot Scale Studies of the Fireside Corrosion Effects of Biomass Co-Firing and / or Oxy-fuel
Coal Firing", Vol. Paper 11188.

[125] Orchard, J. P. and Young, D. J. (1989), "Sulfidation behavior of an iron-nickel alloy", *Journal of the Electrochemical Society,* vol. 136, no. 2, pp. 545-550.

[126] Raask, E. (1985), *Mineral impurities in coal combustion behavior, problems, and remedial measures*.

[127] Simms, N. J. and Fry, A. T. (2010), "Modelling fireside corrosion of heat exchangers in co-fired pulverised fuel power systems. .", in Lecomte-Beckers, J. and Carton, M. (eds).

[128] Rigaku Corporation (2011), *Theory of X-ray Diffraction*, available at: http://www.jeffreycreid.com/Analytical_Methods/XRD_theory.html (accessed June).

[129] Braun, R. D. (1983), *Introduction to Chemical Analysis,* McGraw-Hill.

[130] Hobart, H. W., Lynne, L. M. and John, A. D. (eds.) (1974), *Instrumental Methods of Analysis,* 5th ed, D. Van Nostrand Company.

[131] Syed, A. U., Hussain, T., Oakey, J. E. and Simms, N. J. (2011), "Fireside corrosion of superheater materials in oxy-fired power plants", Vol. paper 4706, 5-8 Sep, Stockholm.

[132] Baker, B.A., Smith, G.D (2004), "Corrosion resistance of alloy 740 as superheater tubing in coal-fired ultra-supercritical boilers", 28 March -1 April, New Orleans, LA, pp. Paper 04526.

[133] Young, D. J. (2008), *High Temperature Oxidation and Corrosion of Metals*.

[134] Bankiewicz, D., Yrjas, P. and Hupa, M. (2009), "High-temperature corrosion of superheater tube materials exposed to zinc salts", *Energy and Fuels,* vol. 23, no. 7, pp. 3469-3474.

[135] Syrett, B. C. (1987), *Corrosion in Fossil Fuel Power Plant',* Metals Handbook Ninth Edition ed, Corrosion, ASM International.

[136] White, M. (1996), *Superheater/intermediate temperature air heater tube corrosion tests in the MHD coal fired flow facility (Montana Rosebud POC tests),* DOE/ET/10815--232; UTSI--95/05.

[137] Otsuka, N., Fukuda, Y., Kawahara, Y. and Hosoda, T. (2000), "Laboratory corrosion tests for simulating fireside wastage of superheater materials in waste incinerators", *Werkstoffe und Korrosion,* vol. 51, no. 4, pp. 236-241.

[138] Labuda, E. M., Cline, D. A. and Shields, K. J. (2000), "Fireside corrsoion in coal- and oil-fired units: Failure mechanims and methods of preventations", Vol. Paper No 00234, .

[139] Nielsen, H. P., Frandsen, F. J., Dam-Johansen, K. and Baxter, L. L. (2000), "The implications of chlorine-associated corrosion on the operation of biomass-fired boilers", *Progress in Energy and Combustion Science,* vol. 26, no. 3, pp. 283-298.

[140] Karlsson, A., Møller, P. J. and Johansen, V. (1990), "Iron and steel corrosion in a system of O2, SO2 and alkali chloride. The formation of low melting point salt mixtures", *Corrosion Science,* vol. 30, no. 2-3, pp. 153-158.

[141] Simms, N. J., Oakey, J. E., Stephenson, D. J., Smith, P. J. and Nicholls, J. R. (1995), "Erosion-corrosion modelling of gas turbine materials for coal-fired combined cycle power generation", *Wear,* vol. 186-187, no. Part 1, pp. 247-255.

APPENDICES

Appendix A Publications and Presentations

A.1 List of Publications

A.1.1 Journal papers

1) Syed, A. U., Simms, N. J. and Oakey, J. E. (2011), "Fireside corrosion of superheaters: Effects of air and oxy-firing of coal and biomass", ***Fuel,***. (In Press).

2) Syed, A. U., Hussain, T., Simms, N. J. and Oakey, J. E. "Microscopy of Fireside Corrosion on Superheater Materials for Advanced Power Plants", ***Materials at High Temperatures*** (Accepted).

A.1.2 Conference papers

1) Syed, A. U., Simms, N. J. and Oakey, J. E. (2010), "Fireside corrosion of superheaters/reheaters in advanced power plants", *9th Liege Conference:* ***Materials for Advanced Power Engineering,*** 27-29 September, Belgium, pp. 976-985.

2) Syed, A. U., Hussain, T., Oakey, J. E. and Simms, N. J. (2011), "Fireside corrosion of superheater materials in oxy-fired power plants", ***Euro Corr*** paper 4706, 5-8 Sep, Stockholm.

A.2 List of Oral and Poster presentations

A.2.1 Oral Presentations

1) 8th European Conference on Coal Research and Its Applications: Eccria 8, University of Leeds, 6-8 Sep 2010. *"Fireside corrosion of superheaters:effects of air and oxy-firing of coal and biomass"*

2) 8th International Conference on Microscopy of Oxidation University of Liverpool 11-13 April 2011. "*Microscopy of Fireside Corrosion on Superheater Materials for Advanced Power Plants''*

3) EUROCORR 2011, 4 – 8 September 2011, Stockholm International Fairs, Sweden "*Fireside corrosion of superheater materials in oxy-fired power plants"*

4) Five presentations at bi annual meetings to 11 industrials sponsors ant three other universities (30-60 people)

A.2.2 Poster Presentation

1) Poster presented at UKERC energy summer school, Warwick University 2010

2) 9th LIÈGE CONFERENCE ON MATERIALS FOR ADVANCED POWER ENGINEERING, September 27th – 29 , 2010 Liège Belgium "*Fireside corrosion of superheaters/reheaters in advanced power plants (Presented by Nigel Simms)*

3) 'High Temperature Corrosion' Gordon Research Conferences USA July 24-29, 2011 "*Fireside corrosion of superheater materials in advanced biomass/coal air- and oxy-fired power plants"*

Appendix B Statistical Analysis

In general the potential sources of errors could be from the experimental design setup or the sample measurement. In this PhD thesis the experimental setup of fireside corrosion tests have followed the 'deposit recoat' technique that has been well established for high temperature corrosion testing [141].

B.1 Samples cutting error due to height

B.2 Tube segmentation

As explained earlier in the samples are machined from commercial tubes in a form of tube segments and a shallow hole was drilled in the samples which are used as a reference point for dimensional metrology investigations. Sources of errors in the samples provided could be due to unsymmetrical segmentation of a tube or could be due to poor sample finishing that leaving a rough surface. To counter this, samples were machined to specific shapes/size with a controlled surface finish. Figure B-1 illustrates how a reference point drilled into metal tube and further machined into number of segments.

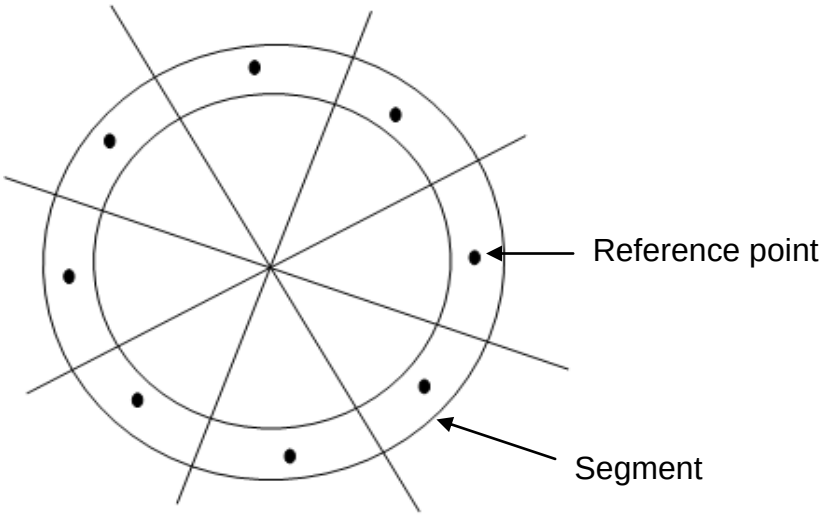

Figure B-1: An example of drawing shows a metal tube cut into segments and drilled hole

B.3 Dimensional metrology statistical errors

The sources of sample measurement errors in dimensional metrology are likely occur during sample preparation particularly during procedures for:

- Mounting
- Cutting
- Grinding and polishing

B.4 Sample height error

One of the possible source of errors is the cutting of samples mounted in resin into halves above or below the reference point (a drilled hole as previously explained) so a rectangular cross-section is obtained. Figure B-2 illustrates the error of cutting the sample below 1mm of the reference point. To determine the effect on the metal thickness due to the error in cutting the sample off the reference point, the equation of a circle is applied:

$$x^2 + y^2 = r^2 \quad \textbf{(B-1)}$$

Where r = radius of the tube

x=distance from origin

y= height away from reference point

At the reference point if the outer radius of the tube is 20 mm and inner radius is 16 mm where y=0. Considering a cut of 1mm below the reference point and put the values in equation. The x value at the outer radius will be

$$x^2 + y^2 = r^2 \quad \textbf{(B-2)}$$

or can be written as

$$x1'^2 = r^2 - y'1^2 \quad \textbf{(B-3)}$$

$$x1'^2 = (20)^2 - (1)^2 \quad \textbf{(B-4)}$$

$$x1' = 19.9749 \text{ mm} \quad \textbf{(B-5)}$$

Similarly the inner radius Where r = 16 mm at point y by putting the values in equation

$$x2'^2 = (16)^2 - (1)^2 \quad \textbf{(B-6)}$$

Further simplification will give

$$x2' = 15.9687 \text{ mm} \quad \textbf{(B-7)}$$

hence the wall thickness will be

$$x1' - x2' = 4.0062 \text{ mm} \quad \textbf{(B-8)}$$

So due to 1mm height error in cutting the effect on metal thickness is

4.0062 mm - 4.0000 mm = 6.2×10^{-3} mm or 6.2 μm.

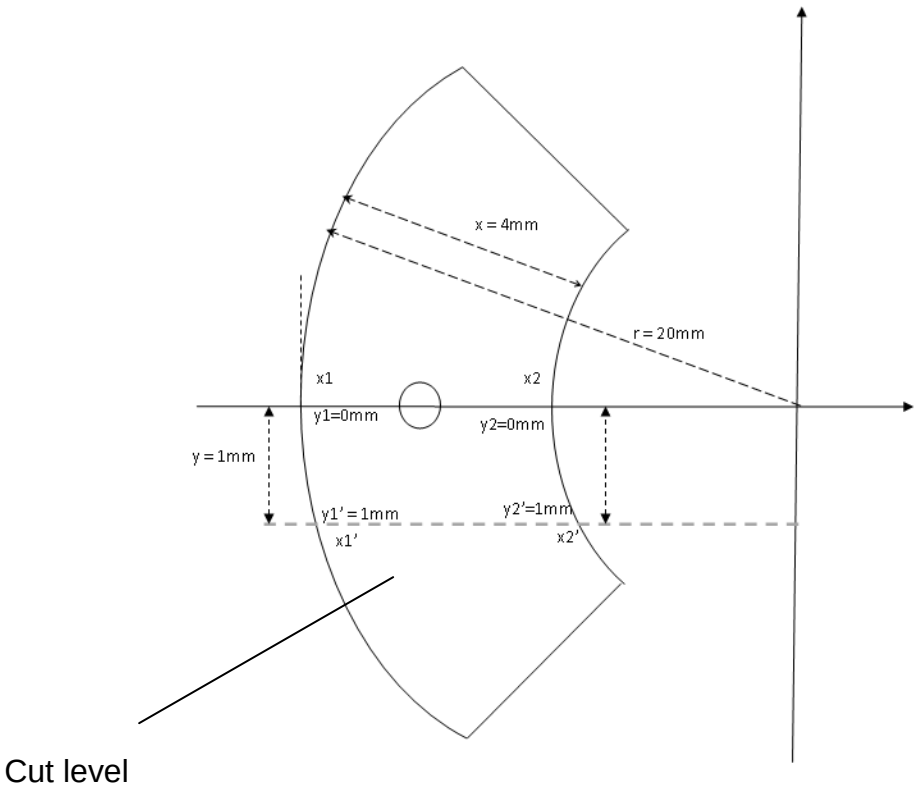

Figure B-2: Schematic of alloy segment shows a cut below the reference point

Depending on the result if 20 mm is the outer radius and 16 mm is the inner radius the sample thickness error at different heights can be calculated in the same manner and is listed in the Table B-1.

Table B-1: Statistical error due to sample cut off the reference point

Height	Thickness	Additional Thickness	Error
mm	μm	μm	%
0	4000	0	0
1	4006.2	6.2	0.155
2	4025.2	25.2	0.63
3	4057.5	57.5	1.4375
4	4104	104	2.6

Missing the cut level by more than 1mm is regarded as unlikely.

Appendix C Calculations spreadsheets

In this appendix section, calculations (spreadsheets) used during this PhD project are presented.

C.1 Calculations spreadsheet for deposits (D1-D4) preparation

Deposits D1-D4 for Corrosion Test

Element	Atomic mass
K	39.1
Na	23
S	32.1
O	16
Cl	35.5
Fe	55.8
Al	27
Si	28.1
H	1

Compound	Molar Mass
K2SO4	174.3
Na2SO4	142.1
KCl	74.6
Fe2O3	159.6
Al2O3.2SiO2.2H2O	258.2
Al2O3.2SiO2.2H2O	kalonite

			kalonite	Na2SO4	K2SO4	KCl	Fe2O3
	Deposit 1	mol%	0	37.5	37.5	0	25
		mass/gm	0	53.288	65.363	0	39.9
mass reduced by 1/2		mass/gm	0	*26.644*	*32.681*	*0*	*19.95*
	Deposit 2	mol%	80	7.5	7.5	0	5
		mass/gm	206.56	10.658	13.073	0	7.98
mass reduced by 1/4		mass/gm	*51.64*	*2.6644*	*3.2681*	*0*	*1.995*
	Deposit 3	mol%	80	7	7	1	5
		mass/gm	206.56	9.947	12.201	0.746	7.98
mass reduced by 1/4		mass/gm	*51.64*	*2.4868*	*3.0503*	*0.1865*	*1.995*
	Deposit 4	mol%	80	5	5	5	5
		mass/gm	206.56	7.105	8.715	3.73	7.98
mass reduced by 1/4		mass/gm	*51.64*	*1.7763*	*2.1788*	*0.9325*	*1.995*

C.2 Calculations spreadsheet for deposits (D5-D10) preparation

Deposits D5-D10 for Corrosion Test

Element	Atomic mass
K	39.1
Na	23
S	32.1
O	16
Cl	35.5
Fe	55.8
Al	27
Si	28.1
H	1

Compound	Molar Mass
K2SO4	174.3
Na2SO4	142.1
KCl	74.6
Fe2O3	159.6
Al2O3.2SiO2.2H2O	258.2
SiO2	60.1
Al2O3.2SiO2.2H2O	kalonite

			kalonite	Na2SO4	K2SO4	KCl	Fe2O3	SiO2
	Deposit 5	mol%	0	0	100	0	0	0
		mass/gm	0	0	174.3	0	0	0
mass reduced by 1/2		mass/gm	0	0	87.15	0	0	0
mass reduced by 1/4					43.575			
	Deposit 6	mol%	0	0	0	100	0	
		mass/gm	0	0	0	74.6	0	
mass reduced by 1/4		mass/gm	0	0	0	18.65	0	
	Deposit 7	mol%	0	0	50	0	50	
		mass/gm	0	0	87.15	0	79.8	
mass reduced by 1/2					43.575	0	39.9	
mass reduced by 1/4		mass/gm	0	0	21.788	0	19.95	
	Deposit 8	mol%	0	0	50	0	0	50
		mass/gm	0	0	87.15	0	0	30.05
mass reduced by 1/2			0	0	43.575	0	0	15.025
mass reduced by 1/4		mass/gm	0	0	21.788	0	0	7.5125
	Deposit 9	mol%	0	0	0	50	50	
		mass/gm	0	0	0	37.3	79.8	
mass reduced by 1/2						18.65	39.9	
mass reduced by 1/4		mass/gm	0	0	0	9.325	19.95	
	Deposit 10	mol%	0	0	0	50	0	50
		mass/gm	0	0	0	37.3	0	30.05
mass reduced by 1/2			0	0	0	18.65	0	15.025
mass reduced by 1/4		mass/gm	0	0	0	9.325	0	7.5125

C.3 Calculations spreadsheet for determination of elemental concentration of deposit D1

Deposits D-1 Elemental concentrationfor Corrosion Test

Element	Atomic mass
K	39.1
Na	23
S	32.1
O	16
Cl	35.5
Fe	55.8
Al	27
Si	28.1
H	1

Compound	Molar Mass	Elemental wt % K	S	O	Na	Fe	Cl	Si	Al	H	Total
K2SO4	174.3	44.86517	18.4165	36.718302							100
Na2SO4	142.1		22.5897	45.038705	32.37157						100
KCl	74.6	52.41287					47.58713				100
Fe2O3	159.6			30.075188		69.924812					100
Al2O3.2SiO2.2H2O	258.2			55.77072				21.7661	20.91402	1.549187	100
SiO2	60.1			53.244592				46.7554			100
Al2O3.2SiO2.2H2O	kalonite										

Deposit	Mole %	wt/g	wt%	100 gm deposit contans	gm contains
kalonite	0	0	0	0.00	0.0000
Na2SO4	37.5	5328.75	33.60927	33.61	0.3361
K2SO4	37.5	6536.25	41.22517	41.23	0.4123
KCl	0	0	0	0.00	0.0000
Fe2O3	25	3990	25.16556	25.17	0.2517
SiO2	0	0	0	0	0.0000
	100	15855	100		

insert sample wt here in gm: 1.000 mg = 1000

if sample is dissolved in litre: 1.000 litre = 1000 ml

Elements	weight/gm	wt %	ppm
K	0.185	18.50	185
Na	0.109	10.88	109
Cl	0.000	0.00	0
S	0.152	15.18	152
Al	0.000	0.00	0
Si	0.000	0.00	0
Fe	0.176	17.60	176
O	0.378	37.84	378
H	0.000	0.00	0
	1.000	100.00	

Potassium K		gm
	K2SO4	0.41
	K	0.185
	KCl	0.00
	K	0
	Total K	0.185

Sodium Na		gm
	Na2SO4	0.34
	Na	0.109

Sulphur S		gm
	K2SO4	0.4123
	S	0.0759
	SO4	0.2273
	Na2SO4	0.3361
	S	0.0759
	SO4	0.227294
	Total Sulphu	0.1518
	total SO4	0.4546

Chloride Cl		gm
	KCl	0.00
	Cl	0

Hydrogen		gm
	kalonite	0.00
	H	0

Aluminium Al		gm
	kalonite	0.00
	Al	0

Iron Fe		gm
	Fe2O3	0.25
	Fe	0.17597
Total wt	1.000	

Silicon Si		gm
	kalonite	0.00
	Si	0
	SiO2	0.00
	Si	0
	total Si	0

Oxygen O	
K2SO4	0.41
O	0.15137181
Na2SO4	0.34
O	0.15137181
SiO2	0
O	0
Fe2O3	0.25
O	0.0756859
kalonite	0.00
O	0
Total Oxyge	0.37842952

C.4 Calculations spreadsheet for determination of elemental concentration of deposit D2

Deposits D-2 Elemental concentrationfor Corrosion Test

Element	Atomic mass
K	39.1
Na	23
S	32.1
O	16
Cl	35.5
Fe	55.8
Al	27
Si	28.1
H	1

Compound	Molar Mass	Elemental wt % K	S	O	Na	Fe	Cl	Si	Al	H
K2SO4	174.3	44.86517	18.4165	36.718302						
Na2SO4	142.1		22.5897	45.038705	32.37157					
KCl	74.6	52.41287					47.58713			
Fe2O3	159.6			30.075188		69.924812				
Al2O3.2SiO2.2H2O	258.2			55.77072				21.7661	20.91402	1.549187
SiO2	60.1			53.244592				46.7554		
Al2O3.2SiO2.2H2O	kalonite									

Deposit D2	Mole %	wt/g	wt%	100 gm deposit contans	gm contains
kalonite	80	20656	86.69157	86.69	0.87
Na2SO4	7.5	1065.75	4.472867	4.47	0.04
K2SO4	7.5	1307.25	5.486423	5.49	0.05
KCl	0	0	0	0.00	0.00
Fe2O3	5	798	3.349142	3.35	0.03
SiO2	0	0	0	0	0.00
	100	23827	100		

insert sample wt here in gm

	mg
1.000	1000

if sample is dissolved in litre

litre	ml
1.000	1000

Elements	weight/gm	wt %
K	0.025	2.46
Na	0.014	1.45
Cl	0.000	0.00
S	0.020	2.02
Al	0.181	18.13
Si	0.189	18.87
Fe	0.023	2.34
O	0.534	53.38
H	0.013	1.34
	1.000	100.00

Potassium K		gm
K2SO4	0.05	
K	0.025	
KCl	0.00	
K	0	
Total K	0.025	

Sodium Na		gm
Na2SO4	0.04	
Na	0.014	

Sulphur S		gm
K2SO4	0.05	
S	0.010	
SO4	0.0302	
Na2SO4	0.04	
S	0.010	
SO4	0.030249	
Total Sulphu	0.020	
total SO4	0.0605	

Chloride Cl		gm
KCl	0.00	
Cl	0	

Hydrogen		gm
kalonite	0.87	
H	0.01343	

Aluminium Al		gm
kalonite	0.87	
Al	0.181307	

Iron Fe		gm
Fe2O3	0.03	
Fe	0.023419	
Total wt	1.000	

Silicon Si		gm
kalonite	0.87	
Si	0.18869	
SiO2	0.00	
Si	0	
total Si	0.18869	

Oxygen O	
K2SO4	0.05
O	0.02014521
Na2SO4	0.04
O	0.02014521
SiO2	0
O	0
Fe2O3	0.03
O	0.01007261
kalonite	0.87
O	0.48348512
Total Oxyge	0.53384816

C.5 Calculations spreadsheet for determination of elemental concentration of deposit D3

Deposits D-3 Elemental concentrationfor Corrosion Test

Element	Atomic mass
K	39.1
Na	23
S	32.1
O	16
Cl	35.5
Fe	55.8
Al	27
Si	28.1
H	1

Compound	Molar Mass	Elemental wt % K	S	O	Na	Fe	Cl	Si	Al	H
K2SO4	174.3	44.86517	18.4165	36.718302						
Na2SO4	142.1		22.5897	45.038705	32.37157					
KCl	74.6	52.41287					47.58713			
Fe2O3	159.6			30.075188		69.924812				
Al2O3.2SiO2.2H2O	258.2			55.77072				21.7661	20.91402	1.549187
SiO2	60.1			53.244592				46.7554		
Al2O3.2SiO2.2H2O	kalonite									

Deposit D3	Mole %	wt/g	wt%	100 gm deposit contans	gm contains
kalonite	80	20656	86.99681	87.00	0.87
Na2SO4	7	994.7	4.189375	4.19	0.04
K2SO4	7	1220.1	5.138691	5.14	0.05
KCl	1	74.6	0.314193	0.31	0.00
Fe2O3	5	798	3.360934	3.36	0.03
SiO2	0	0	0	0	0.00
	100	23743.4	100		

insert sample wt here in gm: 1.000

if sample is dissolved in litre: litre 1.000

Elements	weight/gm	wt %
K	0.025	2.47
Na	0.014	1.36
Cl	0.001	0.15
S	0.019	1.89
Al	0.182	18.19
Si	0.189	18.94
Fe	0.024	2.35
O	0.533	53.30
H	0.013	1.35
	1.000	100.00

Potassium K		gm
K2SO4		0.05
K		0.023
KCl		0.00
K		0.001647
Total K		0.025

Sodium Na		gm
Na2SO4		0.04
Na		0.014

Sulphur S		gm
K2SO4		0.05
S		0.009
SO4		0.0283
Na2SO4		0.04
S		0.009
SO4		0.028332
Total Sulphu		0.019
total SO4		0.0567

Chloride Cl		gm
KCl		0.00
Cl		0.001495

Hydrogen		gm
kalonite		0.87
H		0.01348

Aluminium Al		gm
kalonite		0.87
Al		0.181945

Iron Fe		gm
Fe2O3		0.03
Fe		0.023501
Total wt	1.000	

Silicon Si		gm
kalonite		0.87
Si		0.18936
SiO2		0.00
Si		0
total Si		0.18936

Oxygen O	
K2SO4	0.05
O	0.0188684
Na2SO4	0.04
O	0.0188684
SiO2	0
O	0
Fe2O3	0.03
O	0.01010807
kalonite	0.87
O	0.48518746
Total Oxyge	0.53303234

C.6 Calculations spreadsheet for determination of elemental concentration of deposit D4

Deposits D-4 Elemental concentrationfor Corrosion Test

Element	Atomic mass
K	39.1
Na	23
S	32.1
O	16
Cl	35.5
Fe	55.8
Al	27
Si	28.1
H	1

Compound	Molar Mass	Elemental wt % K	S	O	Na	Fe	Cl	Si	Al	H	Total
K2SO4	174.3	44.86517	18.4165	36.718302							100
Na2SO4	142.1		22.5897	45.038705	32.37157						100
KCl	74.6	52.41287					47.58713				100
Fe2O3	159.6			30.075188		69.924812					100
Al2O3.2SiO2.2H2O	258.2			55.77072				21.7661	20.91402	1.549187	100
SiO2	60.1			53.244592				46.7554			100
Al2O3.2SiO2.2H2O	kalonite										

Deposit D4	Mole %	wt/g	wt%	100 gm deposit contans	gm contains
kalonite	80	20656	88.23957	88.24	0.88
Na2SO4	5	710.5	3.035157	3.04	0.03
K2SO4	5	871.5	3.722927	3.72	0.04
KCl	5	373	1.593404	1.59	0.02
Fe2O3	5	798	3.408945	3.41	0.03
SiO2	0	0	0	0	0.00
	100	23409	100		

insert sample wt here in gm: 1.000

if sample is dissolved in litre: litre 1.000

Elements	weight/gm	wt %	ppm
K	0.025	2.51	25
Na	0.010	0.98	10
Cl	0.008	0.76	8
S	0.014	1.37	14
Al	0.185	18.45	185
Si	0.192	19.21	192
Fe	0.024	2.38	24
O	0.530	52.97	530
H	0.014	1.37	14
	1.000	100.00	

Potassium K		gm
	K2SO4	0.04
	K	0.017
	KCl	0.02
	K	0.008351
	Total K	0.025

Sodium Na		gm
	Na2SO4	0.03
	Na	0.010

Sulphur S		gm
	K2SO4	0.04
	S	0.007
	SO4	0.0205
	Na2SO4	0.03
	S	0.007
	SO4	0.020526
	Total Sulphu	0.014
	total SO4	0.0411

Chloride Cl		gm
	KCl	0.02
	Cl	0.007583

Hydrogen		gm
	kalonite	0.88
	H	0.01367

Aluminium Al		gm
	kalonite	0.88
	Al	0.184544

Iron Fe		gm
	Fe2O3	0.03
	Fe	0.023837
Total wt	1.000	

Silicon Si		gm
	kalonite	0.88
	Si	0.19206
	SiO2	0.00
	Si	0
	total Si	0.19206

Oxygen O	
K2SO4	0.04
O	0.01366996
Na2SO4	0.03
O	0.01366996
SiO2	0
O	0
Fe2O3	0.03
O	0.01025247
kalonite	0.88
O	0.49211842
Total Oxyge	0.52971079

C.7 Calculations spreadsheet for determination of elemental concentration of deposit D5

Deposits D-5 Elemental concentrationfor Corrosion Test

Element	Atomic mass
K	39.1
Na	23
S	32.1
O	16
Cl	35.5
Fe	55.8
Al	27
Si	28.1
H	1

Compound	Molar Mass	Elemental wt % K	S	O	Na	Fe	Cl	Si	Al	H	Total
K2SO4	174.3	44.86517	18.4165	36.718302							100
Na2SO4	142.1		22.5897	45.038705	32.37157						100
KCl	74.6	52.41287					47.58713				100
Fe2O3	159.6			30.075188		69.924812					100
Al2O3.2SiO2.2H2O	258.2			55.77072				21.7661	20.91402	1.549187	100
SiO2	60.1			53.244592				46.7554			100
Al2O3.2SiO2.2H2O	kalonite										

Deposit D5	Mole %	wt/g	wt%	100 gm deposit contans	gm contains
kalonite	0	0	0	0.00	0.00
Na2SO4	0	0	0	0.00	0.00
K2SO4	100	17430	100	100.00	1.00
KCl	0	0	0	0.00	0.00
Fe2O3	0	0	0	0.00	0.00
SiO2	0	0	0	0	0.00
	100	17430	100		

insert sample wt here in gm: 1.000

if sample is dissolved in litre: litre 1.000

Elements	weight/gm	wt %	ppm
K	0.449	44.87	449
Na	0.000	0.00	0
Cl	0.000	0.00	0
S	0.184	18.42	184
Al	0.000	0.00	0
Si	0.000	0.00	0
Fe	0.000	0.00	0
O	0.367	36.72	367
H	0.000	0.00	0
	1.000	100.00	

Potassium K		gm
	K2SO4	1.00
	K	0.449
	KCl	0.00
	K	0
	Total K	0.449

Sodium Na		gm
	Na2SO4	0.00
	Na	0.000

Sulphur S		gm
	K2SO4	1.00
	S	0.184
	SO4	0.5513
	Na2SO4	0.00
	S	0.000
	SO4	0
	Total Sulphu	0.184
	total SO4	0.5513

Chloride Cl		gm
	KCl	0.00
	Cl	0

Hydrogen		gm
	kalonite	0.00
	H	0

Aluminium Al		gm
	kalonite	0.00
	Al	0

Iron Fe		gm
	Fe2O3	0.00
	Fe	0
Total wt	1.000	

Silicon Si		gm
	kalonite	0.00
	Si	0
	SiO2	0.00
	Si	0
	total Si	0

Oxygen O	
K2SO4	1.00
O	0.36718302
Na2SO4	0.00
O	0
SiO2	0
O	0
Fe2O3	0.00
O	0
kalonite	0.00
O	0
Total Oxyge	0.36718302

C.8 Calculations spreadsheet for determination of elemental concentration of deposit D6

Deposits D-6 Elemental concentrationfor Corrosion Test

Element	Atomic mass
K	39.1
Na	23
S	32.1
O	16
Cl	35.5
Fe	55.8
Al	27
Si	28.1
H	1

Compound	Molar Mass	Elemental wt % K	S	O	Na	Fe	Cl	Si	Al	H
K2SO4	174.3	44.86517	18.4165	36.718302						
Na2SO4	142.1		22.5897	45.038705	32.37157					
KCl	74.6	52.41287					47.58713			
Fe2O3	159.6			30.075188		69.924812				
Al2O3.2SiO2.2H2O	258.2			55.77072				21.7661	20.91402	1.549187
SiO2	60.1			53.244592				46.7554		
Al2O3.2SiO2.2H2O	kalonite									

Deposit D6	Mole %	wt/g	wt%	100 gm deposit contans	gm contains
kalonite	0	0	0	0.00	0.00
Na2SO4	0	0	0	0.00	0.00
K2SO4	0	0	0	0.00	0.00
KCl	100	7460	100	100.00	1.00
Fe2O3	0	0	0	0.00	0.00
SiO2	0	0	0	0	0.00
	100	7460	100		

insert sample wt here in gm: 1.000

if sample is dissolved in litre: litre 1.000

Elements	weight/gm	wt %
K	0.524	52.41
Na	0.000	0.00
Cl	0.476	47.59
S	0.000	0.00
Al	0.000	0.00
Si	0.000	0.00
Fe	0.000	0.00
O	0.000	0.00
H	0.000	0.00
	1.000	100.00

Potassium K		gm
K2SO4		0.00
K		0.000
KCl		1.00
K		0.524129
Total K		0.524

Sodium Na		gm
Na2SO4		0.00
Na		0.000

Sulphur S		gm
K2SO4		0.00
S		0.000
SO4		0.0000
Na2SO4		0.00
S		0.000
SO4		0
Total Sulphu		0.000
total SO4		0.0000

Chloride Cl		gm
KCl		1.00
Cl		0.475871

Hydrogen		gm
kalonite		0.00
H		0

Aluminium Al		gm
kalonite		0.00
Al		0

Iron Fe		gm
Fe2O3		0.00
Fe		0
Total wt	1.000	

Silicon Si		gm
kalonite		0.00
Si		0
SiO2		0.00
Si		0
total Si		0

Oxygen O	
K2SO4	0.00
O	0
Na2SO4	0.00
O	0
SiO2	0
O	0
Fe2O3	0.00
O	0
kalonite	0.00
O	0
Total Oxyge	0

C.9 Calculations spreadsheet for determination of elemental concentration of deposit D7

Deposits D-7Elemental concentrationfor Corrosion Test

Element	Atomic mass
K	39.1
Na	23
S	32.1
O	16
Cl	35.5
Fe	55.8
Al	27
Si	28.1
H	1

Compound	Molar Mass	Elemental wt % K	S	O	Na	Fe	Cl	Si	Al	H	Total
K2SO4	174.3	44.86517	18.4165	36.718302							100
Na2SO4	142.1		22.5897	45.038705	32.37157						100
KCl	74.6	52.41287					47.58713				100
Fe2O3	159.6			30.075188		69.924812					100
Al2O3.2SiO2.2H2O	258.2			55.77072				21.7661	20.91402	1.549187	100
SiO2	60.1			53.244592				46.7554			100
Al2O3.2SiO2.2H2O	kalonite										

Deposit D7	Mole %	wt/g	wt%	100 gm deposit contans	gm contains
kalonite	0	0	0	0.00	0.00
Na2SO4	0	0	0	0.00	0.00
K2SO4	50	8715	52.20126	52.20	0.52
KCl	0	0	0	0.00	0.00
Fe2O3	50	7980	47.79874	47.80	0.48
SiO2	0	0	0	0	0.00
	100	16695	100		

insert sample wt here in gm: 1.000

if sample is dissolved in litre: litre 1.000

Elements	weight/gm	wt %	ppm
K	0.234	23.42	234
Na	0.000	0.00	0
Cl	0.000	0.00	0
S	0.096	9.61	96
Al	0.000	0.00	0
Si	0.000	0.00	0
Fe	0.334	33.42	334
O	0.335	33.54	335
H	0.000	0.00	0
	1.000	100.00	

Potassium K		gm
	K2SO4	0.52
	K	0.234
	KCl	0.00
	K	0
	Total K	0.234

Sodium Na		gm
	Na2SO4	0.00
	Na	0.000

Sulphur S		gm
	K2SO4	0.52
	S	0.096
	SO4	0.2878
	Na2SO4	0.00
	S	0.000
	SO4	0
	Total Sulphu	0.096
	total SO4	0.2878

Chloride Cl		gm
	KCl	0.00
	Cl	0

Hydrogen		gm
	kalonite	0.00
	H	0

Aluminium Al		gm
	kalonite	0.00
	Al	0

Iron Fe		gm
	Fe2O3	0.48
	Fe	0.334232
Total wt	1.000	

Silicon Si		gm
	kalonite	0.00
	Si	0
	SiO2	0.00
	Si	0
	total Si	0

Oxygen O	
K2SO4	0.52
O	0.19167415
Na2SO4	0.00
O	0
SiO2	0
O	0
Fe2O3	0.48
O	0.14375562
kalonite	0.00
O	0
Total Oxyge	0.33542977

C.10 Calculations spreadsheet for determination of elemental concentration of deposit D8

Deposits D-8 Elemental concentrationfor Corrosion Test

Element	Atomic mass
K	39.1
Na	23
S	32.1
O	16
Cl	35.5
Fe	55.8
Al	27
Si	28.1
H	1

Compound	Molar Mass	Elemental wt % K	S	O	Na	Fe	Cl	Si	Al	H
K2SO4	174.3	44.86517	18.4165	36.718302						
Na2SO4	142.1		22.5897	45.038705	32.37157					
KCl	74.6	52.41287					47.58713			
Fe2O3	159.6			30.075188		69.924812				
Al2O3.2SiO2.2H2O	258.2			55.77072				21.7661	20.91402	1.549187
SiO2	60.1			53.244592				46.7554		
Al2O3.2SiO2.2H2O	kalonite									

Deposit D8	Mole %	wt/g	wt%	100 gm deposit contans	gm contains
kalonite	0	0	0	0.00	0.00
Na2SO4	0	0	0	0.00	0.00
K2SO4	50	8715	74.36007	74.36	0.74
KCl	0	0	0	0.00	0.00
Fe2O3	0	0	0	0.00	0.00
SiO2	50	3005	25.63993	25.63993	0.26
	100	11720	100		

insert sample wt here in gm: 1.000

if sample is dissolved in litre: litre 1.000

Elements	weight/gm	wt %
K	0.334	33.36
Na	0.000	0.00
Cl	0.000	0.00
S	0.137	13.69
Al	0.000	0.00
Si	0.120	11.99
Fe	0.000	0.00
O	0.410	40.96
H	0.000	0.00
	1.000	100.00

Potassium K		gm
K2SO4	0.74	
K	0.334	
KCl	0.00	
K	0	
Total K	0.334	

Sodium Na		gm
Na2SO4	0.00	
Na	0.000	

Sulphur S		gm
K2SO4	0.74	
S	0.137	
SO4	0.4100	
Na2SO4	0.00	
S	0.000	
SO4	0	
Total Sulphu	0.137	
total SO4	0.4100	

Chloride Cl		gm
KCl	0.00	
Cl	0	

Hydrogen		gm
kalonite	0.00	
H	0	

Aluminium Al		gm
kalonite	0.00	
Al	0	

Iron Fe		gm
Fe2O3	0.00	
Fe	0	

Silicon Si		gm
kalonite	0.00	
Si	0	
SiO2	0.26	
Si	0.11988	
total Si	0.11988	

Oxygen O	
K2SO4	0.74
O	0.27303754
Na2SO4	0.00
O	0
SiO2	0.25639932
O	0.13651877
Fe2O3	0.00
O	0
kalonite	0.00
O	0
Total Oxyge	0.40955631

Total wt 1.000

C.11 Calculations spreadsheet for determination of elemental concentration of deposit D9

Deposits D-9 Elemental concentrationfor Corrosion Test

Element	Atomic mass
K	39.1
Na	23
S	32.1
O	16
Cl	35.5
Fe	55.8
Al	27
Si	28.1
H	1

Compound	Molar Mass	Elemental wt % K	S	O	Na	Fe	Cl	Si	Al	H	Total
K2SO4	174.3	44.86517	18.4165	36.718302							100
Na2SO4	142.1		22.5897	45.038705	32.37157						100
KCl	74.6	52.41287					47.58713				100
Fe2O3	159.6			30.075188		69.924812					100
Al2O3.2SiO2.2H2O	258.2			55.77072				21.7661	20.91402	1.549187	100
SiO2	60.1			53.244592				46.7554			100
Al2O3.2SiO2.2H2O	kalonite										

insert sample wt here in gm

if sample is dissolved in litre

Deposit D9	Mole %	wt/g	wt%	100 gm deposit contans	gm contains
kalonite	0	0	0	0.00	0.00
Na2SO4	0	0	0	0.00	0.00
K2SO4	0	0	0	0.00	0.00
KCl	50	3730	31.85312	31.85	0.32
Fe2O3	50	7980	68.14688	68.15	0.68
SiO2	0	0	0	0	0.00
	100	11710	100		

litre	1.000
1.000	

Elements	weight/gm	wt %	ppm
K	0.167	16.70	167
Na	0.000	0.00	0
Cl	0.152	15.16	152
S	0.000	0.00	0
Al	0.000	0.00	0
Si	0.000	0.00	0
Fe	0.477	47.65	477
O	0.205	20.50	205
H	0.000	0.00	0
	1.000	100.00	

Potassium K		gm
	K2SO4	0.00
	K	0.000
	KCl	0.32
	K	0.166951
	Total K	0.167

Sodium Na		gm
	Na2SO4	0.00
	Na	0.000

Sulphur S		gm
	K2SO4	0.00
	S	0.000
	SO4	0.0000
	Na2SO4	0.00
	S	0.000
	SO4	0
	Total Sulphu	0.000
	total SO4	0.0000

Chloride Cl		gm
	KCl	0.32
	Cl	0.15158

Hydrogen		gm
	kalonite	0.00
	H	0

Aluminium Al		gm
	kalonite	0.00
	Al	0

Iron Fe		gm
	Fe2O3	0.68
	Fe	0.476516
Total wt	1.000	

Silicon Si		gm
	kalonite	0.00
	Si	0
	SiO2	0.00
	Si	0
	total Si	0

Oxygen O	
K2SO4	0.00
O	0
Na2SO4	0.00
O	0
SiO2	0
O	0
Fe2O3	0.68
O	0.20495303
kalonite	0.00
O	0
Total Oxyge	0.20495303

C.12 Calculations spreadsheet for determination of elemental concentration of deposit D10

Deposits D-10 Elemental concentrationfor Corrosion Test

Element	Atomic mass
K	39.1
Na	23
S	32.1
O	16
Cl	35.5
Fe	55.8
Al	27
Si	28.1
H	1

Compound	Molar Mass	Elemental wt % K	S	O	Na	Fe	Cl	Si	Al	H
K2SO4	174.3	44.86517	18.4165	36.718302						
Na2SO4	142.1		22.5897	45.038705	32.37157					
KCl	74.6	52.41287					47.58713			
Fe2O3	159.6			30.075188		69.924812				
Al2O3.2SiO2.2H2O	258.2			55.77072				21.7661	20.91402	1.549187
SiO2	60.1			53.244592				46.7554		
Al2O3.2SiO2.2H2O	kalonite									

Deposit D10	Mole %	wt/g	wt%	100 gm deposit contans	gm contains
kalonite	0	0	0	0.00	0.00
Na2SO4	0	0	0	0.00	0.00
K2SO4	0	0	0	0.00	0.00
KCl	50	3730	55.38233	55.38	0.55
Fe2O3	0	0	0	0.00	0.00
SiO2	50	3005	44.61767	44.61767	0.45
	100	6735	100		

insert sample wt here in gm: 1.000

if sample is dissolved in litre: litre 1.000

Elements	weight/gm	wt %
K	0.290	29.03
Na	0.000	0.00
Cl	0.264	26.35
S	0.000	0.00
Al	0.000	0.00
Si	0.209	20.86
Fe	0.000	0.00
O	0.238	23.76
H	0.000	0.00
	1.000	100.00

Potassium K		gm
K2SO4	0.00	
K	0.000	
KCl	0.55	
K	0.290275	
Total K	0.290	

Sodium Na		gm
Na2SO4	0.00	
Na	0.000	

Sulphur S		gm
K2SO4	0.00	
S	0.000	
SO4	0.0000	
Na2SO4	0.00	
S	0.000	
SO4	0	
Total Sulphu	0.000	
total SO4	0.0000	

Chloride Cl		gm
KCl	0.55	
Cl	0.263549	

Hydrogen		gm
kalonite	0.00	
H	0	

Aluminium Al		gm
kalonite	0.00	
Al	0	

Iron Fe		gm
Fe2O3	0.00	
Fe	0	
Total wt	1.000	

Silicon Si		gm
kalonite	0.00	
Si	0	
SiO2	0.45	
Si	0.20861	
total Si	0.20861	

Oxygen O	
K2SO4	0.00
O	0
Na2SO4	0.00
O	0
SiO2	0.44617669
O	0.23756496
Fe2O3	0.00
O	0
kalonite	0.00
O	0
Total Oxyger	0.23756496

C.13 Calculations spreadsheet for determination of ppm concentration of atoms/ions in deposits (D1-D10)

Deposit1		Deposit 2		Deposit 3		Deposit 4		Deposit 5		Deposit 6		Deposit 7		Deposit8		Deposit9		Deposit10	
Elements		Elements	ppm	Elements	ppm	Elements	ppm	Elements	ppm	Elements	ppm	Elements	ppm	Elements	ppm	Elements	ppm	Elements	ppm
K	185	K	25	K	24.7016	K	25.05447	K	448.6517	K	524.1287	K	234.2019	K	333.6177	K	166.9513	K	290.2747
Na	109	Na	14	Na	13.56166	Na	9.825281	Na	0	Na	0	Na	0	Na	0	Na	0	Na	0
Cl	0	Cl	0	Cl	1.495152	Cl	7.582554	Cl	0	Cl	475.8713	Cl	0	Cl	0	Cl	151.5798	Cl	263.5486
S	152	S	20	S	18.92737	S	13.71267	S	184.1652	S	0	S	96.13657	S	136.9454	S	0	S	0
Al	0	Al	181	Al	181.9453	Al	184.5444	Al	0	Al	0	Al	0	Al	0	Al	0	Al	0
Si	0	Si	189	Si	189.3579	Si	192.0629	Si	0	Si	0	Si	0	Si	119.8805	Si	0	Si	208.6117
Fe	176	Fe	23	Fe	23.50127	Fe	23.83699	Fe	0	Fe	0	Fe	334.2318	Fe	0	Fe	476.5158	Fe	0
O	378	O	534	O	533.0323	O	529.7108	O	367.183	O	0	O	335.4298	O	409.5563	O	204.953	O	237.565
H	0	H	13	H	13.47743	H	13.66996	H	0	H	0	H	0	H	0	H	0	H	0
SO4	454.5885	SO4	60	SO4	56.66417	SO4	41.05259	SO4	551.3483	SO4	0	SO4	287.8107	SO4	409.9829	SO4	0	SO4	0
					the above metal ppm concentration are when 1 g of deposit dissolved in 1 litre of solvent.														

C.14 Determination of ppm concentration for unexposed deposits (D1-D10) calculations spreadsheet example

Spreadsheet shows an example that how absolute wt % values for atoms and anions were calculated

Un-exposed deposits for IC

Deposits ppm concentrations

Deposits	samples wt (g)	mg	Vol in Litre	ml	K	Na	Cl	S	Al	Si	Fe	O	H	SO4
D1	0.0104	10.4	1	1000	1.924	1.134	0.000	1.58	0.00		1.83	3.93		4.72772
D2	0.0112	11.2	1	1000	0.276	0.162	0.000	0.23	2.03		0.26	5.98	0.15	0.672
D3	0.0119	11.9	1	1000	0.294	0.161	0.018	0.23	2.17		0.28	6.34	0.16	0.674304
D4	0.0109	10.9	1	1000	0.273	0.107	0.083	0.15	2.01		0.26	5.77	0.15	0.447473
D5	0.0131	13.1	1	1000	6			2				5		7.222662
D6	0.0131	13.1	1	1000	7		6.234							0
D7	0.0132	13.2	1	1000	3			1			4	4		3.799102
D8	0.0112	11.2	1	1000	4			2				5		4.591809
D9	0.0112	11.2	1	1000	2		1.698				5			0
D10	0.0102	10.2	1	1000	3		2.688					2		0

RESULTS FROM IC

deposits	Retention time Chloride	amount	Retention time-sulphate	amount	Absolute percentages of anions	
	min	Cl-mg/L	min	SO4 mg/L	Cl wt%	SO4 Wt%
D1	n.a.	n.a.	18.944	5.4305	#VALUE!	52.216
D2	n.a.	n.a.	19.03	0.6736	#VALUE!	6.014
D3	n.a.	n.a.	19.027	0.9107	#VALUE!	7.653
D4	6.713	0.0795	19.03	1.0626	0.729358	9.749
D5	n.a.	n.a.	18.927	7.5544	#VALUE!	57.667
D6	6.75	7.4589	n.a.	n.a.	56.93817	#VALUE!
D7	n.a.	n.a.	18.977	5.1779	#VALUE!	39.227
D8	n.a.	n.a.	18.954	6.3387	#VALUE!	56.596
D9	6.703	1.8804	n.a.	n.a.	16.78929	#VALUE!
D10	6.714	3.3924	n.a.	n.a.	33.25882	#VALUE!